Effect of sulphur content on the recrystallisation behaviour of cold worked low carbon Aluminium-killed strip steels

Charles W. Siyasiya

Effect of sulphur content on the recrystallisation behaviour of cold worked low carbon Aluminium-killed strip steels

By

Charles W. Siyasiya

Supervised by

Professor Waldo E. Stumpf

Submitted in partial fulfilment of the requirements for the degree

Philosophiae Doctor (Metallurgy)

in the

Department of Materials Science and Metallurgical Engineering

Faculty of Engineering, Built Environment and Information Technology

University of Pretoria

Republic South Africa

31st March 2007

Acknowledgement

Firstly, I would like to thank God for affording me the opportunity to study for this degree at the University of Pretoria.

I am greatly indebted to my supervisor Professor Waldo E. Stumpf for his invaluable guidance and input in this research project. I benefited a lot from his experience and insights during this research work.

I would like also to extend my gratitude for the valuable contribution from Professor Gerrit T. van Rooyen. His vast experience made life easier for me in setting up the experiments particularly for the thermoelectric power (TEP) technique.

I would like to express my sincere gratitude to my dear wife Daisy and children who have patiently allowed me to study at the expense of having good times together and countless other little things, all of which only love could endure.

I would like to thank Dr. Nic van der Berg for his contribution in the area of electron diffraction indexing and Mr C. van der Merve for helping with the transmission electron microscope. I would like also to thank Mr. Z. Tang for valuable help in the experimental work.

I would like to extend my gratitude to the IMMRI staff, in particular Mrs Alison Tuling and Mr Francois Verdoorn for the training and guidance during laboratory work in transmission electron microscope and Gleeble 1500^{TM} simulator respectively.

I would like to thank Mrs Sarah Havenga, Elsie Snyman-Ferreira and Lilian Barlow for the administrative work.

I would like to acknowledge the cooperation, sponsorship, provision of materials and relevant data from Mittal Steel South Africa.

Finally I would like to thank the University of Pretoria, in particular the Materials Science and Metallurgical Engineering Department for the provision of facilities that made it possible for me to complete my studies successfully.

Summary

Charles W. Siyasiya

Supervisor: Professor Waldo. E. Stumpf

Department: Materials Science and Metallurgical Engineering

University: University of Pretoria

Degree: Philosophiae Doctor (Metallurgy)

The influence of the sulphur and nitrogen content on the static recrystallisation behaviour of cold worked low carbon Al-killed strip steels was investigated. This was in response to the observation made by some users of these steels that the recrystallisation process after cold work was “sluggish” in some steels and, therefore, this was affecting their productivity as the continuous annealing lines had to be run slower and the batch annealing cycles required a higher annealing temperature and thus more energy input.

Two groups of Al-killed low carbon strip steels, one with low (<10 ppm) and the other with medium to high (> 70 ppm) sulphur content were studied. It was found that sulphur had an indirect but significant effect on the recrystallisation behaviour after cold work of these steels. In the high sulphur content steels, the

sulphur precipitated as manganese sulphide (MnS) and copper sulphide (CuS/Cu_2S) coarse particles. These sulphide particles, particularly MnS, were the favoured nucleation sites for aluminium nitride (AlN) and the heterogeneous nucleation encouraged the precipitation of AlN during coiling after hot rolling. The result was that the AlN in medium to high sulphur content steels was generally associated with coarse sulphides and, therefore, the mean particle size of the AlN/MnS particles in the as-coiled steel prior to cold working and annealing, was generally much coarser than in the steels with low sulphur content. In these low sulphur content steels, the AlN nucleated homogeneously in the matrix or heterogeneously on grain boundaries or dislocations during coiling. Consequently the mean particle size of AlN in these low sulphur content steels was significantly finer, often less than 30 nm in diameter and, therefore, these particles were more effective in retarding the recrystallisation process through Zener-pinning of dislocations and moving recrystallisation fronts.

The effect of lower sulphur content was exacerbated by lower coiling temperatures (~600 °C) i.e. the recrystallisation start time increased with a decrease in coiling temperature as the AlN particles remained small due to a low coarsening rate. On the contrary, no significant sensitivity to coiling temperature was observed in the time for the start of recrystallisation after cold work in medium to high sulphur steels within the coiling temperature range 600 to 650 °C. The conclusion was that sulphur, in the presence of manganese, does not hinder

Summary

recrystallisation after cold work in Al-killed steels but promotes heterogeneous nucleation and growth of AlN on the coarser MnS. The effect is that the effective mean particle size of the AlN becomes much larger as it is not isolated homogeneously as in low sulphur steels but is tied to the sulphides. The sulphur (ppm) dependent empirical expressions for the recrystallisation start times $t_{5\%}$ at isothermal annealing temperature of 610 °C for steels coiled at temperatures of 600 and 650 °C were found to be:

$t_{5\%}$ = 33.78exp(-0.0345S) for 600 °C and

$t_{5\%}$ = 0.99exp(-0.008S) for 650 °C.

Recrystallisation arrest was observed during the annealing process after cold work of as-quenched specimens. The apparent activation energy of the process that led to the recrystallisation arrest, being 230 kJ mol^{-1}, is of the order of the activation energy for the diffusion of aluminium in ferrite, i.e. 196.5 kJ mol^{-1}. Since the precipitation process of AlN is controlled by the slower diffusion of aluminium, this was an indication of the nucleation/clustering of fine particles of AlN, which consequently halted the recrystallisation process through effective Zener drag. This Zener-pinning effect was used to estimate indirectly the precipitation start and finish times for the AlN during the isothermal annealing after cold work of these steels.

Summary

The solubility of AlN in austenite has mostly been studied by others using the Beeghly selective dissolution technique which has often been criticised for its limitations in its lack of sensitivity to the presence of very fine AlN particles, i.e. < 10 nm, and its failure to separate the AlN from other nitrides. In this study the thermoelectric power technique [TEP] was used to study the solubility of AlN in austenite in commercial low carbon Al-killed steels; one group with a medium to higher sulphur content and the other with a lower one. The equilibrium solubility equation thus obtained was determined as:

$$\mathrm{Log}[\%\mathrm{Al}][\%\mathrm{N}] = 2.6 - \frac{9710}{\mathrm{T}}$$

where the aluminium and the nitrogen contents are in weight percentages and T is the absolute solution temperature in Kelvin.

It was found that the AlN solubility equation derived here predicted slightly higher solubility temperatures for the AlN if compared to those derived from the Beeghly method. It was also confirmed that the equilibrium solubility of AlN was not sensitive to the sulphur content (unlike the precipitation behaviour), which is in agreement with the results from others obtained through the Beeghly technique.

Summary

Key words: Heterogeneous and homogeneous nucleation, Zener-pinning force, mean particle size, activation energy, driving force, static recrystallisation, Avrami exponent and constant.

Table of contents

Table of contents

Table of contents

Table of contents

Chapter 13

Discussion

List of figures

Figure 12.15: The Zener-pinning effect start Z_{start} and finish Z_{finish} times in minutes which were derived from the recrystallisation arrest times in figure 11.12.

Figure 12.16: The recrystallised volume fraction versus isothermal annealing time for steels LS2-65, LS70-38, HS140-104 and HS90-12 after solution treatment at 1300 °C, water quenching, cold working 70 percent and isothermally annealing at 610 °C for various times.

Figure 12.17: Avrami plots for steels LS70-38 and HS90-12 from the data in figure 11.16.

Figure 12.18: Recrystallised volume fraction for steels HS140-104, LS70-38 and LS2-65 which were coiled at 600 °C and 650 °C, cold worked 70 percent and isothermally annealed at 600 °C and 650 °C in a lead bath for various times. CT stands for coiling temperature.

Figure 12.19: Avrami plots from the sigmoidal curves of recrystallised volume fraction versus isothermal annealing time for the steels and treatment given in figure 11.18.

Figure 12.20: The 5 percent recrystallisation time $t_{5\%}$ in minutes, plotted as a function of the sulphur content of the corresponding steel as labeled in the figure.

List of tables

Chapter 1 Background

1.1 Introduction

SAE 1006 is a typical low carbon-manganese strip steel and is widely used in the automotive and other industries. In South Africa, Mittal Steel (SA), previously known as ISCOR, produces this steel at both its Vanderbijlpark (VDB) as well as at its Saldanha Steel (SS) plants. The former is a conventional strip producing plant using the Cold Charge Route (CCR) in which the slab from the continuous caster is allowed to cool to below the A_{r1} temperature before reheating for hot rolling. The Saldanha Steel plant, however, uses the Hot Charge Route (HCR) in a Compact Strip Plant where the continuously cast slab in the austenitic phase, enters the roller hearth reheating furnace (RHF) directly before hot rolling. The Compact Strip Production (CSP) plant has fewer rolling passes than the conventional plant at VDB with a slab thickness of 75 or 90 mm as opposed to 240 mm of the VDB plant.

After start up of the Saldanha Steel plant in 1998 it was soon found that the mechanical properties as well as the ease of recrystallisation after cold work, was different in nominally equivalent products produced at the respective two plants with the hot rolled strip produced at Saldanha Steel about 50 MPa higher in yield strength and decidedly more "sluggish" in recrystallisation after cold work than its counterpart produced at VDB. Apart from the difference in hot strip production processes, there was a difference in the chemical composition in the steels from these two plants, particularly with regards to sulphur content at the time. Both plants add calcium in their steelmaking process. However, at the time when this project was initiated, Saldanha

Chapter 1 Background

Steel used to add calcium to its liquid steel (calcium ladle treatment) and this resulted in relatively low sulphur content in these steels, i.e. typically less than 10 ppm. The discontinuation of the calcium ladle treatment later resulted in a slight increase in the sulphur content to more than 20 ppm. However this is still lower if compared to the equivalent VDB steel where the sulphur content is usually higher, even up to 100 ppm or more.

The nitrogen content in the steels from the two plants was not significantly different and ranged from 30 to 100 ppm with the latter high values resulting from Electric Arc Furnace melting. Unlike the sulphur content, both plants produced their hot rolled strip within the same carbon and manganese content range as these constituents were not process related.

The primary motivation for this study was the observation that was encountered by the users of these SAE 1006 Al-killed low carbon steels, i.e. the difference in the recrystallisation behaviour after cold work of the steels from the two respective plants, with the steel from Saldanha Steel exhibiting delayed recrystallisation after cold rolling. For customers to accommodate this problem, the continuous annealing (CA) lines had to be run slower (thus reducing productivity) and the batch annealing (BA) cycles required a higher annealing temperature (thus more energy input).

1.2 Previous work

Initial experimental work[1] that involved simulation of different coiling temperatures, the determination of hardnesses and

examination of carbide morphology, led to the preliminary conclusions that the delay in the recrystallisation of SS material was not a result of one single, obvious mechanism. It was suggested that the solute carbon and nitrogen might have contributed to the observed difference in the recrystallisation behaviour. However, the results were not conclusive in this regard as evidenced by the fact that even with lower "solute" nitrogen content, the SS material still exhibited sluggish recrystallisation behaviour. This led to the suggestion that a more comprehensive study on the influence of sulphur on the static recrystallisation of these steels after cold work should be pursued. The only tangible conclusion from this early study was that SS material that had been coiled experimentally at higher temperatures of 710°C and even above, now recrystallised rapidly, and this was considered as evidence of the role played by the precipitation of AlN prior to cold work and annealing of these steels. However, coiling at higher temperatures could not be implemented in practice due to the difficulty in the removal of scale from the coiled strip.

The results from hot rolling studies also indicated that the difference in the process routes, CCR versus HCR, would unlikely have a significant influence on the final austenite grain size of the hot strip at the finishing mill head (FMH)[2-4]. Despite SS material having a finer ferrite grain size, there was no significant difference in the work hardening behaviour of these two steels[1]. Hence, for the same amount of cold deformation, the amount of stored energy for recrystallisation would be almost the same for the two steels. Therefore, the emphasis of this study was placed on understanding the role played by chemical composition differences

rather than effects arising from differences in the respective process routes.

No comprehensive study to elucidate the factors that influence the kinetics of the recrystallisation behaviour of these two steels that were of nominally very similar chemical composition, with the exception of sulphur, had been done before. Therefore, the intention of this research project was to understand the cause of the difference in the recrystallisation behaviour of these steels and to suggest a remedy for the problem. Two groups of low carbon strip steels; one from Saldanha Steel with low to medium sulphur content, designated LS onwards, and the other from Vanderbijlpark with medium to high sulphur content, designated HS onwards, were obtained for this study.

Chapter 2 An overview of the processing of low carbon steel plate and hot strip

2.1 Introduction

Low carbon strip steels are steels with invariably low carbon, mostly below 0.1%, and with less than 1% total alloying additions. These steels are produced in sheet and strip form and they form a large share of the low carbon flat products steel market. Table 2.1 shows the typical chemical composition of these steels.

Table 2.1: Typical chemical composition of hot rolled low carbon steel sheet and strip[5].

Element [wt%]	C	Mn	S	P
Composition range	0.05 – 0.1	0.25 – 0.5	0.04 max	0.035 max

The manganese is added for solid solution strengthening and prevention of hot shortness through the precipitation of MnS instead of FeS formation. The production process of these low carbon steel flat-rolled products is summarised in a simplified flow chart in figure 2.1.

Low carbon steels have a wide range of yield strengths from 250 to 500 MPa. The different combinations of yield strength and ductility are achieved through a combination of adding alloying elements and thermomechanical processing. The latter involves reheating of the semi-finished products (slabs and ingots), the hot

rolling that finishes at a specific finishing temperature, controlled accelerated cooling on the run-out table that promotes the nucleation of a fine ferrite grain size from austenite and coiling at a specific temperature to achieve the desired mechanical properties.

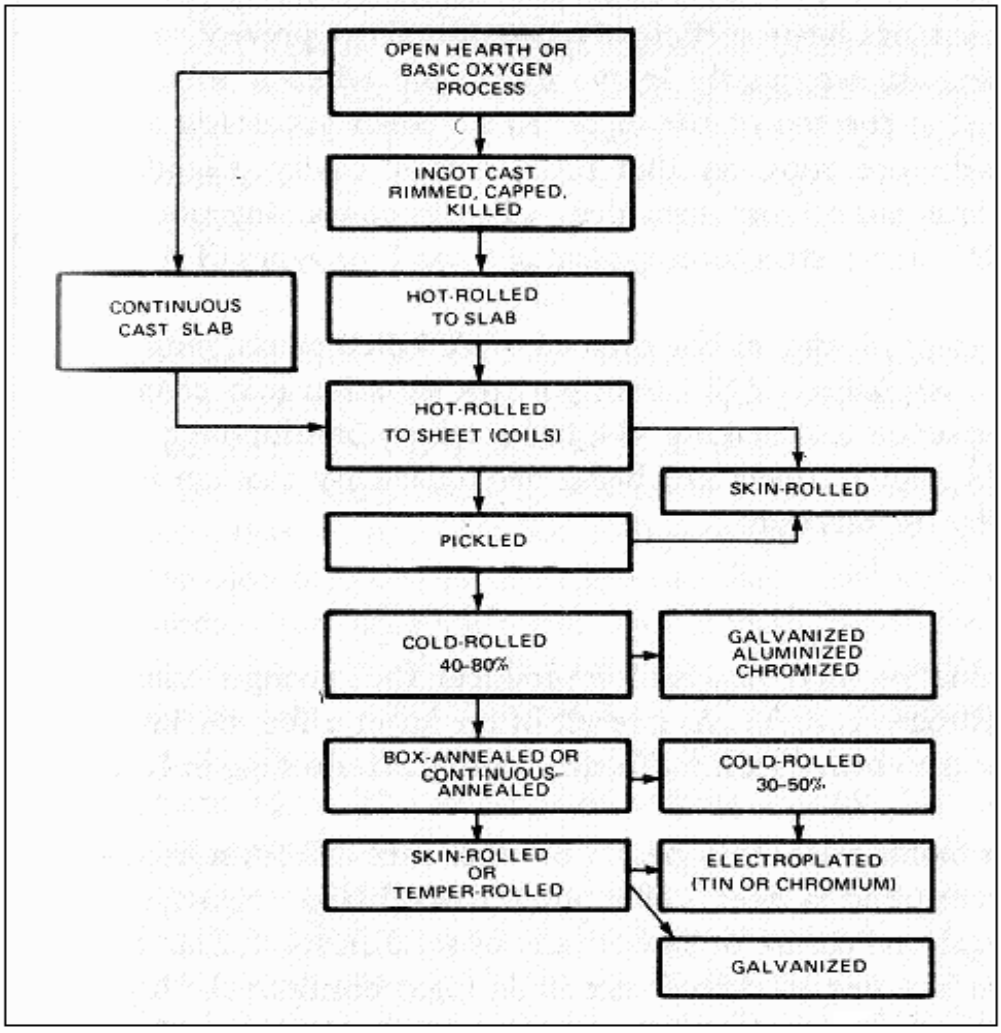

Figure 2.1: The simplified flow-chart for the production of low carbon strip steel[6].

Chapter 2 An overview of the processing of low carbon steel plate and hot strip

The low carbon content is essential for cold-formability requirements, as is also the low residual alloy content. In general, these low carbon strip steels can be divided into two categories[7]:

(i) Steels in which formability is of primary importance and strength is of lesser consequence. These steels are commonly used in car body pressings and similar applications.

(ii) Steels in which a higher strength is required and with a lesser cold-forming capability, such as the high-strength tin-plate steels where weight can be reduced by using thinner gauges.

2.2 Hot rolling of low carbon strip steel

There are mainly two types of hot strip mills namely, the Compact Strip Production (CSP) plants which usually employ the hot charge route (HCR) and the conventional strip production plants that use the cold charge route (CCR), see figure 2.2. The former are considered to be a more efficient way of producing steel vis-à-vis its design and the heat input. In the HCR process, after continuous casting, the slab is directly transferred to the reheat furnace for temperature equalization and while still in the austenite phase, is hot rolled. This is in contrast with the older conventional CCR processes where the continuous cast slab is allowed to cool from the austenite phase to room temperature to within the ferrite region and thereafter is reheated to the austenite phase and then hot rolled.

Chapter 2 An overview of the processing of low carbon steel plate and hot strip

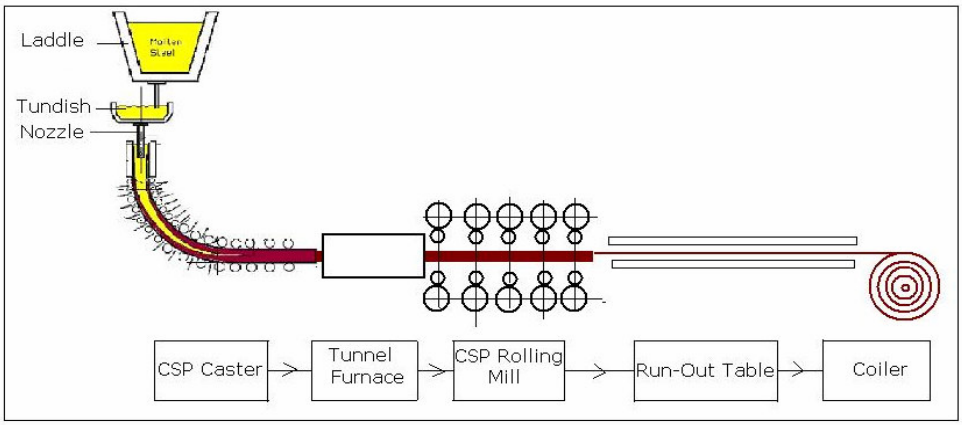

(a)

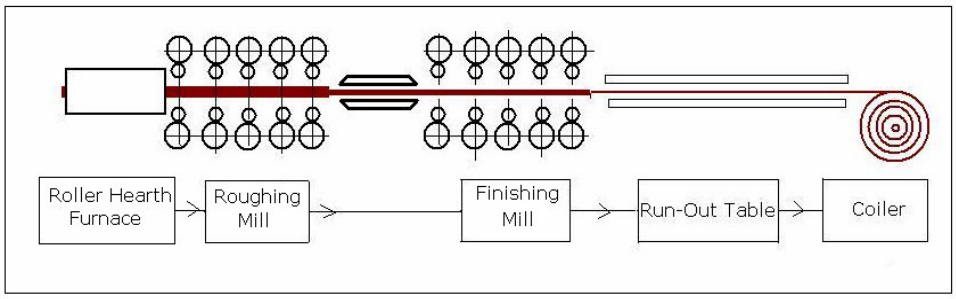

(b)

Figure 2.2: Hot strip rolling processes (a) the CSP and (b) the CCR.

Generally, most modern CSP plants are usually designed compactly with less hot rolling stages and they mostly start from thinner (typically 95 or 75 mm) continuously cast slabs compared to the conventional CCR where the slab thickness may typically be as large as 240 mm. The hot rolling process in a CSP is mostly characterised by higher pass strains, lower strain rates and longer interpass times. The longer interpass times and lower strain rates encourage dynamic and static recrystallisation during hot rolling. However this is off-set by the effect of the coarser as-cast starting

austenite grain size on recrystallisation and recovery during hot rolling. The starting austenite grain size in a CCR plant is generally smaller because of the prior austenite to ferrite phase change in the cast slab. However, these differences are smoothed out in the rolling process although some authors have observed finer final austenite grain sizes in CSP products that were attributed to the high pass strains in the last passes of the finishing mill[2-4].

Immediately after exiting the finishing mill, at temperatures mostly slightly above A_{r3}, the hot strip is sprayed with water on the run-out table in what is called accelerated cooling. The aim is to increase the driving force for the nucleation of ferrite from austenite. The resulting finer ferrite grain size improves both the yield strength and the toughness of these steels.

The hot strip is only cooled down to the coiling temperature which, for low carbon Al-killed strip steels, usually ranges between 580 and 650 °C. The coiling process is also an important stage in the production of these steels. The general practice is to ensure that the coiling temperature is not so high that excessive scaling or grain growth occurs nor too low that the steel is too stiff and "springy".

In aluminium treated steels, the coiling temperature and the cooling rate of the coil must be such that the AlN does not precipitate at this stage, because it is required to precipitate later during annealing after cold work in order to control the texture and subsequent cold formability of the strip. The precipitation of

Chapter 2 An overview of the processing of low carbon steel plate and hot strip

AlN during annealing after cold work promotes the nucleation of a preferred crystallographic texture ({111} texture in the plane of the sheet) that is necessary for deep drawing. The precipitation of AlN in these steels, therefore, performs a vital function and has been studied and reviewed extensively[8-11].

Aluminium is not only added to these low carbon steels for texture control alone but for other reasons which include deoxidation of the liquid steel, prevention of strain aging by nitrogen and also for grain refinement. In general, the aluminium content is kept within the range 0.02 to 0.05%Al.

3.1 Nucleation in solid solutions

The fundamental reason why a phase transformation takes place in a system is that the initial state is thermodynamically unstable relative to the final state i.e. the phase transformation allows the system to move to a lower free energy state. For phase transformations that take place at constant pressure and temperature the relative stability of the system is determined by its Gibbs free energy G where:

$$G = H - TS \tag{3.1}$$

where H is the enthalpy, T is the absolute temperature and S is the entropy of the system.

The free energy change ΔG between the initial and final state determines whether the reaction will proceed or not i.e. for the system to lower its free energy status, ΔG must be negative or alternatively $d\Delta G/dr$ must be negative for a still growing embryo. Therefore a necessary criterion for any phase transformation is:

$$\Delta G = G_2 - G_1 < 0 \tag{3.2}$$

where G_1 and G_2 are the free energies of the initial and final states respectively i.e.:

For a homogeneous nucleation and where the strain energy between the second phase and the host matrix is negligible, the free energy change ΔG can be presented mathematically by the

chemical driving force $(\frac{4}{3}(\pi r^3 \Delta G_v))$ and the retarding force $(4\pi r^2 \gamma_s)$, see figure 3.1. i.e.:

$$\Delta G = -\left(\frac{4}{3}(\pi r^3 \Delta G_v)\right) + 4\pi r^2 \gamma_s \qquad (3.3)$$

where r is the particle radius, γ_s is the interfacial energy and for an ideal solid solution, the chemical driving force $\triangle G_v$ is given by:

$$\Delta G_v = RT \ln K_s \qquad (3.4)$$

where K_s is the solubility product.

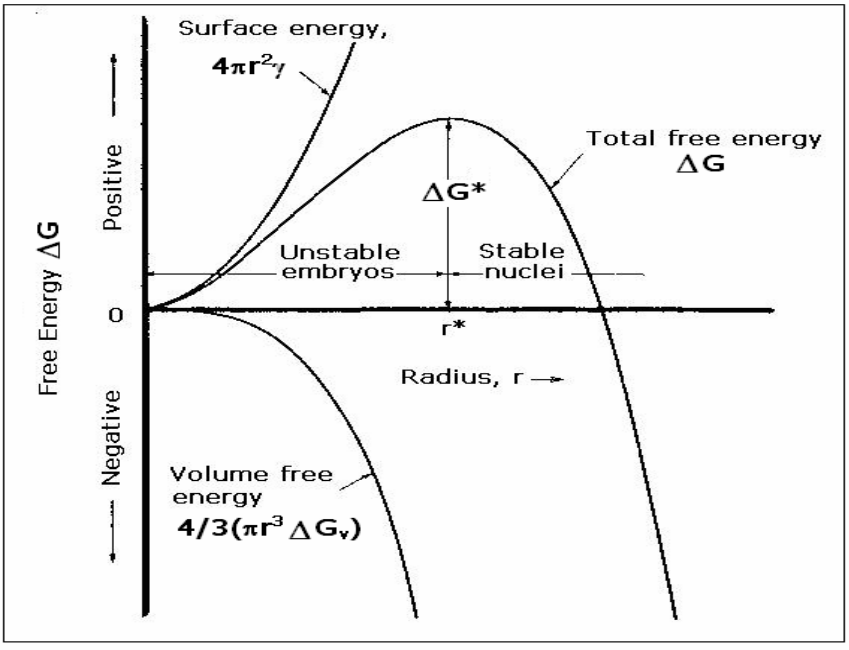

Figure 3.1: Free energy of formation of a stable nucleus where the retarding strain energy is very small

The activation energy ΔG^* and the critical embryo size r^* are given by equations 3.5 and 3.6:

$$r^* = \frac{-2\gamma_s}{\Delta G_v} \tag{3.5}$$

$$\Delta G^* = \frac{16\pi\gamma_s^3}{3(\Delta G_v)^2} \tag{3.6}$$

Any embryo that may form by statistical fluctuations in the matrix will grow only if the radius exceeds the critical size r^*. If it is smaller than r^* it can lower its free energy by re-dissolving into the matrix, figure 3.1.

At equilibrium the chemical driving force ΔG_v is given by:

$$\Delta G_v = \frac{\Delta H(T - T_e)}{T_e} = \frac{\Delta H \cdot \Delta T}{T_e} \tag{3.7}$$

A higher undercooling provides a greater chemical driving force for the phase change i.e. below the equilibrium temperature T_e the chemical driving force ΔG_v is negative and increases with undercooling. The values of the surface energy γ_s in equations 3.5 and 3.6 are generally assumed to be independent of temperature. Therefore, substituting for ΔG_v:

$$r^* = \frac{-2\gamma_s}{\Delta G_v} = -2\gamma_s\left(\frac{T_e}{\Delta H \Delta T}\right) \tag{3.8}$$

$$\Delta G^* = \frac{16\pi\gamma_s^3}{3(\Delta G_v)^2} = \frac{16\pi\gamma_s^3}{3}\left(\frac{T_e}{\Delta H \Delta T}\right)^2 \qquad (3.9)$$

The temperature dependence of r* and ΔG^* may, therefore, be assessed in terms of the temperature dependence of the chemical driving force ΔG_v i.e.:

$$r^* \propto \frac{1}{\Delta T}, \qquad \Delta G^* \propto \frac{1}{\Delta T^2} \qquad (3.10)$$

From equation 3.10, it may be seen that a higher undercooling results in smaller critical embryos and a smaller activation energy is required for the nucleation of those embryos. As a result, the nucleation rate would be higher and would generally lead to finer particles.

Precipitation of a particle from solid solution may cause some lattice strain because of differences in lattice spacing between the matrix and the particle or because of differences in densities between the two. Hence equation 3.3 then becomes:

$$\Delta G = \frac{4}{3}\pi r^3(\Delta G_v + \Delta G_\varepsilon) + 4\pi r^2 \gamma_s \qquad (3.11)$$

where ΔG_ε is the strain energy around the second phase and is a further retarding force.

The subject of strain energy ΔG_ε around a precipitate has been given attention by many authors[12-15]. The structural misfit δ due to differences in lattice spacing between the precipitate and the matrix is given by:

$$Misfit \quad \delta = \frac{\left(a_{ppt} - a_m\right)}{a_m} \tag{3.12}$$

where a_{ppt} and a_m are the lattice parameters for the precipitate and matrix respectively.

The magnitude of the strain is determined by a number of factors. The important ones are the disregistry, the elastic characteristics of the two phases, the nature of the strain and the shape of the particles. For a spherical particle with radius $(1+\delta)r_o$, the strain energy around a coherent particle is given by[12-14]:

$$\Delta G_{\varepsilon-coh} = \frac{6G_m V\delta^2}{\left[1+\frac{4G_m}{3K}\right]} \tag{3.13}$$

where G_m is the shear modulus, K is the bulk modulus and V is the volume of the particle $V = (4/3)\pi r^3$

and for incoherent particles[15]:

$$\Delta G_{\varepsilon-incoh} = 6G_m V\delta^2 f\left(\frac{c}{a}\right) \tag{3.14}$$

where f(c/a) depends on the shape of the particle through the dimensions a and c of a spheroid.

Since the strain energy ΔG_ε is positive (for both positive and negative δ misfit values) and the chemical driving force ΔG_v is negative, the result is that lattice strain increases both the activation energy ΔG^* and the critical r^* for the nucleation of the new phase, see equations 3.8, 3.9 and 3.11. The overall effect is that the nucleation rate $\dot{N}$ of the new phase may be significantly reduced or completely halted. Some authors[16-18] have modeled the effect of the strain energy ΔG_ε on the homogeneous nucleation parameters (critical radius r*, activation energy ΔG^* and nucleation rate $\dot{N}$) in a Cu-1at% Co alloy with a lattice misfit of 1.7% and their results are shown in figure 3.2.

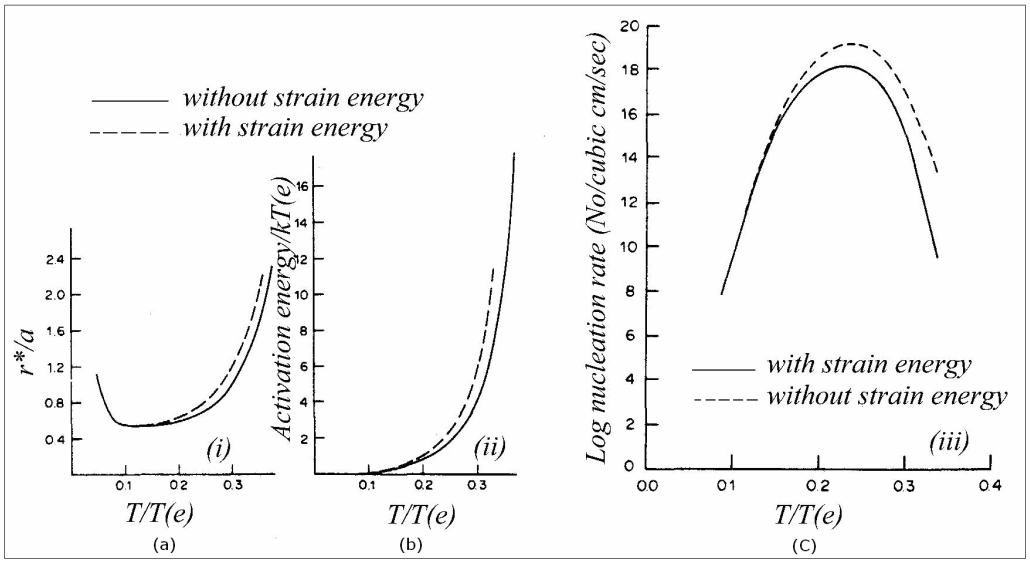

Figure 3.2: The effect of strain energy on the calculated nucleation parameters for the homogeneous nucleation of spherical Co precipitates in a Cu – 1at%Co alloy with a misfit of 1.7% between the

two phases. (a) The critical radius r* for nucleation normalised to the atomic radius a, (b) The activation energy ΔG* normalised to the temperature parameter kT_e and (c) the nucleation rate Ṅ. In all three cases these are shown as a function of the undercooled temperature T/T_e where T_e is the equilibrium solubility temperature[16].

The system may lower the strain energy around the particle by a number of ways, *inter alia* the formation of misfit dislocations, formation of ledges and kinks in the interface and eventually complete loss of coherence.

3.2 Heterogeneous nucleation in solid solutions

The nucleation of a second phase in solid solutions is a subject that has been given attention by many authors[16-26]. Nucleation of a second phase can either occur homogeneously or heterogeneously. Homogeneous nucleation occurs when embryos form as stable nuclei randomly in the matrix while heterogeneous nucleation occurs where embryos grow into stable nuclei on preferred sites such as dislocations, vacancies, grain boundaries, stacking faults, other precipitates and inclusions. These preferred nucleation sites lower the nucleation barriers by, generally, lowering the surface and strain retarding energies during nucleation of the second phase and, therefore, a smaller activation energy for nucleation would be required for heterogeneous nucleation than for homogeneous nucleation $\left(\Delta G^*_{hom} > \Delta G^*_{het}\right)$. Figure 3.3 is an illustration of the surface energy

balance for heterogeneous nucleation of a particle α on another particle β with both of them in the matrix M.

When nucleation takes place on an existing particle instead of nucleating homogeneously in the matrix, a certain surface area of the particle A_β is removed from the system. This provides an additional driving force for nucleation and, therefore, is a negative term in the basic energy equation for nucleation as illustrated through the surface energy balance in figure 3.3. Therefore, the free energy with heterogeneous nucleation on any surface is given by:

$$\Delta G_{het} = -V\left(\Delta G_v - \Delta G_\varepsilon\right) + A_\alpha \gamma_{M\alpha} + A_\beta(\gamma_{\alpha\beta} - \gamma_{M\beta}) \qquad (3.15)$$

where A_α and A_β are the interface areas between the matrix and the particle α and the two particles respectively.

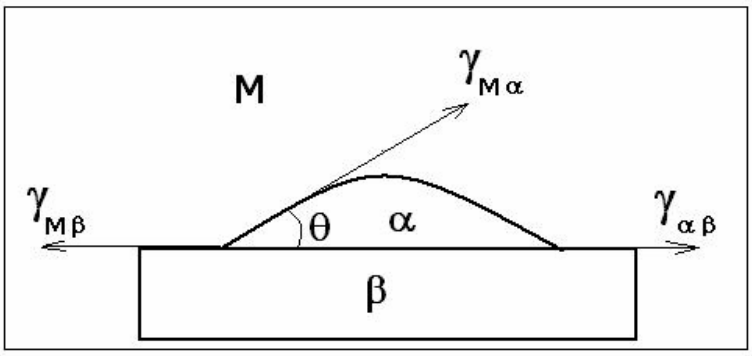

Figure 3.3: Heterogeneous nucleation of a particle α on another particle β in matrix M, where θ is the contact angle of the embryo α with the particle β, $\gamma_{\alpha\beta}$, $\gamma_{M\alpha}$ and $\gamma_{M\beta}$ are the surface energies on the particle α - particle β, particle α - matrix M and particle β - matrix M interfaces respectively.

Equation 3.15 indicates that the system will preferentially select those high energy sites first where it will gain the most energy through the additional driving force $A_\beta\gamma_{M\beta}$ for the nucleation of the second phase.

3.3 The nucleation rate of second phase

According to the classical theory of nucleation, the general time-dependent equation for the rate of homogeneous isothermal nucleation $\dot{N}$ is given by[27,28]:

$$\dot{N} = \frac{dN}{dt} = N_o Z\beta \exp\left(-\frac{\Delta G^*}{kT}\right)\exp\left(\frac{\tau}{t}\right) \qquad (3.16)$$

where N_o is the number of potential nucleation sites per unit volume, Z is the Zeldovich factor that accounts for the departure of the steady state from the equilibrium concentration of the critical nuclei, β is the frequency factor and is given by the number of atoms that reach the embryo per unit of time and is a function of the diffusion constant ($D = D_o\exp\{-Q/kT\}$), τ is the incubation time, k is the Boltzmann constant and N_o is the number of potential nucleation sites.

What equation 3.16 means is that if the incubation period τ is relatively large compared with the transformation time t, the transient nucleation will occupy a significant fraction of the whole isothermal transformation time. The ratio t/τ increases towards unity as the activation energy ΔG^* increases so that transient

effects are significant when nucleation is difficult. In the case of recrystallisation by the strain induced boundary migration mechanism, however, where pre-existing embryos (pre-existing recrystallisation interfaces) are involved, an "apparent" incubation time is believed to rather represent a time of slow growth or development of the pre-existing embryos to reach a critical size where more rapid growth is made thermodynamically possible.

If $t >> \tau$, equation 3.16 reduces to:

$$\dot{N} = \frac{dN}{dt} = N_o Z \beta \exp\left(-\frac{\Delta G^*}{kT}\right) \qquad (3.17)$$

The nucleation rate $\dot{N}$, which is the first derivative of the number of nuclei per unit volume versus time, is mostly not constant but decreases with the decrease in the driving force for nucleation from supersaturation as time progresses. In mathematical modelling, it is either assumed that all the nuclei form at a very early stage of transformation (i.e. site saturation) or are activated uniformly in time in the untransformed matrix (constant nucleation rate, $\dot{N}$).

3.4 Growth of precipitates from supersaturation

Once nucleation is practically complete (i.e. $\dot{N} = 0$), the particles continue to grow from the still supersaturated matrix at a rate controlled by the diffusion rate of the diffusing elements involved. This process is governed kinetically by the expression[29]:

$$r^2 - r_c^2 = 2D\Delta C\left(t - t_c\right) \tag{3.18}$$

where r_c and t_c are the particle radius and time when nucleation has ceased and all nuclei grow further only through diffusion of solute to the particle from the still supersaturated matrix, ΔC is the supersaturated concentration difference of solute between the particle surface and the surrounding matrix and D is the diffusion coefficient of the solute in the matrix.

3.5 Coarsening of precipitates

When growth of precipitates from supersaturation has ceased and the matrix has attained a quasi-equilibrium state, the system continues to lower its free energy through coarsening whereby the larger precipitates grow at the expense of the smaller ones. Unlike normal growth from supersaturation where the driving force is derived from the decrease in the chemical free energy ΔG_v, the driving force for coarsening is the decrease in the total surface energy $\gamma_s \Sigma A$ of the system as the smaller particles dissolve and the material is added to the larger ones. This process is modelled by the Lifshitz-Slyosov-Wagner [LSW] equation[30,31]:

$$\left(\bar{r}\right)^3 - \left(\bar{r_o}\right)^3 = \frac{8\gamma_s D C_e V_m^{\,2} t}{9RT} \tag{3.19}$$

where $\bar{r}_0$ is the mean particle size at time $t = 0$ and $\bar{r}$ is the mean particle size after time t, C_e is the equilibrium concentration of solute in the matrix, D is the diffusion

coefficient of the rate controlling diffusing species and V_m is the molar volume of the precipitate.

The rate at which the coarsening process takes place is practically always controlled in solid systems by the diffusion of the solute from the dissolving to the growing particles with the alternative interface control mechanism confined to only some liquid systems and a few very special solid systems.

3.6 Dissolution of precipitates above the solvus temperature

During dissolution of a precipitate there is no nucleation or dissolution barrier as in the case of precipitation. The precipitates have a finite non-zero initial radius R_o and decrease in size by mass transfer of the solute into the matrix behind the receding interface. Consequently, the resulting solute concentration profile is different from that obtained during growth, figure 3.4.

As is the case with coarsening, the particle dissolution process is mostly controlled by the diffusion of the detached solute into the matrix and in an infinite matrix, the dissolution velocity of the spherical precipitate is given by[32,33]:

$$\frac{dR}{dt} = k\left(\frac{D}{R} + \sqrt{\frac{D}{\pi t}}\right) \tag{3.20}$$

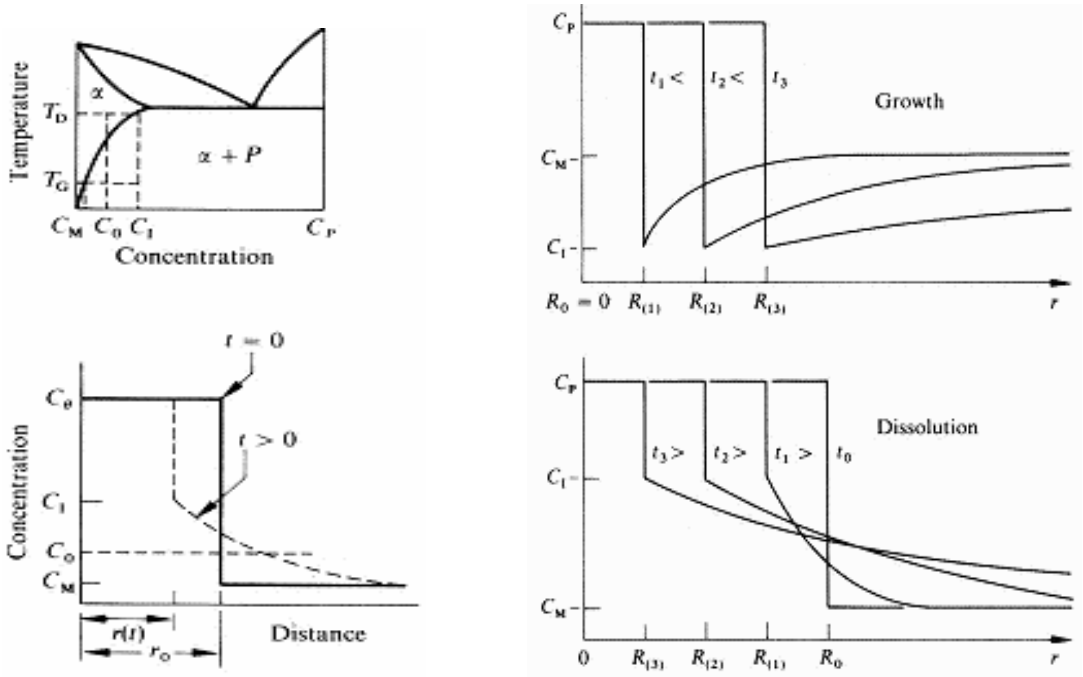

(a) (b)

Figure 3.4: (a) The solute concentration profiles around a dissolving precipitate which was initially in equilibrium with the solute depleted matrix and its corresponding binary phase diagram, (b) schematic comparison of the solute concentration profiles for precipitate growth and dissolution as a function of time[33].

where $$k = \frac{2(C_I - C_M)}{(C_P - C_I)} \qquad (3.21)$$

and where, as illustrated in figure 3.4, C_p is the composition of the precipitate and is considered constant with particle radius r and time t, C_I is the precipitate-matrix interface concentration, C_M is the equilibrium concentration in the matrix and D is the diffusion coefficient of the solute in the matrix.

The interface concentration, C_I, varies with the interface curvature and is governed by the Gibbs-Thompson equation which was modified by Hillert et al[32]:

$$C_{I(r)} = C_{I(\infty)} \exp\left[\frac{\gamma_p V_p}{RTC_p r}\right] \qquad (3.22)$$

where γ_p is the specific interfacial energy on the precipitate-matrix interface, V_p is the molar volume of the precipitate and C_p is the mole fraction of the solute in the precipitate.

Equation 3.20 is solved for R subject to the following boundary conditions[33,34]: $C_{(r=R,t)} = C_I \quad 0 < t \leq \infty$ and $C_{(r,\, t=0)} = C_M \quad r \geq R$.

Aaron et al[33] pointed out that since most alloys have a small supersaturation parameter, typically $|k| \approx 0.1$, i.e. $(C_p - C_M) >> (C_I - C_M)$, it is the concentration inequality $(C_p - C_M)$ rather than the interface reaction that controls the dissolution kinetics of precipitates in solid systems.

4.1 Introduction

AlN is a compound with a hexagonal close packed [wurtzite hcp] crystallographic structure and has a density of 3.262 g.cm^{-3} [35]. Its lattice parameters a and c are 0.311 and 0.4975 nm respectively[36] while the ratio c/a = 1.599. Probably due to a high nucleation barrier of the AlN-hcp lattice phase, it has been reported that AlN nucleates first with a metastable coherent fcc crystallographic structure that transforms later to the stable incoherent hcp crystallographic structure[37,38]. Wever et al[39] observed that the nitride was of the form Al-X-N where X could be oxygen, carbon or iron and Kang et al[37] observed that the nitride was of the form [Al, Cr]N. However the mechanism by which the nitride Al-X-N transforms to the stable hcp AlN has not been clearly identified, that is, whether the AlN forms after dissolution of the intermediate [Al, Cr]N or the latter transforms to the hcp AlN by local atomic migration, with Cr being rejected into the matrix.

4.2 The equilibrium solubility of AlN in steel

The solubility of AlN in steel conforms to the normal solubility product equation given by:

$$Log[\%M][\%X] = A - \left(\frac{B}{T}\right) \qquad (4.1)$$

$$Log[\%M]^{a/b}[\%X] = A' - \left(\frac{B'}{T}\right) \qquad (4.2)$$

where [%M] and [%X] represent the acid soluble aluminium (i.e. excluding Al bound up in alumina inclusions) and nitrogen contents respectively in wt% , T is the absolute temperature in K and A and B are constants.

The free energy of solution $\triangle H$ is given by[40]:

$$\Delta H = 1.15RA \tag{4.3}$$

or for equation 4.2:

$$\Delta H = 2.3RA\left(\frac{b}{a+b}\right) \tag{4.4}$$

where R is the universal gas constant, a and b are the valences for X and M respectively.

The solubility limit equations of AlN in austenite and ferrite have been obtained by a number of authors and are given in the appendix. The differences in these equations probably arose from the different techniques that were used to determine those solubility equations. For instance Darken et al[41] used the equilibrium Sieverts method that is based on the solubility of gasses in metals and their dependence on the applied pressure, i.e.

$$N_{gas} = k\sqrt{p} \tag{4.5}$$

where N_{gas} is the solubility of the dissolved gas, p is the pressure and k is a constant.

The solubility limit is established by measuring the point of departure from Sieverts' law at constant temperature. Sieverts' method generally gives higher solubility limit values compared to the Beeghly method (see below).

Most workers[41-48] used the Beeghly analysis[53] in which the iron matrix is dissolved in an ester-halogen solution (bromide-methyl acetate) and the insoluble nitrides are sieved/filtered. The limitations with this method are firstly, that it does not reliably distinguish AlN from other nitrides e.g. TiN, CrN and Si_3N_4 and secondly, it is insensitive to finer precipitates (< 10 nm) which could pass through the filter[42]. The latter effect would tend to lower the predicted solubility limit. As a result a reduced solubility is then reported when compared to the methods based on the Sieverts equation.

4.3 The precipitation of AlN in Al-killed low carbon steels

The chemical driving force for the nucleation of AlN is governed by the aluminium and nitrogen supersaturation, which is determined by the steel composition. The chemical driving force ΔG_V and the activation energy for nucleation ΔG^* are given by equations 3.4 and 3.6 respectively. The rate of isothermal nucleation is given by equation 3.16.

The rate of AlN precipitation is mainly controlled by the chemical driving force for nucleation, the interfacial energy and the mobility of aluminium atoms in ferrite or austenite. The diffusion of aluminium and nitrogen in austenite are given as [54,55]:

$$D_{Al} = 5.9\exp\left(-\frac{241000}{RT}\right) \quad (\text{cm}^2\ \text{s}^{-1}) \qquad (4.6)$$

$$D_N = 4.88x10^{-3}\exp\left(-\frac{76780}{RT}\right) \quad (\text{cm}^2\ \text{s}^{-1}) \qquad (4.7)$$

Due to the high diffusivity of nitrogen, it is generally assumed that no nitrogen concentration gradient will occur during particle growth and, therefore, the diffusion of aluminium atoms is likely to be the rate controlling species in the precipitation of AlN. Therefore, the parameter Zβ would be given as[56]:

$$Z\beta = D_{Al}(X_{Al}^{\ o} - X_{Al}^{\ equ})\left(\frac{F}{a^3}\right) \qquad (4.8)$$

where D_{Al} is the diffusion coefficient of aluminium, X_{Al}^{o} is the actual concentration in the matrix and X_{Al}^{equ} is the thermodynamic equilibrium concentration of solute aluminium, F is the number of atoms per unit cell (FCC = 4) and a is the lattice parameter.

If nucleation occurs heterogeneously on dislocations, the parameter N_o in equation 3.15 is given by[57,58]:

$$N_o = 0.5\rho^{1.5} \tag{4.9}$$

where ρ is the dislocation density at the start of precipitation.

Typical TTT diagrams for the precipitation of AlN in austenite and ferrite are given in figures 4.1 and 4.2. As may be seen in figure 4.1, the onset of the austenite to ferrite phase change has a significant accelerating effect on the precipitation of AlN due to the higher diffusivity of aluminium in ferrite and a decreased solubility of AlN in ferrite. At 800 °C and in ferrite, AlN precipitates almost without an incubation time at the estimated nose of the TTT diagram, see figure 4.2 below.

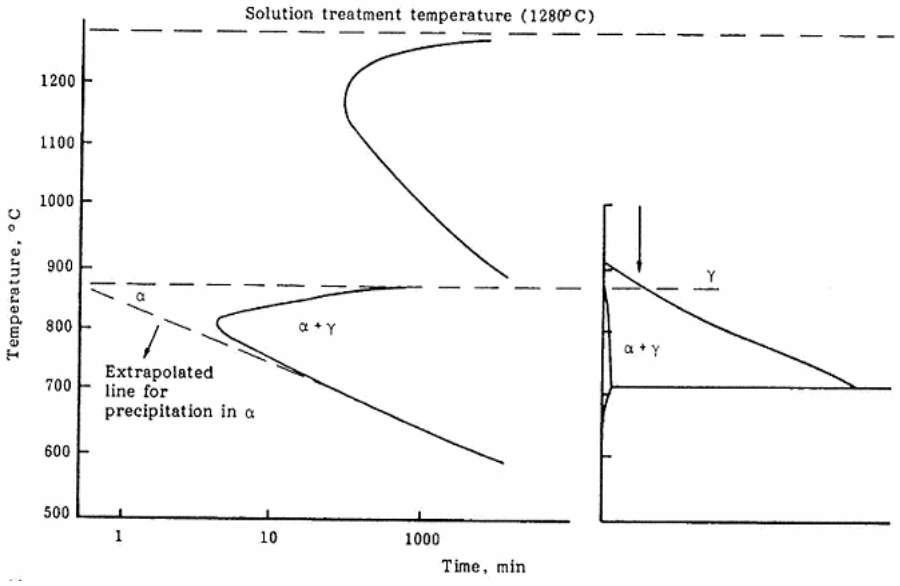

Figure 4.1: The time required for 50% precipitation of AlN, showing the pronounced effect of the austenite to ferrite phase change in Fe-0.05C-0.3Mn-0.12Al-0.007N, from Mayrhofer et al[47].

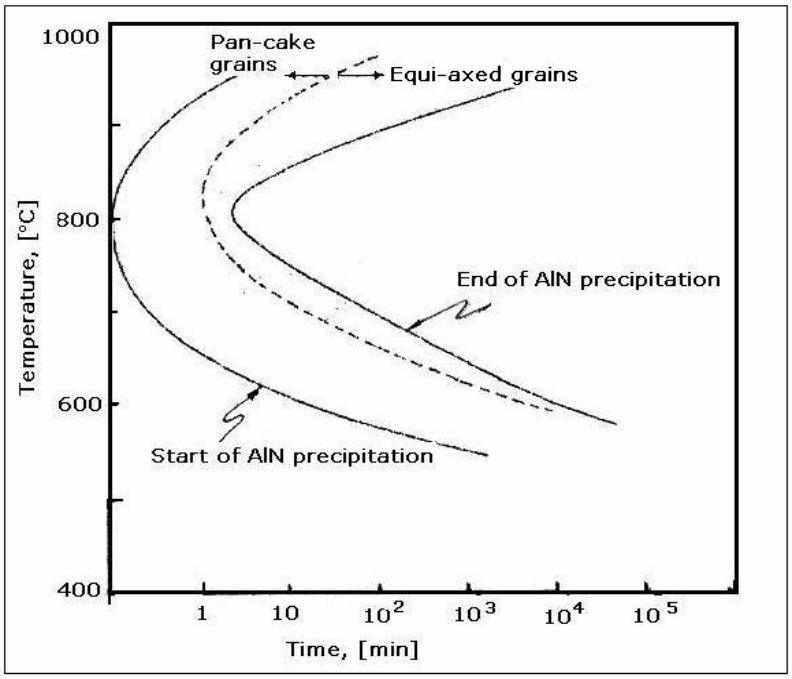

Figure 4.2: The TTT diagram for AlN precipitation in a low carbon Al-killed steel hot band[65]

In recent studies[52,59,60] done on commercial Al-killed low carbon steels, it was observed that the AlN precipitation in austenite took place at earlier times contrary to what is shown in figure 4.1. The AlN reportedly precipitated during hot rolling above the A_{r3} temperature and nucleated heterogeneously on MnS particles. Engl et al[60] observed heterogeneous nucleation of AlN on MnS during coiling of low carbon Al-killed steels within the temperature range of 600 °C to 800 °C. The AlN nucleated heterogeneously with ease on the MnS particles as the latter reduced the nucleation barrier of the former.

During re-austenitisation of low carbon-manganese Al-killed steels, freshly precipitated AlN grows according to the relationship[11]:

$$Log\left(r\right)=2.593+\frac{\log\left(t\right)}{3}-\frac{5167}{T} \qquad (4.10)$$

where r is the mean particle radius (μm), t is the isothermal holding time (hr) and T is the absolute temperature (K).

In the same steels, the following relationship was found in ferrite[155]:

$$Log\left(r_t-r_o\right)=12.3+0.85\log(t)-\frac{14433}{T} \qquad (4.11)$$

while in 50 percent deformed ferrite the following relationship was found:

$$Log\left(r_t-r_o\right)=16.4+0.85\log(t)-\frac{14433}{T} \qquad (4.12)$$

where r_t is the mean particle radius (nm) at time t (min), r_o is the initial mean particle radius and T is the absolute temperature (K).

4.4 Crystallographic orientation relationship between AlN and the iron matrix

Work has been done on the orientation relationship between the bcc and fcc iron matrix and the fcc and hcp AlN. Cheng et al[68] observed the following orientation relationship between the fcc iron matrix and the hcp AlN:

$$\left[0\bar{1}\bar{1}0\right]_{AlN} // \left[\bar{1}\bar{1}2\right]_{fcc-Fe}$$

$$\left(0001\right)_{AlN} // \left(1\bar{1}\bar{1}\right)_{fcc-Fe}$$

$$\left(2\bar{1}\bar{1}0\right)_{AlN} // \left(110\right)_{fcc-Fe}$$

while Sennour et al[38] and Massardier et al[69] observed a Bain orientation relationship between the cubic (NaCl type) structure and the bcc iron matrix:

$$\left(001\right)_{AlN} // \left(100\right)_{bcc-Fe}$$

$$\left[110\right]_{AlN} // \left[001\right]_{bcc-Fe}$$

The following orientation was also observed between the hcp AlN and the ferrite matrix[38]:

$$\left(03\bar{3}4\right)_{AlN} // \left(110\right)_{bcc-Fe}$$

$$\left[2\bar{1}\bar{1}0\right]_{AlN} // \left[2\bar{2}\bar{3}\right]_{bcc-Fe}$$

The orientation relationship between the hcp AlN and the fcc MnS was found to be as follows[52]:

$$\left(0001\right)_{AlN} // \left(1\bar{1}1\right)_{MnS}$$

$$\left[10\bar{1}0\right]_{AlN} // \left[121\right]_{MnS}$$

$$\left[2\bar{1}\bar{1}0\right]_{AlN} // \left[110\right]_{MnS}$$

As may be seen, the orientation relationship between the hcp AlN and the fcc MnS is the same as that between hcp AlN and fcc Fe. It is also worthwhile mentioning that both electron energy loss spectroscopy [EELS] and the energy dispersive X-ray [EDX] micro-analyses revealed the stoichiometric Al and N composition of the AlN[38].

4.5 The dissolution of AlN during reheating

As may be seen from the solubility models in the appendix, it is predicted that the equilibrium solubility of AlN in steels is not affected by other alloying elements. Mayrhofer et al[47] established that even in the presence of coarse AlN, equilibrium was attained within minutes (< 10 min) at temperatures above 1000 °C. This implies that during austenitisation under industrial processing conditions, the equilibrium dissolution of AlN is easily attained regardless of the process route whether it is the cold charge or hot charge route.

Chapter 5 The precipitation of manganese sulphide [MnS] in steels

5.1 Introduction

Sulphur may be present in steel in solute atom or sulphide form. Sulphides in steel generally comprise one or more of the phases, FeS, MnS, CuS and CaS. Frequently there can be extensive solid solution of other elements in the sulphide[61]. However, MnS is the normal form of sulphide in many steels. MnS (alabandite) has an fcc crystallographic structure and the lattice parameter is 0.5222 nm [62]. Depending on the Mn to S ratio of the steel and the cooling rate, it can contain variable amounts of FeS. Diffusion may then occur during subsequent reheating to produce "pure" MnS, which is virtually free from iron.

The morphology of the MnS in as-cast steel depends on the degree of deoxidation of the melt. In general as the degree of deoxidation increases the morphology changes from the globular through dendritic (branched rods) to the angular type[63,64]. MnS is readily deformed during hot rolling and, therefore, it changes its morphology to string-type or even plate-like which adversely affects the mechanical properties of the steel. Therefore, generally, calcium or rare earths such as cerium are added for shape control of the sulphides.

5.2 The solubility of MnS in low carbon steels

The equilibrium solubility of MnS in steel conforms to the normal solubility product of equation 4.1. The equilibrium solubility limit of MnS in austenite obtained by different workers is given in Table 5.1.

Chapter 5 The precipitation of manganese sulphide [MnS] in steels

Table 5.1: The equilibrium solubility limit of MnS in austenite.

Solubility model: Log[%Mn][%S]	Ref
$2.929-\left(\frac{9020}{T}\right)$	Turkdogan et al[65]
$10.6-\left(\frac{19427}{T}\right)$	Leslie et al[66]
$5.02-\left(\frac{11625}{T}\right)$	Parks et al[162]

5.3 The precipitation kinetics MnS in low carbon steels

Depending on the cooling rate and the Mn to S ratio in the steel, the Mn and S can either exist as solute atoms or precipitates in the steel. The re-precipitation of the sulphides in a low carbon steel (Fe - 0.11-0.14C - 0.6Mn - 0.25Si - 0.22Cr - 0.025-0.037S) was studied by Gabarz et al[67] and their TTT diagram is given in figure 5.1.

No pure MnS precipitates were observed; the EDS analysis showed that the MnS contained some Cu, probably due to the higher copper content in the steel. The dissolution temperatures

for each type of the sulphides were established to be about 1300 °C for MnS, 1100 to 1150 °C for [Mn,Cu]S and 950 °C for CuS and Cu_2S as shown in figure 5.1.

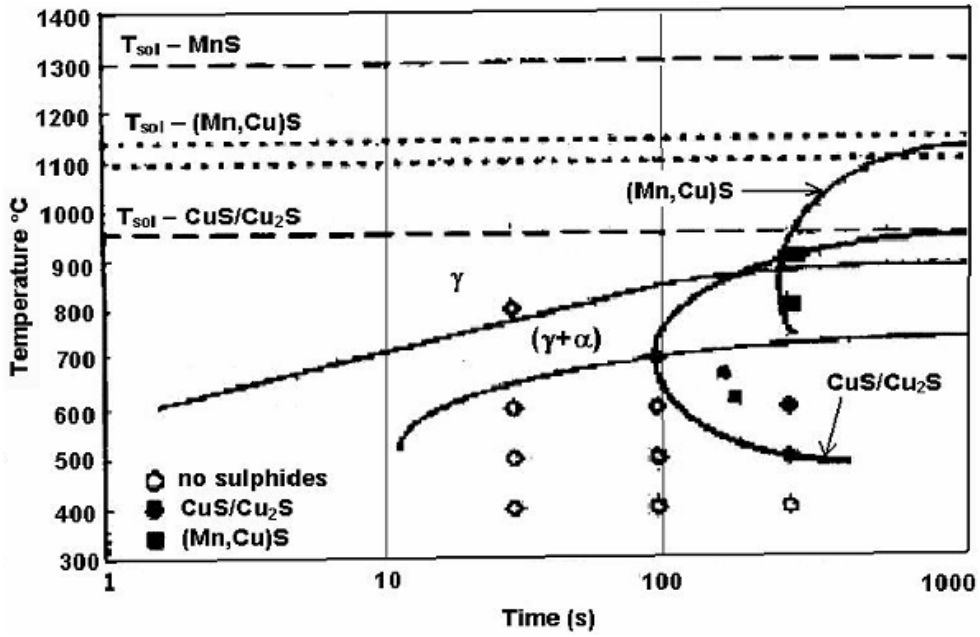

Figure 5.1: The re-precipitation start curves for nano-sulphides in a laboratory ingot. Note that no "pure" MnS was observed[67].

The MnS particle size and distribution depends on the cooling rate and the Mn to S ratio, which in turn affect the supersaturation and the nucleation and growth of the MnS particles. Apart from the Mn to S ratio, the thermal history plays an important role in the thermokinetics of the precipitation of the MnS. For instance, in a previous study on a low carbon high sulphur steel (Fe-0.04C-0.25Mn-0.2Si-0.005Al-0.0026N- 0.005-0.04S), Frawley et al[68] observed that the particle size and distribution of MnS in the Hot

Chapter 5 The precipitation of manganese sulphide [MnS] in steels

Charge Route (HCR) specimens were different from that in the Cold Charge Route (CCR) specimens, the former being a finer dispersion of MnS of 5 to 30 nm as a result of the higher supersaturation, and the latter a combination of finer and larger ones, 100 to 200 nm in size. The two populations in the CCR specimens were believed to be a result of the partial dissolution of the MnS during the reheating process. In previous studies[67,71], it was observed that during hot rolling, MnS generally precipitated heterogeneously on the grain boundaries and dislocations, more than inside the grains themselves.

In steels that contain substantial amounts of copper due to higher scrap steel recycling, the MnS is mostly associated with copper. As the MnS forms at a higher temperature, Madariaga et al[72] found that the hcp CuS (covellite), with parameters a = 0.379 nm and c = 1.633 nm, formed a shell around the MnS. It was suggested that the lowest misfit orientation of 6% (calculated from the Bramfitt[73] equation) existed between the CuS and the ferrite matrix:

$$(0001)_{CuS} // (111)_{bcc-Fe}$$

$$\left[2\bar{1}\bar{1}0\right]_{CuS} // \left[1\bar{1}0\right]_{bcc-Fe}$$

Liu et al[74] also observed a [Cu, Fe]S shell around the MnS particles by EDS analysis. Fine fcc Cu_2S particles, (diginite), < 50

nm with the lattice parameter a = 0.5735 nm, were observed as well. The cube-cube orientation relationship between this precipitate and the matrix was observed to be:

$$(001)_{Cu_2S} // (001)_{bcc-Fe}$$

$$[110]_{Cu_2S} // [110]_{bcc-Fe}$$

Chapter 6 The theory of recovery and recrystallisation in metals

6.1 Introduction

When a metal is subjected to plastic deformation by cold work, most of the energy in the deformation process is converted into heat and the remainder is stored in the metal. It is this stored energy that provides the driving force for either recovery or recrystallisation during the annealing process, i.e. in the deformed state the material is thermodynamically unstable and upon increasing the temperature to generally near to or above half of the melting temperature [$0.5T_m$], the material lowers its free energy ΔG by the reduction in number and rearrangement of the lattice defects. Detailed reviews of this subject have been done by different authors over the years[75-78].

Recovery embraces all of the earliest structural and property changes that do not involve the sweeping of the deformed structure by migrating high angle grain boundaries. The deformed structure thus retains its identity while the density of crystal defects and their distribution changes. This involves annealing of point defects, annihilation and rearrangement of dislocations, formation of sub-grains (polygonisation) and their subsequent growth that leads to the formation of recrystallisation nuclei.

Recrystallisation takes place by the nucleation and growth of new grains. The nucleation stage involves the formation of a small volume of relatively dislocation free material which is at least partially bound by a high angle grain boundary within the deformed material. In order to be viable a nucleus, this volume of

material must be of sufficient size to be able to grow into the deformed material. In the case of the Strain Induced Boundary Migration mechanism, what is perceived as an "incubation time" actually involves the early development of the pre-existing recrystallisation interfaces (pre-existing high angle grain boundaries). This early development stage involves the initial migration of the high angle grain boundaries into the deformed material to a hemi-spherical size, which is a critical nucleus size for full recrystallisation to proceed. Further annealing after recrystallisation causes the grains to grow larger in size through grain growth. As mentioned earlier, there is no distinct demarcation between these processes and, therefore, grain growth, which has no incubation time, may start before the completion of the recrystallisation process, depending on the prevailing local conditions in the material.

6.2 Kinetics of recovery

The rate of property change is highest at the start of the annealing process and gradually decreases as recovery progresses. At longer times the rate of property change becomes negligible. The kinetics of recovery in metals has been investigated as a function of time through the release of stored energy, the decrease in electrical resistance, the change in magnetic properties and x-ray line broadening[79-82]. Unlike recrystallisation, there is no incubation period for the recovery process.

Chapter 6 The theory of recovery and recrystallisation in metals

The temperature dependence of the rate of recovery is generally of the Arrhenius type i.e. for the rate of change of any property X:

$$\frac{dX}{dt} \; or \; \frac{C_1}{t} = C\exp\left(-\frac{Q}{RT}\right) \qquad (6.1)$$

where C_1 is some constant representing a fixed percentage of recrystallisation within the linear portion of the property X versus time t curve, C is the frequency factor (a combination of the vibration frequency and the entropy term), Q is the activation energy in J mol^{-1} for the process, R is the universal gas constant (8.314 J mol^{-1} K^{-1}) and T is the absolute temperature in K.

By taking logs on both sides of equation 6.1, it becomes:

$$\ln\left(\frac{1}{t}\right) = \ln C_2 - \left(\frac{Q}{RT}\right) \qquad (6.2)$$

where $\ln C_2 = (\ln C - \ln C_1)$

Thus, when the rate $\ln\left(\frac{1}{t}\right)$ is plotted versus $\frac{1}{T}$, the slope is $-\frac{Q}{R}$ and this gives the activation energy of the process.

There is a tendency for equation 6.2 to deviate from linearity as recovery progresses and Kuhlmann et al[83] assumed that the instantaneous rate of recovery depends on the extent of recovery according to the expression:

$$\frac{dX}{dt} = C_3 X.\exp\left[-\frac{(Q - mX)}{RT}\right] \qquad (6.3)$$

where X is the quantity of the measured property that has departed from equilibrium at time t, while C_3 and m are constants.

The activation energy for recovery then increases linearly with the increase in recovery. Li et al[84] made similar observations that the activation energy for recovery should be a linear function of the extent of recovery.

6.3 Recrystallisation Kinetics

The kinetics of recrystallisation can be followed successfully, in most cases, by applying the MAJK (Kolmogorov[85] Johnson-Mehl[86] and Avrami[87]) equation also known as the Avrami equation. This equation is based on a sigmoidal relationship between the recrystallised volume fraction X and the isothermal annealing time t that is found often.

The problem of relating the volume fraction recrystallised X to the annealing time t is complicated by the situation that as recrystallisation proceeds, the volume of unrecrystallised material into which the new nuclei can form keeps on diminishing. In order to circumvent this complication, Johnson et al[86] introduced the concept of an "extended volume" that takes into account the

impingement of grains on each other as recrystallisation proceeds. The general MAJK expression that predicts the volume fraction of the material recrystallised X in time t is then given by:

$$X = 1 - \exp\left(-kt^{n}\right) \qquad (6.4)$$

where n is the Avrami exponent and k comprises the shape factor *f*, the nucleation frequency Ṅ and the growth rate *G*.

It is generally assumed that the nucleation sites are randomly distributed in the deformed matrix, that the growth is isotropic and that the growth rate is constant. If the nucleation rate Ṅ remains constant, [Johnson-Mehl nucleation kinetics] then n = 4. If all the nuclei are present at time zero and no further nucleation takes place afterwards, i.e. "site saturation" has occurred, n = 3.

In order to determine the exponent n and the parameter k, it is customary to plot $\ln\left\{\ln\left(\frac{1}{1-X}\right)\right\}$ versus ln(t). The plot is usually a straight line of slope n and with k the intercept. Factors that contribute to deviation from linearity are discussed in the following section 6.4.

Another way of studying the kinetics of the recrystallisation process is to measure the time $t_{0.5}$ taken for the 50 percent recrystallised volume fraction to be reached during the isothermal annealing process. This assumes that nucleation has stopped before 50 percent recrystallisation i.e. Ṅ = 0, (site saturation)

and that the extent of recrystallised volume fraction is governed solely by the growth rate G.

The effect of increasing the annealing temperature T, is the reduction in the time $t_{0.5}$ taken to recrystallise to 50 percent volume fraction. When the reciprocal of the annealing temperature is plotted versus the logarithm of the annealing time for the 50 percent recrystallisation, a straight line is obtained i.e.:

$$t_{0.5} = C_4 \exp\left(\frac{Q_r}{RT}\right) \tag{6.5}$$

where C_4 is a parameter that is structure dependent and Q_r is the apparent activation energy for recrystallisation. Q_r is an "apparent" activation energy because there is generally an overlap between recovery, recrystallisation and grain growth during the annealing process.

6.4 The Avrami exponent n

The assumptions of constant nucleation $\dot{N}$ and growth rate G in the derivation of the MAJK equation are seldom achieved in practice. It is quite usual for both to vary with time during annealing and, therefore, the $\ln\left[\ln\left(\frac{1}{1-X}\right)\right]$ versus ln(t) plot is not always linear[88,89]. For many materials, the experimentally determined JMAK exponent does not only vary as the recrystallisation progresses but is generally smaller than predicted by the ideal JMAK model. Significantly smaller JMAK exponents

are obtained in the later stages of recrystallisation due to the diminishing driving force in the deformed matrix caused by concurrent or preceding recovery. The implication is that a constant exponent n may overestimate the recrystallisation kinetics in the later stages of the annealing process. The extent of recovery is dependent on the type of material (i.e. materials with a high stacking fault energy recover easier), annealing temperature, amount of deformation and the heating rate (in the case of a continuous annealing process).

The deviation from the ideal MAJK behaviour is also attributed to non-uniform distribution of the stored energy of deformation, non-random distribution of nuclei, anisotropic growth of recrystallised nuclei and sometimes the presence of second phase particles[88,90-92]. In spite of these deficiencies, the MAJK equation is still widely used in the study of the kinetics of recrystallisation in materials.

6.5 Nucleation in recrystallisation

Nucleation during recrystallisation involves the formation of a small volume of relatively dislocation-free material, which is partly bound by a high angle grain boundary that is capable of migrating within the deformed material. The mechanisms for the nucleation of the recrystallisation can be classified into basically three models, namely classical nucleation through an embryo, the Strain Induced Boundary Migration (SIBM) and the subgrain coalescence and rotation models.

Chapter 6 The theory of recovery and recrystallisation in metals

In a recent publication in which the nucleation of recrystallisation is reviewed, Humphreys[93], concluded that the main mechanisms are thought to involve the growth of subgrains by the migration of low angle boundaries in an orientation gradient or the strain induced boundary migration of existing boundaries. It was also concluded that to date, there is no firm experimental evidence that subgrain coalescence and rotation play a significant role in the nucleation of recrystallisation. As for classical nucleation through an embryo, it has been long recognised that new grains generally do not form by thermal fluctuation on an atom by atom basis as is the case in homogeneously nucleated solid state phase transformations, mainly due to rather low driving forces for nucleation of a stable recrystallised embryo. There is, furthermore, adequate evidence that recrystallised grains do nucleate and grow from pre-existing volumes/embryos such as cells or subgrains in the deformed material[78,94,95].

6.5.1 Classical nucleation theory

The application of classical nucleation theory to recrystallisation was first examined by Burke and Turnbull[91]. This may be a homogeneous or heterogeneous process with the latter nucleating at grain boundaries or other defects in the deformed matrix e.g. high deformation zones surrounding inclusions[92] as in Particle Stimulated Nucleation or PSN found in some aluminium alloys. It is to be noted, however, that in the PSN model, nucleation around inclusions is not a result of reduced retarding forces as in classical heterogeneous nucleation but is rather due to an increased driving

force present in the intensified deformation zones in these near-particle areas.

In the classical nucleation model where a potential spherical nucleus of recrystallised material is formed in the matrix, the free energy change is given by equation 3.3, where ΔG_v is the deformation energy or driving force in the matrix per unit volume, r is the radius of the nucleus and γ_{gb} is the grain boundary energy. The strain energy term ΔG_ε as a retarding force, is not included in equation 3.11 as there is no density difference between the deformed and undeformed matrix.

Here a critical nucleus will be stable if it reaches a critical size r* which is governed by the surface energy and the difference in deformation energy per unit volume between the recrystallised state and the deformed matrix, equation 3.3, while the activation energy in equation 3.6 is normally taken as the activation energy for grain boundary diffusion.

Contrary to Burke and Turnbull[91], Bailey[94] and Cahn[95] showed that homogeneous nucleation by the classical fluctuation mechanism is generally unlikely in recrystallisation due to the small driving forces and the high surface free energy of a high angle grain boundary. However, heterogeneous nucleation is a possibility since the critical energy to form a stable nucleus is reduced by a factor ξ [96]:

$$\xi = \frac{(2+\cos\theta)(1-\cos\theta)^2}{2} \qquad (6.6)$$

where θ is the is the included angle as shown in earlier figure 3.3.

Byrne et al[97] showed that theoretical calculations of the driving force and nucleation rate as a function of deformation showed that the classical theory of nucleation through formation of stable embryos on a pre-existing interface could possibly apply at deformations greater than 15 to 20 % where sufficient driving force will be available to form a measurable stable nucleus.

Classical nucleation theory predicts that the nucleus will form in such an orientation that the surface energy γ_s will be small in order to minimise this retarding force. This should, therefore, lead to a minimum critical radius r* and activation energy ΔG* through a good lattice fit of the nucleus and the matrix. One weakness with the classical nucleation theory is that in practice, the opposite is very often found because grain boundary mobility requires a high orientation difference between the new grain and the deformed matrix. For high angle grain boundaries (HAGB) in aluminium, Gottstein et al[98] suggested that, if the special 40°<111> tilt boundary is ignored, the grain boundary mobility M versus the misorientation θ curve is sigmoidal (see figure 6.1 below) with a form:

$$M = M_m\left[1-e^{-B(\theta/\theta_m)^n}\right] \qquad (6.7)$$

where M_m is the mobility of a high angle grain boundary, n ~ 4 and B ~ 5.

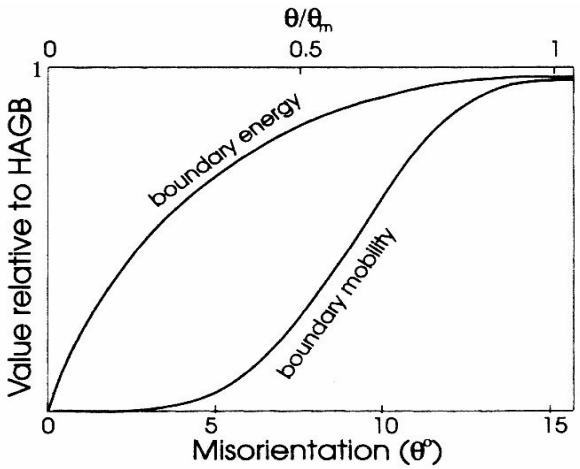

Figure 6.1: The variation in grain boundary energy and mobility with misorientation[98].

6.5.2 The Strain Induced Boundary Migration (SIBM) mechanism

Strain induced boundary migration was first reported by Beck and Sperry[99] (see figure 6.2 (a)) and the thermodynamics of the process was analysed by Bailey and Hirsch[100]. In this model, no formation of new embryos as stable nuclei is required. New grains grow from pre-existing nuclei present on grain boundaries by the sweeping up of the dislocations ahead of them by the interface moving into the deformed matrix. This model takes care of the constraint posed by the low driving forces for embryo formation through thermal fluctuations as proposed by the classical nucleation theory as no "stable nucleus" needs to be formed first.

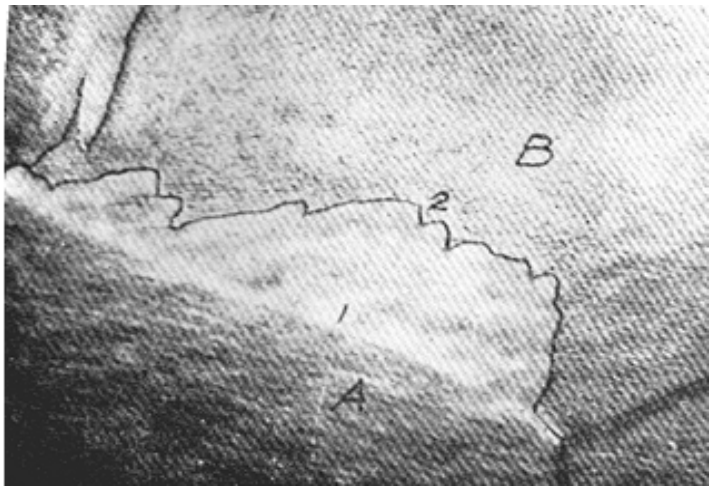

(a)

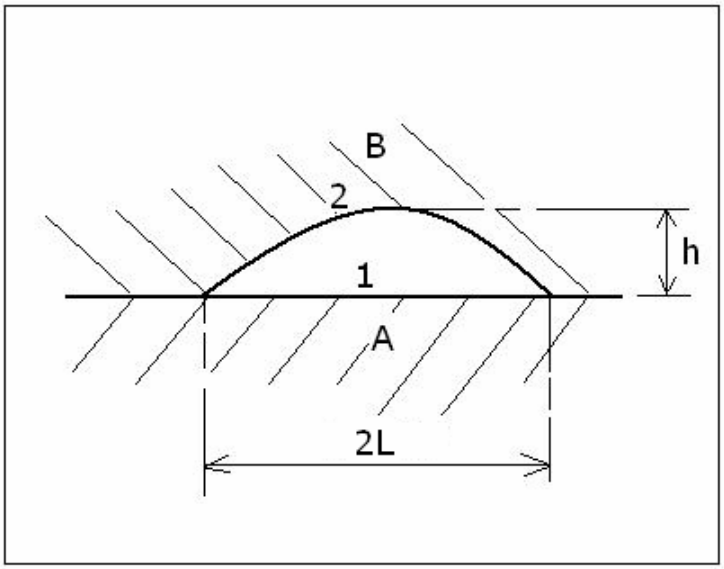

(b)

Figure 6.2: (a) Strain induced migration of a recrystallisation boundary[76] (b) schematic presentation of figure 6.2 (a).

The migrating grain boundary in figure 6.2 (a) is anchored at the two points on either side of the grain boundary portion that bulges out. The anchoring may be due to subgrain boundaries or pinning

by particles on the grain boundaries. In figure 6.2, the upper grain B has a higher dislocation density than the area between 1 and 2 so that the boundary tends to bulge out, as seen in the micrograph, in order to satisfy the local energy condition that balances the grain boundary interfacial energy γ_{gb} and the strain energy difference between the recrystallised grain and the deformed matrix (ΔG_{Rx}).

The rate of movement of the migrating front dh/dt is governed by the rate of net movement of atoms across the interface (boundary 2 in figure 6.2 above). Bailey et al[100] used the absolute reaction rate in this derivation i.e.:

$$\frac{dh}{dt} = \frac{2V_a^{1/3}\upsilon}{RT}\exp\left(-\frac{\Delta G_A}{RT}\right)\left[\left|\Delta G_{Rx}\right| - \left|\frac{\left(\gamma_{gb}4h\right)}{\left(L^2+h^2\right)}\right|\right] \quad (6.8)$$

where V_a is the volume of the migrating atoms, υ is their jump frequency, ΔG_A is the activation energy for the movement of the atoms across the interface, L and h are as shown in figure 6.2 (b) above, γ_{gb} is the grain boundary surface energy and the rest are as defined in the previous sections.

For growth to take place dh/dt > 0 and, therefore:

$$\left|\Delta G_{Rx}\right| > \left|\frac{\left(\gamma_{gb}4h\right)}{\left(L^2+h^2\right)}\right| \quad (6.9)$$

and with the maximum h = L i.e. for the subgrain to grow to a hemisphere and beyond:

$$\left|\Delta G_{Rx}\right| \geq \left|\frac{2\gamma_{gb}}{L}\right| \qquad (6.10)$$

The integration of equation 6.8 is complex and was examined schematically through inspection as shown in figure 6.3 below. The conclusion was that at low values of the driving force, i.e. $\Delta G_{Rx} < (2\gamma_{gb}/L)$, pre-existing embryos (pre-existing recrystallisation interfaces) will not grow into new full recrystallised grains. For full growth to take place at all values of h, $\Delta G_{Rx} > (2\gamma/L)$. It is also concluded that since no nucleation through thermally activated embryos is required, there should not be any incubation period as in the classical embryo/nucleus model. The extrapolation of the constant dh/dt portion of the curve in figure 6.4, however, gives an "apparent incubation" period which, according to the SIBM theory, is simply the time of slow growth in the early stages of the recrystallisation process.

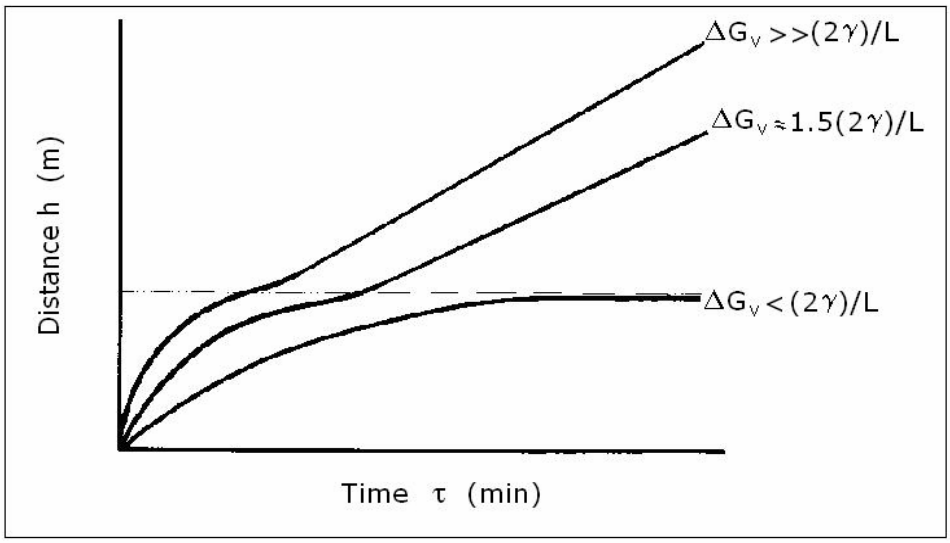

Figurer 6.3: Schematic rate of migration of the transformation front as a function of the driving force ΔG_{Rx}

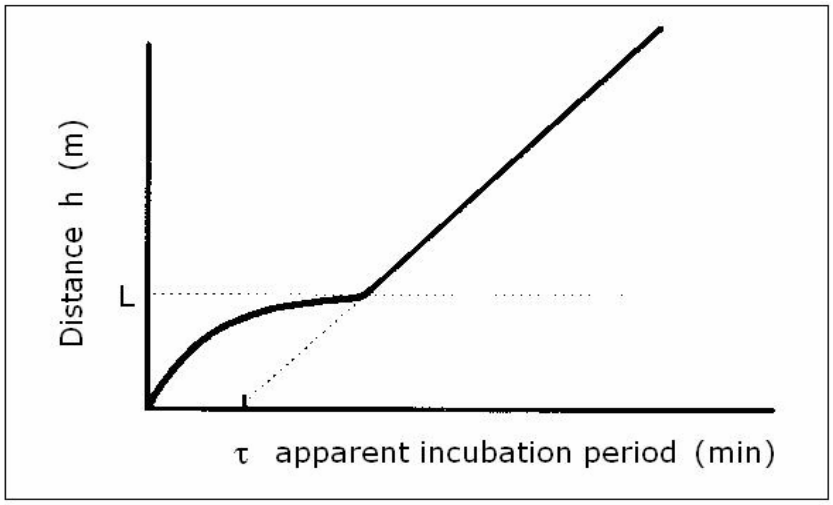

Figure 6.4: Apparent incubation time due to slow movement of the recrystallisation front at early stages of the recrystallisation process.

6.5.3 Subgrain coalescence and rotation

The mechanism proposed by Li requires that the subgrain coalescence and rotation of several subgrains lead into the formation of a potential embryo with a HAGB capable of growing into the deformed matrix[102,103] as illustrated in figure 6.5. The coalescence and rotation takes place through subgrain boundary diffusion. However, a number of authors[104,-106] have found no experimental evidence to substantiate this nucleation model.

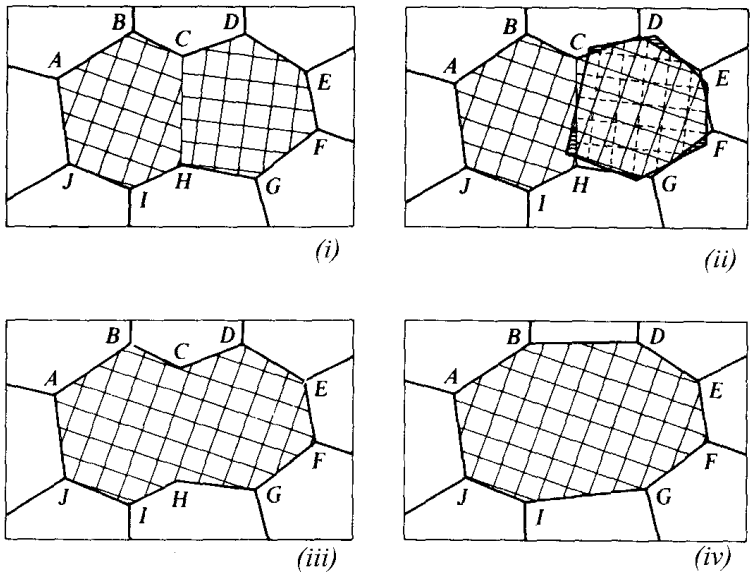

Figure 6.5: Schematic representation of subgrain rotation, leading to coalescence and an increase in orientation difference at the growth front. (i) Original subgrain structure before coalescence, (ii) Subgrain CDEFGH rotates through boundary diffusion (iii) The original orientation difference between the two subgrains has disappeared and the orientation difference at the front DEFG is now larger, (iv) Grain boundary sections BCD and IHG straighten out to achieve a lower energy state[102].

6.6 Effect of cold work on recrystallisation kinetics

Increasing the amount of deformation increases the amount of stored energy in the deformed matrix[79]. This stored energy is the driving force for the recrystallisation process and is given by:

$$P_d = \alpha G_m b^2 \Delta N_d \qquad (6.11)$$

where α is a constant with the value between 0.5 and 1.0, G_m is the shear modulus, b is the Burgers vector and ΔN_d is the difference in dislocation density between the deformed and the recrystallised state. However, $N_{d\text{-}\varepsilon} >> N_{d\text{-}Rx}$ so that $\Delta N_d \sim N_{d\text{-}\varepsilon}$; where $N_{d\text{-}\varepsilon}$ and $N_{d\text{-}RX}$ are the dislocation densities after cold work and recrystallisation respectively.

As a result, with increasing deformation recrystallisation will take place at earlier times during isothermal annealing, or at lower temperatures during isochronal annealing. The higher driving force resulting from the higher deformation (stored energy) decreases both the activation energies for nucleation and growth of the new grains[107], as found in aluminium, see figure 6.6.

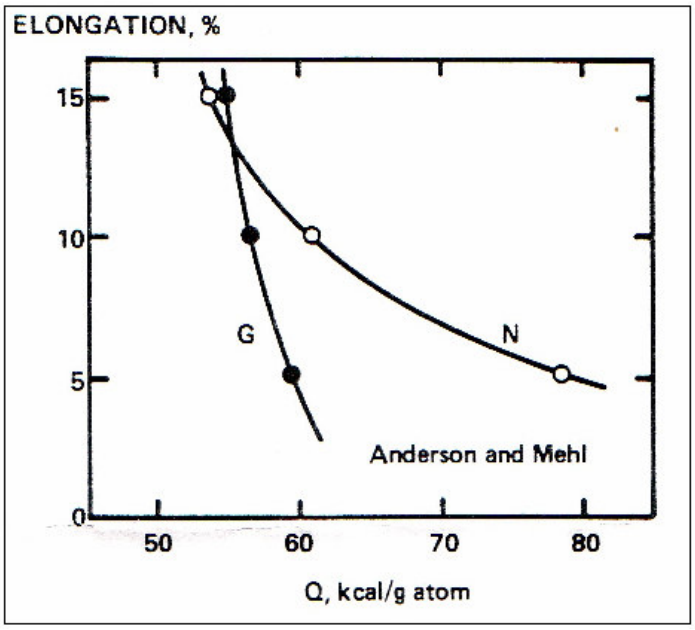

Figure 6.6: The activation energy for nucleation rate $\dot{N}$ and for growth rate G_R in aluminium as the function of the amount of deformation[107].

6.7 The effect of annealing temperature on the recrystallisation kinetics

Increasing the annealing temperature shifts the annealing time to earlier times, see figure 6.7 below, as recrystallisation is a thermally activated process and diffusion is faster at higher annealing temperatures. Apart from the driving force that arises from the stored deformation energy (equation 6.11), the grain boundary movement V_B of the new grains is also dependent on the grain boundary mobility m which is dependent on temperature, i.e. grain boundary mobility is higher at higher temperatures:

$$V_B = mP_{Rx} \tag{6.12}$$

$$m = m_o \exp\left[-\frac{Q_{gb}}{RT}\right] \tag{6.13}$$

where Q_{gb} is the activation energy for the grain boundary mobility.

As recovery and recrystallisation processes sometimes overlap, it is worthwhile mentioning that at lower annealing temperatures, recovery dominates over recrystallisation and, therefore, this reduces the driving force available for recrystallisation. In figure 6.7, the decrease in growth rate of new grains at later stages of recrystallisation was attributed to concurrent recovery at lower annealing temperatures[88].

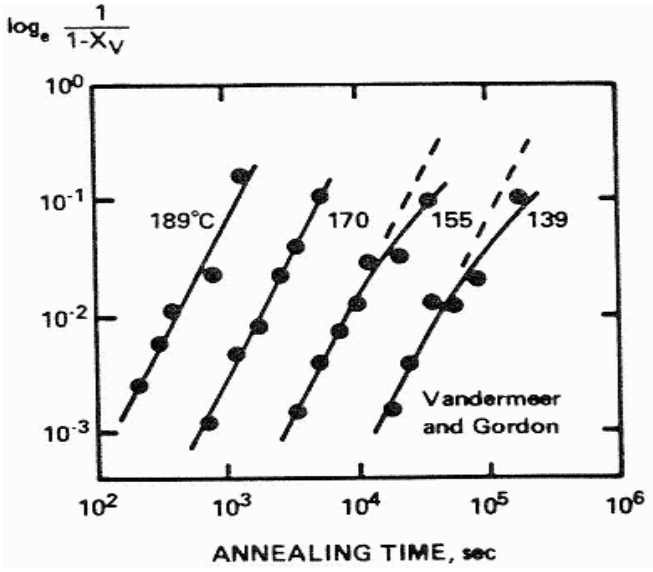

Figure 6.7: The effect of annealing temperature on the recrystallisation kinetics of a zone refined aluminium containing 6.8 ppm copper,

deformed 40% by rolling at 0°C then isothermally annealed at temperatures indicated: note that the recrystallisation process shifts to earlier times as the annealing temperature increases[88].

6.8 Effect of grain size on the recrystallisation kinetics

Indirectly, a smaller grain size may affect recrystallisation through a more intense work hardening process for a given deformation, thereby providing a higher driving force. In smaller grain size material, therefore, recrystallisation shifts to earlier annealing times during isothermal annealing and to lower temperatures during isochronal annealing because of the higher dislocation density[108]. Figure 6.8 shows the effect of grain size on the recrystallisation process of cold worked low carbon manganese steel.

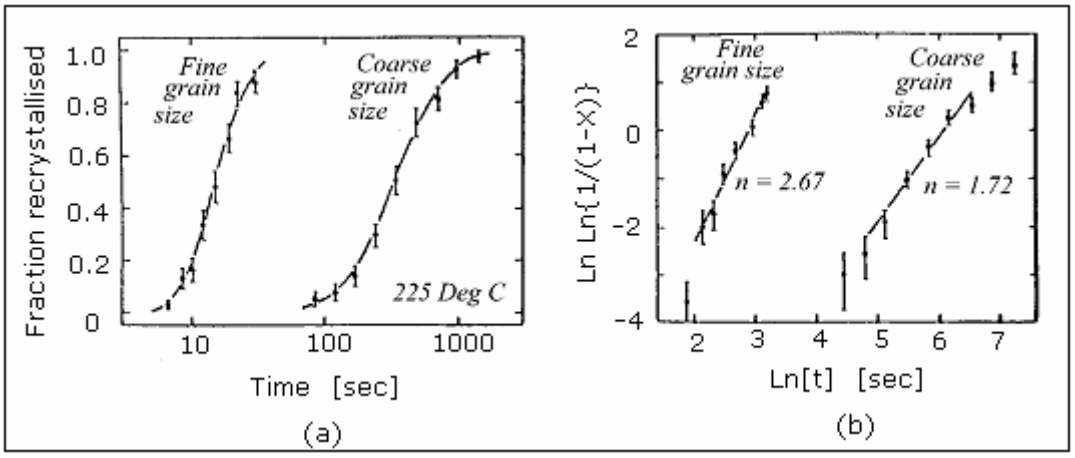

Figure 6.8: (a) Isothermal recrystallisation curves for pure Cu showing the effect of annealing at 225°C after cold work for a fine grained and

a coarse grained material and (b) the kinetics plotted according to the JMA equation. In both figures the vertical bars represent the 95 percent confidence limits. [108]

6.9 The influence of solutes and second phase particles on recrystallisation

The recrystallisation process in two-phase materials is usually quite complex. It is generally found that second phase particles may either retard or accelerate the recrystallisation process, if compared to an equivalent single phase material, depending on the conditions.

For instance, the presence of precipitates may affect the intensity and homogeneity of cold work during deformation. When an alloy is plastically deformed, the non-shearable particles will cause an increased dislocation density, thus increasing the driving force for subsequent recrystallisation, if compared to a single phase material. The regions around large particles may also act as preferred nucleation sites for recrystallisation due to inhomogeneous deformation (Particle Stimulated Nucleation PSN as has been found in aluminium alloys) while at the same time, small particles or closely spaced ones, may pin the grain boundaries and in effect limit their mobility. The dissolved elements (solute atoms and their clusters) can also affect the recrystallisation kinetics by segregating to dislocations, subgrain boundaries and grain boundaries with the result that their mobility is decreased by "impurity drag" or "solute drag".

Chapter 6 The theory of recovery and recrystallisation in metals

The situation becomes more complex as transformation processes of nucleation and growth or transformation of the precipitates to a more stable state and recrystallisation take place simultaneously or sequentially. In the case where semi-coherent precipitates transform to a stable incoherent state, followed by coarsening, an extra driving force is provided in the process as the system energy is lowered further and this promotes continuous recrystallisation[79]. Coarse particles may form in the rolling microbands whereas the metastable precipitates may form along side the microbands and this may lead to an evolution of banded recrystallised microstructures of coarser and finer grains respectively[78,109-112].

The interaction of particles with the grain or subgrain boundaries is generally explained by the Zener "drag" effect[113]. When a grain boundary migrates into a field of spherical incoherent particles of concentration n per unit volume of a mean radius r (whose interfacial energy γ_s is unchanged by the passage of a high angle grain boundary), the reduction in driving force per unit volume (also called the "pinning force") is, therefore, given by:

$$P_Z = \left(\frac{3\gamma_s}{4}\right)\left(\frac{V_v}{r}\right) \qquad (6.14)$$

Equation 6.14 indicates that finer precipitates and large volume fractions (or more closely spaced and fine precipitates) are more

effective in pinning subgrain or grain boundaries. In general, the driving force for recrystallisation (typically 10^7 J m^{-3}) is higher by three orders of magnitude than the Zener "drag" pinning force (typically 10^4 J m^{-3} for reasonably low volume fractions and somewhat coarsened particles). Consequently, small quantities of medium sized to large precipitates on grain boundaries may not have a significant effect on the overall thermodynamics of recrystallisation. If significantly small in size and large in number, however, they do have an effect through their impact on the mobility of the grain or subgrain boundaries.

Analysis of the drag effect by solute or impurity atoms around a moving boundary is more complex than the effect by particles, but that some atom-based drag effect does exist, has been shown often. For instance, many workers[92,114-116] have observed an initial retardation of recrystallisation at high concentrations of solute atoms that was followed by accelerated recrystallisation after the precipitation of the solute atoms into a particle and its subsequent coarsening. Figure 6.9 shows the effect of the solute atoms and their subsequent precipitation and coarsening on recrystallisation i.e. at higher annealing temperatures, recrystallisation precedes precipitation while at lower annealing temperatures there is an interaction between precipitation and recrystallisation and the latter is initially retarded and only accelerates after precipitation and coarsening of the particles. The general condition for the recrystallisation to proceed is, therefore:

$$P_d + P_c > P_z \qquad (6.15)$$

where P_d and P_c are the driving forces due to deformation and precipitation of the second phase given by equations 6.11 and 3.4 respectively and P_z is the retarding force due to Zener drag given by equation 6.14.

In extreme cases of the Zener "drag" effect, the recrystallisation process can completely stop, called "recrystallisation arrest", shown below schematically in the temperature range between T_2 and T_3 for the case of a dislocation density of ρ_2. The Zener "drag" effect can also be manifested by a large deviation of the Avrami exponent n from linearity as shown in figure 6.10.

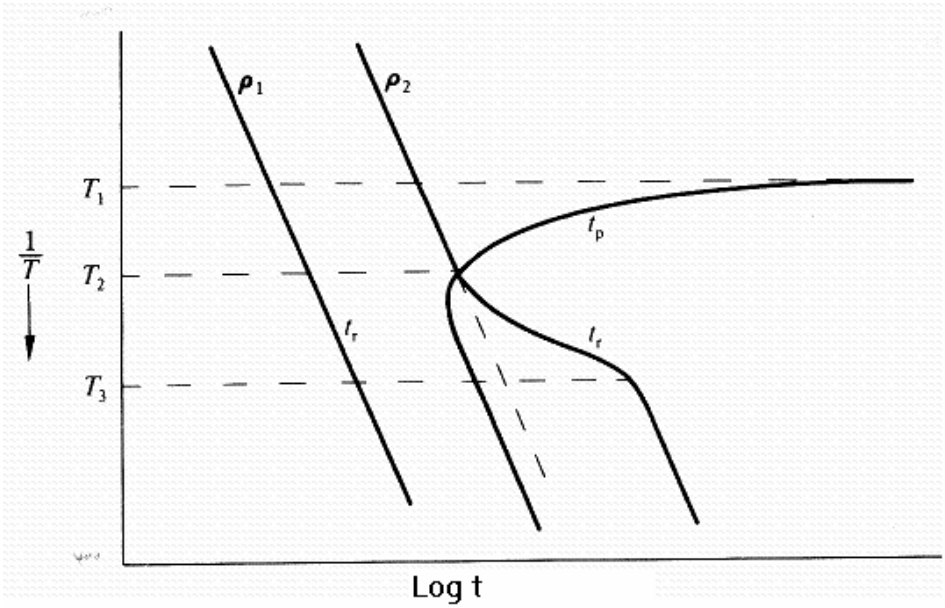

Figure 6.9: The time dependence of the precipitation start time t_p and recrystallisation start time $t_r^{(112)}$.

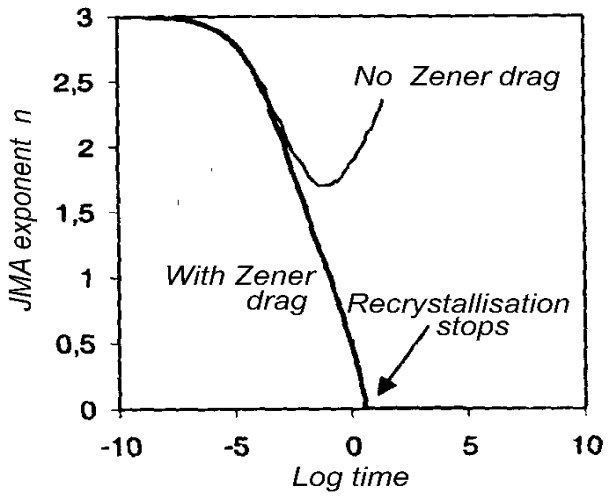

Figure 6.10: The effect of Zener drag on the recrystallisation process as modelled for Ta with oxide particles[117].

Chapter 7 Recrystallisation after cold work of low carbon Al-killed strip steels

7.1 Introduction

The annealing of cold worked Al-killed steels has been a subject of many investigations[8-11,60,122-124]. These studies have been concerned with the kinetics of recrystallisation, with microstructure and texture development and with the individual and combined effects of composition, thermal history prior to cold work and heating rates during subsequent annealing.

The extent of isothermal recrystallisation with time follows the normal sigmoidal relationship and is mostly modelled by the JMAK equation. This is with the exception in some cases of Al-killed steels where the process is inhibited by the precipitation of AlN precipitates.

7.2 Interaction between AlN precipitation and the recrystallisation process after cold work

The greatest limitation in the study of the interaction between the precipitation of AlN and the recrystallisation process in low carbon Al-killed strip steels has been the difficulty in observing the very early stages of AlN precipitation in deformed structures by electron microscopy. Meyzaud et al[8] studied the precipitation of AlN indirectly by the electrical resistivity method, see figure 7.1.

Chapter 7 Recrystallisation after cold work of low carbon Al-killed strip steels

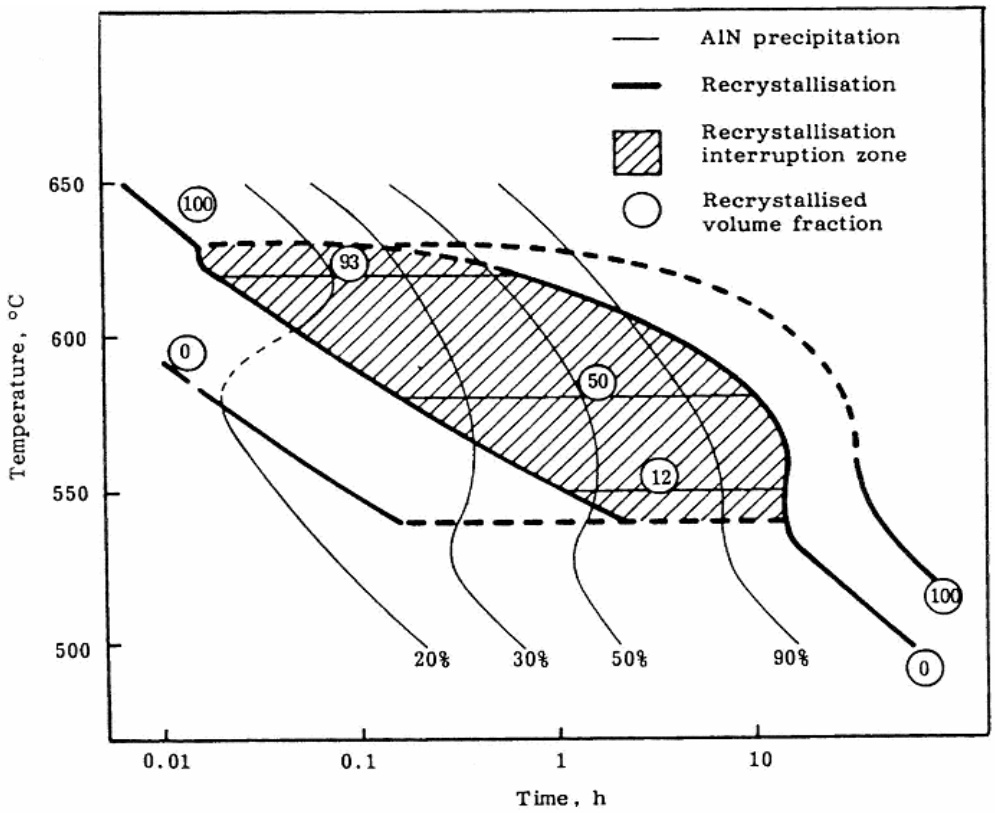

Figure 7.1: The TTT curves for recrystallisation and AlN precipitation in cold rolled (70 percent deformation) Al-killed steel[8].

The interaction between AlN precipitation and recrystallisation can be described as follows: at higher temperatures (> 650 °C), recrystallisation precedes precipitation, at lower temperatures (< 550 °C) precipitation precedes recrystallisation, while at intermediate temperatures both proceed together. However, at these intermediate temperatures, the recrystallisation process is retarded and only accelerates again after growth and coarsening of the AlN precipitates has made their pinning force ineffective. This observation agrees with earlier studies on the effect of solute

atoms and their subsequent precipitation on the recrystallisation process[8-11,92,112]. It has been observed that in Al-killed steels and during isothermal annealing after cold work, the recrystallisation process is inhibited by the nucleation/clustering of AlN on subgrain boundaries and dislocations. Goodenow et al[118] observed that during isothermal annealing at 580 °C after cold work, recrystallisation took place at shorter times in rimmed steels than in Al-killed steels and it was suggested that this was caused by the "precipitation/clustering" of AlN. As mentioned earlier, the greatest challenge has always been the failure to observe the pinning effect directly by electron microscopy on the recrystallisation process in the early stages of the clustering/precipitation of the AlN. Nevertheless, this effect has been used with relative success in microstructure and texture control during annealing after cold work in these steels.

7.3 Influence of S, Mn and MnS on the recrystallisation process after cold work

In a study[119] on the influence of sulphur in solid solution on static recrystallisation of cold worked low carbon manganese strip steels, it was found that increasing the content of sulphur in solid solution in the steel, retarded the recrystallisation process, see figure 7.2. As may be seen, the increase in sulphur in solid solution did not only increase the incubation period for recrystallisation but also resulted in only partial recrystallisation of the steel. It was suggested that the sulphur or both the sulphur and manganese, inhibit the nucleation and growth of new grains

by segregating to the grain boundaries. Prior annealing of the steel at 700 °C to precipitate the MnS before cold work, increased the recrystallisation kinetics as shown in figure 7.2, with the top curve for the steel with less than 10 ppm sulphur in solid solution, recrystallising faster. Although their results were not conclusive, Baird et al[120] made similar observations earlier that sufficient amount of sulphur in solid solution (50 ppm) gave rise to difficulty in recrystallisation of iron. Their evidence was based on the fact that when manganese was added to the iron to form MnS, the iron recrystallised normally without exhibiting any "sluggish" behaviour.

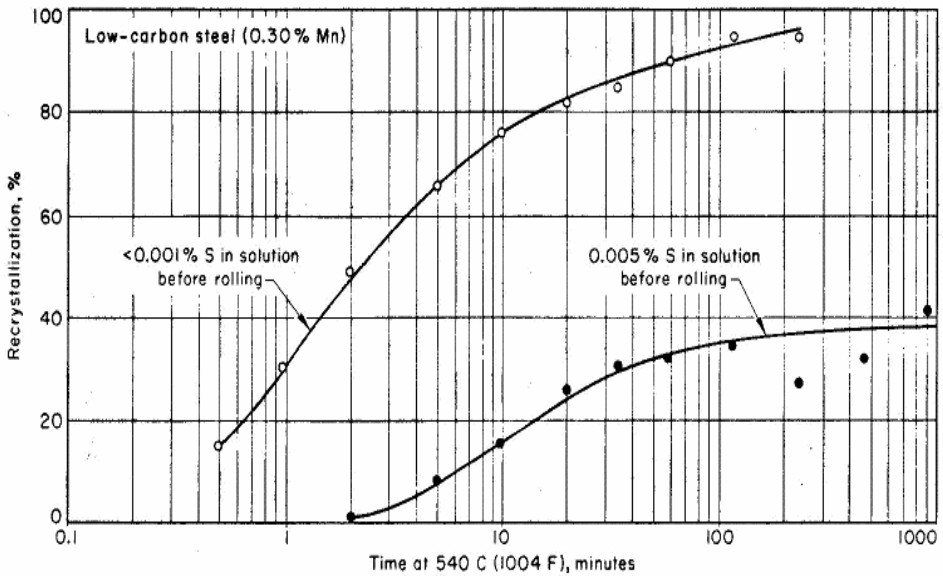

Figure 7.2: Effect of annealing time at 540 °C on the percentage of recrystallisation in 60 percent cold worked low carbon manganese strip steels containing two different amounts of S in solid solution before cold rolling. Note the retarded recrystallisation of the steel with more S in solid solution[119].

Chapter 7 Recrystallisation after cold work of low carbon Al-killed strip steels

In another study[122] on the influence of solute manganese on static recrystallisation of cold worked Al-killed steels with 70 ppm sulphur, it was found that increasing the solute content of manganese, retarded the recrystallisation process by increasing the incubation period without affecting the nucleation and growth rate of the recrystallisation, see figure 7.3. It was proposed that the prolonged incubation period was probably not directly as a result of the solute manganese as such but rather as a result of Mn-C complexes that had strong interaction with dislocations.

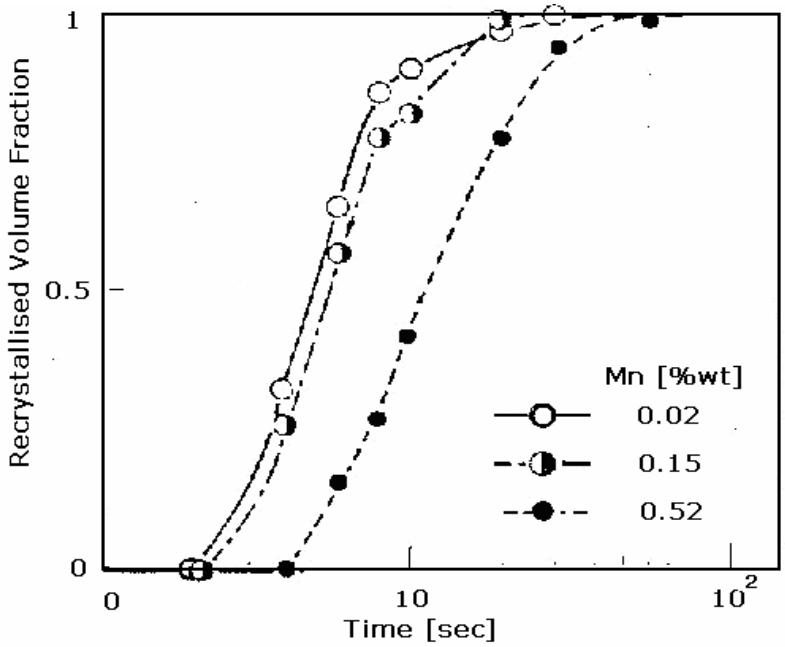

Figure 7.3: Influence of solute Mn on the recrystallisation progress in 80 percent cold worked Al-killed low carbon-manganese steel during isothermal annealing at 650 °C[122]

Chapter 7 Recrystallisation after cold work of low carbon Al-killed strip steels

Frawley et al[68] also observed in high sulphur low carbon steels that the finer MnS with a diameter of 5 to 30 nm, and or the sulphur in solid solution, retarded the dynamic recrystallisation of austenite during laboratory hot rolling in thin slab direct rolling (TSDR), i.e. in a simulated HCR experiment. However this study did not separate the effect of sulphur from that of MnS on the dynamic recrystallisation process in these steels.

Chapter 8 Techniques to determine the solubility of AlN and free nitrogen in Al-killed low carbon strip steels

8.1 Introduction

Methods of measuring free nitrogen in steels may be direct or indirect. Some of the direct techniques include chemical analysis and hot hydrogen extraction while the indirect techniques, include the strain ageing index method, thermoelectric power techniques (TEP), resistivity techniques, magnetic techniques and internal friction. Some of these techniques are discussed briefly in the following sections.

8.2 Chemical analysis

The iron matrix is dissolved without dissolving the aluminium nitride and the insoluble nitrides are then separated through filtration. The most common used chemical dissolution technique for separating AlN from the iron matrix is that developed by Beeghly[53]. Although the Beeghly technique was criticized for lack of sensitivity to small particles of less than 10 nm in size and failure to isolate the AlN from other nitrides, it is still widely used in the determination of free nitrogen in low carbon steels[66].

8.3 Hot hydrogen extraction method

The use of hydrogen to combine with free nitrogen in a steel in a hydrogen furnace at about 500 °C, is one of the oldest techniques that is still used today to determine the free nitrogen content in steels. The diffusivity and solubility of both nitrogen and hydrogen at the test temperature need to be established in order to determine the annealing time that would ensure adequate

diffusion of hydrogen into the steel, taking into account the sample size and temperature. Fine metal shavings are preferred as this ensures efficient combination of the hydrogen and nitrogen through shorter diffusion paths.

The hydrogen also accelerates the rate of escape of nitrogen by reducing the oxide layer that may form on the surface of the metal and inhibit the escape of nitrogen. Hydrogen combines with the free nitrogen on the surface in a suggested sequence as follows[53]:

$$N_{ads} + H_{ads} \rightarrow NH_{ads} \quad (8.1)$$

$$NH_{ads} + H_{ads} \rightarrow NH_{2ads} \quad (8.2)$$

$$NH_{2ads} + H_{ads} \rightarrow NH_{3ads} \quad (8.3)$$

$$NH_{3ads} \rightarrow NH_{3gas} \quad (8.4)$$

The captured ammonium gas is then quantitatively analysed by conventional chemical analysis techniques.

Chapter 8 Techniques to determine the solubility of AlN and free nitrogen in Al-killed low carbon strip steels

8.4 Strain aging index method

Free carbon and nitrogen atoms fill the interstitial positions of the iron crystal lattice, creating strain within the lattice structure due to the atom misfit. As a result, these interstitial atoms segregate to dislocations in order to lower the system's strain energy. Since the interstitial voids for austenite (fcc) are greater than that for ferrite (bcc), the driving force for segregation to dislocations is less in austenite than in ferrite. These interstitial atoms form a cloud of atoms or "Cottrell atmospheres" on the dislocations, locking the glissile ones in the process. This phenomenon has a strengthening effect that is reflected in the increase in yield strength of the material and, therefore, can be used indirectly to measure the content of interstitial solutes. This technique is generally called the "strain aging index method" and is preferred to the other techniques for its simplicity, see figure 8.1. However, as may be seen in figures 8.2 and 8.3, one should be mindful of the large scatter in results associated with this technique. Morrison et al[126] correlated the increase in yield strength ΔY to the free nitrogen content as shown in figure 8.2.

Chapter 8 Techniques to determine the solubility of AlN and free nitrogen in Al-killed low carbon strip steels

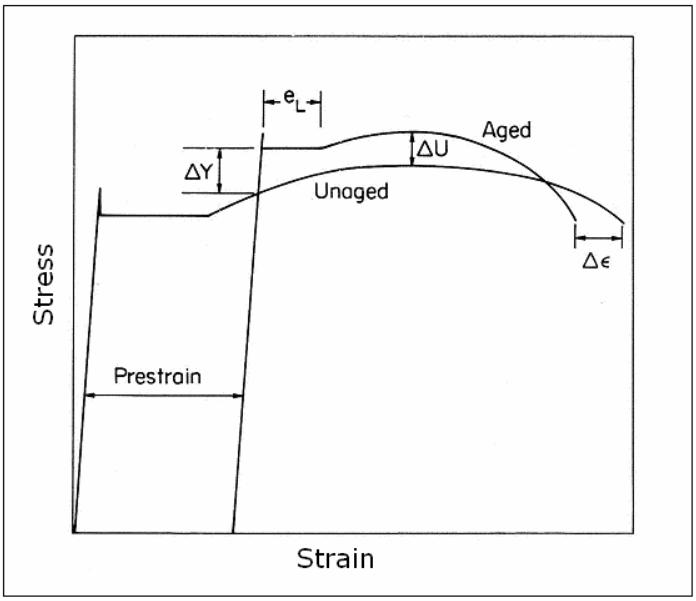

Figure 8.1: Effect of static aging on the load-elongation curve of iron containing interstitial solutes: ΔY = change in yield stress due strains aging, e_L = Lüder's strain after strain aging, ΔU = increase in ultimate tensile strength and Δϵ = decrease in elongation due to strain aging[125].

The diffusivity of nitrogen at low temperatures (<400 °C) is higher than that of carbon and, therefore, in the absence of aluminium in the steel, strain aging is mainly caused by nitrogen. At temperatures below 100 °C, the effect of nitrogen is about twice that of carbon[127] (see figure 8.3). As may be seen, solute nitrogen at levels as low as 5 ppm, would give an increase of about 20 MPa in yield strength.

Chapter 8 Techniques to determine the solubility of AlN and free nitrogen in Al-killed low carbon strip steels

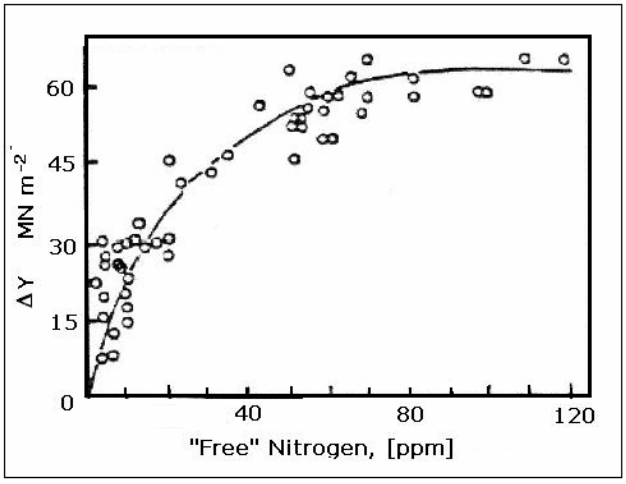

Figure 8.2: Influence of free nitrogen content on the magnitude of strain aging in low carbon sheet steels, (Morrison et al[126]).

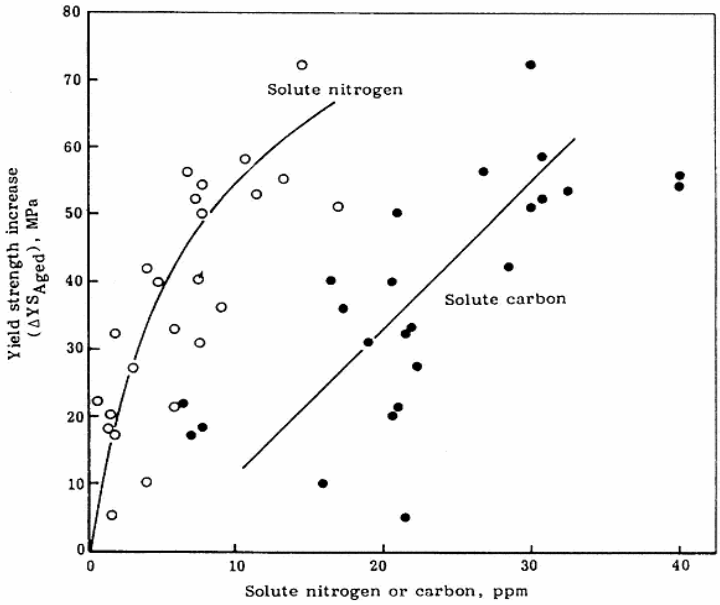

Figure 8.3: Influence of C and N on the yield strength of a low carbon and aluminium-killed steel after 70 percent cold reduction and aging at 38 °C for 30 days[127].

Chapter 8 Techniques to determine the solubility of AlN and free nitrogen in Al-killed low carbon strip steels

8.5 Internal friction methods (Snoek effect)

The redistribution of interstitial atoms (C and N) following elastic lattice distortion, causes the strain to lag behind the stress. This behaviour is also known as the Snoek effect, after its discoverer[128]. When a crystal is elastically stretched in the z-direction then there is a preference for the interstitial atoms to occupy the elongated z sites and a shift in the equilibrium positions occurs, such that the number of occupied z (octahedral or tetrahedral) sites increases whilst those sited in the x and y axis directions decrease. This redistribution of interstitial atoms takes a little while upon instantaneous application and removal of stress. The rate at which this happens is determined by the frequency of jumping of these atoms and consequently by the temperature. The characteristics of the jump frequency are unique to particular interstitial atoms and, therefore it is possible to separate the effects of nitrogen from those of carbon, at least in principle.

The maximum internal friction is attained when the period of application of stress equals the jump time. The Snoek effect is usually observed through free torsional oscillations of the sample and its peak is proportional to the concentration of the interstitial atoms in solid solution.

The interstitial solutes that contribute to internal friction in the manner described above are those that occupy the normal sites in the undistorted lattice. Atoms within the strain field of a

Chapter 8 Techniques to determine the solubility of AlN and free nitrogen in Al-killed low carbon strip steels

dislocation, those neighbouring a substitutional solute atom, or those at grain boundaries will not react in the same way to the applied stress[129]. For this reason, internal friction measurements have not been successfully used in determining the carbon and nitrogen concentrations in solid solution of commercial steels.

8.6 Thermoelectric power (TEP) method (Seebeck effect)

The TEP technique is based on the phenomenon called the Seebeck effect[130], named after its discoverer in 1822. This effect occurs because at the hot junction, the Fermi energy of the electrons is higher than at the cold junction. The higher energy electrons at the hot end lower their energy by diffusing to the cold junction. Consequently the cold junction becomes negatively charged and the hot junction positively charged and a voltage drop is induced between the two junctions. This technique is applicable to materials that conduct electricity.

The TEP is a proportionality coefficient between the electron flux (emf) and the temperature gradient $\triangle T$ that exists between the cold and hot junctions of the test sample, as illustrated in figure 8.4. The TEP is affected by lattice defects and is the sum of various contributions i.e.

$$\Delta S = \Delta S_{ss} + \Delta S_{d} + \Delta S_{pp} \qquad (8.5)$$

where ΔS_{ss}, ΔS_d, and ΔS_{pp} are due to the elements in solid solution, dislocations and precipitates respectively

The TEP measurement between the test specimen and the reference specimen is given by:

$$\Delta S = \frac{\Delta V}{\Delta T} = S - S_0 \qquad (8.6)$$

where ΔV is the emf difference between the test specimen and the reference specimen, ΔT is the temperature difference between the cold and hot junctions of both the test specimen and the reference, S and S_0 are the absolute TEP values of the test specimen and the reference respectively.

When using the Seebeck effect to analyse the chemical composition of a metal, two distinct phenomena may affect the TEP: the diffusion of electrons through the test metal and the phonon drag. If a temperature gradient exists across the conductor, phonons (thermal lattice vibrations) will move from the hot to the cold junction against the flow of electrons causing, what is known as phonon drag. This phenomenon is significant at temperatures below twenty percent of the Debye temperature[131-134]. It is, therefore, important that the TEP measurements are carried out above the twenty percent level of the Debye temperature of iron, which is 477 K, where the diffusion of electrons dominates over phonon drag in order to separate the two effects. Measurements at and around 0°C to room

temperature are, therefore, adequate to separate these two effects.

8.6.1 Effect of solid solution on the TEP

For concentrations of <0.1 at% of an element in solid solution, the TEP decreases proportionally with the increase in concentration of the element in solid solution, as illustrated in figure 8.4. It is worthwhile to note that a concentration >0.1 at% results in interactions between the solute atoms themselves and, therefore, this affects the Gorter-Nordheim linear relationship between the TEP and the concentration of the solute atoms, equation 8.7.

The slope of the graph of the TEP versus the concentration of the element in solid solution, gives the proportionality constant known as the TEP coefficient, see figure 8.5. This is represented by the Gorter-Nordheim law[135], which is expressed as follows:

$$\Delta S_{ss} = K_i.[i]_{ss} \qquad (8.7)$$

where $[i]_{ss}$ represents the content of the solute element and K_i is the TEP coefficient of the element.

Chapter 8 Techniques to determine the solubility of AlN and free nitrogen in Al-killed low carbon strip steels

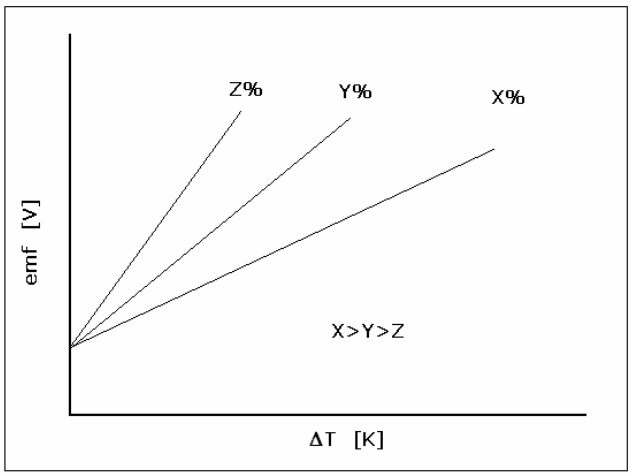

Figure 8.4: Schematic graph showing variation of emf with change in temperature. The slopes are the TEP values for the solute element in different concentrations X, Y and Z, with all concentrations <0.1 at%.

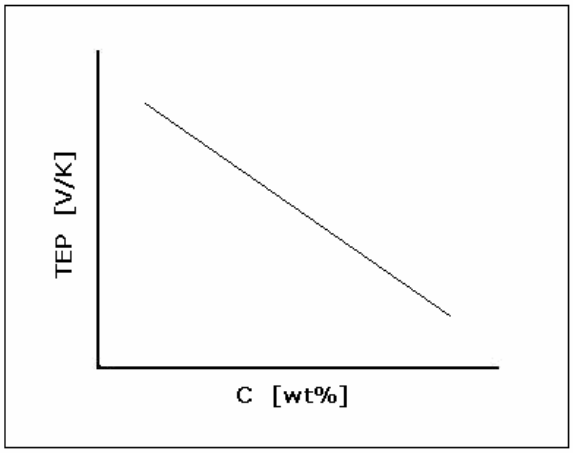

Figure 8.5: Schematic diagram of TEP versus content of the element in solid solution and the slope of this graph is the TEP coefficient of the latter.

8.6.2 Effect of dislocations and precipitates on TEP measurements

It has been observed[136] that cold working has a negative effect on the TEP just the same as adding solute atoms to the matrix. It is worth noting that solute atoms that segregate to dislocations and grain boundaries and thereby relieve their strain energies in the matrix, do not contribute to the TEP. It is for this reason that measuring of nitrogen in solid solution using this technique, has to be done immediately after quenching from the solution temperature or on samples that are stored in liquid nitrogen in order to avoid strain aging. The contribution of precipitates on the TEP is negligible unless they are small and coherent.

Chapter 9 Techniques for measuring recrystallised volume fraction in metals

9.1 Introduction

There are direct and indirect methods of measuring the volume fraction of the recrystallised material. Some of the techniques are discussed in the following sections.

9.2 Hardness test

This is the easiest and quickest technique of estimating the volume fraction of the recrystallised material. The amount of recrystallisation is related to the drop in hardness as the annealing time is extended and the volume fraction of the recrystallised material X is given proportionally as[137]:

$$X = \frac{h_o - h_i}{h_o - h_f} \qquad (9.1)$$

where h_o is the microhardness at the start of recrystallisation, (generally measured at the 5% recrystallised state taken as a datum point to avoid the effects of recovery[137]), h_i is the microhardness after annealing for a time t_i and h_f is the microhardness in the fully recrystallised state.

As this method assumes a linear or direct relationship of hardness with volume fraction recrystallised (which is not always the case), it is necessary to authenticate the recrystallised volume fraction with metallographic analysis although the 5% recrystallisation volume fraction may not be easy to measure accurately.

Chapter 9 Techniques for measuring recrystallised volume fraction in metals

In isothermal annealing of cold worked nickel (fcc) and aluminium (fcc), it was observed that hardness was not significantly affected by the recovery process but only by the recrystallisation process[138,139], see figure 9.1. This technique has also been successfully applied to the study of the recrystallisation process in low carbon steels (bcc) [140].

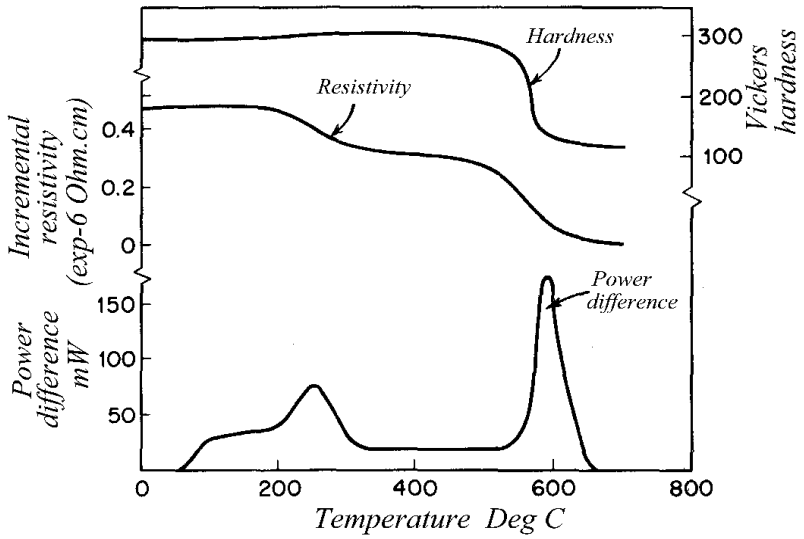

Figure 9.1: Isothermal annealing curves for cold worked nickel (fcc)[138].

Note that both the calorimetry and resistivity techniques are sensitive enough to register both the recovery and recrystallisation peaks whereas the hardness test registers only recrystallisation[138].

9.3 Metallographic analysis

This is a widely used technique whereby the material is polished and etched and observed by optical microscopy. The recrystallisation volume fraction is measured by the point count method or through

the use of computer software that computes the volume fraction through area fraction analysis from the phase contrast between the recrystallised and non-recrystallised regions of the material. These metallographic techniques are based on the equivalence between the volume fraction and the intercepted area, line or point fractions in opaque two-dimensional material. This principle is well documented in the literature[141]. This method, if a reliable phase contrast can be obtained by etching, is preferred as it provides a direct measurement of the volume fraction X of recrystallised material and is not an indirect one as with hardness measurements.

9.4 Electrical resistivity method

Plastic deformation increases the electrical resistivity of the deformed material slightly. This phenomenon is used to indirectly measure the degree of recovery and recrystallisation during the annealing process, provided there is no other phase change taking place simultaneously. One of the weaknesses of this technique is that it is sensitive to specimen size and, therefore, it is imperative to ensure that the different resistivity measurements take into account differences in specimen size.

9.5 Differential Scanning Calorimeter

When a piece of metal is plastically deformed, part of the expended energy in the deformation process is retained as stored energy that is later on released in the form of heat during subsequent annealing. The released heat is used to measure the extent of the recrystallisation process. A well annealed reference

specimen of the same material as the plastically deformed one and in which no recrystallisation is taking place, is normally used.

Non-isothermal experiments are easier to set up as both the sample and the reference are heated up at the same rate[142]. The heat flux $\dot{E}$ or (dE/dt), is measured as a function of temperature T and the heating rate β is the measuring parameter. As the sample releases the stored energy, less heat is required to maintain the heating rate. The $\dot{E}_{(T,\beta)}$ heat flux curves often have a peak more or less bell-shaped, figure 8.1, and the total energy $E_{(T,\beta)}$ released is obtained by integrating the area under the curve within the specified temperature limits. The recrystallised volume fraction can be derived in energy terms[143]:

$$X_{(T,\beta)} = \frac{E_{(T,\beta)}}{E_{stored}} \qquad (9.2)$$

where E_{stored} is the energy released in a fully recrystallised material.

The advantage of this technique is that during the annealing process, it is quite common to observe two energy peaks, one for recovery and the other for recrystallisation. This makes it possible to separate the two processes.

9.6 Electron Back Scattering Diffraction (EBSD)

The electron back scattering diffraction (EBSD) technique is one of the modern techniques that are used to study the recrystallisation process by determining crystal orientation mapping (COM). The grain boundaries are characterised by the orientation relationship between adjacent regions, the grains and subgrains are displayed in a colour code according to their orientation relationships as defined in the software program. The recrystallisation process may be studied through the observation of the number of HAGB i.e. angles above about 10° to 15°.

One weakness with this technique is that it is time consuming when it is required to investigate an area that would be a fair representation of the bulk. In these instances, a compromise between the scanning step size (nm) and the precision of the information to be extracted has to be made.

Chapter 10 Experimental procedure for determining the AlN solubility in low carbon Al-killed steel using TEP measurements

10.1 Introduction

Low carbon strip steels with different amounts of sulphur were received from Mittal Steel (South Africa), with high and low sulphur contents. The steel alloys were received in the as-cast condition and the chemical compositions are given in table 10.1 below.

The alloys were hot rolled on a laboratory rolling mill at Mintek into 10 mm thick plates and the schematic diagram for the rolling process is given in figure 10.1 below. The finishing temperature for the last pass was checked by pyrometer and for all the alloys was above 900 °C.

10.2 Sample preparation for TEP measurements

Although TEP measurements are not sensitive to specimen size, these were prepared in two sets of strips; the first set was 90 mm long, 4 mm wide and 1 mm thick and the second set was 20 mm long, 4 mm wide and 1 mm thick. The latter set was from material on which the hot deformation and coiling treatment was simulated on a Gleeble 1500^{TM} hot compression facility. In general, thin specimens were preferred for TEP measurements because of the reduced heat transfer path between the cold and hot junctions which aided thermal equilibrium conditions on these junctions.

Chapter 10 Experimental procedure for determining the AlN solubility in low carbon Al-killed steel using TEP measurements

Table 10.1: Chemical compositions of the low carbon strip steels that were studied: HS = high sulphur and LS = medium to low sulphur, the first numeral is for the sulphur content and the second for the nitrogen content, both in ppm.

Element (ppm)	HS130-50	HS90-34	HS90-12	HS140-104	LS70-38	LS10-83	LS2-65	LS16-101
C	320	280	270	510	580	510	380	590
Mn	**2300**	**1870**	**1720**	**2240**	**2560**	**3140**	**2500**	**3600**
P	130	60	90	80	210	70	50	76
S	**130**	**90**	**90**	**140**	**70**	**10**	**2**	**16**
Si	160	60	50	140	210	330	200	140
Cu	257	140	130	260	30	30	90	-
Ni	175	100	20	110	60	50	10	-
Cr	308	130	200	270	110	110	80	98
Mo	20	20	30	10	0	10	10	33
V	20	10	10	20	60	70	70	80
Nb	30	10	10	10	10	10	20	55
Ti	7	20	20	20	20	20	10	-
Al_{total}	**480**	**430**	**390**	**500**	**200**	**340**	**450**	**240**
$Al_{acid\ sol}$	**458**	**379**		**470**		**333**	**370**	**-**
Ca	2	0	0	1	14	26	20	9
N	**50**	**34**	**12**	**104**	**38**	**83**	**65**	**101**

Chapter 10 Experimental procedure for determining the AlN solubility in low carbon Al-killed steel using TEP measurements

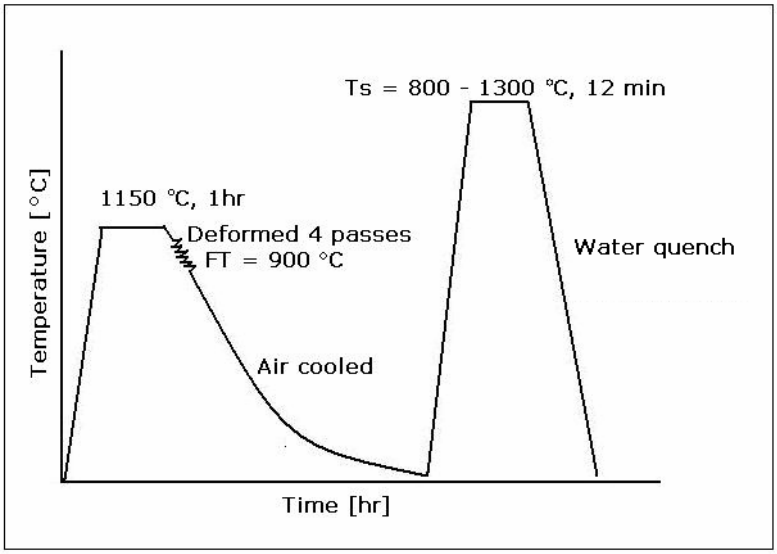

Figure 10.1: Schematic diagram for the hot rolling schedule and the solution heat treatment in the dilatometer and furnace.

10.3 TEP solution treatment

The solution heat treatment (mainly for the dissolution of the AlN) was done under argon gas in a vertical tube furnace and the temperature range was varied from 800 to 1300 °C, figure 10.1. The specimens were suspended in the furnace as shown in figure 10.2 and were soaked for 12 minutes at the test temperature to ensure that equilibrium dissolution conditions of the AlN was attained before quenching into water.

Chapter 10 Experimental procedure for determining the AlN solubility in low carbon Al-killed steel using TEP measurements

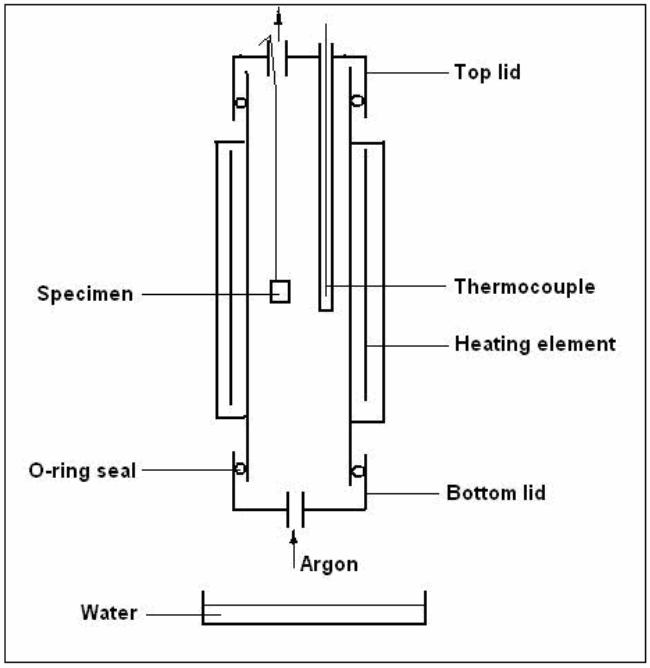

Figure 10.2: The furnace heat treatment arrangement.

10.4 TEP measurements in as-quenched condition

The specimens were clamped to the copper blocks and the TEP measurements were recorded after 1 minute. TEP measurements were immediately taken after the samples had been quenched from the solution treatment furnace in order to avoid strain aging by nitrogen. The furnace and the TEP equipment were, therefore, arranged close to each other.

The photograph and schematic diagram for the TEP measurement arrangement are given in figures 10.3 and 10.4 respectively. The

Chapter 10 Experimental procedure for determining the AlN solubility in low carbon Al-killed steel using TEP measurements

two copper blocks were kept at a temperature difference of 15 ºC in order to maintain a temperature gradient ΔT between the cold and hot junctions of the specimen. For this, one block was filled with ice and the temperature at the cold junction was maintained at 5° ± 1°C while the other one at the hot junction was filled with water at room temperature at 20° ± 1°C. K-type thermocouples were spot welded onto the hot and cold junctions of the specimen.

A data logger was used to log both the temperature data and the voltage drop ΔV across the hot and cold junctions (as shown schematically in figure 10.4) into different analog channels of the Data-Taker dt800 which amplified and converted this data into digital data that was recorded using Delogger software. The voltage drop ΔV was measured from the Chromel wires from the cold and hot junctions. The advantage with the arrangement in figure 10.4 was that the instantaneous voltage difference ΔV was measured together with the corresponding temperature difference ΔT between the cold and the hot junctions of the sample out of which the instantaneous absolute TEP measurement was obtained.

Chapter 10 Experimental procedure for determining the AlN solubility in low carbon Al-killed steel using TEP measurements

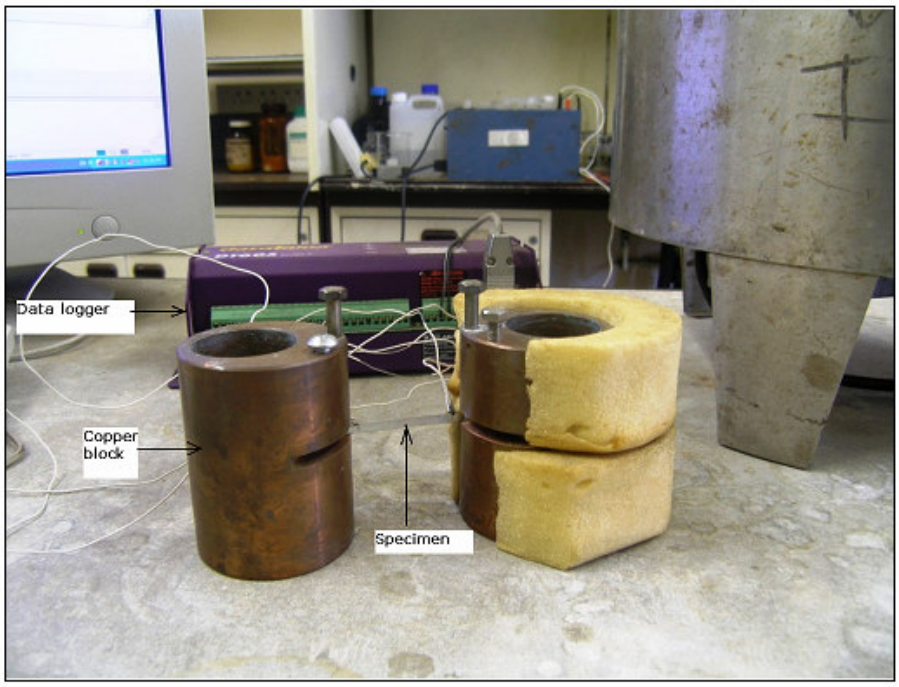

Figure 10.3: Photograph of the TEP measurement arrangement.

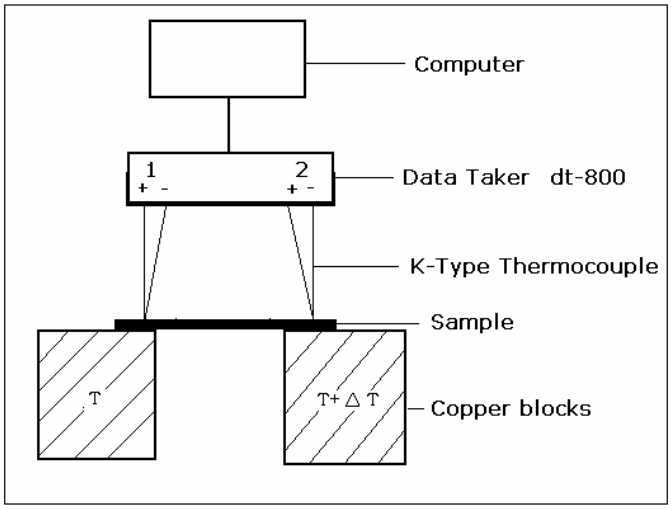

Figure 10.4: Schematic diagram for the TEP measurements.

Chapter 10 Experimental procedure for determining the AlN solubility in low carbon Al-killed steel using TEP measurements

10.5 TEP measurements after hot rolling and coiling simulations on the Gleeble 1500™

TEP measurements were conducted on the specimens after hot rolling and coiling simulated in the Gleeble 1500™ according to the rolling schedule and heat treatment cycle specified in table 11.1 and figure 11.1 below. The objective was to assess whether the AlN had partially or fully precipitated during coiling. These measurements were carried out on the specimens that were simulated in their hot rolling and coiling at 600 °C as this lower coiling temperature was more sensitive to the precipitation of AlN.

The heat treatment cycle prior to the TEP measurements is given in figure 10.5 below. The first set of the absolute TEP measurements, i.e. TEP1, measured the trend of nitrogen in solid solution immediately after coiling while the second one (TEP2) checked whether further precipitation of AlN took place after coiling or not. If there is no significant variation in the TEP values between the first and second set that would imply complete precipitation of AlN after coiling. Further precipitation of AlN after coiling, that is, during the second heat treatment of isothermal annealing at 800 °C for 2 hours, would lead to further depletion of nitrogen from solid solution which would lead to higher measured TEP2 values and from this observation it would be possible to establish whether the AlN had partially or fully precipitated during the coiling process.

Chapter 10 Experimental procedure for determining the AlN solubility in low carbon Al-killed steel using TEP measurements

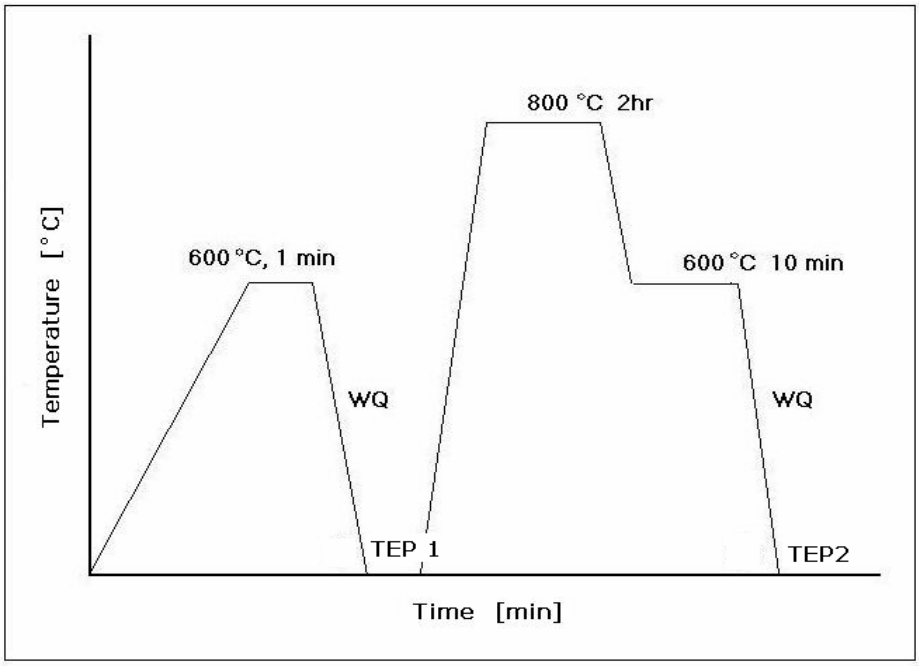

Figure 10.5: Heat treatment cycles for TEP measurement after coiling simulation on the Gleeble 1500™, TEP 1 is TEP measurement after the first heat treatment cycle while TEP 2 is after the second one.

In the first heat treatment cycle in which TEP measurements TEP1 were carried out, the specimens were annealed at 600 °C for 1 minute and quenched into water. The purpose for this heat treatment was to ensure that all specimens had the same amount of carbon in solid solution during the TEP measurements and these measurements were carried out immediately after quenching into water in order to avoid strain aging by nitrogen. In the second set of TEP2 measurements, the same specimens were soaked at 800 °C for 2 hours to precipitate any remaining nitrogen into AlN and, thereafter, the specimens were cooled to

Chapter 10 Experimental procedure for determining the AlN solubility in low carbon Al-killed steel using TEP measurements

600 °C, annealed for 10 minutes and then quenched into water. The purpose for holding the sample at 600 °C for 10 minutes was to ensure that the same amount of carbon was in solid solution before the TEP measurements were taken.

10.6 TEP methodology for the determination of the dissolution of AlN during reheating

Figure 10.6 shows a schematic illustration of the heat treatment cycles and TEP measurement sequences for the study of the dissolution of AlN during reheating of the hot rolled Al-killed low carbon steel. In the as-hot-rolled condition, the AlN is either fully or partially precipitated and the expected absolute TEP value would be S_o. The volume fraction of the precipitated AlN in austenite and ferrite X_v, which is dependent on the cooling rate, is estimated by[48]:

$$X_v = K\phi^m \qquad (10.1)$$

where K is a constant dependent on the initial nitrogen and aluminium levels, the grain size and the transformation behaviour of the steel; ϕ is the cooling rate (K h^{-1}) and m is the cooling rate exponent (for C-Mn steel, Honer et al[48] found that K = 10.8 and m = -0.49).

All the specimens were first (before solution treatment) annealed at 800 °C for six hours in order to ensure that the AlN precipitated

Chapter 10 Experimental procedure for determining the AlN solubility in low carbon Al-killed steel using TEP measurements

into incoherent particles because the strain field around any undissolved coherent particles would contribute to the TEP effect, and would thereby, have affected its measurement.

The annealing temperature of 800 °C was chosen because it is close to the TTT nose for the precipitation of AlN in austenite, see figure 4.2. The absolute TEP measurement at this temperature S_{800}, became the reference for "no dissolution". The TEP measurements were conducted near or at room temperature after the steel had fully transformed to ferrite.

The samples were then soaked at various test temperatures and quenched into water, after which the absolute TEP measurements S_i were recorded. Assuming the diffusion component of the TEP was predominant at room temperature and as the concentrations of both the aluminium and nitrogen were low (< 0.1 percent), the Gorter-Nordheim rule could be used with confidence. Therefore, for a stoichiometric composition of the AlN, the relative TEP value ΔS_N could be obtained through the linear relationship:

$$\Delta S_N = S_{800} - S_i = K_{AlN}[N] \qquad (10.2)$$

where K_{AlN} is the aluminium nitride TEP coefficient and N is the nitrogen content (wt percent) in solid solution at the test temperature.

Chapter 10 Experimental procedure for determining the AlN solubility in low carbon Al-killed steel using TEP measurements

It is important to point out that the TEP coefficient K_{AlN} includes the specific influence on the TEP measurement of both aluminium (K_{Al}) and nitrogen (K_N) leaving the solid solution during the precipitation of AlN [144].

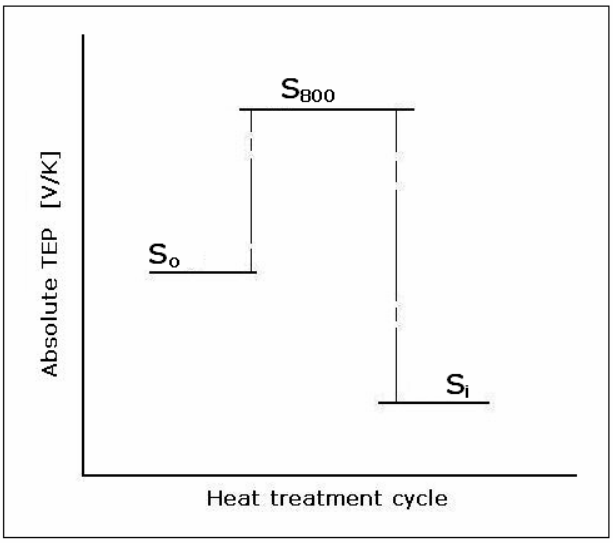

Figure 10.6: Schematic diagram of the sequence of heat treatment cycles and TEP measurements for determining the dissolution of AlN during reheating of Al-killed low carbon steel.

10.7 Checking the validity of the AlN equilibrium solubility trend in section 10.6

The trend of the nitrogen in solid solution determined by the schedule in figure 10.6 above was checked by the one in figure 10.7 below and the results were in good agreement as the relative TEP values tallied well with the nitrogen and carbon contents in

Chapter 10 Experimental procedure for determining the AlN solubility in low carbon Al-killed steel using TEP measurements

solid solution, see figure 10.8 below. The TEP coefficient for the dissolved nitrogen K_{AlN} was found to be 10 nV/K.ppm-N which is within the range observed by other authors[148].

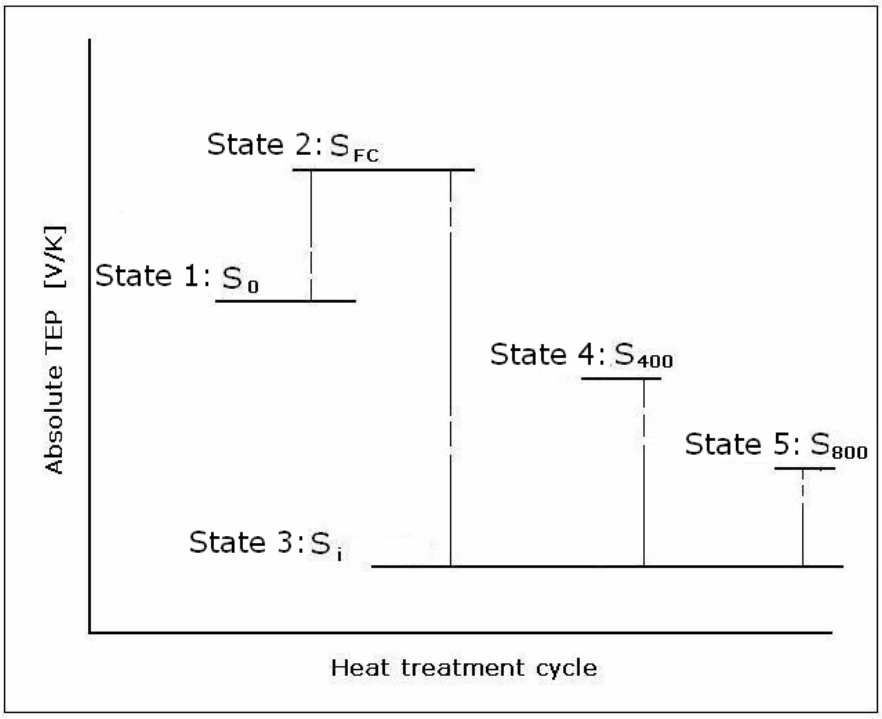

Figure 10.7: Schematic diagram of the sequence of heat treatment cycles and TEP measurements for determining the carbon and the nitrogen content in solid solution.

10.7.1 State 1, 2 and 3 of the TEP schedule

In figure 10.7, the absolute TEP measurement S_o represented the initial condition of the steel thus as-received condition which, generally, is as-hot rolled condition. The specimens were then soaked at 1150 °C for 12 minutes and furnace cooled to room

temperature to fully precipitate both the cementite (Fe_3C) and AlN and the corresponding absolute TEP measurement was designated S_{FC}. The specimens were then heated to the test temperature, (1300 °C in order to dissolve all the AlN), soaked for 12 minutes and thereafter quenched into water as schematically shown in figure 10.1. The absolute TEP measurement S_i represented the carbon and nitrogen that were in solid solution assuming negligible or constant TEP contributions from quenched-in defects and other alloying elements in solid solution.

10.7.2 State 4 and 5 of the TEP schedule

In order to separate the contribution of the carbon from that of nitrogen to the TEP measurements, one set of specimens was annealed at 400 ºC for 3 hours to precipitate the Fe_3C without precipitating the iron nitride (Fe_4N) as this temperature was above the solubility limit of the (Fe_4N) [144,145].

The equilibrium solubility of carbon in α-iron is given by[146]:

$$C_{C\text{-}eq} = 6.63 \exp\left[-\frac{49400}{RT}\right] \qquad (10.3)$$

where R is the universal gas constant which is 8.314 J mol^{-1} K^{-1} and T is the absolute temperature in K.

Chapter 10 Experimental procedure for determining the AlN solubility in low carbon Al-killed steel using TEP measurements

Therefore, at 400 ºC, the equilibrium solubility of carbon $C_{c\text{-}eq}$ would be 9.72×10^{-4} wt% (10 ppm). This implied that the contribution of the residual carbon to the TEP value would be negligible compared with the amount originally in solid solution that was between 250 and 500 ppm.

According to Fast et al[145], the solubility of nitrogen in equilibrium with Fe_4N in α-iron is given by:

$$C_{N\text{-}eq} = 12.3 \exp\left[-\frac{34700}{RT}\right] \qquad (10.4)$$

Therefore, at 400 ºC, the solubility of nitrogen in equilibrium with Fe_4N would be 250 ppm. Since the maximum nitrogen content for all the steels that were studied was 104 ppm, no iron nitride was expected to form at 400 ºC. The absolute TEP measurement after annealing at 400 ºC is designated as S_{400}. The nitrogen solubility trend could then be correlated to:

$$\Delta S_N = (S_{FC} - S_i) - (S_{FC} - S_{400}) = K_N \bullet N_{ss} \qquad (10.5)$$

where K_N is the TEP coefficient for the nitrogen in solid solution

In state 5, the specimens are annealed at 800 °C to precipitate the AlN while the carbon remains in solid solution and thereafter quenched in water. At this annealing temperature, AlN equilibrium

Chapter 10 Experimental procedure for determining the AlN solubility in low carbon Al-killed steel using TEP measurements

solubility models predict that less than 5 ppm nitrogen will be in solid solution[41,42]. The carbon content can then be correlated to:

$$\Delta S_C = \left(S_{FC} - S_i\right) - \left(S_{FC} - S_{800}\right) = K_C \bullet C_{ss} \qquad (10.6)$$

where K_C is the TEP coefficient for carbon in solid solution.

Figure 10.8 shows typical results obtained from the TEP measurement sequence shown in figure 10.6.

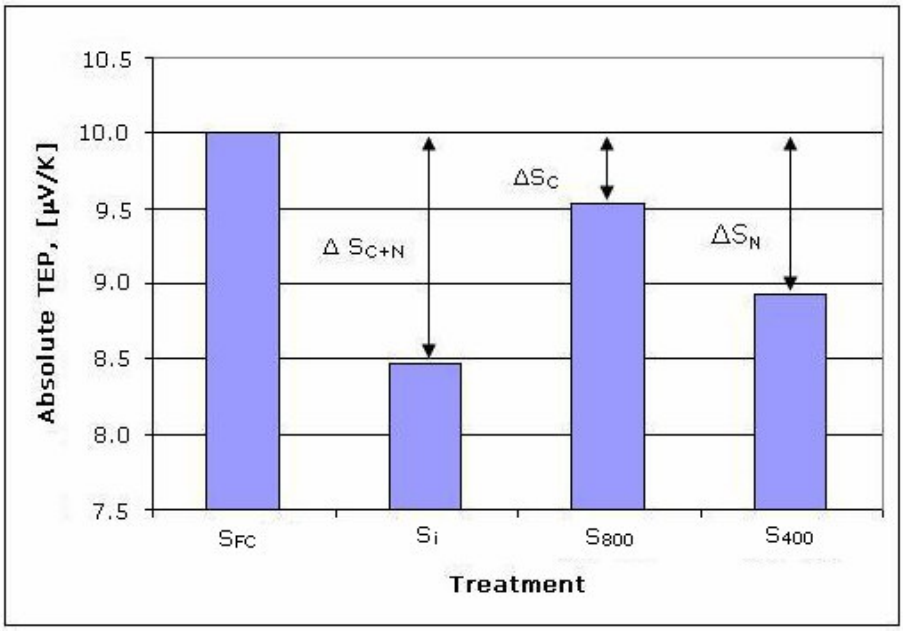

Figure 10.8: Typical absolute TEP measurements for steel LS16-101 where ΔS_{C+N} represents carbon plus nitrogen, ΔS_C the carbon and ΔS_N the nitrogen in solid solution.

Chapter 11 Experimental procedures for the study of the recrystallisation after cold work

11.1 Introduction

The static recrystallisation after cold work was studied in two stages. Firstly, the study was done on the as-cast steels, which were solution treated at 1300 °C and quenched into water. The purpose for this treatment was to dissolve the AlN, CuS/Cu_2S and MnS before cold working and annealing. Secondly, specimens from the as-cast steels were hot rolled and coiled by simulation on the Gleeble 1500^{TM} to follow the industrial conditions before cold working and annealing. In both cases, the primary objective was to investigate the influence of the sulphur and nitrogen content on the recrystallisation process.

11.2 Hot rolling simulation and cold working before isothermal annealing

Steels HS140-104, LS70-38 and LS2-65 whose chemical compositions are given in table 10.1, were hot rolled and coiled according to the hot rolling schedule given in table 11.1 and the heat treatment cycle given in figure 11.1 below. Both the hot rolling and the coiling were done in an argon atmosphere in order to avoid excessive oxidation.

As may be seen in table 11.1, the only variable was the coiling temperature. It was not possible to simulate the very high industrial strain rates on the Gleeble due to machine and friction limitations. The highest strain rate that could be achieved with

Chapter 11 Experimental procedures for the study of the recrystallisation after cold work

good repeatability was 2 s^{-1} which was significantly below the industrial strain rates in hot rolling that are as high as 150 s^{-1}.

Table 11.1: The hot rolling and coiling schedule simulating the industrial hot rolling and coiling processes on the Gleeble 1500™, the interpass time is before the rolling pass, RT = reheat temperature, FMH = finishing mill head and F = rolling pass.

Simulated CCR hot rolling on the Gleeble 1500™						
Sample size: length 15 mm; diameter 10 mm						
RT : 1150 ºC						
Parameter	**RT**	**F1**	**F2**	**F3**	**F4**	**FMH**
Initial height H in (mm)		15.00	11.11	7.83	5.80	4.75
Final height h out (mm)		11.11	7.83	5.80	4.75	4.75
Entry temperature (ºC)	1150	1100	1050	980	900	900
True strain per pass		-0.30	-0.35	-0.30	-0.20	
Cumulative true strain		-0.30	-0.65	-0.95	-1.15	
Cumulative Δh in (mm)		-3.89	-7.17	-9.20	-10.25	
Strain rate per pass (s^{-1})		-2.0	-2.0	-2.0	-2.0	
Interpass time (s)		30.00	2.00	2.00	2.00	
Coiling for 1hr (°C)						650
Coiling for 1hr (°C)						600

Chapter 11 Experimental procedures for the study of the recrystallisation after cold work

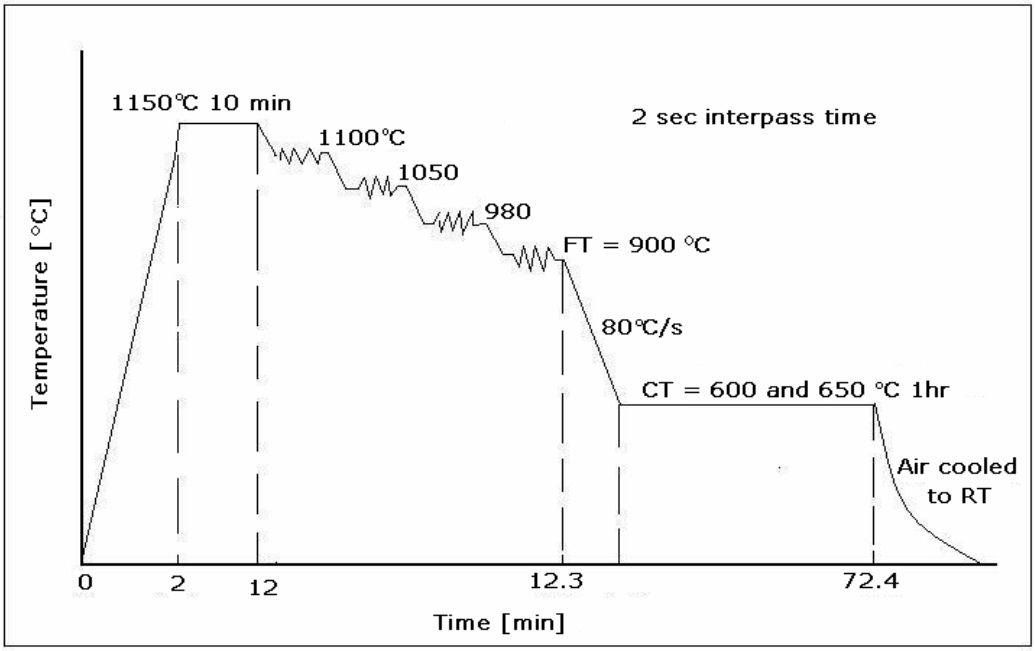

Figure 11.1: The schematic diagram for the simulated hot rolling and coiling processes on the Gleeble 1500™ hot rolling simulator.

After coiling, the specimens were cold worked using a laboratory cold rolling machine and the total reduction in thickness was 70 percent. The rolling was done in small reductions of less than 5 percent per pass in order to achieve a final uniformly deformed structure as large reductions had produced "cobbles" on the specimens, probably arising from the small diameter rolls on this machine.

Chapter 11 Experimental procedures for the study of the recrystallisation after cold work

11.3 Isothermal Annealing after cold work

The isothermal annealing was carried out in a lead bath that was pre-heated to the annealing temperature. The specimens were immersed for different times and temperatures depending on the experimental requirements. The arrangement for the lead bath is shown in figure 11.2.

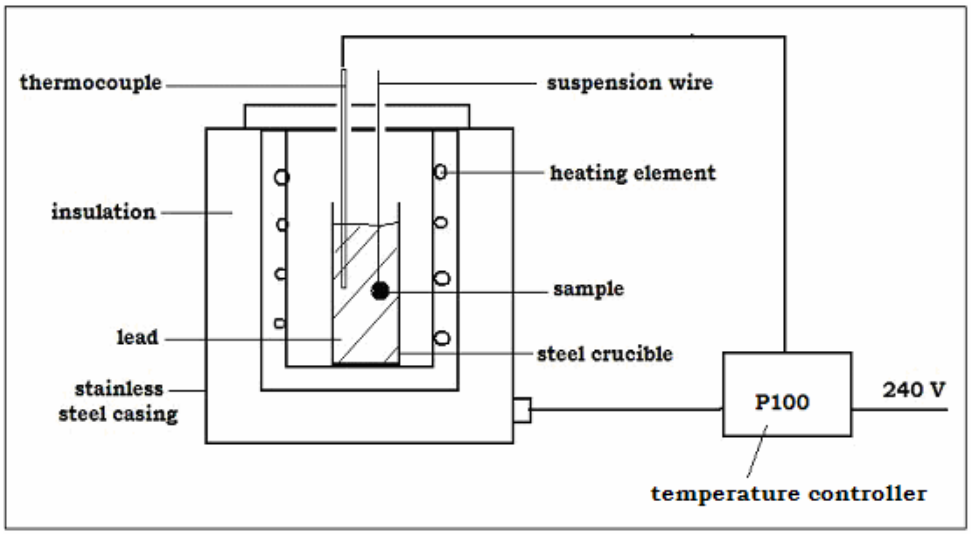

Figure 11.2: The experimental arrangement for isothermal annealing in the lead bath.

The specimen size was minimised to avoid undesirable temperature gradients with time between the surface and the interior of the sample, which was relevant at very short annealing times. The optimum specimen size was found to be 15 mm long, 4 mm wide and 1.5 mm thick. The steel crucible that contained the molten lead was 65 mm in diameter and 140 mm deep. The

Chapter 11 Experimental procedures for the study of the recrystallisation after cold work

volume of the molten lead was approximately 400 cm^{-3} and no temperature change was observed in the lead when immersing the 0.09 cm^{-3} specimen as the thermal mass of the specimen was negligible compared to that of the lead. In optimising the specimen size, it was observed that when larger specimens were immersed in the lead bath there was an immediate drop in temperature of up to 20 °C, depending on specimen size, and it took up to 200 seconds for the lead bath to be reheated to the programmed annealing temperature, in the process affecting the accuracy of the annealing temperature as well as the entire results. The experimental arrangement that was used to determine the heating rate of the 15 x 4 x 1.5 mm specimen in the lead bath is shown in figures 11.3 and 11.4.

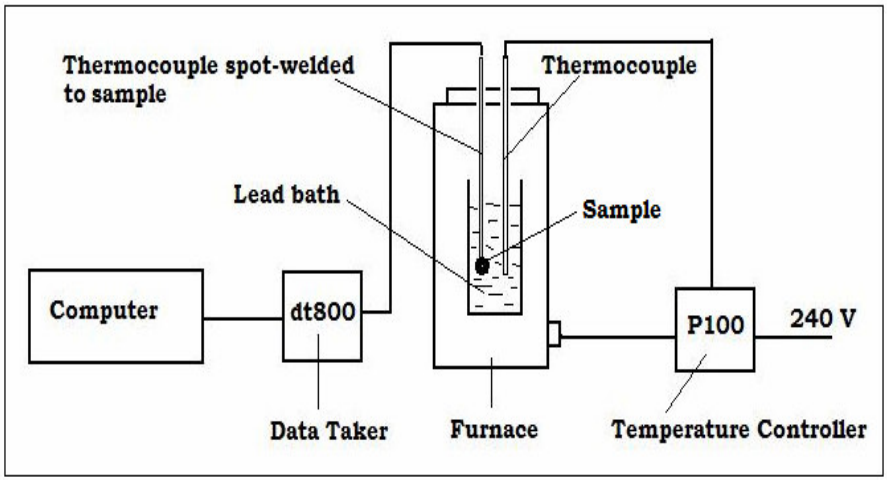

Figure 11.3: The schematic experimental arrangement for measuring the heating rate of the specimen at the start of isothermal annealing in a lead bath.

Chapter 11 Experimental procedures for the study of the recrystallisation after cold work

A 0.384 mm diameter R-Type (Pt/Pt-13%Rh) thermocouple was spot welded onto the sample to measure the heating rate upon immersion into the lead bath. The thermocouple was coated with a paste of alumina and insulated with a high temperature sheath. The data logger sampled the analogue voltage signal from the thermocouple at a frequency of 1 Hz. The data was downloaded and was analysed using Microsoft Excel, see figure 11.5.

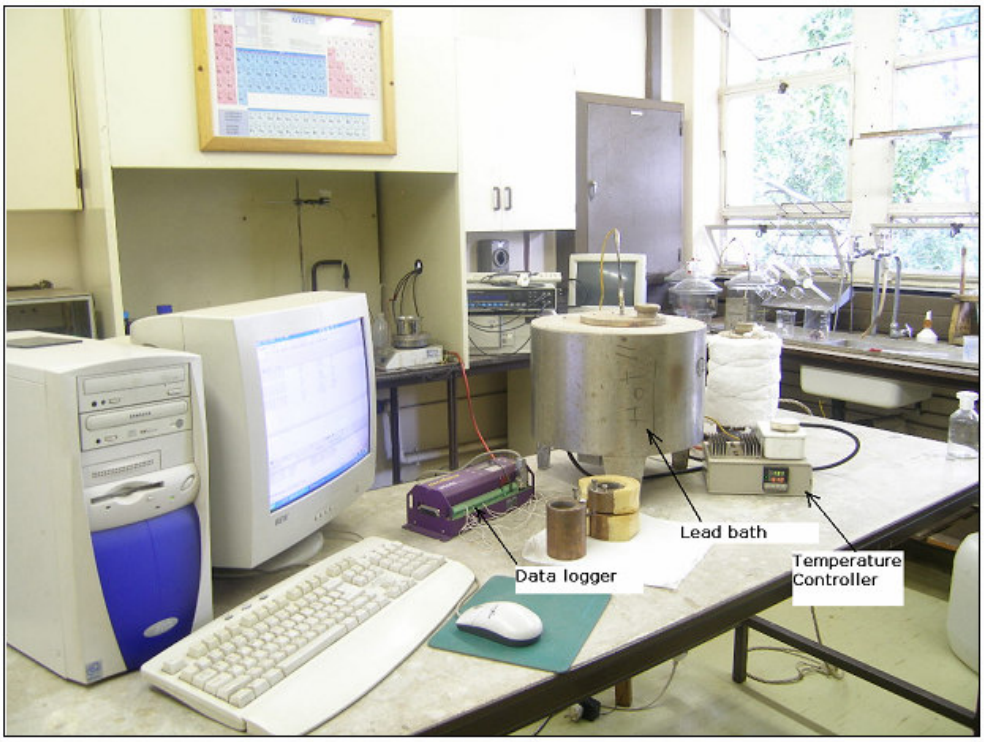

Figure 11.4: Photograph of the experimental arrangement for measuring the heating rate of the specimen at the start of isothermal annealing.

As may be seen from figure 11.5, both the heating to the annealing temperature and the quenching to room temperature

were almost instantaneous when compared to the longer isothermal annealing times of more than 15 seconds i.e. the respective heating and cooling time of the specimens was negligible compared to the isothermal annealing time.

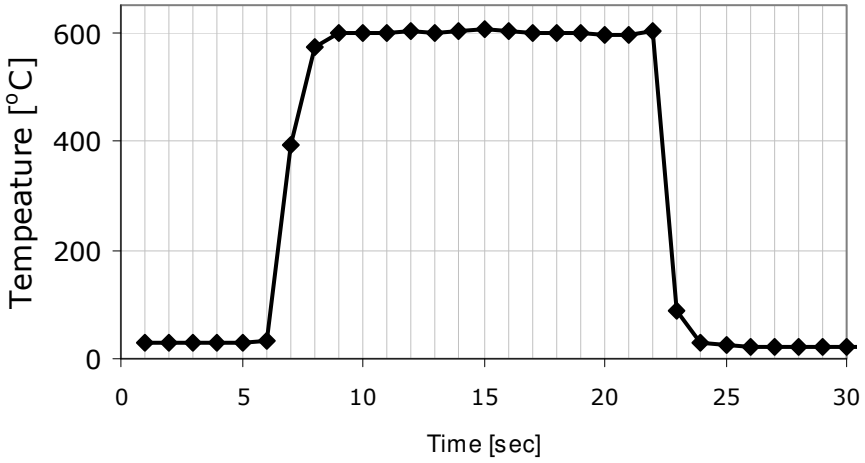

Figure 11.5: A typical heating rate curve for a 15 x 4 x 1.5 mm specimen at the start of isothermal annealing for steel HS140-104 in a lead bath followed by water quench.

11.4 Experimental procedures for the metallographic analysis

Metallographic analysis of the microstructures was done for three reasons; namely to confirm the AlN equilibrium solubility trend for the TEP results, to study the percentage recrystallisation after cold work and to study the precipitation of AlN and MnS in these steels. Both optical and electron microscopy methods were applied in this study.

Chapter 11 Experimental procedures for the study of the recrystallisation after cold work

11.4.1 Preparation of the carbon extraction replicas for the observation of MnS and AlN particles

The samples were mounted in epoxy, ground to 3 μm and etched in 4% Nital. The carbon was then deposited on these samples using a carbon coating unit (Speedivac Coating Unit 12E6/1419) under a vacuum pressure of 10^{-4} Torr. Squares of approximately 3 x 3 mm^2 were scribed on the carbon coated surface using a surgical knife and removed by electrolytic etching of the substrate using an electrolytic solution of 10 percent nitric acid and 90 percent ethanol at a potential of 10 volts and a current density of about 0.2 A cm^{-2}. Higher voltages were avoided because faster separation of the extraction replica from the substrate resulted in broken carbon replicas. The replicas generally floated off after about 4 to 10 minutes etching times.

Alternatively, the samples were floated off by chemical etching in the same 10 percent Nital. In these instances, the floating off took a bit longer, 10 to 60 minutes depending on the microstructure and depth of etching. After floating off, the replicas were stripped in distilled water and dried on filter paper.

The carbon extraction replicas were observed by transmission electron microscopy (TEM) on a Phillips CM200, which uses a tungsten filament and was operated at 160 kV. The particles were

identified by electron dispersive x-ray spectroscopy (EDS) and X-ray diffraction patterns.

All diffraction work was carried out at the same TEM settings which were as follows: the accelerating voltage was 160 kV, selected area diffraction (SAD) aperture number 1, the condenser lens current C2 (intensity) was set at 1600 mA, the camera length was 950 mm, the exposure time was 40 seconds and the diffraction lens current was 1.170 mA.

The TEM's camera constant was calibrated with a gold film that was sputtered onto a carbon film. Figure 11.6 shows the diffraction pattern for the gold layer that was used to determine the camera constant.

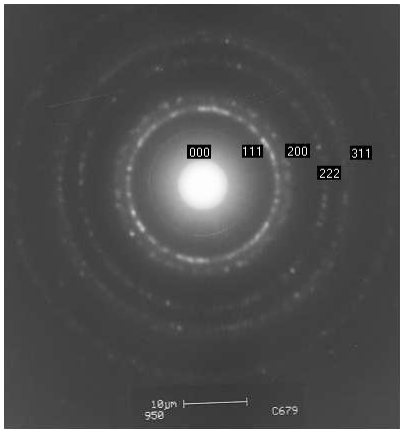

Figure 11.6: The diffraction pattern for the polycrystalline gold film that was used to calibrate the camera constant for the Phillips CM200 TEM.

Chapter 11 Experimental procedures for the study of the recrystallisation after cold work

Using the lattice parameter for gold of 0.40788 nm, the camera constant was determined from the following equation which is derived from the Bragg equation:

$$\lambda L = r_{(hkl)} d_{(hkl)} \qquad (11.1)$$

where λ is the wavelength of the incident beam, L [mm] is the camera length and the product λL is the camera constant, d [nm] is the lattice spacing of the reflecting plane and r is the measured spacing of the $d_{(hkl)}$ planes on the photographic plate.

From this calibration, the camera constant was found to be 2.776 (nm.mm). This value was compared to one determined from the calculated camera constant where:

$$\lambda = \frac{h}{\sqrt{2m_0 Ee\left(1+\frac{Ee}{2m_0 c^2}\right)}} \qquad (11.2)$$

where h is Planck's constant (6.626 x 10^{-34} J Hz^{-1}), m_0 is the rest mass of an electron (9.11 x 10^{-31} kg), e is the elementary charge (1.602 x 10^{-19} C), c is the speed of light in vacuum (2.998 x 10^8 m s^{-1}) and E is the accelerating voltage in volts (160 kV).

The camera length that was used to photograph diffraction patterns was 950 mm and the calculated camera constant was found to be 2.66 (nm.mm), giving an error of 4 percent from the

experimentally determined one. In the identification of the particles from the diffraction patterns the experimentally determined camera constant was used.

11.4.2 Optical metallography for the study of the recrystallised volume fraction

The samples were mounted in epoxy, ground and polished to 6 μm and chemically polished by immersing them in a 3 ml hydrofluoric acid (HF) and 97 ml hydrogen peroxide (H_20_2, 30 percent) solution for 5 seconds and rinsed in H_2O_2. Immersing the samples for longer times resulted in undesirable pitting. An alternative chemical polishing solution that was equally suitable was 14 ml HF, 100 ml H_2O_2, 100 ml H_2O solution.

Generally, grinding disturbs the structure of the surface metal and, therefore, the chemical polishing was intended to remove this disturbed metal in order to minimise any artefacts that would interfere with the quantification of the recrystallised volume fraction. After polishing, the samples were etched by swabbing up to 5 seconds in 4 percent Nital. Under the optical microscope, the recrystallised regions appeared lighter while the unrecrystallised ones darker, creating the needed phase contrast for the quantitative analysis of the recrystallisation process.

Two methods, both of them based on metallographic analysis were used, namely, the point count method and the image

analysis technique that employs a computer software package called anlySIS^{TM}. Each point that was plotted in the graphs of recrystallised volume fraction versus the isothermal annealing time was an average of the recrystallised volume fraction taken from twenty-five different areas of the specimen and the error bar was the standard deviation.

11.4.3 Preparation of thin foils for TEM observations

Specimens for thin foil TEM observations were electro-erosion cut into discs 3 mm in diameter and 0.6 mm thick. They were then mechanically ground to a thickness between 40 and 100 μm before thinning them in a twinjet thinning apparatus. The electrolyte that was used was 1.25 litres of acetic acid, 0.08 litres of perchloric acid and 0.7 g of chromium oxide (CrO_3) while the voltage was set at 50 V. Figure 11.7 shows the characteristic curve of current versus voltage that was obtained from the twinjet that was used in the thinning of the foils. The flat region was the applied voltage range where electrolytic polishing was achieved and below that, etching took place instead of polishing.

After thinning i.e. after a small hole appeared in the foil, the foil was rinsed thoroughly in ethanol to remove all the acids that could corrode and contaminate the specimen.

Chapter 11 Experimental procedures for the study of the recrystallisation after cold work

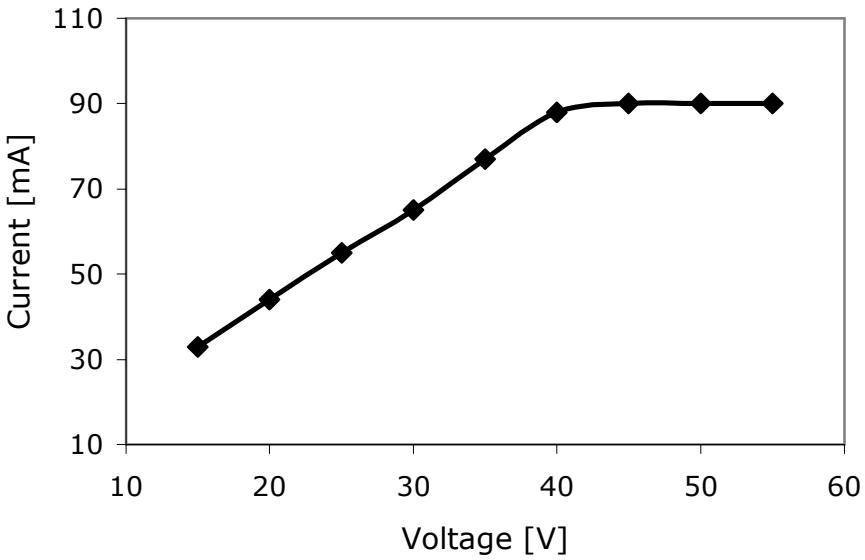

Figure 11.7: Voltage-current characteristic curve for electrolytic polishing in the twin jet apparatus that was used in this work.

Chapter 12 Results

12.1 Introduction

Results from this study are in four parts:

- the first part deals with the equilibrium solubility trends of AlN in low and high sulphur low carbon Al-killed hot rolled strip steels during reheating;
- the second part deals with the study of the static recrystallisation behaviour after cold work of these steels in the as-quenched form;
- the third part presents the recrystallisation behaviour in laboratory coiled steels; and
- the last part deals with the nucleation of AlN on MnS and its impact on static recrystallisation in these steels.

12.2 Equilibrium solubility trends of AlN in low and high sulphur Al-killed strip steels

The equilibrium solubility trends of AlN in low and high sulphur low carbon Al-killed strip steels were studied in five steels with sulphur content ranging from 2 ppm to 140 ppm using the TEP technique. The steels were LS2-65, LS10-83, LS70-38, HS130-50 and HS140-104 and their compositions are given in table 10.1. The first numeral figure represents the sulphur and the second the nitrogen content, both in ppm.

The aim of this study was to investigate if the sulphur content does have an effect on the equilibrium solubility of the AlN in these steels and to compare the results from the TEP technique with the results from other workers that used other methods, in particular the Beeghly method.

12.2.1 Effect of soaking time on the dissolution of the AlN

Figure 12.1 shows the evolution of the relative TEP values after isothermally soaking two steels with high and low sulphur content, steels HS140-104 and LS2-65 respectively, at 1150 °C for various times and then quenching them into water. The relative TEP values were taken with reference to the "no dissolution" TEP values at 800 °C as these specimens were given a prior isothermal annealing at 800 °C for 2 hours to precipitate the AlN.

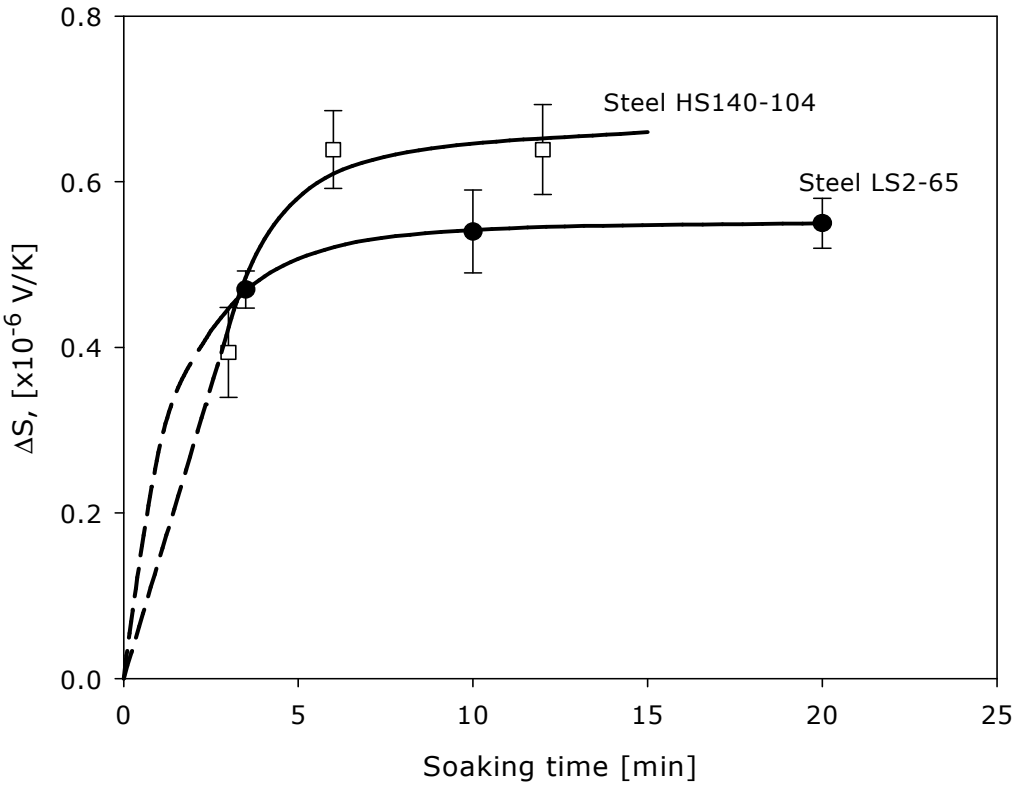

Figure 12.1: Relative TEP measurements ΔS for steels HS140-104 and LS2-65 after soaking for various times at 1150 °C and quenching into water.

The TEP values leveled off after soaking for more than 5 minutes and this was an indication of equilibrium condition in the solubility of the dissolving AlN. An important observation from this study was that equilibrium dissolution of AlN is not affected by the sulphur content in these steels.

12.2.2 Equilibrium solubility trends of AlN in low and high sulphur low carbon Al-killed hot strips during reheating

The TEP results for the equilibrium solubility trend of AlN in austenite are given in table 12.1 and the corresponding curves of relative TEP values versus the soaking temperature are given in figure 12.2 below. The leveling off of the TEP values at higher soaking temperature may indicate the solubility limit of the dissolving AlN and the final relative TEP values are, therefore, dependent on the nitrogen content.

Instead of plotting the relative TEP value ΔS versus the solution temperature as in figure 12.2, the logarithm of the solubility product log[%Al][%N] derived from ΔS through equation 8.7, is plotted against the inverse of the absolute solution temperature in figure 12.3. This data is for 5 to 95 percent AlN dissolution and this was approximated from the sigmoidal curves in figure 12.2. Despite some scatter in the results, an important observation was that the sulphur content did not have a significant effect on the equilibrium solubility trend of AlN as the data points for all the five steels were within the reasonable scatter. It is to be noted that it

was the solubility product of the stoichiometric composition of the AlN that was plotted against the inverse of the absolute temperature in figure 12.3.

The equation from the regression analysis of the plot of the logarithm of the solubility product of the AlN, i.e. Log[%Al][%N], versus the inverse of the absolute solution treatment temperature in figure 12.3, was found to be:

$$\mathrm{Log[\%Al][\%N]} = 2.6 - \frac{9710}{T} \qquad (12.1)$$

where the aluminium and the nitrogen contents are in weight percentage and T is the absolute solution temperature in Kelvin.

In addition, the equilibrium solubility of AlN in steel HS140-104 was modelled by Thermo-Calc and the results are shown in figure 12.4. Curve number 5 in figure 12.4 shows the modelled precipitation behaviour of AlN as the sulphur content is varied with no predicted effect of the sulphur content.

Chapter 12 Results

Table 12.1: TEP measurements for the various steels that were solution treated at different temperatures for 12 minutes and quenched into water. The TEP values were within an error of ± 0.033 μV K^{-1} while the ΔS values were taken relative to the "no dissolution" TEP values at 800°C.

Steel	Solution Temperature [°C] and TEP [μV/K]									
	800	**925**	**1000**	**1050**	**1100**	**1150**	**1200**	**1225**	**1250**	**1290**
HS130-50	9.01		8.734	8.741	8.668	8.61	8.5	8.511	8.68	
$\Delta S = S_{800} - S_i$	0		0.28	0.27	0.35	0.41	0.46	0.45	0.39	
LS10-83	9.15		9.00	8.96	8.80	8.55	8.52	8.50		
$\Delta S = S_{800} - S_i$			0.15	0.19	0.35	0.60	0.63	0.65		
HS140-104	8.63			8.48	8.25	8.28	7.91			7.84
$\Delta S = S_{800} - S_i$				0.15	0.38	0.35	0.72			0.79
LS2-65	8.12	8.10	7.86		7.74	7.65	7.82		7.89	
$\Delta S = S_{800} - S_i$	0.00	0.02	0.25		0.38	0.47	0.30		0.23	
HS90-34	8.99	8.93	8.76		8.78					
$\Delta S = S_{800} - S_i$	0.00	0.06	0.23		0.21					

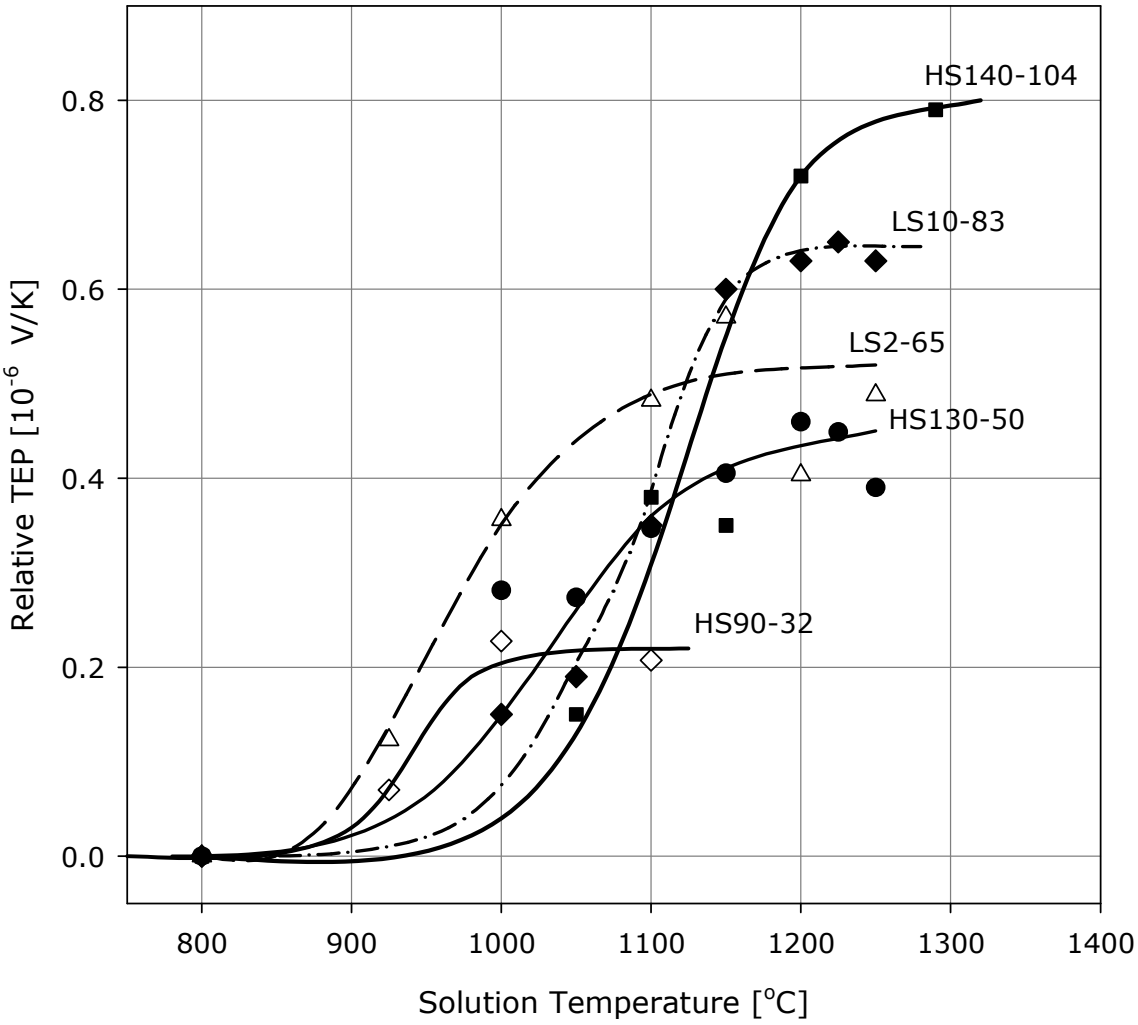

Figure 12.2: Equilibrium solubility trends for AlN in low carbon Al-killed hot rolled strip steels during reheating for the steels which are labeled on corresponding solubility curve.

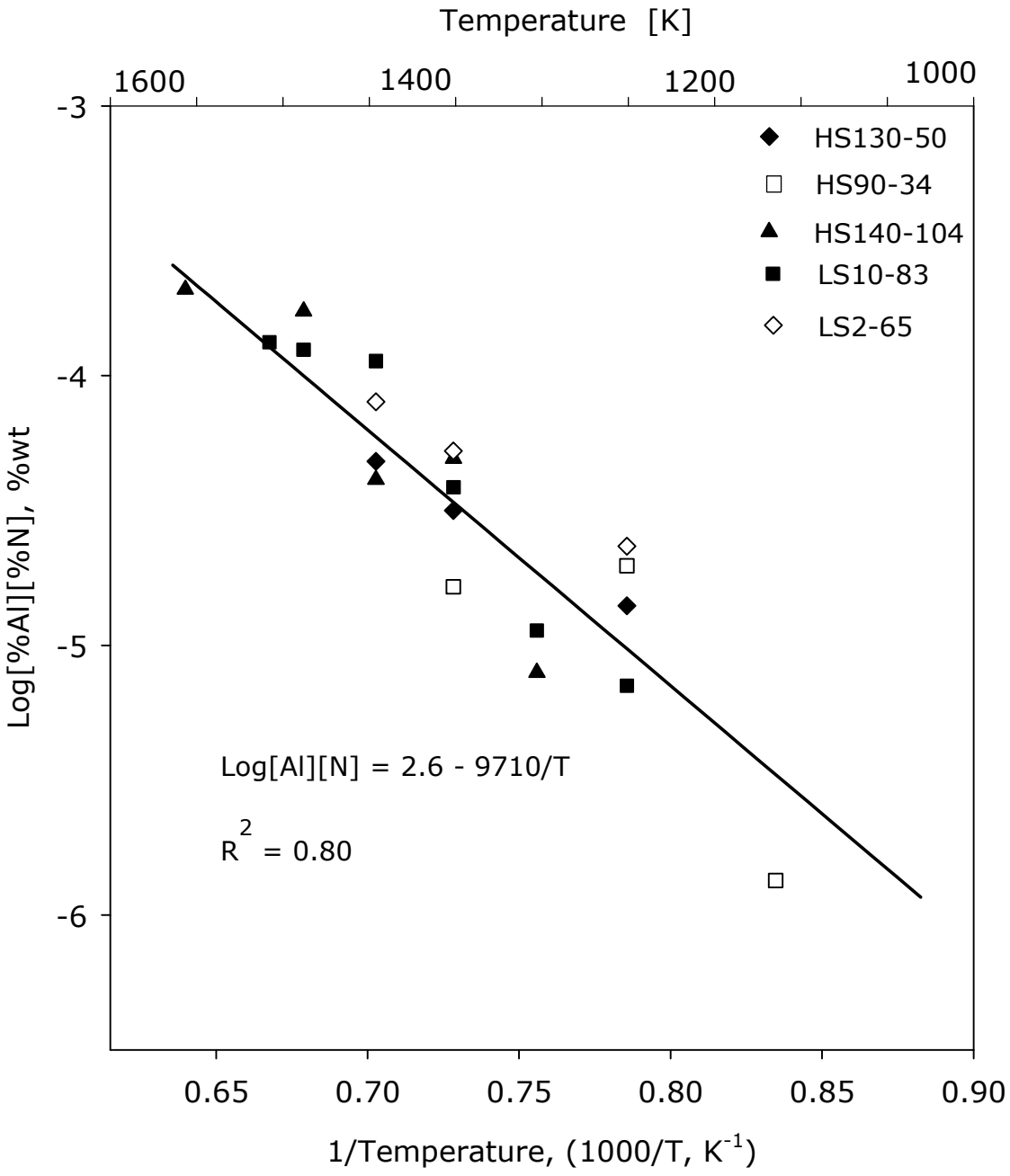

Figure 12.3: The logarithm of the AlN solubility product log[%Al][%N] as a function of the inverse of the absolute solution treatment temperature.

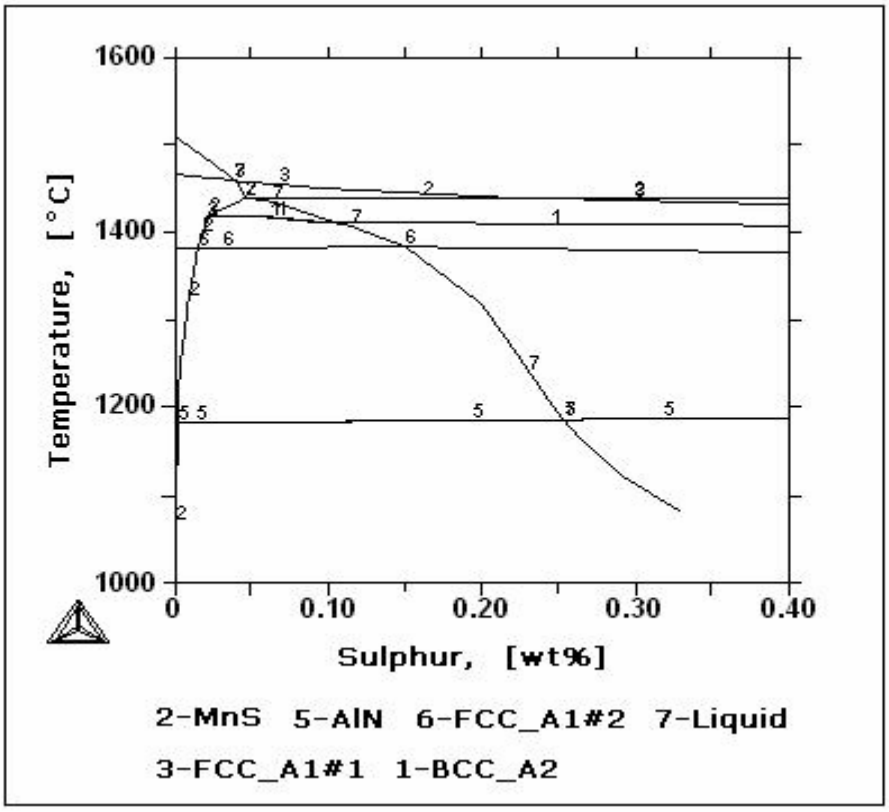

Figure 12.4: Thermo-Calc results for steel HS140-104: note curve number 5 that represents the precipitation of AlN.

12.2.3 Metallographic analysis

The results from the TEP measurements were checked metallographically in order to confirm that the AlN had been fully dissolved. Both extraction carbon replicas and thin foil techniques were used for this. Out of the five steels that were studied by TEP, two steels, one with the highest and the other with the lowest sulphur contents were chosen for metallographic analysis i.e. steels HS140-104 and LS2-65. Figure 12.5 shows micrographs and corresponding EDS spectra for the particles in steels HS140-104 and LS2-65 after solution treatment at 1150 °C, hot rolling

and annealing at 800 °C for 6 hours as shown in the schematic diagram in figure 10.1. After isothermal annealing at 800 °C for 6 hours, the AlN precipitated into coarse cuboids and fine round particles.

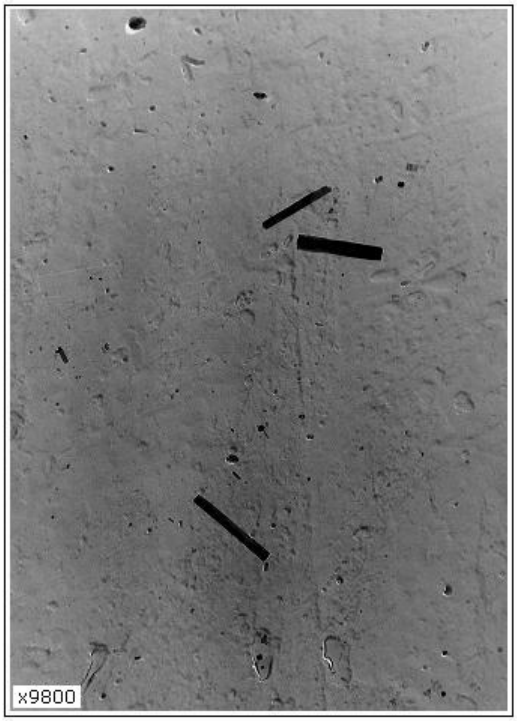

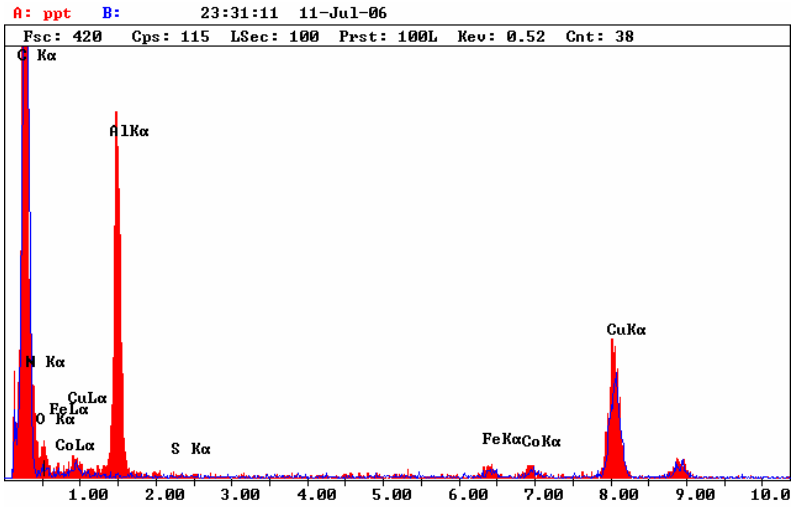

(a)

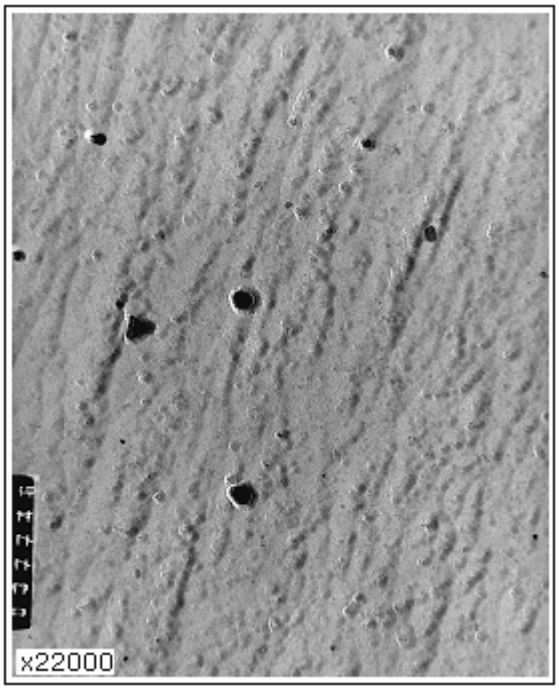

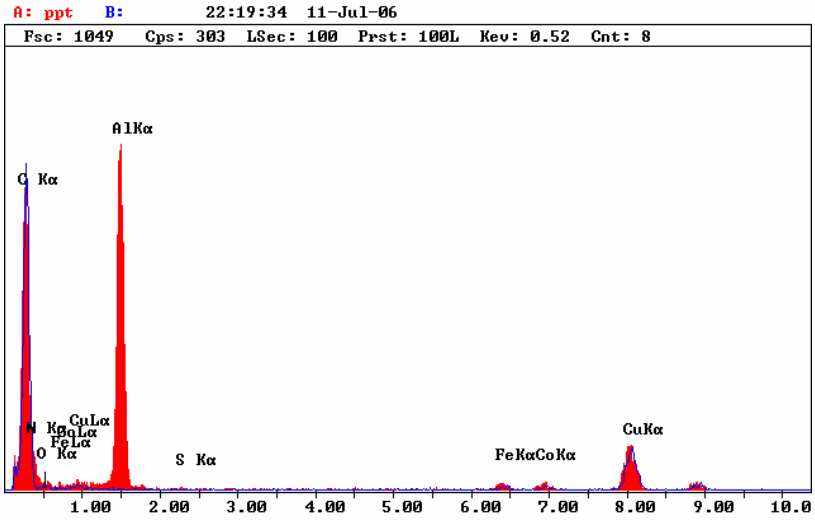

(b)

Figure 12.5: Micrographs and the corresponding EDS spectra for the steels (a) HS140-104 and (b) LS2-65 which were hot rolled, cooled to room temperature and then isothermally annealed at 800 °C for 6 hours and then quenched into water.

Extraction carbon replicas were also prepared for specimens that were only solution treated at 1150 °C for 12 minutes and water

quenched and their micrographs are shown in figure 12.6. As may be seen in the carbon extraction replicas below, there was partial dissolution of AlN in the higher nitrogen steel HS140-104 (micrograph (a)) while almost complete dissolution in the medium nitrogen steel LS2-65 (micrograph (b)). The particles in micrograph 12.6 (a) were also analysed by the x-ray EDS and were found to be AlN as in figure 12.5 above.

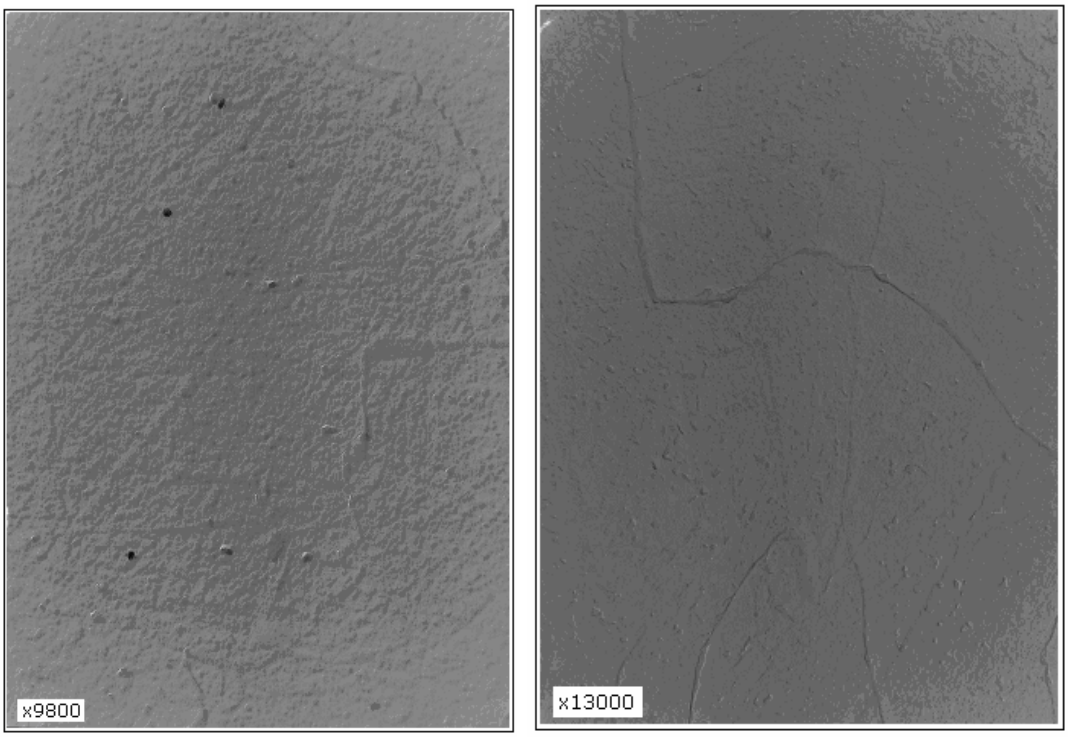

(a) (b)

Figure 12.6: Micrographs for the two steels (a) HS140-104 and (b) LS2-65 after solution treatment at 1150 °C for 12 minutes and quenched into water.

The fact that AlN particles could not be seen in steel LS2-65 did not necessarily mean that there were not any as the extraction carbon replica technique is known to be insensitive to very small

particles and, therefore, TEM thin foils were prepared. Figure 12.7 shows the TEM thin foil results for steel LS2-65 after solution treatment at 1150 °C for 12 minutes and then quenched into water. Some AlN particles (< 30 nm) were observed but they were sporadic. No AlN particles could be observed when the solution treatment temperature was raised to 1200 °C. This meant that the dissolution of AlN in this steel was some where between 1150° and 1200 °C, which was about 50 °C above the temperature determined by the TEP technique.

Similarly, steel HS140-104 was solution treated further at 1250 °C for 12 minutes to dissolve the still remaining AlN at 1150 °C and the results are shown in figure 12.8 i.e. no more AlN was observed after quenching from 1250 °C, instead only Al_2O_3 particles were observed. This observation agreed with the TEP equilibrium solubility results.

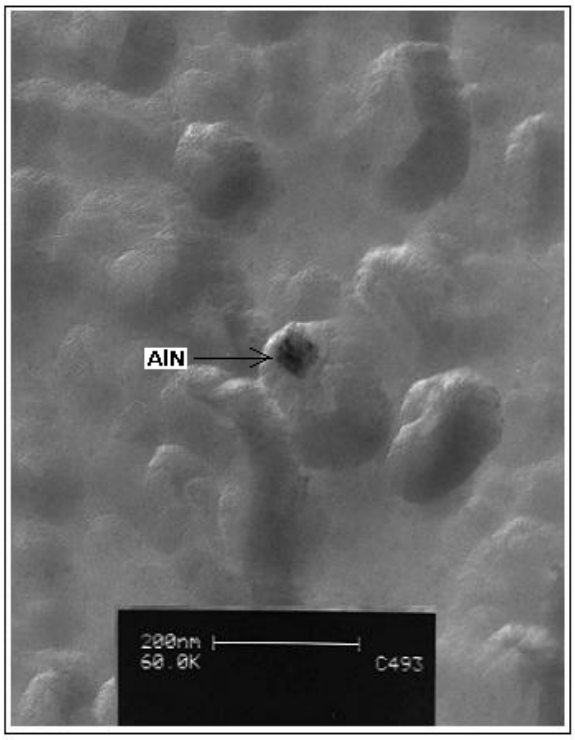

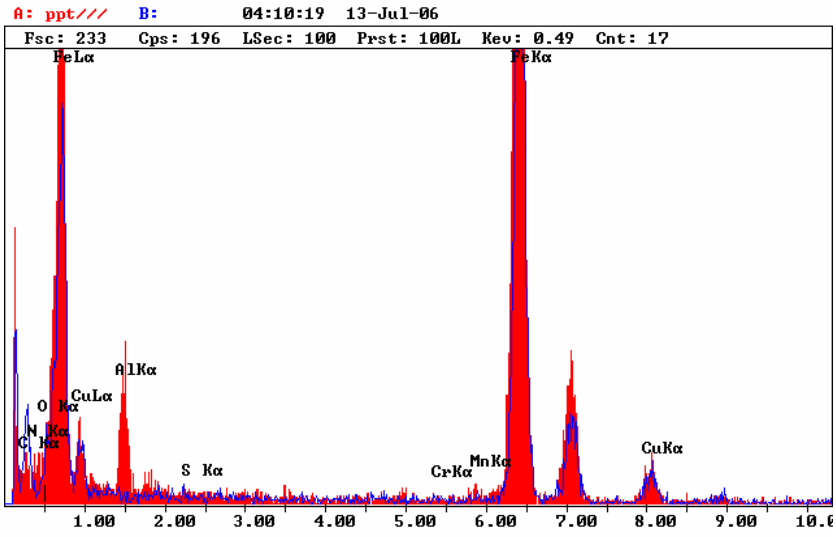

(b)

Figure 12.7: (a) Thin foil micrograph for steel LS2-65 after solution treatment at 1150 °C for 12 minutes and quenching into water and (b) the corresponding EDS spectrum of the single particle in the micrograph.

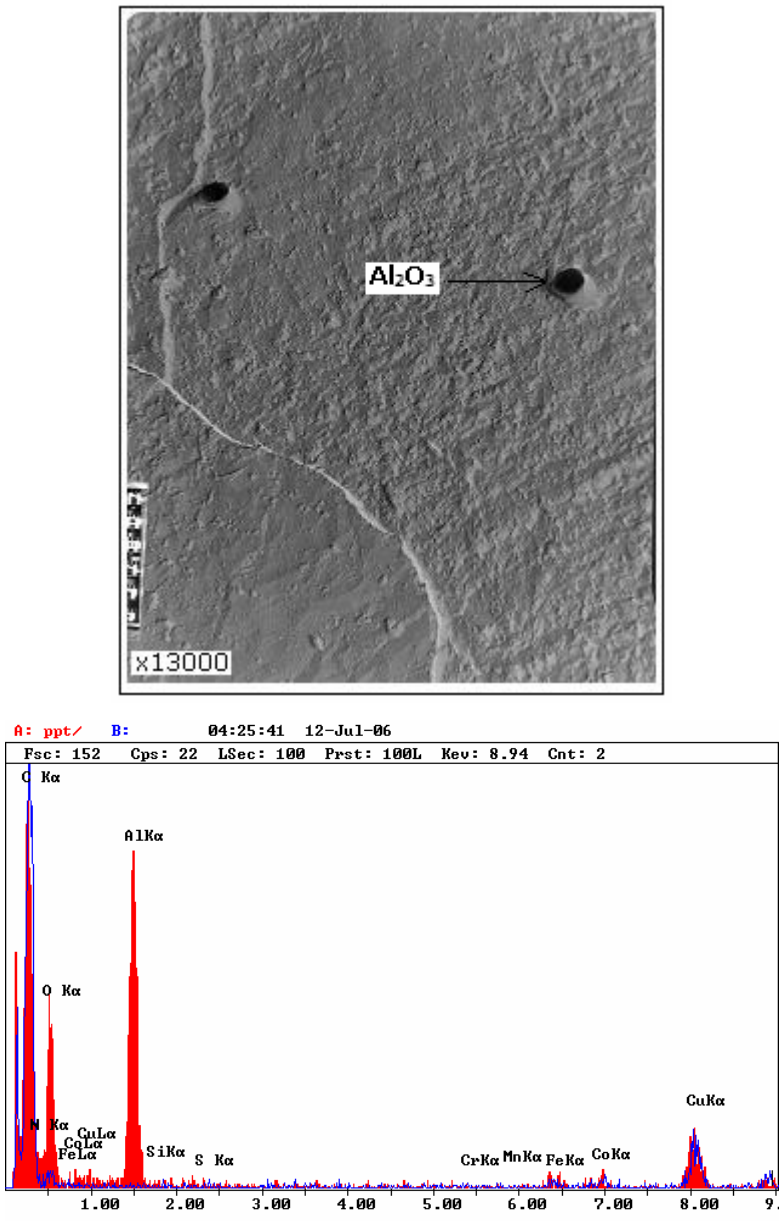

Figure 12.8: Micrograph and corresponding EDS spectrum for the particles which were observed in steel HS140-104 after solution treatment at 1250 °C for 12 minutes and quenching into water.

12.3 Recrystallisation behaviour in the as-quenched condition

The recrystallisation behaviour of low and high sulphur low carbon Al-killed strip steels was studied in steels HS140-104, HS90-12, LS70-38 and LS2-65 with the first digit representing the sulphur content and the second digit the nitrogen content respectively, both in ppm. As mentioned earlier in the experimental procedures, the study was done in two stages. Firstly, the recrystallisation behaviour was investigated in the as-quenched condition in order to observe the effects of both sulphur and nitrogen when they are in solid solution at the start of recrystallisation. Secondly, the study was extended to as-hot rolled and coiled specimens in order to investigate the effect of coiling and the interaction of AlN with the sulphides vis-à-vis the recrystallisation process in the two groups of steels; one with low sulphur content and the other with medium to high sulphur content. The latter set of results will be presented in section 12.4 below.

12.3.1 Progression of the recrystallisation as investigated by metallography

Steels HS140-104, HS90-12, LS70-38 and LS2-65 were solution treated at 1300 °C for 10 minutes and quenched into water and the resulting microstructure was massive ferrite. The as-quenched steels were immediately given a 70 percent cold deformation and, thereafter, isothermally annealed at different temperatures for various times to induce the static recrystallisation.

Chapter 12 Results

The micrographs in figure 12.9 show the progression of the recrystallisation process during isothermal annealing at 610 °C in steel HS140-104 with the light coloured areas the recrystallised regions and the dark ones the non-recrystallised ones. The micrographs in figure 12.9 show that there was no significant change in the recrystallised volume fraction as the isothermal annealing time was extended from 5 to 18 minutes i.e. there was a recrystallisation arrest. The recrystallisation process resumed again after 18 minutes.

Figure 12.10 shows the progression of the recrystallisation process in the same steel HS140-104 but now annealed at 550 °C. No recrystallisation arrest was observed at this annealing temperature.

Figure 12.11 shows the micrographs of the progression of the recrystallisation process in steel HS90-12 with the lowest nitrogen content of 12 ppm. This steel was also solution treated at 1300 °C for 10 minutes, quenched into water, given a 70 percent cold deformation and isothermally annealed at 610 °C for various times. No recrystallisation arrest was observed in this steel.

Chapter 12 Results

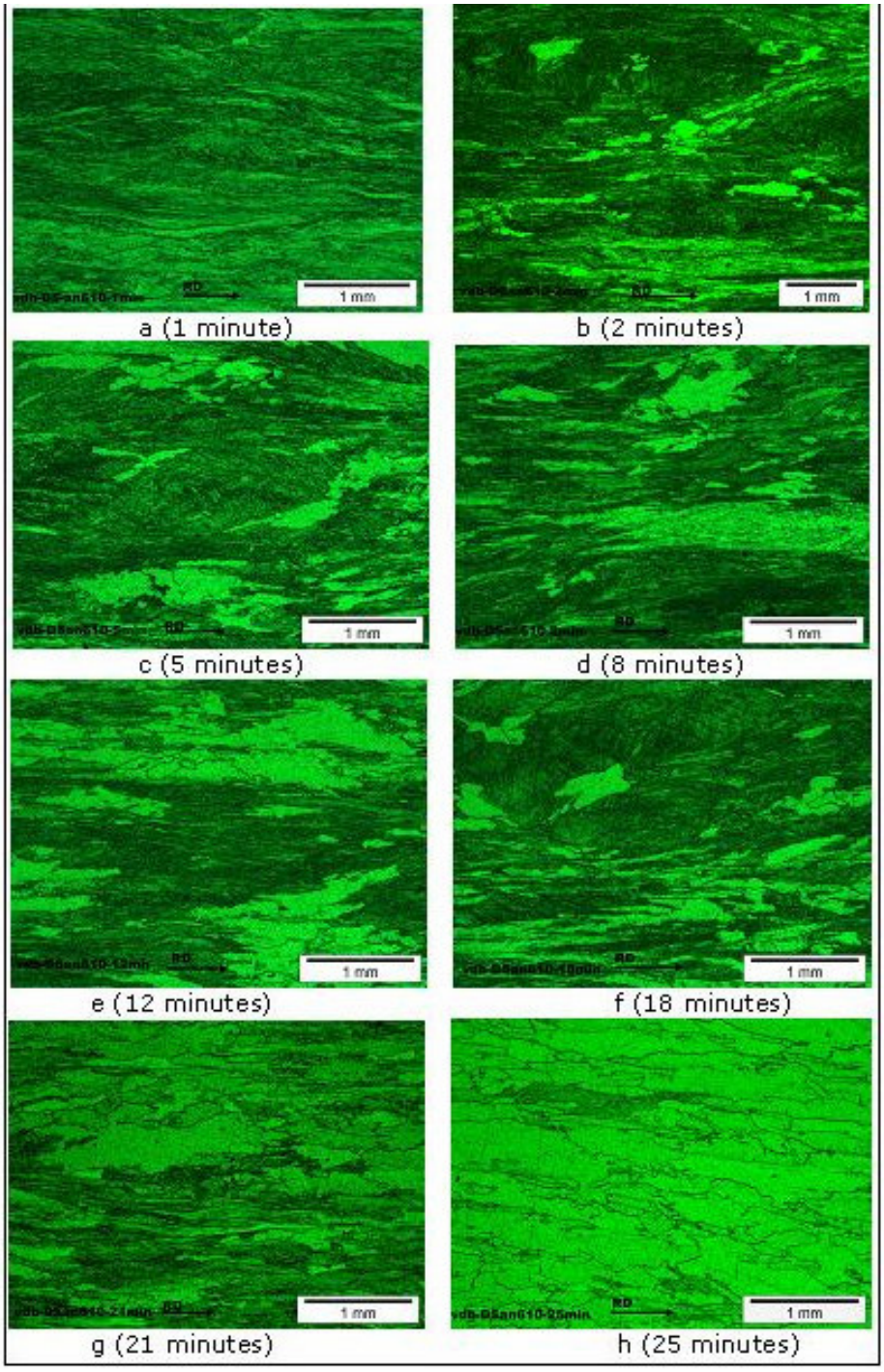

Figure 12.9: Progression of the static recrystallisation in steel HS140-104 after solution treatment at 1300 °C, quenching into water, cold working 70 percent and annealing at 610 °C for various times.

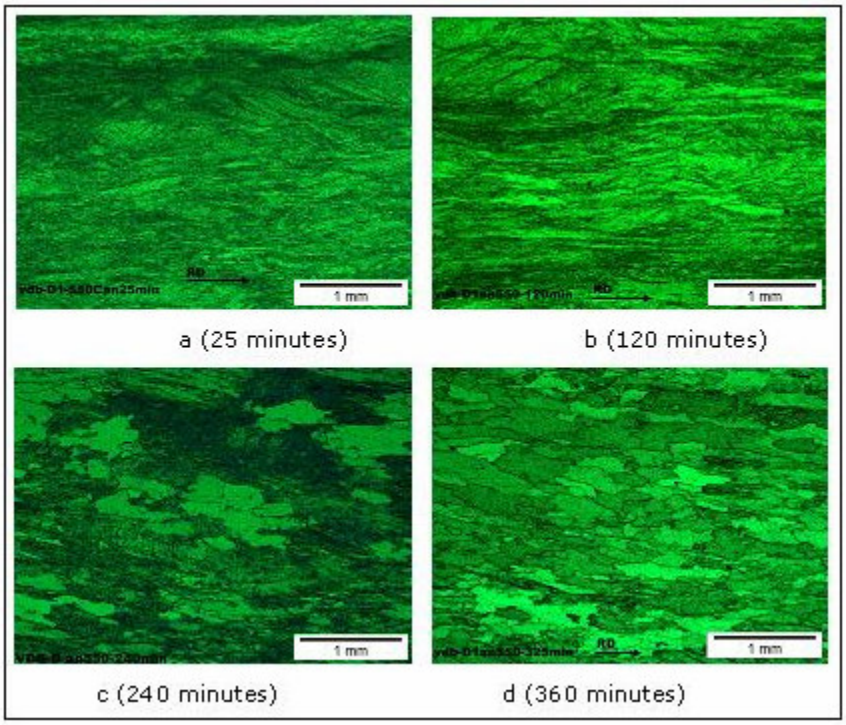

Figure 12.10: Progression of the static recrystallisation in steel HS140-104 after solution treatment at 1300 °C, quenching into water, cold working 70 percent and annealing at 550 °C for various times

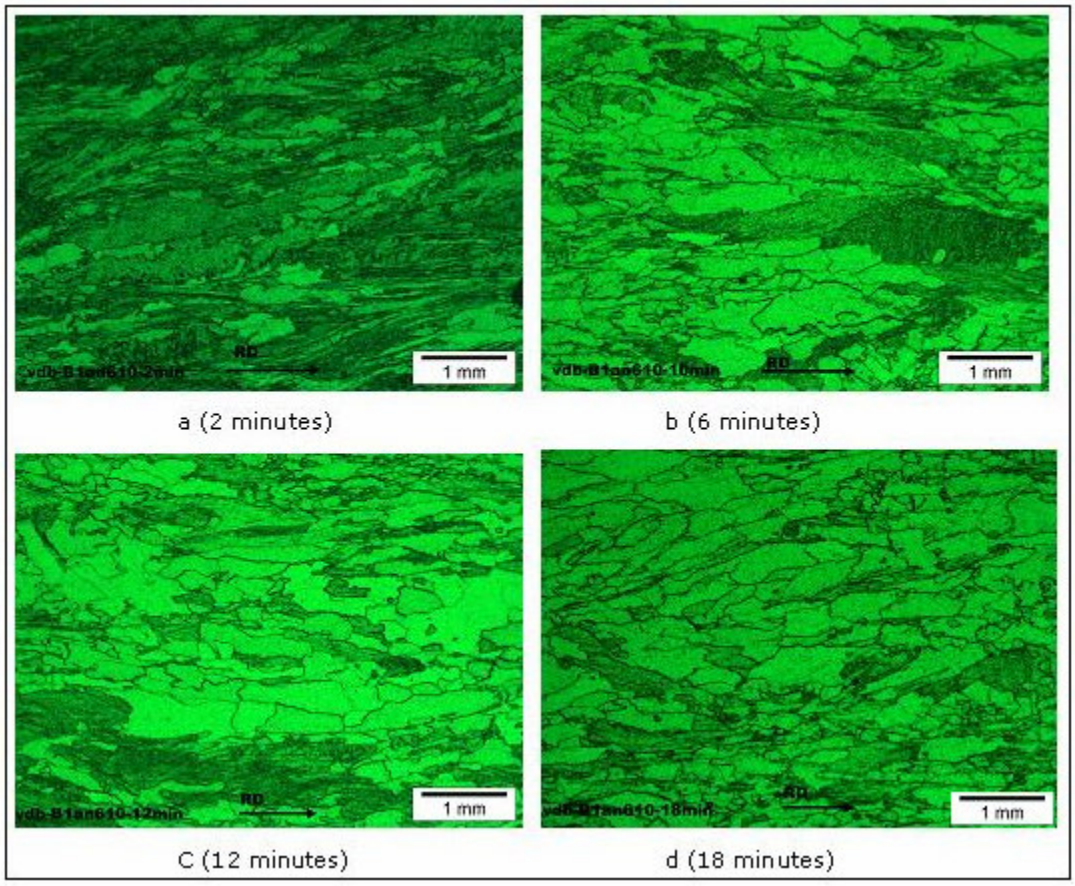

Figure 12.11: Progression of static recrystallisation in steel HS90-12 after solution treatment at 1300 °C, quenching into water, cold working 70 percent and annealing at 610 °C for various times

12.3.2 Quantitative results of the static recrystallisation kinetics in steel HS140-104 in as-quenched condition

In figure 12.12, the recrystallised volume fraction as determined through area analysis micrographic software, is plotted against the isothermal annealing time for various recrystallisation temperatures for steel HS140-104 that was given the treatment as mentioned in section 12.3.1 above. In some cases a clear

region of "recrystallisation arrest" was found as shown collectively by the cross hatched area in figure 12.12.

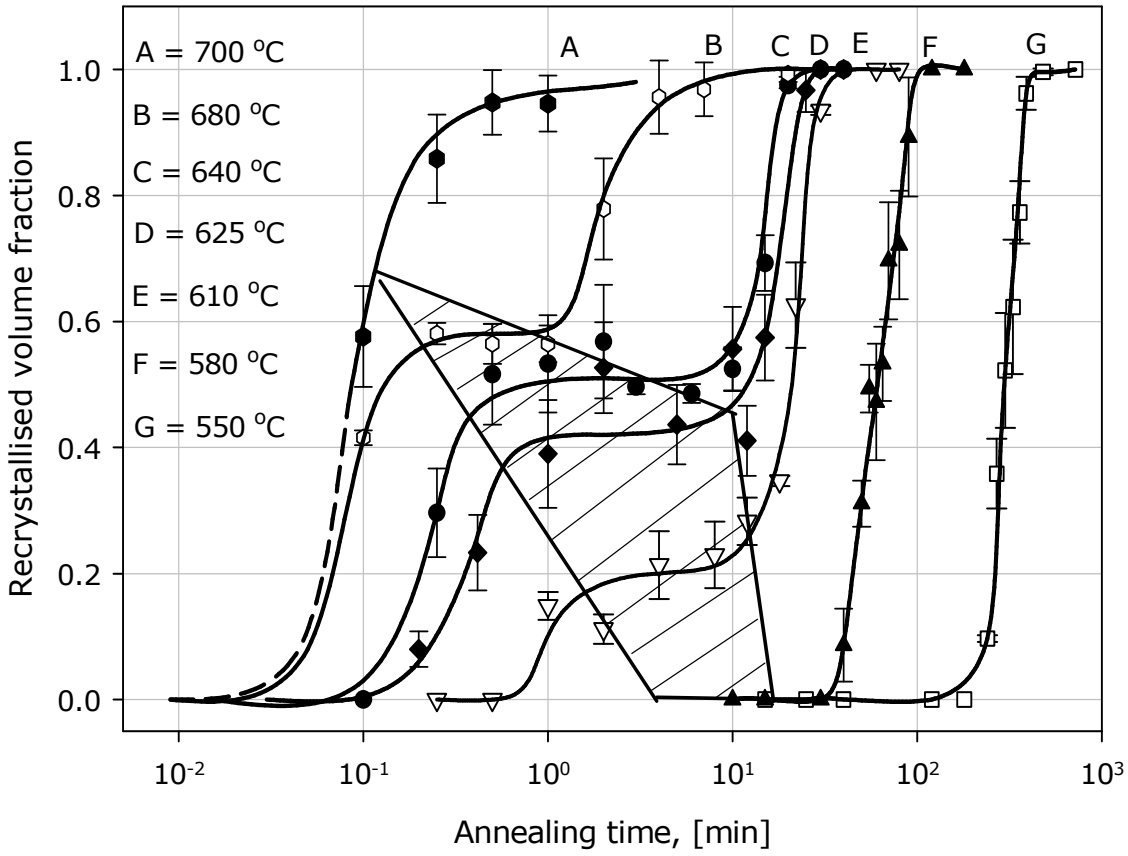

Figure 12.12: Recrystallised volume fraction versus isothermal annealing time for steel HS140-104 after solution treatment at 1300 °C, quenching into water, cold working 70 percent and annealing at various temperatures for various times. The cross hatched area is the recrystallisation arrest region.

Some specimens of steel HS140-104 were also annealed at 450 °C for 30 minutes in order to precipitate the Fe_3C prior to the 70 percent deformation and the recrystallisation annealing. According to Konig et al[44] and Leslie et al[66], see figure 4.2, no AlN is

expected to precipitate at this temperature at shorter annealing times and, therefore, only the cementite would be precipitated. This was done to investigate the possible effects of the carbon (in or out of solid solution) in the as-quenched specimens on the recrystallisation process after cold work. The results are given in figure 12.13 which confirmed that the movement of carbon does not appear to play any role in the kinetics of the recrystallisation process in these steels.

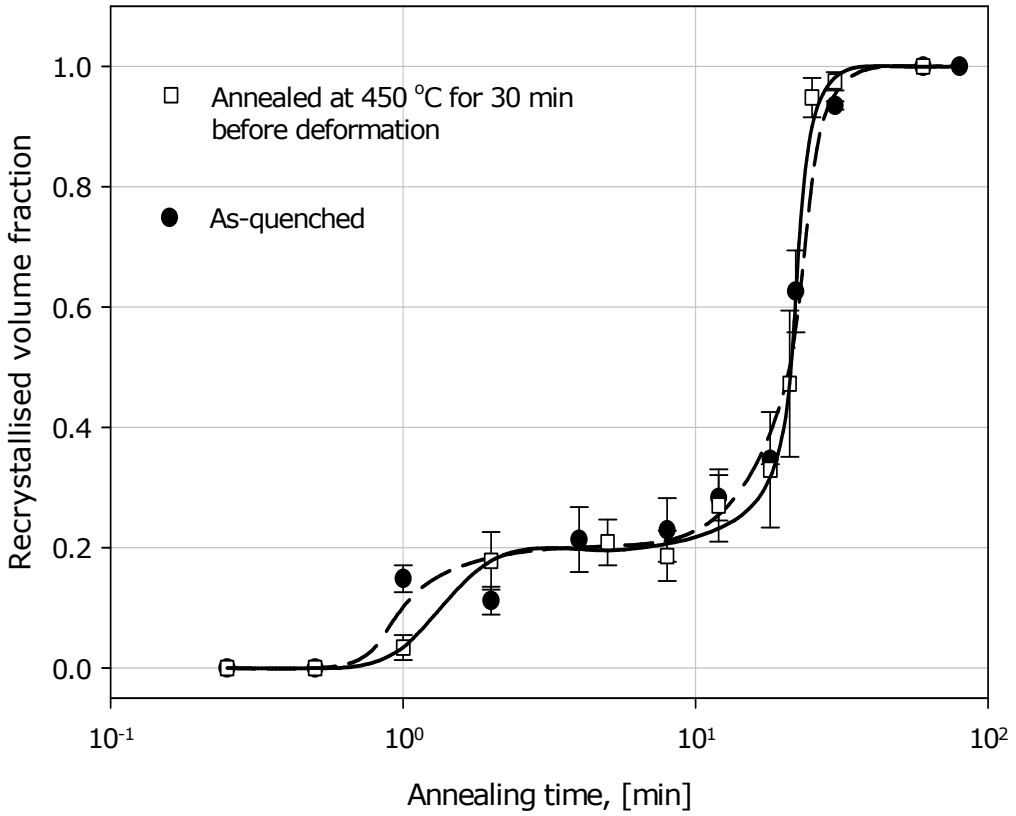

Figure 12.13: Recrystallised volume fraction versus isothermal annealing time for steel HS140-104 that was solution treated at 1300 °C, quenched in water; one annealed at 450 °C for 30 minutes and the other as-quenched, then both cold worked 70 percent and isothermally annealed at 610 °C for various times.

Chapter 12 Results

The log of the inverse of the recrystallisation arrest start time t_{RA} is, therefore, plotted against the inverse of the absolute isothermal annealing temperature in figure 12.14. The apparent activation energy of the process that led to the recrystallisation arrest was derived from the slope of this graph and its value was 230 kJ mol^{-1}. This activation energy is reasonably close to that for the diffusion of aluminium in ferrite which Germaz et al[149] found to be 196.5 kJ mol^{-1}.

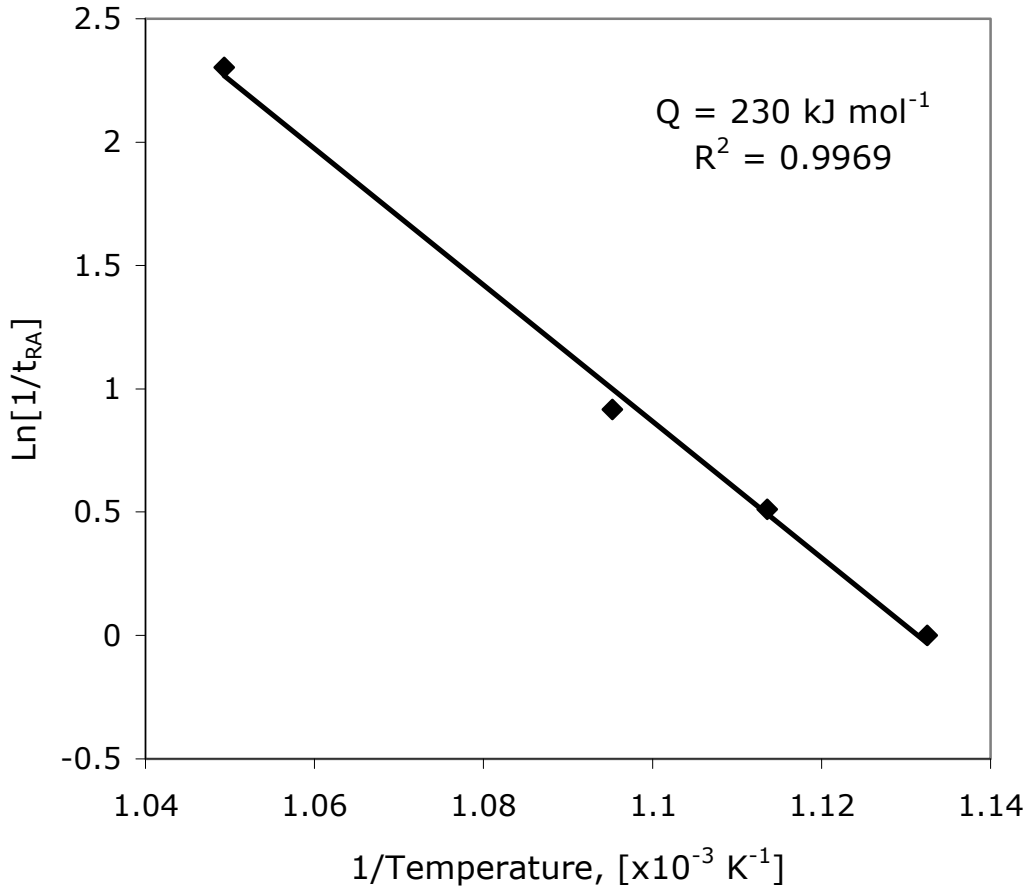

Figure 12.14: The inverse of the recrystallisation arrest start time t_{RA} versus the inverse of the isothermal annealing temperature.

Chapter 12 Results

The Zener-pinning effect start Z_{start} and finish Z_{finish} times observed in figure 12.12 above and plotted separately in figure 12.15 can indirectly be used to measure an estimated AlN precipitation start P_{start} and finish P_{finish} times in these steels. This is, of course, only an approximation measured indirectly by a Zener-like recrystallisation pinning effect which is dictated by the ratio (V_v/r) of AlN particles. For instance, some AlN precipitation may, therefore, already be present before the estimated P_{start} but is merely ineffective due to a very low volume fraction.

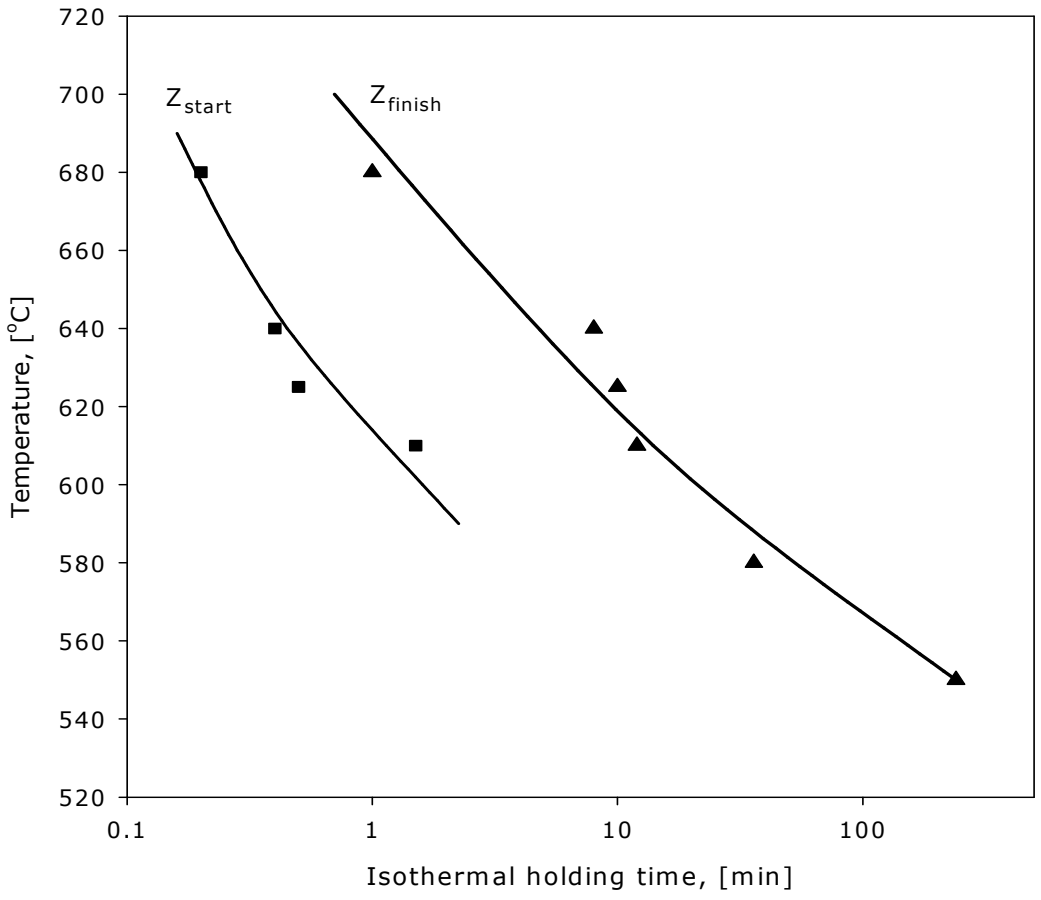

Figure 12.15: The Zener-pinning effect start Z_{start} and finish Z_{finish} times in minutes which were derived from the recrystallisation arrest times in figure 12.12.

12.3.3 Comparison of the recrystallisation kinetics in low and high sulphur content steels in as-quenched condition

The recrystallisation behaviour of four steels, two with low to medium sulphur content (LS2-65 and LS70-38) and the other with medium to high sulphur content (HS90-12 and HS140-104) is compared in figure 12.16. All four steels were solution treated at 1300 °C, quenched into water, cold worked 70 percent and annealed at 610 °C for various times. It is worthwhile observing that, regardless of the nitrogen content, the steels with lower sulphur content in solid solution recrystallised at earlier times compared with the ones with the higher sulphur content.

The Avrami plots for steels LS70-38 and HS90-12 are given in figure 12.17 and it is evident that the sulphur content does not affect the recrystallisation kinetics but rather the incubation period as there was significant no difference in the values of the MAJK exponent n.

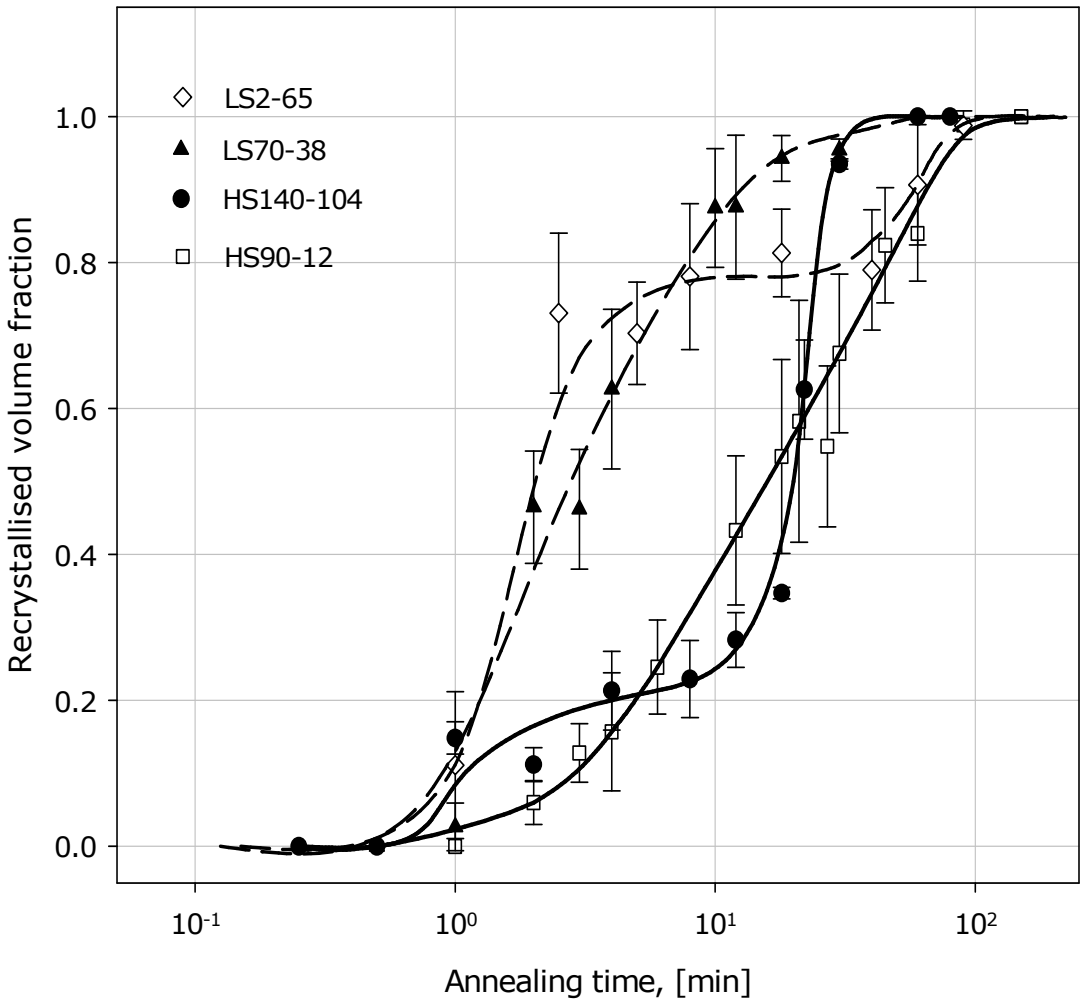

Figure 12.16: The recrystallised volume fraction versus isothermal annealing time for steels LS2-65, LS70-38, HS140-104 and HS90-12 after solution treatment at 1300 °C, water quenching, cold working 70 percent and isothermally annealing at 610 °C for various times.

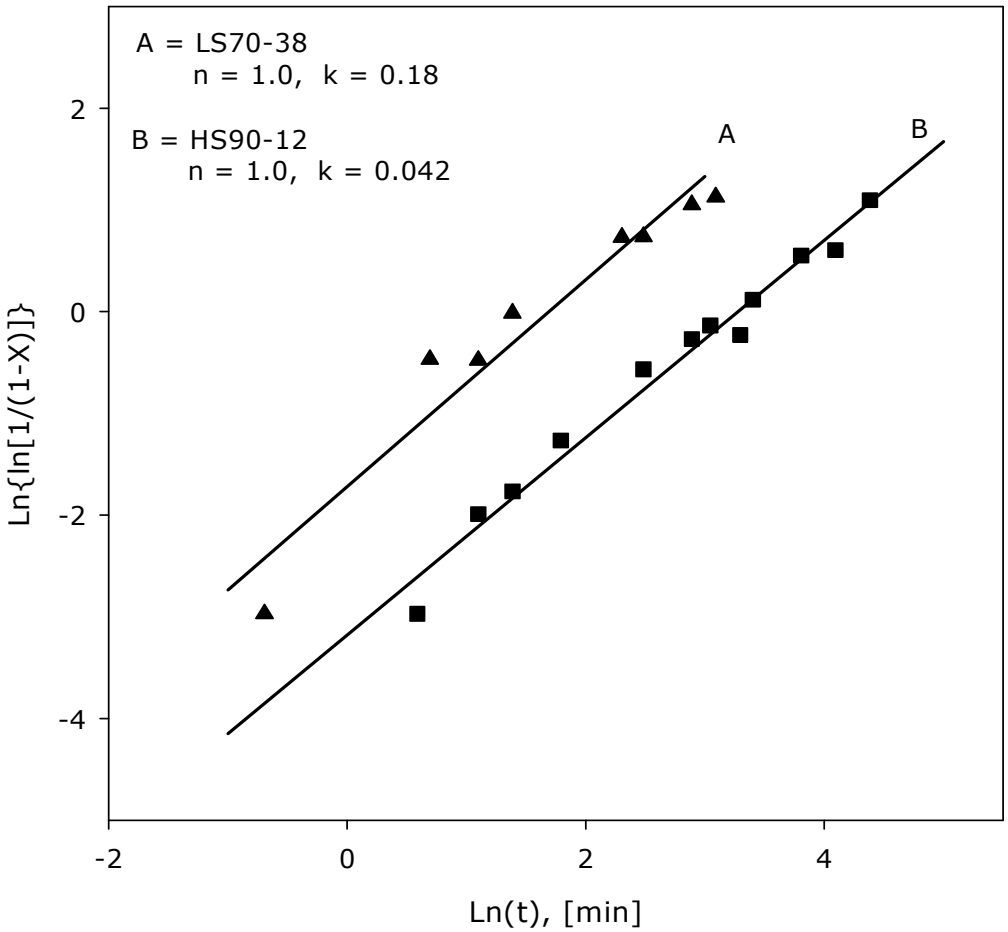

Figure 12.17: Avrami plots for steels LS70-38 and HS90-12 from the data in figure 11.16.

12.4 Recrystallisation behaviour in as-coiled condition

The recrystallisation behaviour of steels HS140-104, LS70-38 and LS2-65 with sulphur contents of 140, 70 and 2 ppm respectively was studied in this series. These three steels were hot rolled and coiled through simulation on the Gleeble 1500^{TM} and details of the process were given in table 11.1 and figure 11.1. The main

variables in these experiments were the coiling temperature (600° and 650 °C) and the sulphur content of the steel.

12.4.1 Quantitative results of the recrystallisation behaviour of the as-coiled hot strips

Figure 12.18 shows the plots of the recrystallised volume fraction versus isothermal annealing time for steels HS140-104, LS70-38 and LS2-65. These steels were coiled in the Gleeble 1500^{TM} at 600 °C and 650 °C, given a cold deformation of 70 percent and isothermally annealed respectively at 600 °C and 650 °C in the lead bath for various times.

The Avrami plots derived from the sigmoidal curves in figure 12.18 are given in figure 12.19. The main observation from these two figures was that, unlike in the as-quenched condition with all the sulphur in solid solution, steels with lower sulphur content recrystallised at later times and this effect was more prominent at the lower coiling temperature of 600 °C.

In figure 12.20, the static recrystallisation time i.e., 5 percent recrystallisation $t_{5\%}$, has been plotted against the corresponding sulphur content of the three steels that were studied in this series. A very pronounced effect of "sluggish" recrystallisation at low sulphur contents and low coiling temperature is apparent, which confirms the differences in recrystallisation behaviour reported within industry from nominally the same product but from different process plants that originally led to this study.

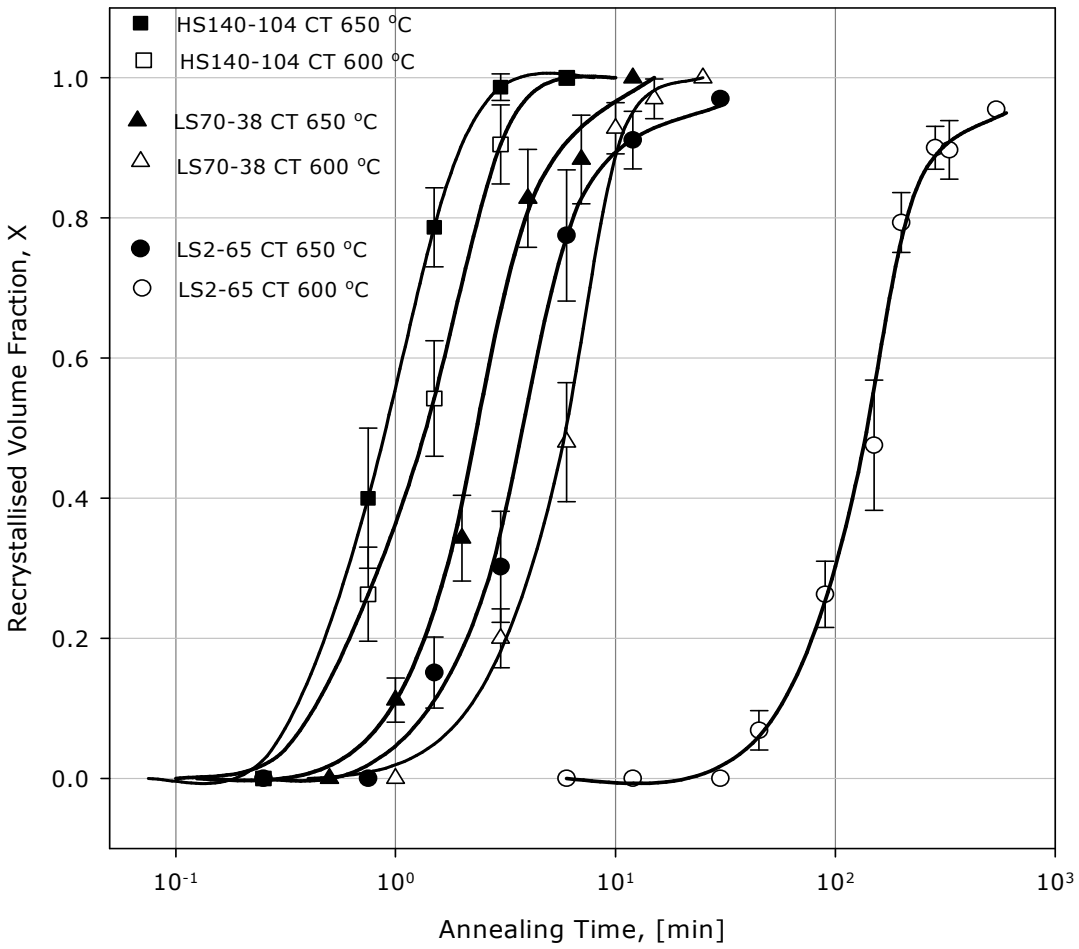

Figure 12.18: Recrystallised volume fraction for steels HS140-104, LS70-38 and LS2-65 which were coiled at 600 °C and 650 °C, cold worked 70 percent and isothermally annealed at 600 °C and 650 °C in a lead bath for various times. CT stands for coiling temperature.

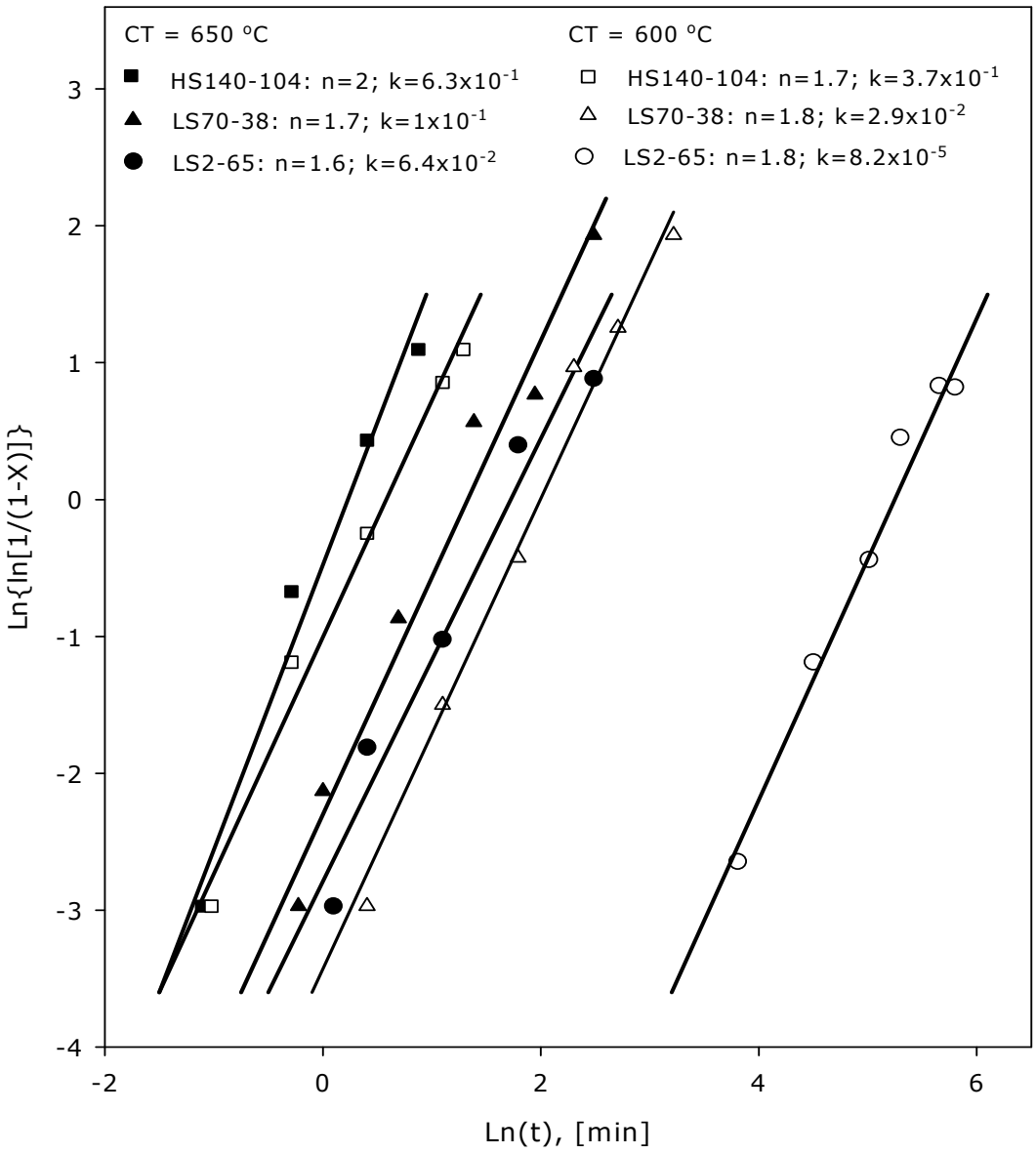

Figure 12.19: Avrami plots from the sigmoidal curves of recrystallised volume fraction versus isothermal annealing time for the steels and treatment given in figure 12.18.

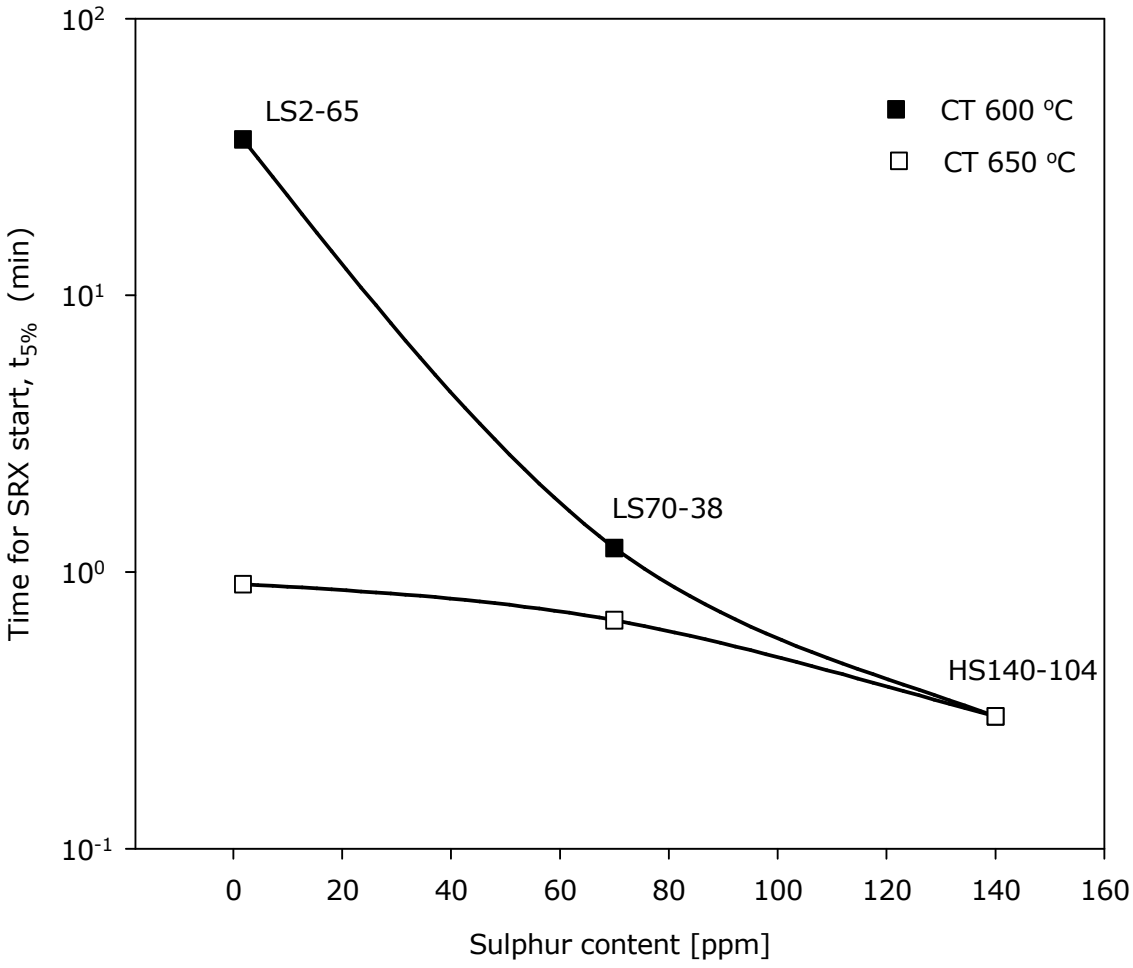

Figure 12.20: The 5 percent recrystallisation time $t_{5\%}$ in minutes, plotted as a function of the sulphur content (ppm) of the corresponding steel as labeled in the figure.

The logarithm of the recrystallisation start time $t_{5\%}$ is plotted against the sulphur content in ppm in figure 12.21. The empirical expressions for predicting the recrystallisation start time $t_{5\%}$ as a function of the sulphur content in ppm, are given in table 12.2 and these expressions have been derived from the results given in figure 12.21. It is, however, necessary to mention that these are

not universal equations; they are specific for these steels under the processing conditions specified above.

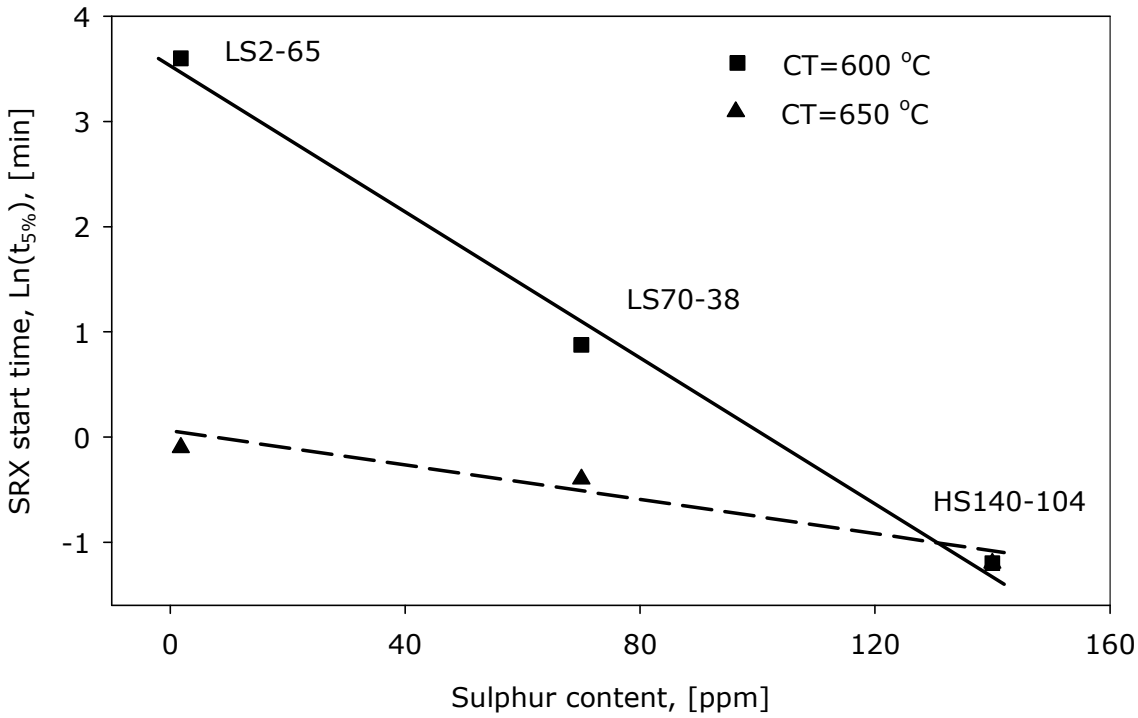

Figure 12.21: Logarithm of the static recrystallisation start time $t_{5\%}$ versus the sulphur content in ppm.

Table 12.2: Empirical expressions for predicting the recrystallisation start time $t_{5\%}$ as a function of the sulphur content in ppm derived from the results in figure 12.21 above; CT = coiling temperature.

CT (°C)	SRX $t_{5\%}$	R^2 value
600	$t_{5\%}$ = 33.78exp(-0.0345S)	0.993
650	$t_{5\%}$ = 0.99exp(-0.008S)	0.94

12.4.2 Metallographic analysis on static recrystallisation in steels HS140-104 and LS2-65

The metallographic analysis through TEM of thin foils focused on the nucleation of recrystallisation during the annealing process and the possible influence of the AlN particles on the kinetics of the recrystallisation process. Figures 12.22 to 12.24 show preferential nucleation of new recrystallised grains on subgrain boundaries and around extensively cold worked regions around Fe_3C particles in both steels HS140-104 and LS2-65. These areas provided extra driving force for the nucleation of new recrystallised grains in both low and high sulphur steels.

Figure 12.23 shows a new grain that nucleated on the deformation band in steel HS140-104, and is growing in the direction of the arrows parallel to the deformation bands while growth normal to the sides parallel to the deformation bands is probably inhibited by orientation pinning from low angle grain boundaries.

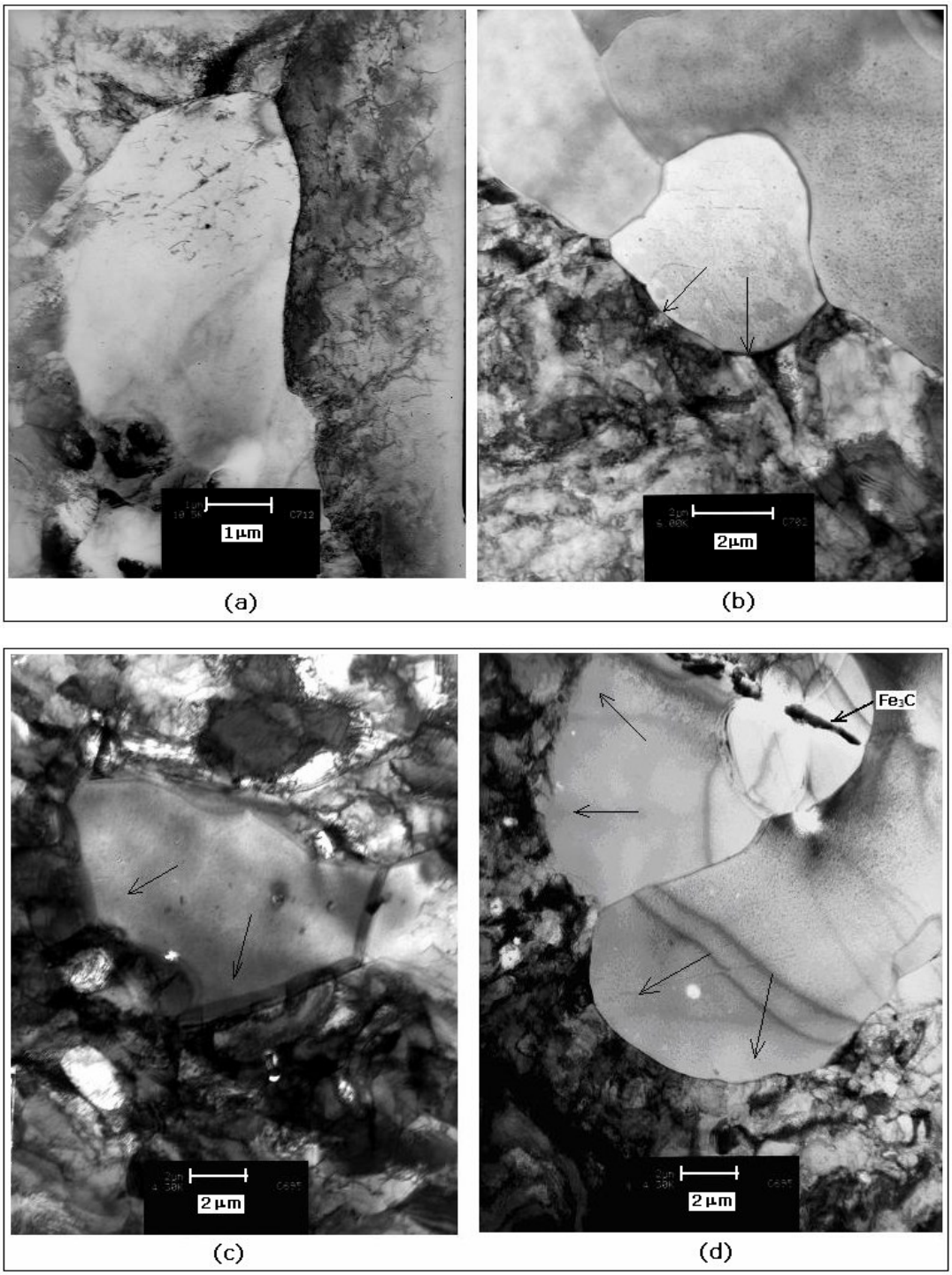

Figure 12.22: Nucleation of new recrystallised grains on subgrain boundaries growing into the deformed matrix by Strain Induced Boundary Migration (SIBM): (a) and (c) new recrystallised grains are

formed in steels LS2-65 and HS140-104 respectively while in (b) and (d) the grains are growing into the deformed matrix as indicated by the arrows in steels LS2-65 and HS140-104 respectively.

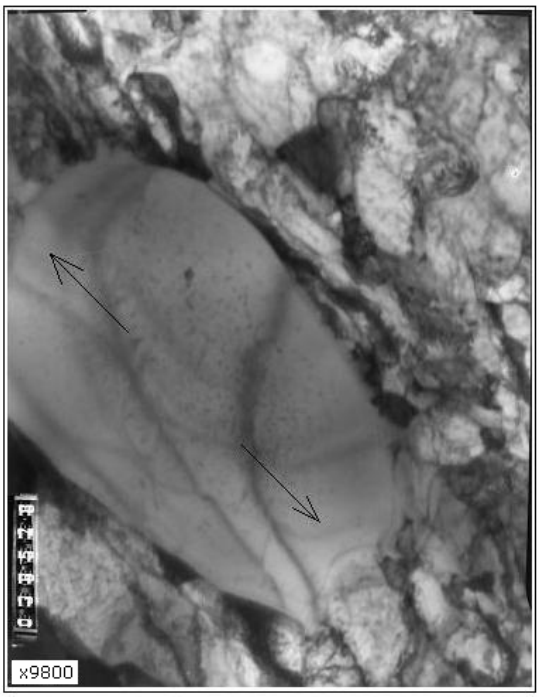

Figure 12.23: Steel HS140-104, showing a new grain that nucleated on a deformation band and is growing in the direction of the arrows parallel to the deformation bands.

Chapter 12 Results

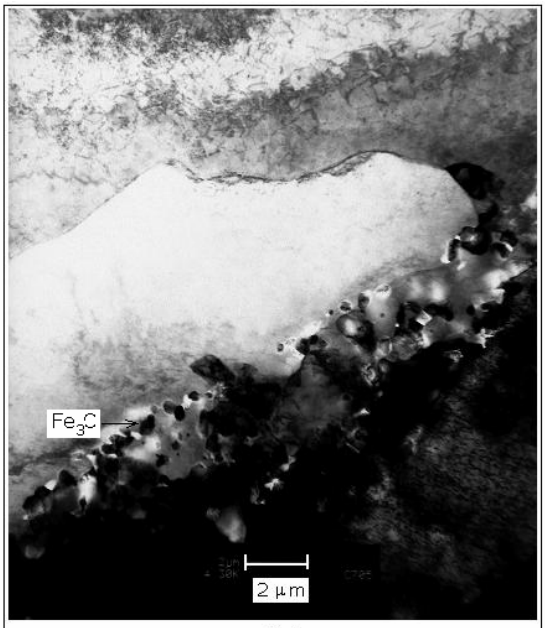

(a)

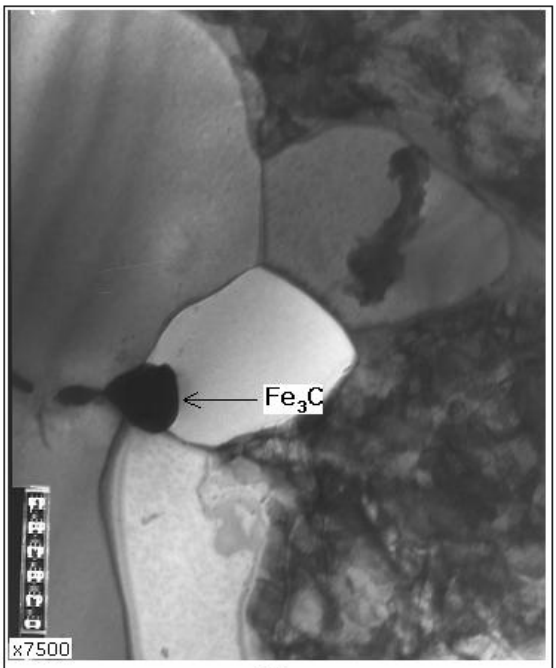

(b)

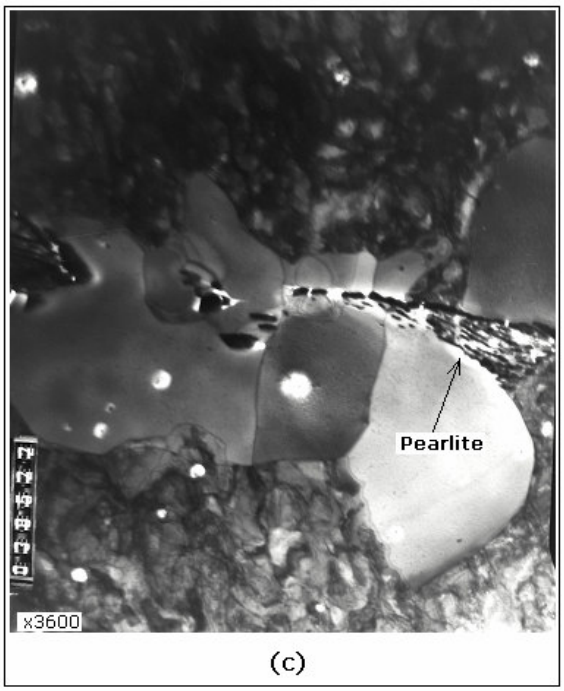

Figure 12.24: Nucleation of new recrystallised grains within extensively cold deformed regions around pearlite colonies and Fe_3C particles. (a) steel LS2-65, (b) and (c) steel HS140-104 .

Figure 12.25 shows the micrographs from TEM thin foils in which observations of the pinning interaction of AlN fine particles (< 30 nm) with the recrystallisation process in the low sulphur content steel LS2-65, were made. The wavy recrystallisation front observed in figure 12.25 (a) shows the pinning effect of the fine AlN precipitates in the low sulphur steel LS2-65 which, consequently, retards the recrystallisation process in this steel. More evidence of the pinning of the recrystallisation front by the Zener drag effect is seen in the micrographs in figures 12.25 (b) and (c) which were taken at higher magnification. The same investigation was done on the higher sulphur content steel HS140-

Chapter 12 Results

104 and no particle pinning of the recrystallisation front was observed, see figure 12.26 below.

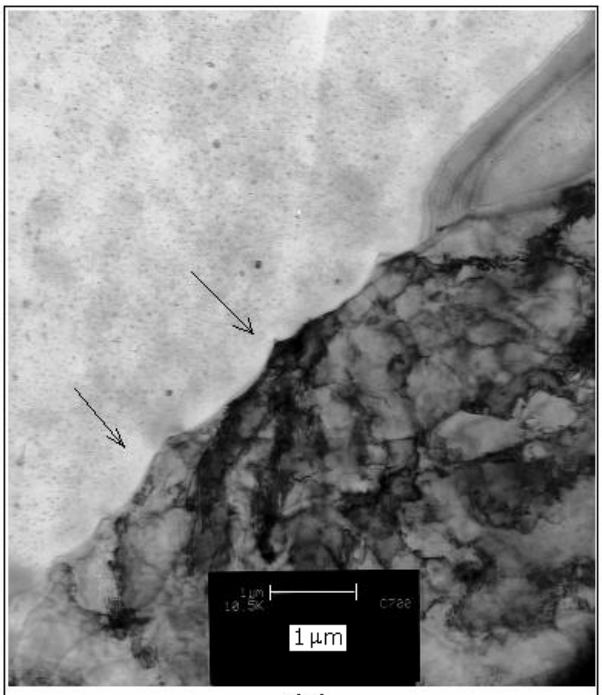

(a)

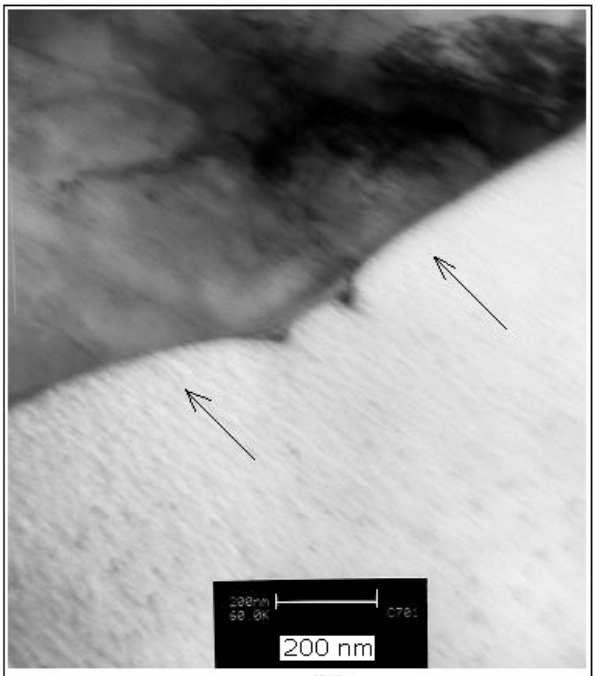

(b)

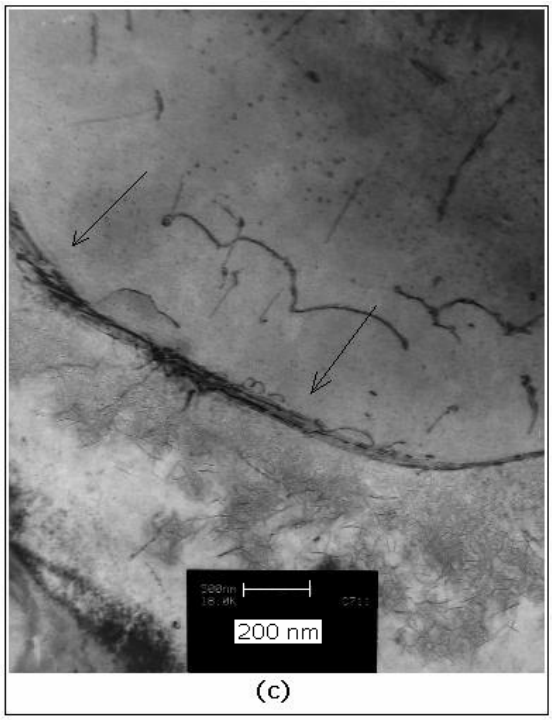

(c)

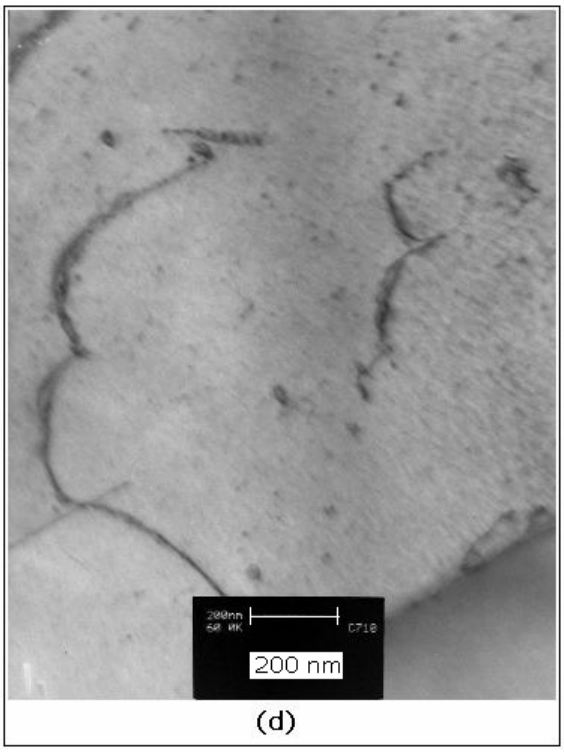

(d)

Figure 12.25: Particle pinning of recrystallisation (SRX) in steel LS2-65: (a) a wavy recrystallisation front, (b) particle pinning of the SRX front by two AlN particles which were about 100 nm apart, (c) dislocation

pinning in and around the SRX front and (d) dislocations pinned by AlN particles just behind the SRX front.

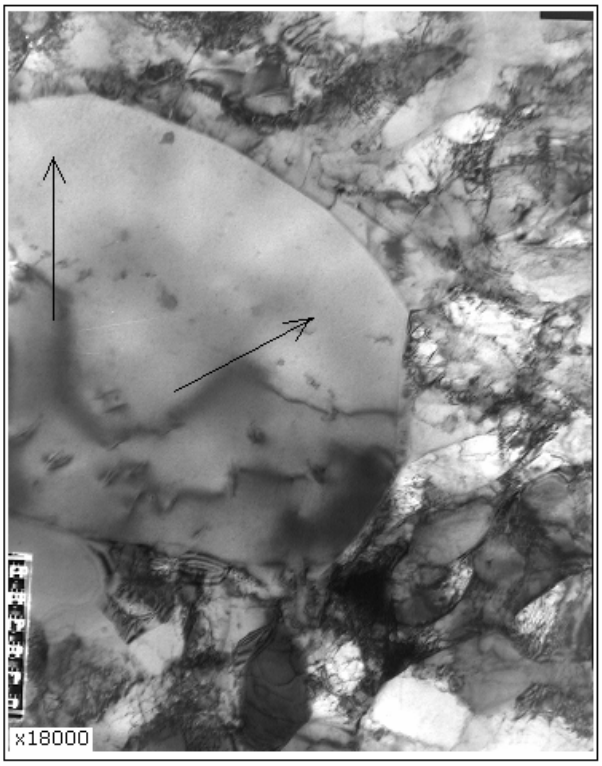

Figure 12.26: Recrystallisation front that is growing into the deformed matrix without encountering particle pinning in higher sulphur steels HS140-104.

12.5 Precipitation of AlN on MnS and the resulting mean particle size of the former

Steels HS140-104 and LS2-65, one with high and the other with low sulphur contents respectively were hot rolled and coiled in the Gleeble 1500^{TM} according to the schedule and heat treatment cycle specified in table 11.1 and figure 11.1 respectively. The TEP measurements were carried out according to the procedure given in section 10.5.

12.5.1 TEP measurements in an as-coiled condition

The absolute TEP measurements were taken from eight specimens which were obtained from each of the steels and the results are given in table 12.3 below. As may be seen in table 12.3 and figure 12.27, there was no significant change in the absolute TEP values immediately after coiling and after isothermal annealing at 800 for 2 hours. This was evidence that there was no further significant precipitation of AlN, in both steels, after hot rolling and coiling for 1 hour at 600 °C in a Gleeble 1500^{TM} simulator.

Chapter 12 Results

Table 12.3: Absolute TEP values for the steels LS2-65 and HS140-104 which were solution treated at 1150 °C for 10 minutes, hot rolled in 4 passes and then coiled at 600 °C for 1 hour; TEP1 = absolute TEP value immediately after coiling while TEP2 = absolute TEP value after annealing at 800 °C for 2 hours cooled to 600 °C and annealed for 10 minutes and quenched in water. Error = 0.033 μV K^{-1}.

Specimen	Steel LS2-65		Steel HS140-104	
	TEP1 μV/K	TEP2 μV/K	TEP1 μV/K	TEP2 μV/K
1	9.21	9.10	9.40	9.40
2	9.20	9.14	9.26	9.14
3	9.14	9.00	9.31	9.32
4	9.28	9.06	9.28	9.38
5	9.10	9.12	9.10	9.23
6	9.06	9.00	9.16	9.17
7	9.21	9.20	9.10	9.21
8	9.10	9.10	9.07	9.00
Mean	9.16	9.09	9.21	9.23
Std. dev.	0.07	0.07	0.12	0.13

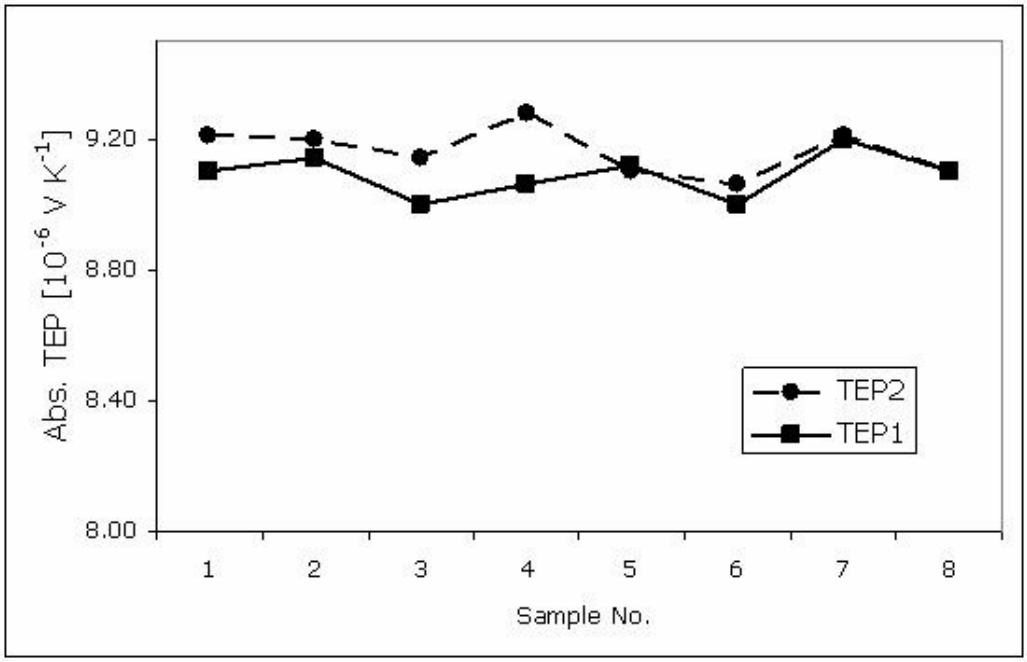

(a)

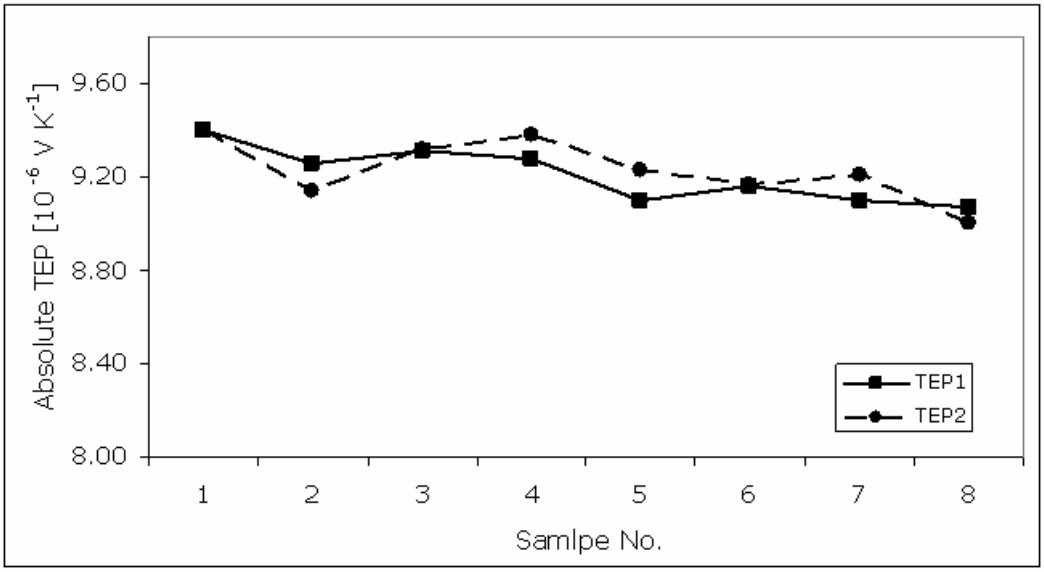

(b)

Figure 12.27: Absolute TEP measurements for the as-coiled condition of steels (a) LS2-65 and (b) HS140-104 where TEP1 and TEP2 are as defined in table 12.2 above.

12.5.2 Precipitation of AlN during hot rolling and coiling simulations

Metallographic analysis was carried out on steels HS140-104, LS70-38 and LS2-65 in the hot deformed and as-coiled condition in the Gleeble 1500^{TM} in order to investigate the possible influence of the sulphur content on the precipitation of AlN during coiling at 600 and 650 °C. The hot rolling and coiling schedules were given in table 11.1 and figure 11.1. The results from the metallographic analysis are given in figures 12.28 to 12.31.

It was observed that in the higher sulphur content steel HS140-104, the AlN was associated with MnS and [Mn,Cu]S, see figures 12.28 (b) and (c) below, and the particles were generally coarse between 50 and 300 nm in size. In the medium sulphur content steel LS70-38, the AlN was also associated with [Mn,Ti,V]S complex sulphides but the particles were relatively finer compared with steel HS140-104, between 50 and 100 nm, see figure 12.29. In the lowest sulphur content steel LS2-65; no AlN could be observed on extraction carbon replicas as this technique is not sensitive enough to reveal the very fine particles and, therefore TEM thin foils were used. Through this technique fine AlN particles (< 30 nm) were observed and these were not associated with the MnS as there was none due to the very low sulphur content of only 2 ppm in this steel, see figure 12.30 below.

Chapter 12 Results

The main observation here was that the heterogeneous association of AlN with the MnS in medium to high sulphur content steels, modified the effective particle size of the former if compared with the low sulphur content steels in which the AlN nucleated homogeneously in the matrix or heterogeneously on grain boundries as shown in figures 12.30 and 12.31 respectively. This difference in effective particle size of the AlN between the higher and the lower sulphur content steels contributed later to the difference in the recrystallisation behaviour of these two groups of steels i.e. it is generally "sluggish" in the lower sulphur content steels due to presence of much finer AlN particles which may pin the dislocation sub-boundaries and the static recrystallisation fronts through Zener drag.

The mean particle size for steels HS140-104, LS70-38 and LS2-65 was measured from approximately one hundred particles and their mean is plotted against the sulphur content of their respective steels in figure 12.32. The error bars represent the standard deviation from the diameter measurements. The main observation in figure 12.32 was that the 5 percent recrystallisation time $t_{5\%}$ increased as the mean particle size decreased with the decrease in sulphur content of the steel.

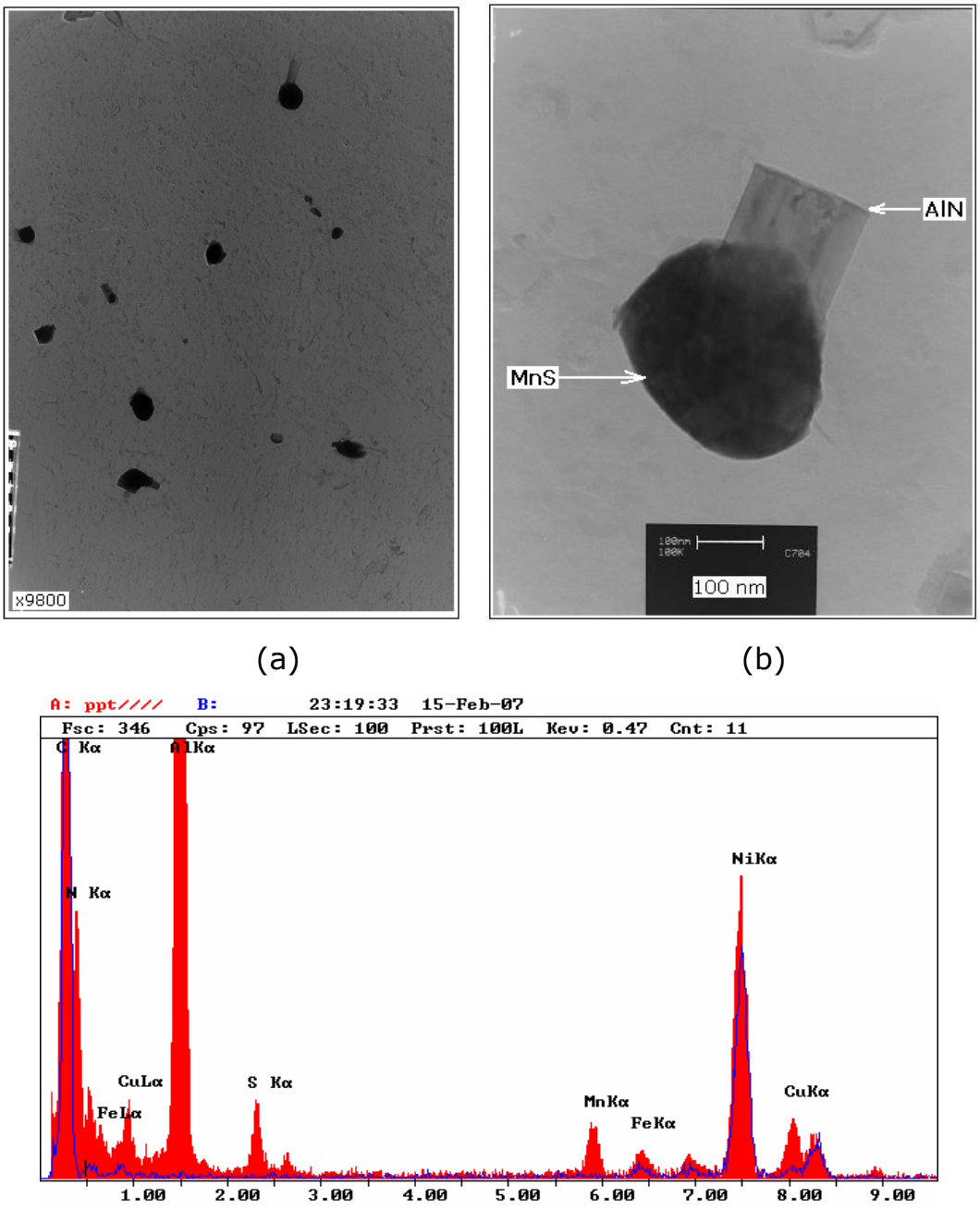

Figure 12.28: TEM replica micrographs and EDS spectrum for the higher sulphur content (140 ppm) steel HS140-104 in the as-coiled condition, hot rolled and coiled at 600 °C. (a) AlN particles observed at low magnification, (b) about 150 nm particle in micrograph (a) now

observed at higher magnification, (c) EDS spectrum of the particle in micrograph (b).

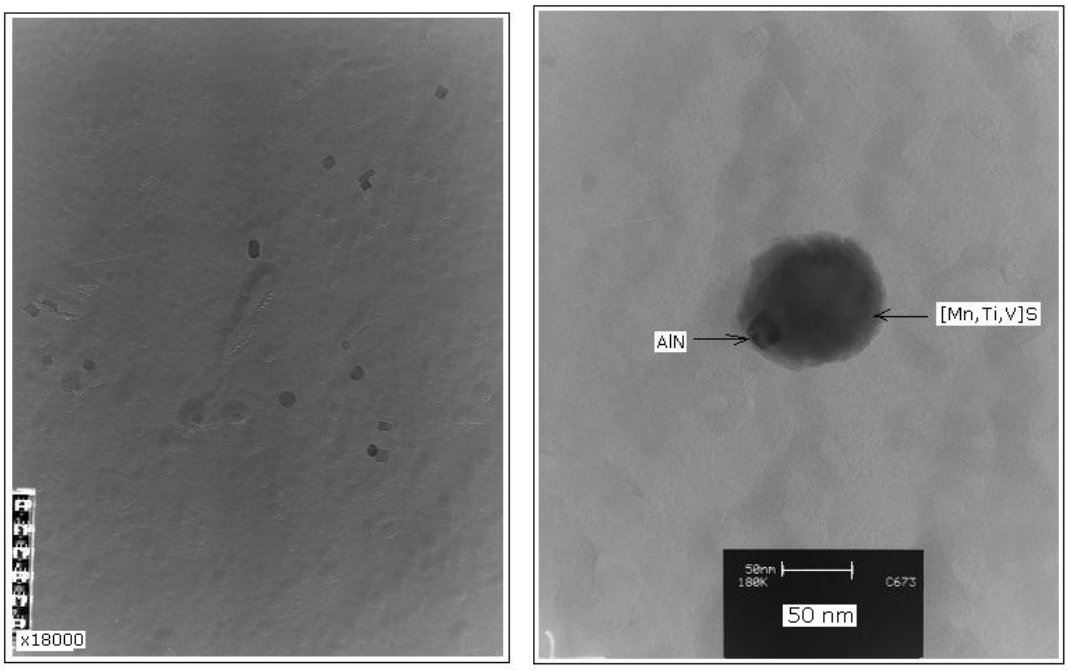

(a) (b)

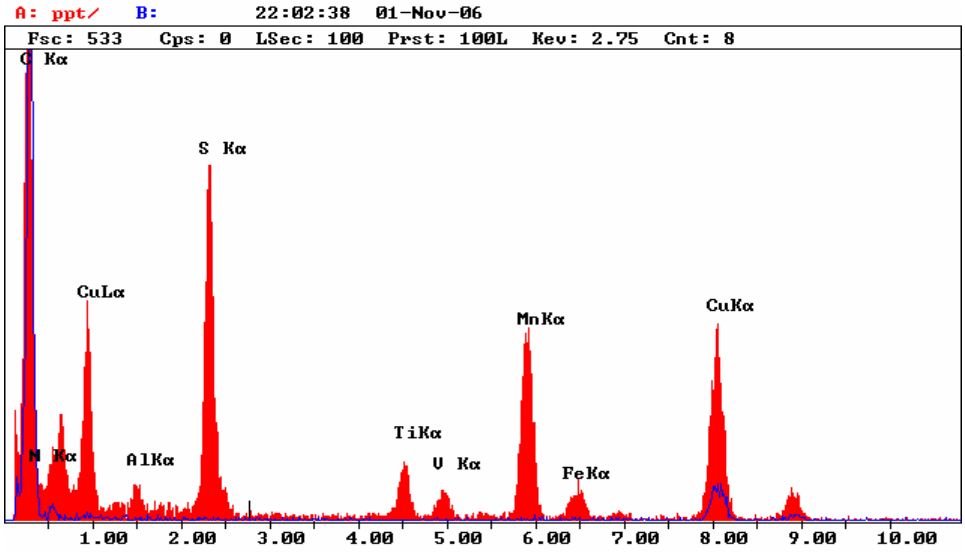

(c)

Figure 12.29: TEM replica micrographs and EDS spectrum for the medium sulphur content (70 ppm) steel LS70-38 in the as-coiled condition, hot rolled and coiled at 600 °C. (a) AlN particles observed at low magnification, (b) about 80 nm particle in micrograph (a) now

observed at higher magnification, (c) EDS spectrum of the particle in micrograph (b).

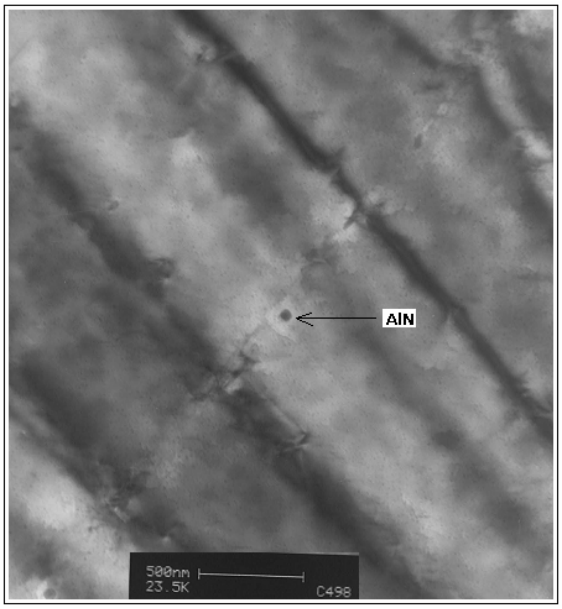

(a)

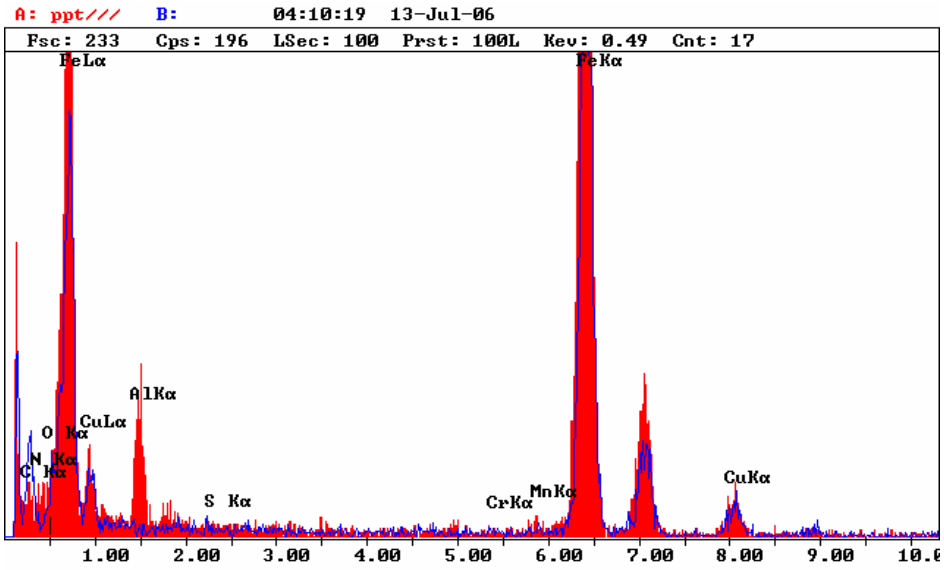

(b)

Figure 12.30: TEM thin foil micrograph and EDS spectrum for the low sulphur content steel LS2-65 in the as-coiled condition, hot rolled and

coiled at 600 °C. (a) micrograph showing a typical AlN particle, (b) the EDS spectrum for the particle in (a).

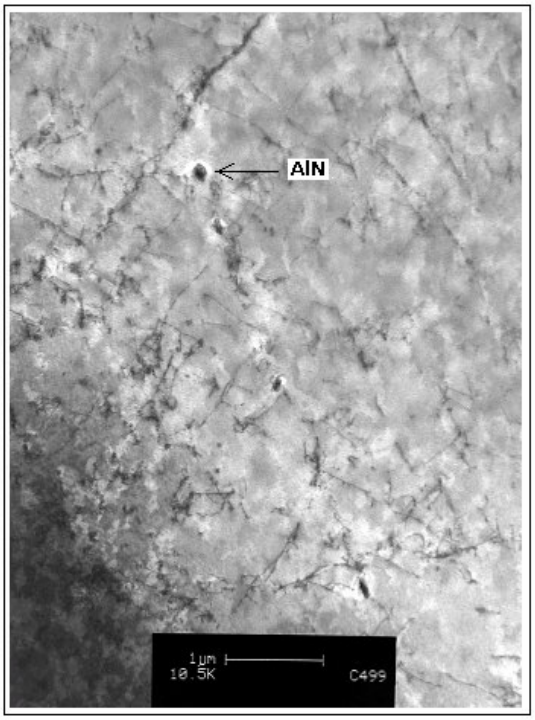

(a)

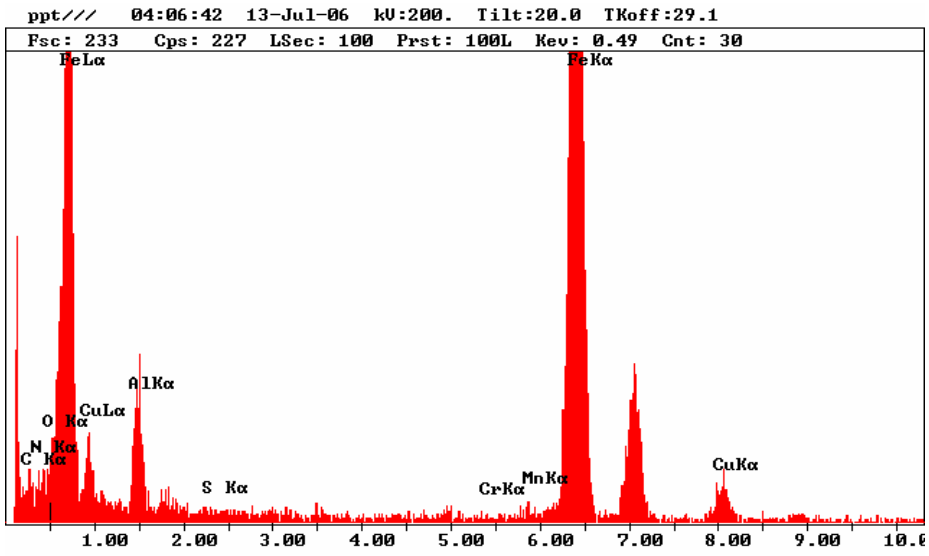

(b)

Figure 12.31: (a) TEM thin foil micrograph showing precipitation of AlN on prior grain boundary and on dislocations and (b) EDS spectrum of the AlN particles that were observed in (a) for the low sulphur content

steel LS2-65 in the as-coiled condition, hot rolled and coiled at 650 °C for 1 hour.

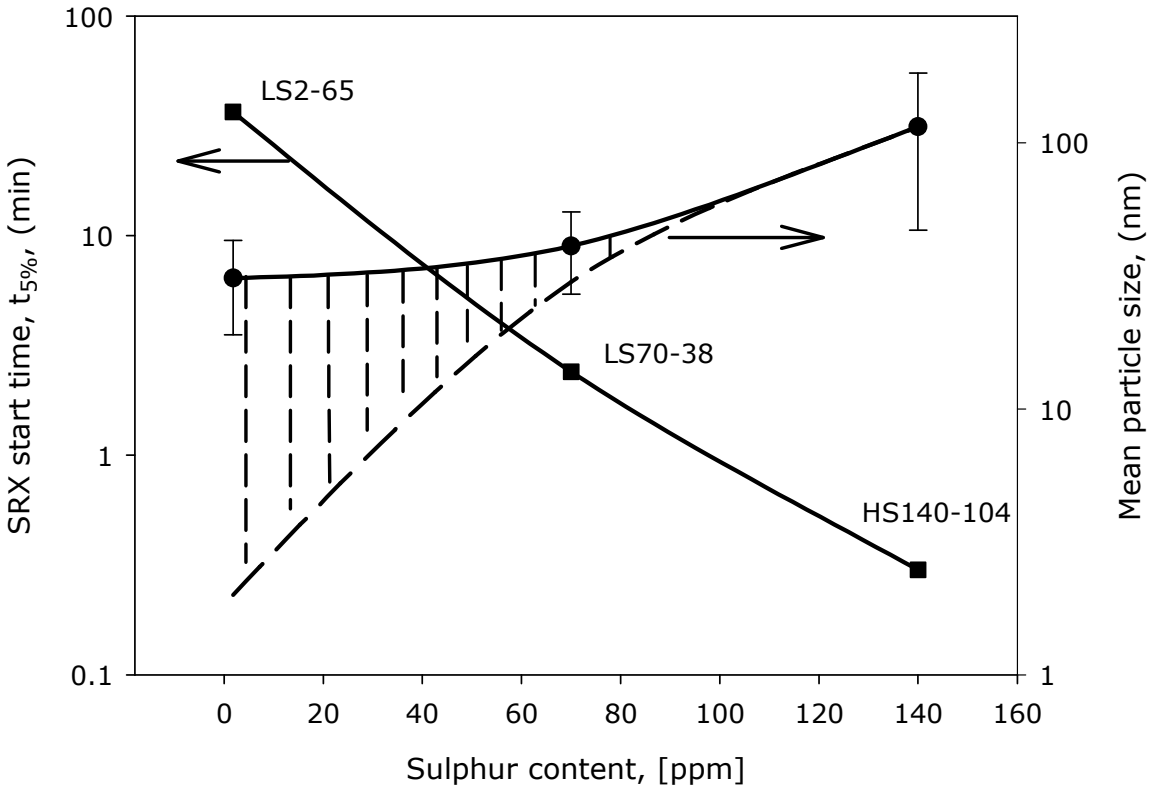

Figure 12.32: The recrystallisation start time $t_{5\%}$ and the AlN mean particle size as measured from thin foils, are plotted as a function of the sulphur content in steels HS140-104, LS70-38 and LS2-65. The cross hatched area represents possible particles that were "missed" due to a lower limit of detection of about 20 nm by thin foil TEM.

12.5.3 Crystallographic orientation relationship between AlN and MnS

As mention earlier in section 11.3.1, the TEM camera constant was calibrated using a gold film and from which the lattice parameter for the AlN and the MnS were found to be 0.318 and

0.529 nm respectively. This was in reasonable agreement with literature values where the lattice parameters for AlN and MnS were found to be 0.311 and 0.522 nm respectively[36,48].

The compound MnS/AlN particle and the electron diffraction patterns for the AlN, MnS and the compound particle are given in figure 12.33. The zone axis for the AlN was $[2\bar{1}\bar{1}0]$ while that for the MnS was [110]. The orientation relationship between the AlN and the MnS was found to be $(1\bar{1}1)_{MnS}//(0001)_{AlN}$ and $[110]_{MnS}//[2\bar{1}\bar{1}0]_{AlN}$ which agrees with the observation of Ushioda et al[52] in a 0.036%C steel with 150 ppm sulphur and 41 ppm nitrogen. The schematic diagram of the electron diffraction pattern for the compound particle is given in figure 12.33 (e) below.

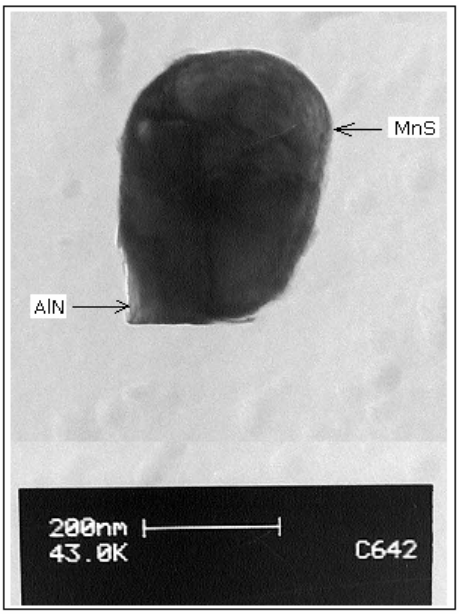

(a)

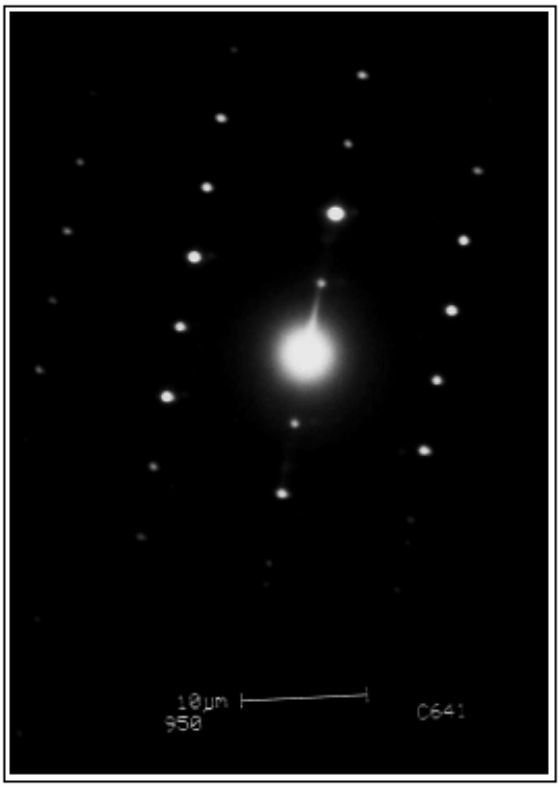

(b)

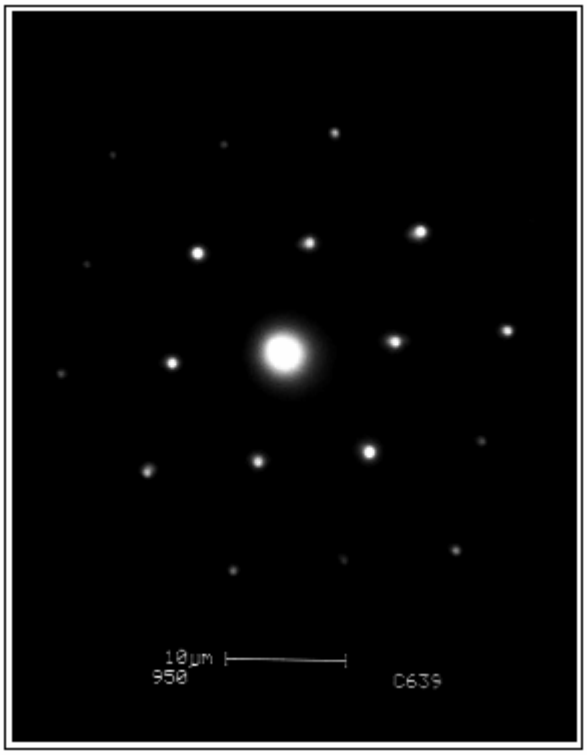

(c)

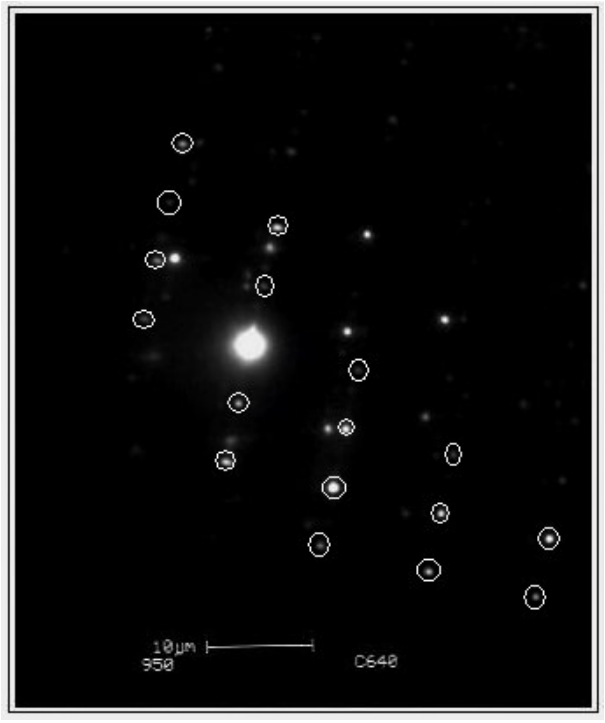

(d)

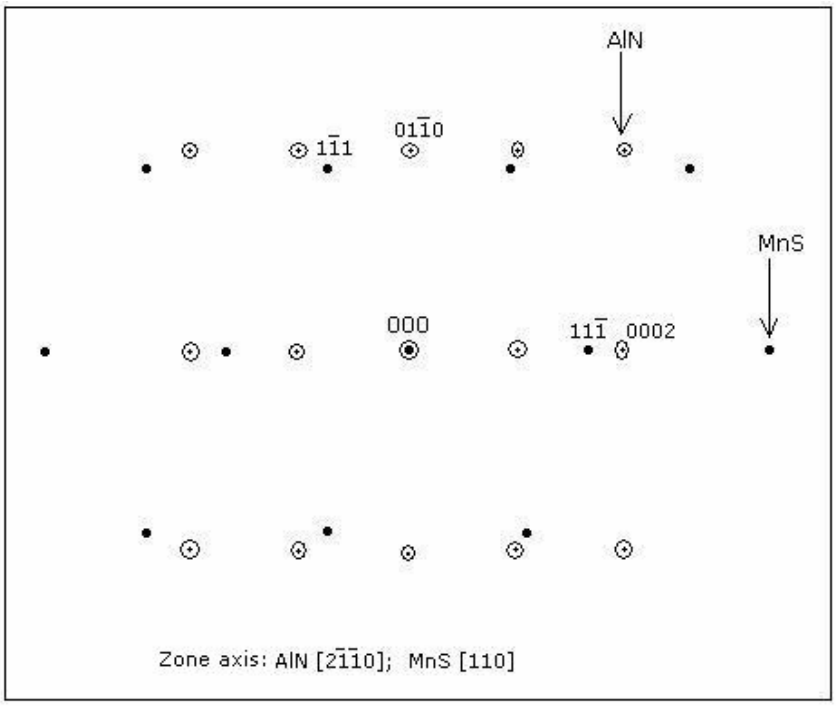

(e)

Figure 12.33: Crystallographic orientation relationship between AlN and MnS: (a) an AlN particle that nucleated on MnS (b) diffraction pattern

of AlN on $[2\bar{1}\bar{1}0]$ zone axis, (c) diffraction pattern of MnS on $[110]$ zone axis, (d) diffraction patterns of both AlN (in open symbols) and MnS (in solid symbols) (e) schematic diagram of the diffraction pattern in (d) with $(1\bar{1}1)_{MnS}//(0001)_{AlN}$, $[110]_{MnS}//[2\bar{1}\bar{1}0]_{AlN}$.

Chapter 13 Discussion

13.1 Introduction

The discussion of the results given in the previous chapter is divided into four parts:

- the first part, which comprises section 13.2 and 13.3, deals with the equilibrium solubility trends of AlN in low and high sulphur low carbon Al-killed hot rolled strip steels during reheating;
- the second part, which consists of section 13.4, deals with the study of the concurrent static recrystallisation and precipitation of AlN during isothermal annealing of the cold worked steels HS140-104, HS90-12, LS70-38 and LS2-65 in the as-quenched condition;
- the third part, which is in section 13.5, presents the recrystallisation behaviour in laboratory simulated coiled steels HS140-104, LS70-38 and LS2-65 in which the sulphur content and the simulated coiling temperatures were varied; and
- the last part, which is in section 13.6, deals with the nucleation of AlN on MnS particles during hot rolling and coiling and its impact on the static recrystallisation after cold working in these steels.

13.2 Effect of soaking time on the dissolution of the AlN

In figure 12.1, the relative TEP values $\triangle S$ are plotted against the isothermal soaking times at 1150 °C for high and low sulphur content steels HS140-104 and LS2-65 respectively. Assuming that

the contribution from lattice defects and other substitutional alloying elements was negligible and/or the same for all of these specimens, the measured relative TEP value ΔS after quenching from the solution treatment temperature represented the carbon and nitrogen in solid solution. At this solution treatment temperature of 1150 °C, the carbon was already completely in solid solution and, therefore, any variations in measured TEP values could be attributed to the partial or complete dissolution of the AlN particles.

As may be seen in figure 12.1, there was no significant change in the relative TEP values after about 5 minutes and up to 20 minutes soaking times and this meant that no further significant dissolution of AlN took place after soaking the steels for more than 5 minutes. The soaking time of about 5 minutes or more was, therefore, adequate to achieve equilibrium conditions during AlN solution heat treatment of these two steels, which were at the extreme limits of the range of sulphur contents used here. This already suggests that differences in the sulphur levels in these steels do not affect the kinetics of equilibrium dissolution of the AlN after soaking for 5 minutes or more at a solution treatment temperature of 1150 °C. The differences in the relative TEP values were, therefore, only due to the differences in nitrogen content whereby the steel with the higher nitrogen content registered higher TEP values. Similar observations were made by Mayrhofer et al[47] that, during AlN solution treatment even in the presence of coarse AlN, equilibrium was achieved in less than 10 minutes at temperatures above 1000 °C. It may, therefore, be concluded that

Chapter 13 Discussion

AlN dissolves relatively quickly in low carbon Al-killed steels during a solution or reheating treatment.

13.3 Equilibrium solubility trends during reheating of AlN in low carbon Al-killed strip steels with low and high sulphur contents

As may be seen in both figures 12.2 and 12.3, there is some scatter in the TEP results and this may possibly be attributed to quenched-in defects, presence of coherent or semi-coherent particles and interaction of nitrogen and carbon with other alloying elements in these commercial low carbon strip steels. Interstitials that segregate to dislocations and other lattice defects may not contribute measurably to the TEP effect any more while the strain field around coherent particles and lattice defects such as dislocations, on the other hand, may do so[(147)]. As a result there will be some variation in TEP measurements from such metallurgical effects and, of course, also from purely extraneous experimental effects in measurement. However, the R-squared value (R^2 = 0.8) from the regression analysis in figure 12.3, shows that the effects of the scatter are still reasonable.

In order to correlate the nitrogen content in solid solution to the measured relative TEP or $\triangle S$ values, some assumptions had to be made:

(a) All the nitrogen had precipitated into coarse and incoherent AlN during the prior annealing process at 800 °C for 6 hours and that the nitrogen in solid solution that was in equilibrium with the AlN at that temperature, was negligible. This assumption was tested with an existing AlN equilibrium solubility equation in ferrite (equation 13.3 below) and it predicts that at 800 °C, only about 3 ppm of the nitrogen would be in solid solution[38].

(b) All the nitrogen was in solid solution at the points where the TEP measurements leveled off after the specimens had been solution treated at higher temperatures, as was shown in figure 12.2.

(c) TEP contributions from other dissolving substitutional alloying elements were negligible and/or constant.

(d) TEP contributions from quenched-in lattice defects were negligible and/or constant.

(e) As TEP measurements were done at room temperature and the fact that all the steels that were studied were low carbon steels with a maximum of 0.058%C and 104 ppm N, the specimens were fully ferritic and there were no TEP contributions from matrix phase variations.

The amount of nitrogen in solid solution could then be deduced from the Gorter-Nordheim law[135] using equation 10.2 ($\triangle S_N$ =

$S_{800} - S_i = K_{AlN}[N]$). The amount of aluminium required to combine with the nitrogen was calculated from the stoichiometric composition of AlN, which was less than the analysed acid soluble aluminium content for all the steels that were studied, see chemical compositions in table 10.1.

The equation from the regression analysis of the plot of the logarithm of the solubility product of the AlN, i.e. Log[%Al][%N], versus the inverse of the absolute solution treatment temperature in figure 12.3, is the equilibrium solubility equation for the AlN in austenite in these steels as determined by the TEP technique and was found to be:

$$\text{Log}[\%\text{Al}][\%\text{N}] = 2.6 - \frac{9710}{\text{T}} \qquad (13.1)$$

where the aluminium and the nitrogen contents are in weight percentage and T is the absolute solution temperature in Kelvin.

From figure 12.3, the most important observation is that the sulphur content does not appear to have any measurable effect on the equilibrium solubility of the AlN in these steels, at least within the experimental scatter found, i.e. the AlN equilibrium solubility of both the low and high sulphur steels that were studied could be modelled by the same equation 13.1. This is in agreement with the observations made by many workers in these steels using other techniques than TEP[41-52].

Chapter 13 Discussion

The results in figure 12.3 were checked by Thermo-Calc and the results predicted that sulphur should not influence the equilibrium solubility of AlN in low carbon Al-killed steels, see figure 12.4. This was not surprising as Thermo-Calc employs similar thermodynamic models (given in the appendix) to compute the solubility limits of the AlN.

The AlN equilibrium solubility model from this work is compared with models from others workers in figure 13.1 below. The results from this study give slightly higher solubility limits when compared with the results obtained through the Beeghly technique and could be due to a number of reasons arising from the different techniques employed. While the TEP technique is based on the assumptions made above, the Beeghly technique also has its own shortfalls, mainly the lack of sensitivity to particles of less than 10 nm in diameter and its failure to isolate the AlN from other nitrides[42]. Consequently, lower solubility temperatures are reported by the Beeghly technique compared to other techniques.

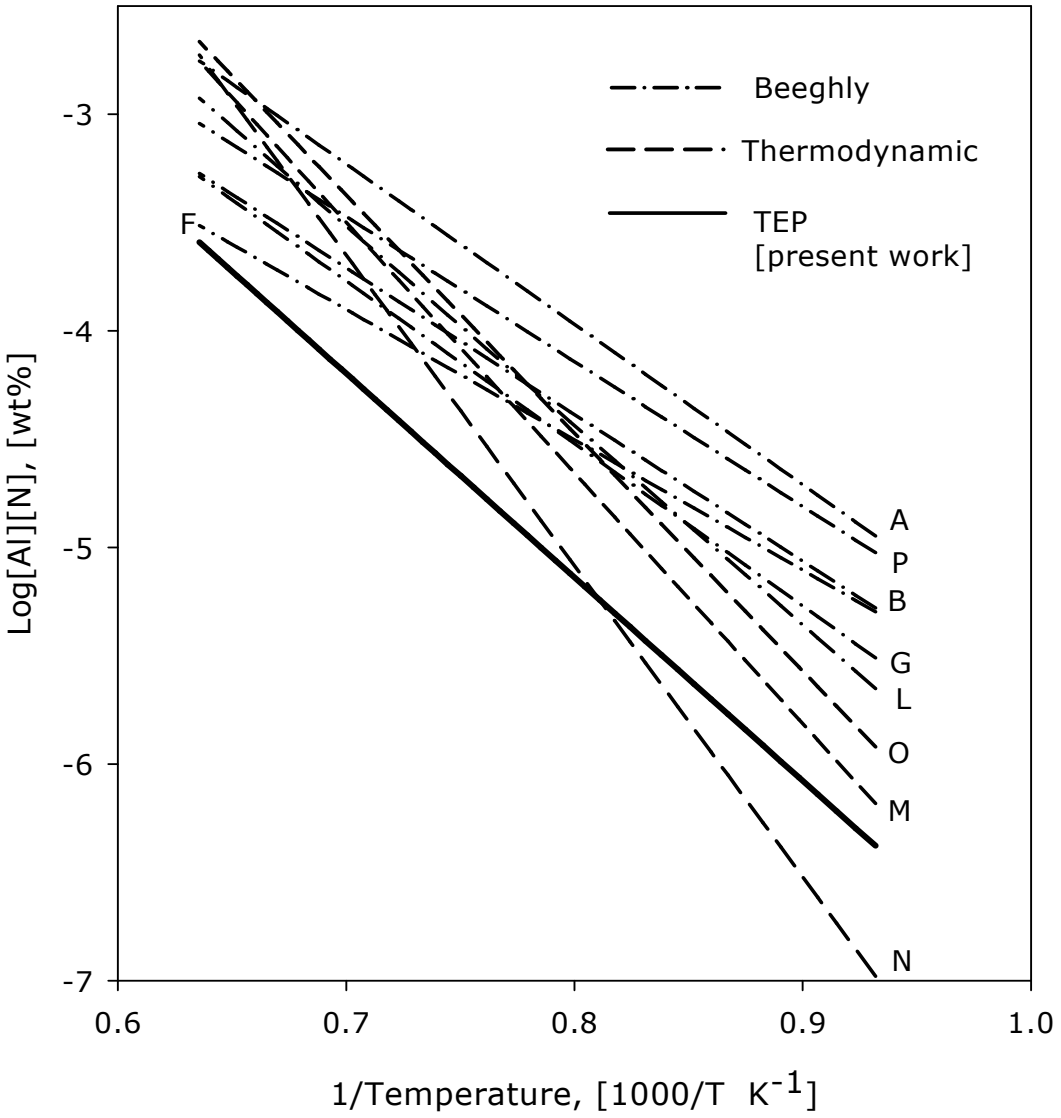

Figure 13.1: Comparison of the TEP equilibrium solubility model from this work with the models from other authors; details for the other curves are given in the appendix.

Curves M, N and O in figure 13.1 were calculated from thermodynamic data and are based on the Fe-Al-N system[49-51].

Hence, any possible interactions of the AlN with other alloying elements, as may be the case in commercial strip steels, are not taken into account by this approach. This may account for the difference between the solubility model from this work and those derived from the thermodynamic data.

Despite the differences in the predicted AlN solubility limits, all models including the one from this work, indicate that the sulphur content in these low carbon Al-killed strip steels does not influence the equilibrium solubility of AlN.

It may be worthwhile to also compare the TEP coefficient K_{AlN} for AlN from this work with those from other work. Using equation 10.2 and with the assumptions regarding TEP measurements made above, the solubility coefficient K_{AlN} is given by:

$$K_{AlN} = \frac{\left(S_{800} - S_f\right)}{[N]} = \frac{\Delta S}{[N]}$$

where S_{800} is the absolute TEP measurement for the specimen that was solution treated at 800 ºC for 6 hours, S_f is the absolute TEP value at the solution temperature where the absolute TEP values level off and $[N]$ is the nitrogen content in solid solution, in this case the one that was obtained from the LECO analyses.

Values of the TEP coefficient K_{AlN} for AlN obtained in this work are compared with values from the literature in table 13.1.

Chapter 13 Discussion

Table 13.1: TEP coefficients K_{AlN} for AlN obtained from the five steels that were studied and compared to published values.

Steel	N [ppm]	ΔS [μV/K]	K_{AlN} [$x10^{-9}$ V/K.ppm]	Literature [$x10^{-9}$ V/K.ppm]
HS130-50	50	0.43	8.6	6.7 to 10 (Biron et al[148])
HS90-34	34	0.21	6.4	
HS140-104	104	0.79	7.6	
LS10-83	83	0.63	7.5	
LS2-65	65	0.46	7.1	

As may be seen from table 13.1, the TEP coefficients for AlN obtained in this work are in good agreement with those obtained by Biron et al[148] on low carbon (0.02 to 0.066%C) and 17 to 102 ppm nitrogen Al-killed steels.

The TEP results were checked by TEM on carbon extraction replicas and the results are given in figures 12.5 to 12.8. After isothermal annealing at 800 °C for 6 hours, the AlN had precipitated into coarse cuboids and fine round particles as shown in figure 12.5. When these specimens were solution treated at higher temperatures in order to dissolve the AlN, in the medium nitrogen steel LS2-65 the AlN disappeared at 1200 °C and this was somewhat higher by nearly 50 °C than the dissolution temperature determined by the TEP technique, which was about 1150 °C. The difference might be due to the scatter in the TEP results, see figure 12.3. As for steel HS140-104, there was good

agreement between the dissolution temperature determined by TEM on carbon extraction replicas and the TEP technique as no more AlN could be observed after a soaking temperature of 1250 °C, see figure 12.8.

13.4 Concurrent static recrystallisation and precipitation of AlN during isothermal annealing of a low carbon Al-killed cold worked steel HS140-104 in an as-quenched condition

Steel HS140-104 was solution treated at 1300 °C for 12 minutes to dissolve both the AlN and MnS and quenched into water (see figure 10.1), cold worked 70 percent, and isothermally annealed at 610 °C to induce static recrystallisation. Figure 12.9 shows the progression of the recrystallisation process and it is evident from the micrographs that between 5 and 18 minutes, there was a complete recrystallisation arrest i.e. there was no significant increase in the recrystallised volume fraction with an extension of the isothermal annealing time. This observation was supported by the quantitative results given in figure 12.12 in which the recrystallised volume fraction was plotted against the isothermal annealing time, see the cross hatched area. However, no recrystallisation arrest was observed in this steel at temperatures of 580 °C and below or above 700 °C, see figures 12.10 and 12.12.

Chapter 13 Discussion

A recrystallisation arrest in Al-killed low carbon steels within the intermediate temperature range of 550 to 650 °C, has also been observed by other workers and was attributed to the clustering or nucleation of AlN[8,9,119]. It was reported that at an isothermal annealing temperature of 550 °C and below, AlN precipitation precedes recrystallisation while at temperatures higher than 650 °C the latter precedes the former. However, in this study, it was observed that even at 580 °C, AlN still preceded recrystallisation and, therefore, this suggests that the lower temperature limit may also depend on the chemical composition and the supersaturation of the nitrogen and aluminium of the steel. Both of these will reflect in the ratio V_v/r which dictates effective Zener pinning above a certain critical value.

It was also established that in cold worked low carbon Al-killed steels, AlN nucleates predominantly on dislocation sub-boundaries whereas grain boundaries are preferred nucleation sites in recrystallised material[11,122,149], probably due to a lack of dislocations and subgrain boundaries. As a result, the recrystallisation process is inhibited through particle pinning of the dislocation sub-boundaries as well as the recrystallisation interfaces in what is commonly called the "Zener drag" or "Zener pinning" effect.

As may be seen from figure 12.13, there was no significant difference between the as-quenched material and the one that was annealed at 450 °C for 30 minutes to precipitate the Fe_3C prior to cold working. The presence of carbon in or out of solution,

therefore, does not appear to affect the kinetics of the recrystallisation process. It, therefore, appears that the precipitation of AlN and not Fe_3C may be responsible for the recrystallisation arrest, with the start of the arrest time, representing the start time for AlN nucleation that becomes effective in Zener drag. This start time was estimated from the crossing point of an extrapolation of the horizontal arrest plateau and the slope of the rising curve in Figure 12.12 just before the arrest started.

The arrest finish time should also represent a stage where the particle size of the AlN becomes ineffective for Zener drag on moving recrystallisation interfaces and this time is assumed to be associated with the "end of nucleation", i.e. the time where there are no new very small precipitates that are forming and that can still exercise Zener drag. This time was also estimated through the extrapolation of the two lines as indicated above for the start time.

While it is impossible to observe directly by electron microscopy the very early stages of the precipitation of AlN and its effect on the recrystallisation process in cold worked material, it was observed in this work that the apparent activation energy of the process that led to the recrystallisation arrest was 230 kJ mol^{-1}, and this was somewhat close to that for the diffusion of aluminium in the matrix of α-ferrite which is quoted as 196.5 kJ mol^{-1} [149], see figure 12.14. The observed value of 230 kJ mol^{-1} differs slightly from that obtained by Ogawa et al[150] in an assessment of

the activation energy for the precipitation of AlN in both annealed and cold worked iron, which was reported as 243 kJ mol^{-1}. Biron et al[148] used the TEP technique to assess this same activation energy in Al-killed low carbon-manganese steels and also found a value of 243 kJ mol^{-1}. Using the same TEP technique, however, Brahmi et al[144] observed two temperature regimes for the nucleation of AlN in an Fe-Al-N alloy with different activation energies; the first was 250 kJ mol^{-1} for the temperature range of 500 to 575 °C and the second was 210 kJ mol^{-1} for the range of 600 to 700 °C. Due to the high diffusivity of nitrogen in ferrite, it is generally assumed that no rate controlling nitrogen concentration gradient will occur during nucleation and growth of AlN and, therefore, the diffusion of aluminium atoms is likely to be rate controlling in the precipitation of AlN[11,55].

13.4.1 Modelling the activation energy for the nucleation of AlN in ferrite, ΔG^*_{AlN} and the critical radius r*

The classical model for the rate of homogeneous nucleation of AlN is given by equation 3.16 and is as follows[28,29]:

$$\dot{N}_{AlN} = N_0 Z \beta Exp\left[-\frac{\left(Q_{D(Al)} + \Delta G^*_{AlN}\right)}{RT}\right] \qquad (13.2)$$

where $Q_{D(Al)}$ is the activation energy for the diffusion of aluminium in ferrite, ΔG^*_{AlN} is the activation energy for the

nucleation of AlN in ferrite and the rest is as defined in equation 3.16.

The activation energy for the isothermal and homogeneous nucleation of AlN in ferrite is modelled using data from literature, which are given in table 13.2.

Table 13.2: Parameters that have been used to calculate the activation energy for the isothermal and homogeneous nucleation of AlN in ferrite ΔG^*_{AlN}.

Parameter	Values	Reference
Interface energy, (J m^{-2})	0.2	151
Enthalpy of formation of AlN in ferrite ΔH, (kJ mol^{-1})	138	49
Bulk Modulus K for AlN (GPa)	210	152
Shear Modulus G_m for AlN (GPa) $G_m = \frac{\left(\frac{3}{2}\right)K(1-2\nu)}{1+\nu}$	151	
Poisson's ratio ν of AlN	0.21	152
Lattice parameter of fcc AlN a_{AlN} (nm)	0.4071	38
Lattice parameter of bcc iron a_{Fe} (nm)	0.286	153
Density of AlN (kg m^{-3})	3200	35
Molar volume V_m for AlN (m^{-3} mol^{-1})	1.28 x 10^{-5}	

Chapter 13 Discussion

Previous studies have shown that AlN nucleates with a coherent cubic (NaCl-type) crystal structure and with a Bain crystallographic orientation relationship with respect to the bcc iron matrix[37-39]. Using equation 3.12, the resulting misfit strain is calculated as:

$$\text{Misfit, } \quad \delta = \frac{\left(0.407-\left(\sqrt{2}\ \text{x}\ 0.286\right)\right)}{0.286} = 8.86 \text{ x } 10^{-3}$$

Since this study did not cover the equilibrium solubility of AlN in ferrite but only in austenite, the enthalpy of formation of AlN in α-iron has been derived from the AlN equilibrium solubility model given in reference 38 and using equation 4.3 ($\triangle H = 1.15RA$). The equilibrium solubility equation for the AlN in α-ferrite is given as follows:

$$\text{Log}[\%\text{Al}][\%\text{N}] = 6.061-\frac{14442}{\text{T}} \qquad (13.3)$$

where both the aluminium and the nitrogen content are in weight percent and the absolute temperature T is in Kelvin.

At equilibrium, the driving force for the isothermal nucleation of AlN in ferrite, in this case during isothermal annealing at 610 °C, has been calculated from equation 3.7 as:

$$\Delta G_v = \Delta H\left(\frac{\Delta T}{T_e}\right) = 138000\left(\frac{668}{1550}\right) = 59.5 \text{ kJ mol}^{-1}$$

where the equilibrium solubility limit temperature T_e (in K) has been predicted from the solubility model developed from this work, equation 13.1, to be about 1280°C.

For homogeneous nucleation and negligible strain energy around the nucleus, the activation energy ΔG^* for isothermal nucleation of a particle of critical radius r^* is given by equation 3.6 as:

$$\Delta G^*_{AlN} = \frac{16\pi\gamma_s^3 V_m^2}{3(\Delta G_v)^2} = 6.2 \times 10^{-21} \text{ J}$$

where a value of the surface energy γ_s of 0.2 J m^{-2} for a coherent interface of the AlN in ferrite has been used[151].

The critical radius r^* for homogeneous nucleation without strain energy around the embryo is given by equation 3.5 i.e.:

$$r^*_{AlN} = \frac{-2\gamma_s V_m}{\Delta G_v} = 8.6 \times 10^{-11} \text{ m}$$

This modelled value of the critical radius r^* is very small and appears to be less than the size of an aluminium atom (~0.14 nm). This might be as a result of the overestimation of the driving force ΔG_v or underestimation of the surface energy γ_s or a combination of both. However, AlN particles of about 15 nm in size were observed in these steels and, therefore, it is believed that the critical radius r^* should actually be somewhere between about 3 and 10 nm, where the latter is the estimated lower limit

of effective observation in thin foil TEM. The fact that the value of the critical radius r^* diminishes to practically zero ($r^* \rightarrow 0$) may signify that AlN nucleates with ease in ferrite at temperatures above 600 °C as already observed by other workers[65].

By dividing and multiplying the activation energy ΔG^*_{AlN} per critical radius (of an assumed value of $r^* = 3$ nm) by the volume of the critical radius ($V^* = 1.13 \times 10^{-25}$ m^3) and the molar volume of AlN ($V_m = 1.28 \times 10^{-5}$ m^3 mol^{-1}) respectively the modelled activation energy ΔG^*_{AlN} for homogeneous nucleation of AlN in ferrite during isothermal annealing at 610 °C becomes 0.7 J mol^{-1}. This seems very low compared with the value observed in this work of about 30 kJ mol^{-1} i.e. ($Q_{D(Al)} + \Delta G^*_{AlN}$) = 230 kJ mol^{-1} where $Q_{D(Al)}$ has been found elsewhere[149] to be 196.5 kJ mol^{-1}. The discrepancy might be a result of overestimation in the assumed values of the critical radius r^* or/and the driving force ΔG_v. Therefore, the value of 30 kJ mol^{-1} may be a realistic estimation of the activation energy for the nucleation of the AlN in ferrite.

The strain energy ΔG_ε resulting from a coherent interfacial misfit of the AlN/ferrite interface, is very small if compared to the chemical driving force ΔG_v and was neglected in the calculation for r^* and ΔG^* above. Its size may be estimated through equation 3.13 i.e.:

Chapter 13 Discussion

$$\Delta G_{\varepsilon-coh} = \frac{6G_m V^* \delta^2}{\left[1+\frac{4G_m}{3K}\right]} = 4.1 \times 10^{-18} \text{ J}$$

$$= 460 \text{ J mol}^{-1}$$

where V* is the volume of the critical radius r* of the AlN embryo.

The rather relatively small value of the activation energy ΔG^*_{AlN} for the homogeneous nucleation of AlN in ferrite of 30 kJ mol^{-1} is not surprising because previous workers[44] have found that in α-ferrite the isothermal nucleation of AlN is controlled by the diffusion of aluminium (which means that the activation energy for nucleation, must be very low in comparison) while at higher temperatures and in austenite, it is limited by the nucleation barrier i.e. by a high activation energy ΔG^*_{AlN} [44,47,153,154]. The modelled low strain energy of 460 J mol^{-1} is the result of a low misfit (δ = 8.86 x 10^{-3}) between the coherent cubic structure of AlN and the α-ferrite matrix. Furthermore, the activation energy for nucleation of AlN in ferrite may even reduce further than the above estimated 30 kJ mol^{-1} if the reported heterogeneous nucleation on subgrain boundaries and dislocations of AlN is considered.

The results from this work, therefore, confirm that $Q_{D(Al)} >> \Delta G^*_{AlN}$ i.e. $(Q_{D(Al)} + \Delta G^*_{AlN}) \approx Q_{D(Al)}$, and $\Delta G^*_{AlN} \rightarrow 0$. This leads to the conclusion that the activation energy for the nucleation of AlN is very small and may be ignored without affecting its

predicted nucleation rate. The nucleation rate of AlN in ferrite should, therefore, be very high and it may be assumed that in an as-quenched microstructure during annealing at 610°C in these steels, that the nucleation of the AlN is over relatively quickly with effective recrystallisation arrest through Zener pinning setting in soon thereafter. This means that the recrystallisation arrest, which is associated with the diffusion of aluminium, can indeed be used to indirectly observe the start of precipitation of AlN in cold worked low carbon Al-killed strip steels as:

$$\frac{\left(P_{start} - Z_{start}\right)}{\left(P_{start} - P_{finish}\right)} \rightarrow 0 \qquad (13.4)$$

and

$$\frac{\left(P_{finish} - Z_{finish}\right)}{\left(P_{start} - P_{finish}\right)} \rightarrow 0 \qquad (13.5)$$

where P_{start} is the AlN precipitation start time, Z_{start} is the recrystallisation arrest start time, P_{finish} is the AlN precipitation finish time and Z_{finish} is the recrystallisation arrest finish time.

Figure 12.15 may, therefore, represent a reasonable estimate of the TTT-diagram for the precipitation of AlN in ferrite in cold worked material, as measured indirectly from this arrest-effect.

Since this method of estimating the TTT diagram for AlN is based on the recrystallisation arrest effect, the end of the arrest, Z_{finish} may not necessarily mean the end of growth by supersaturation i.e. the AlN precipitation finish time P_{finish} (which is generally

included in the classical process of nucleation) but it does represent the end of "particle effectiveness" which is due to coarsening and may, therefore, reasonably represent the end of the precipitation process.

13.4.2 Recrystallisation in an as-quenched condition of the steels with various nitrogen and sulphur contents

Steels HS140-104 , LS70-38, LS2-65 and HS90-12 were solution treated at 1300 °C for 12 minutes to dissolve both the AlN and MnS and quenched into water (see figure 10.1), cold worked 70 percent, and isothermally annealed at 610 °C to induce static recrystallisation.

At the beginning of the isothermal annealing process directly after quenching from solution treatment, both the aluminium and the nitrogen were in solid solution and the volume fraction of the precipitated AlN during the isothermal annealing process can be predicted from the equilibrium solubility of AlN in ferrite which is given in equation 13.3 (log[%Al][%N] = 6.061-14442/T) and it is found to be less than 1 ppm of nitrogen in solid solution at a temperature of 610 °C.

Sennour et al[38] also observed that the AlN had a stoichiometric composition and with this information the volume fraction of precipitated AlN can be estimated. Assuming that the volume fraction of the other alloying elements in solution in these steels

are negligible compared with that of iron, the volume fraction V_v of the AlN is given by:

$$V_v = \frac{(m/\rho)_{AlN}}{(m/\rho)_{Fe} + (m/\rho)_{AlN}} \qquad (13.6)$$

where m and ρ are the weight percentages and the densities of the respective elements. The densities of iron and AlN are taken as 7.8 and 3.2 g cm^{-3} respectively.

The estimated volume fractions V_v of the precipitated AlN during isothermal annealing at 610 °C in the four steels that were studied in this series, are given in table 13.3 below.

In this study, the recrystallisation arrest was observed in the steels with nitrogen content of 65 ppm and above while none was observed for the steels with nitrogen content of 38 ppm and less. Assuming that nucleation by site saturation condition was met and that during the early stages of nucleation and growth of the AlN, the mean particle size for all four steels in table 13.3, did not vary much from steel to steel, then the difference in the Zener pinning effect, which is governed by the ratio (V_v/r), would be proportional to the volume fraction V_v of the particles which, in turn, is dependent on the chemical composition of the steel. Therefore, it is not surprising that no recrystallisation arrest was observed in the lower nitrogen steels LS70-38 and HS90-12 with AlN volume fractions of only 2.67×10^{-4} and 8.4×10^{-5} respectively, see figures 12.11 and 12.16.

Chapter 13 Discussion

Table 13.3: Estimated volume fraction V_v of the precipitated AlN during isothermal annealing at 610 °C in 70 percent cold worked steels HS140-104, LS70-38, LS2-65 and HS90-12.

Steel	N (%wt)	Al (%wt) (acid soluble)	Estimated V_v ($x10^{-4}$)
HS140-104	0.0104	0.047	7.29
LS2-65	0.0065	0.037	4.56
LS70-38	0.0038	0.02	2.66
HS90-12	0.0012	0.039	0.84

It also needs to be recognised that within the isothermal annealing temperature range of 550 to 700 °C, there must have been other alloying elements which were diffusing out of solid solution as well, among them manganese, copper and sulphur, see figure 5.1. However, it has been observed from this work that in low nitrogen but high sulphur material, for instance in steel HS90-12 with a very low volume fraction of AlN (8.4×10^{-5}), there was no recrystallisation arrest, see figure 12.16. This suggests that it was the AlN precipitation alone that was responsible for the recrystallisation arrest that was observed in the medium to high nitrogen steels, HS140-104 and LS2-65 where the volume fraction V_v of AlN was sufficiently high ($V_v \geq 4.555 \times 10^{-4}$) to provide an effective arrest.

The results in figure 12.16 also show that the steels with a lower sulphur content in solid solution, i.e. steels LS2-65 and LS70-38, despite having higher a nitrogen content than steel HS90-12,

recrystallised at earlier times compared to the steels with higher sulphur content, such as steels HS140-104 and HS90-12. The advantage of a lower nitrogen content with regards to a faster recrystallisation process in steel HS90-12, was completely overshadowed by the higher sulphur content in solid solution. This observation is in agreement with the results of Jolley et al[120] that the sulphur content in solid solution retards the start of the recrystallisation process by segregating to dislocation sub-boundaries and recrystallisation fronts in low carbon-manganese steels, see the earlier figure 7.2. However, as was observed in this work, the sulphur does not necessarily cause a complete recrystallisation arrest as in the case with the nucleation ("clustering") of AlN. It appears that the higher sulphur content affected the incubation period of the recrystallisation process through boundary drag rather than affecting the kinetics as the Avrami exponents for both the low and high sulphur content steels were the same, i.e. $n \approx 1$ see figure 12.17, but the values for the MAJK constant k differed significantly; 0.18 for the low sulphur content steel LS2-65 and 0.042 for the higher content one, steel HS140-104.

13.4.3 Modelling the Zener drag force P_z in steel HS140-104 in the as-quenched and cold worked condition during isothermal annealing at 610 °C

The loss in Zener pinning effect as the annealing time is extended can be explained in terms of the ratio (V_v/r) which governs the Zener pinning effect as illustrated with steel HS140-104 that was solution treated at 1300 °C for 12 minutes, quenched into water, given a 70 percent cold deformation and isothermally annealed at 610 °C, see figure 13.2 below.

In this model, it has been assumed that all the nuclei with the estimated critical radius $r^* = 3$ nm were activated in the early stages of precipitation in what is called site saturation and that $r^* = r_o$, i.e. although the particles were very small, at time $t < P_{z(start)}$ time the volume fraction V_v was also very small $(V_v \rightarrow 0)$ and, therefore, $P_z \approx 0$. The time dependent mean particle size has been estimated by equation 4.12 $(\ln(r - r_o) = 16.4+0.85\ln(t)-14433/T)$ while the precipitation volume fraction V_v and its corresponding precipitation time has been obtained from the TTT-diagram in figure 12.15. The MAJK model for precipitation kinetics has been assumed for the transformation time between 2 and 12 minutes during the isothermal annealing process at 610 °C, and working backwards, the following expression was obtained for the volume fraction X of recrystallised material in a time t in minutes:

Chapter 13 Discussion

$$X = 1 - \exp(-0.0232t^{1.96}) \qquad (13.7)$$

The Avrami exponent of n =1.96 is in agreement with the values of between 1.4 to 2.3 which Brahmi et al[144] found in an Fe-Al-N alloy.

For Zener pinning to be effective in arresting the recrystallisation process, P_z must be above a certain critical value. In the case of the recrystallisation arrest in figure 12.12 that was observed in steel HS140-104 in the as-quenched and cold worked condition during isothermal annealing at 610 °C, the estimated critical value for P_z must be above 0.53 J mol^{-1}, see figure 13.2 below. This value may vary depending on the isothermal annealing temperature and steel composition.

As mentioned earlier, the nucleation of the AlN is over relatively quickly with effective recrystallisation arrest through Zener pinning setting in soon thereafter. The curved dashed line in figure 13.2 may, however, be a better representation of the time dependent Zener-pinning force P_z than the solid curve which was obtained from the MAJK model through equation 13.7 ($X = 1 - \exp(-0.232t^{1.96})$ which possibly underestimates the precipitation rate of the AlN. The observed early start of the recrystallisation arrest is enough evidence that there is an adequate volume fraction of AlN to induce an arrest.

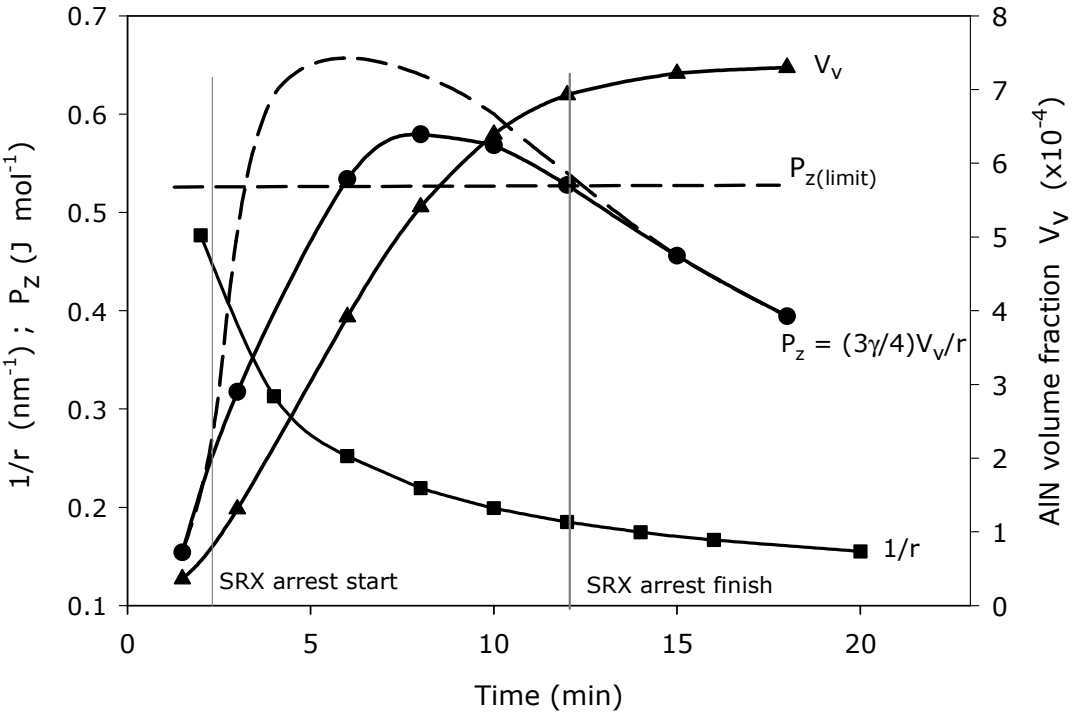

Figure 13.2: The time dependent particle volume fraction V_v, the inverse of the particle radius 1/r, and the Zener drag force $P_z = (3\gamma/4)(V_v/r)$ modelled for steel HS140-104 at 610°C after solution treatment at 1300°C, quenching into water and 70 percent cold work.

As may be seen from figure 12.12, the recrystallisation arrest times decrease with an increase in the isothermal annealing temperature. This may be attributed to the faster diffusion rates that accelerate both the recrystallisation process and the precipitation and coarsening rate of the AlN, with the latter leading to lowering of the pinning force and, therefore, to the end of arrest.

Chapter 13 Discussion

Using equation 4.12 ($\ln(r - r_o) = 16.4+0.85\ln(t)-14433/T$) that predicts the particle size as a function of time t (recrystallisation arrest time) and isothermal annealing temperature T and assuming that the end of recrystallisation arrest coincides with the end of isothermal nucleation of the AlN, and from the predicted volume fractions of AlN particles V_v (that are assumed constant) and given in table 13.3 above, the Zener drag force P_z can be modelled for steel HS140-104 in the as-quenched and cold worked condition during isothermal annealing at various temperatures. The modelled time and temperature dependent Zener-pinning force P_z at the point when it becomes ineffective is given in figure 13.3 below.

As may be seen in figure 13.3, the modelled Zener drag force P_z increased with an increase in annealing temperature and reached a peak at about 610 °C and started declining as the isothermal annealing temperature was increased further. The practical implication of this observation is that for the Zener pinning force P_z to cause recrystallisation arrest, it must lie at least above the "non-arrest" point on the curve.

The value of P_z is dependent on the particle radius $r_{(t)}$ which is dependent on temperature and time as:

$$P_z = \left(\frac{3\gamma_s}{4}\right)\left(\frac{V_v}{r_o + \exp\left[16.4 + 0.85\ln(t) - \frac{14433}{T}\right]}\right) \qquad (13.8)$$

where $r_o = r^*$ and the rest are as defined in equations 4.12 and 6.14.

The value of r in equation 4.12 ($\ln(r - r_o) = 16.4+0.85\ln(t)-14433/T$) is dependent on the isothermal annealing time (during recrystallisation arrest) t and the temperature T. Since at low isothermal annealing temperatures (<580 °C), recrystallisation can only resume when the values of P_z are low, this leads to longer recrystallisation arrest times (apparent incubation period when precipitation precedes recrystallisation) in order to allow the particles to become ineffective by coarsening. Although the Zener-pinning effect is low at lower isothermal annealing temperatures, it is still effective because of a lower diffusion and coarsening rate of the AlN particles.

The values of P_z increase with a decrease in isothermal annealing time and an increase in temperature respectively, as the AlN particle radius r is a function of both of them, until a peak is reached at about 600 °C. The decline in the values of P_z at temperatures higher than 610 °C could be attributed to the faster growth rate and coarsening rate of the AlN particles at higher isothermal annealing temperatures due to higher diffusivity of the aluminium atoms, leading to smaller values of $V_{v/}r$ again.

The observed peak in the Zener-pinning effect in figure 13.3 below has no significant practical (industrial) application as the AlN particle size in an as-coiled condition is influenced by the coiling temperature and the chemical composition of the steel.

Chapter 13 Discussion

Although the Zener-pinning force may not be substantially effective in an as-coiled condition in medium to high sulphur content steels (as it will be learnt later), the modelled results in figure 13.3 still paint a picture of its variation with isothermal annealing temperature at a time when the Zener-pinning loses its effectiveness and the recrystallisation resumes after the arrest, i.e. the point at which the AlN particles have coarsened large enough to render the Zener-pinning ineffective.

Table 13.4: Isothermal annealing temperatures and times, the modelled particle radii $r_{(t)}$ and their corresponding modelled Zener drag force P_z in J m^{-3} at the point when the recrystallisation resumes after the arrest.

Temperature (°C)	Time (min)	$r_{(t)}$ (nm)	Pz = $(3\gamma/4)(V_v/r)$ (kJ m^{-3})
640	8	14.5	35.87
625	10	13.94	38.60
610	12	8.71	43.40
580	36	21.54	30.40
550	240	77.0	11.28

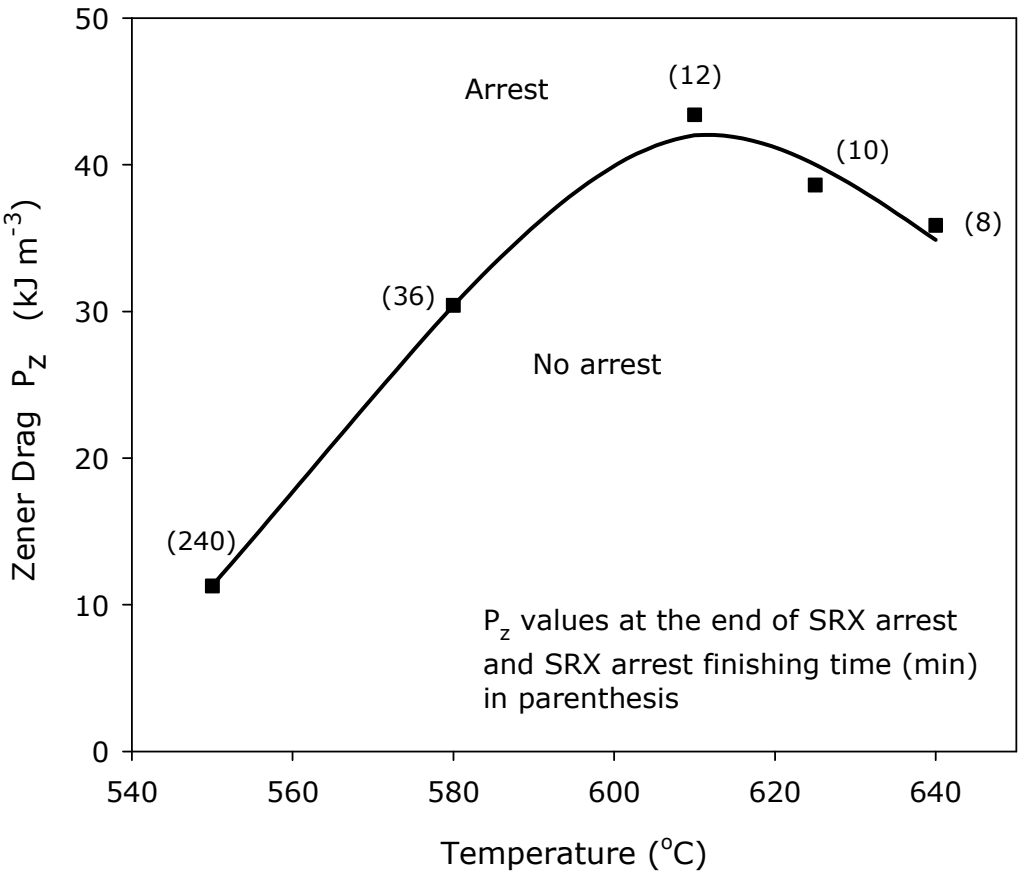

Figure 13.3: Estimated temperature and time dependent Zener drag force $P_z = (3\gamma/4)(V_v/r)$ for as-quenched steel HS140-104 at times t (in parenthesis) when the recrystallisation resumes after the arrest.

13.5 Recrystallisation behaviour in an as-coiled condition

This study was carried out on steels HS14-104, LS70-38 and LS2-65, which were hot rolled and coiled according to the schedule in table 11.1 and the heat treatment in figure 11.1. There were two parameters which were varied in this study; the coiling

temperature and the sulphur content. Two coiling temperatures were employed, i.e. 600 and 650 °C while the sulphur content varied from 2 to 140 ppm.

13.5.1 Quantitative results of the recrystallisation behaviour in an as-coiled condition

In this series of tests, steels HS140-104, LS70-38 and LS2-65 were solution treated at 1150°C for 10 minutes, hot deformed in the temperature range from 1100 to 900 °C to a total strain of 1.15, cooled at 80 °C s^{-1} to two different simulated coiling temperatures of 600 and 650 °C for 1 hour, cold worked 70 percent at room temperature and then isothermally annealed at 610 °C.

In figure 12.18, the recrystallised volume fraction at 610°C is plotted against the isothermal annealing time in the as coiled steels HS140-104, LS70-38 and LS2-65. As may be seen, in all three steels a higher coiling temperature shifted the recrystallisation process to earlier times. The higher coiling temperature did not only promote the precipitation of AlN but its coarsening as well which, in effect, reduced the Zener pinning effect on the dislocation sub-boundaries and the recrystallisation fronts.

It is also evident from figures 12.18 and 12.19 that for both coiling temperatures of 600 and 650 °C, the recrystallisation

process was shifted to longer times as the sulphur content decreased. In general, the recrystallisation start time $t_{5\%}$ increased with a decrease in the sulphur content. The sensitivity in $t_{5\%}$ to sulphur content was exacerbated by a decrease in coiling temperature to 600°C after simulated hot rolling, as the recrystallisation start time $t_{5\%}$ for the low sulphur steel LS2-65 was two orders of magnitude higher than that for the high sulphur content steel HS140-104.

As may be seen from figure 12.19, the parameter that contributed to the variations in the recrystallisation behaviour between the low and high sulphur steels was the Avrami constant k (it varied from 3.7×10^{-1} to 8.2×10^{-5} for the steels that were coiled at 600 °C) rather than the exponent n (which was $n \sim 2$ for all the three steels) as there was no large variation in the latter among these steels.

In the MAJK equation, the constant k comprises the shape factor of the nucleus, nucleation frequency and growth rate of the new grains. In both groups of steels, it was observed that nucleation of recrystallisation was by a SIBM mechanism. Since it is suggested that there is no nucleation of thermally activated embryos in this nucleation mechanism[94,99.100], the Avrami constant k in this case will strongly depend on the initial growth rate of the pre-existing recrystallisation interfaces and not on the nucleation rate per se and secondly, it will depend on how these developing "nuclei" interact with any second phase particles[89,117] that may also provide effective pinning.

Chapter 13 Discussion

This is presented schematically in figure 13.4 below in which the pre-existing recrystallisation interfaces of the low sulphur content steel are shown to take longer to grow into a critically sized "nucleus" of hemispherical shape for further growth into new recrystallised grains. The presence of the finer AlN particles in this steel reduces the net driving force for growth of these pre-existing recrystallisation interfaces through the Zener pinning effect. As was observed in the as-quenched condition above, complete recrystallisation arrest occurred in the instances where the Zener drag force P_z was greater than the net driving force for recrystallisation, equation 6.15 ($(P_{Rx} + P_c) > P_z$).

Messager et al[156] observed that the growth of dislocation sub-boundaries was more sensitive to the levels of impurities (solute atoms) through "solute drag" effects than the dislocation rearrangement during the annealing process of cold worked aluminium. In these steels studied here, instead of solute atoms, fine AlN particles are likely to have been responsible through Zener drag for the slow growth rate of the pre-existing recrystallisation interfaces in the low sulphur content steel LS2-65, thereby providing a longer effective "incubation" time. This arose in this particular steel because of a lack of MnS particles, which "forced" the nucleation of AlN to be effectively homogeneous and thus to be very fine particles.

13.5.2 Modelling the minimum value of L and the net driving force for recrystallisation P_{Rx} in steels HS140-104 and LS2-65 in an as-coiled condition

If pinning of recrystallisation interfaces by particles is the effective SIBM initiating mechanism, the recrystallisation process will be thermodynamically possible if the actual pinning distance in the steel $L_{act} > L_{min}$ where L_{min} is the minimum L value given by $L_{min} = 2\gamma_{gb}/\Delta G_{Rx}$ and ΔG_{Rx} is the driving force for recrystallisation and γ_{gb} is the surface energy of the moving interface. For the same amount of deformation energy in both steels, ΔG_{Rx} will be the same and, therefore L_{min} is given by:

$$L_{\min} = \frac{2\gamma_{gb}}{\Delta G_{Rx}} = \frac{2\gamma_{gb}}{\left(\alpha G_m b^2 N_d\right)} = 2.3\ \mu m$$

for values of $\alpha = 1$, shear modulus for iron $G_m = 8.6 \times 10^{10}$ Pa, Burger's vector for iron $b = 2.48 \times 10^{-10}$ m, estimated dislocation density for cold deformed metal $N_d = 10^{14}$ m^{-2}, ($\Delta G_{Rx} = 528$ kJ m^{-3}) and the grain boundary surface energy of $\gamma_{gb} = 1.0$ J m^{-2}.

The fact that the recrystallisation process was able to take place in both steels is enough evidence that $L_{act} > L_{min}$ and was somewhere between $L_{min} = 2.3$ μm and the observed subgrain diameter of about 5 μm (see figure 12.22). However, the kinetics of the growth of the pre-existing recrystallisation interfaces was significantly different between the two steels because in steel

Chapter 13 Discussion

HS140-104, the subgrain diameter of about 5 μm was observed after about 2 minutes while in steels LS2-65 it was found only after 240 minutes at 610°C.

The net driving force for recrystallisation P_{Rx} is given by[166]:

$$P_{Rx} = P_d - \frac{3\gamma_s V_v}{4r} - \frac{2\gamma_{gb}}{L} \qquad (13.9)$$

where P_d is given by equation 6.11, i.e. $P_d = \alpha G_m b^2 N_d$ and the rest are as previously defined in equations 6.10 and 6.14.

As may be seen from equation 13.9, recrystallisation in the SIBM mechanism will only proceed when $P_{Rx} > 0$ i.e:

$$\left|P_d\right| \geq \left|\frac{3\gamma_s V_v}{4r} + \frac{2\gamma_{gb}}{L}\right| \qquad (13.10)$$

Assuming that the values for the interface energies for the incoherent particle-matrix interface and the high angle grain boundary are $\gamma_s = 0.75$ J m^{-2} the values for P_d for the respective steels can be modelled as follows:

$$P_{d(LS2\text{-}65)} \geq \frac{3(0.75)(4.555\text{x}10^{-4})}{4(7.5\text{x}10^{-9})} + \frac{2\gamma_{gb}}{L_{act\text{-}LS2\text{-}65}}$$

$$\geq 34{,}000 + \frac{2\gamma_{gb}}{L_{act\text{-}LS2\text{-}65}}$$

Chapter 13 Discussion

and

$$P_{d(HS140\text{-}104)} \geq \frac{3(0.75)(14.665x10^{-4})}{4(57.5x10^{-9})} + \frac{2\gamma_{gb}}{L_{act\text{-}HS140\text{-}104}}$$

$$\geq 14{,}350 + \frac{2\gamma_{gb}}{L_{act\text{-}HS140\text{-}104}}$$

With finer AlN particles in steels LS2-65, $L_{act\text{-}LS2\text{-}65}$ is expected to be smaller than $L_{act\text{-}HS140\text{-}104,}$ thus, assuming that the bulge is anchored by particles rather than the subgrain boundaries, i.e. $L = (4(1\text{-}V_v)r/3V_v)$ as observed by Corti et al[164]. Therefore, assuming that the grain boundary surface energy γ_{gb} is the same in both steels, steel LS2-65 will require a higher driving force P_d for recrystallisation for the condition $P_{Rx} > 0$ to be met.

The growth rate (movement) of the recrystallisation front is given by equation 6.12 ($v_B = mP_{Rx}$) and is governed not only by the mobility m of the recrystallisation front but also by the net driving force for recrystallisation P_{Rx} as well. Therefore, for the same amount of deformation energy ($\Delta G_{Rx} = P_d = \alpha G_m b^2 N_d = 528$ kJ m^{-3}) in both steels, steel HS140-104 with the higher net driving force P_{Rx}, see equation 13.9 above, is expected to have a shorter "apparent" incubation time than steel LS2-65 and this was exactly what was observed in this study. Figure 13.4 is a schematic illustration of the initial slow growth rate of the pre-existing recrystallisation interfaces of the two steels.

Chapter 13 Discussion

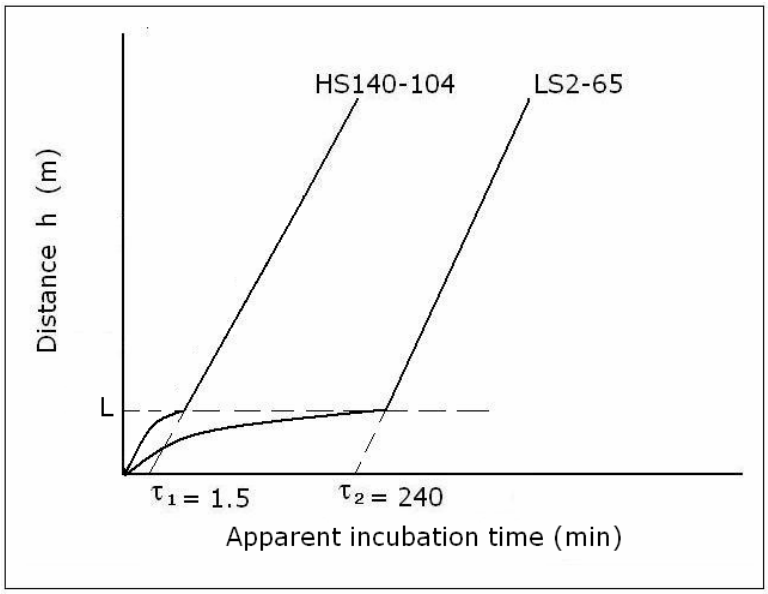

Figure 13.4: Schematic presentation of the apparent incubation time due to the initial slow movement of the recrystallisation fronts in steels HS140-104 and LS2-65 which were coiled at 600 °C and isothermally annealed at 610 °C, where $L \approx L_{min}$.

In steel HS140-104, with a dispersion factor (V_v/r) of 0.26 μm^{-1}, the recrystallisation process proceeded normally while in steel LS2-65 with a dispersion factor of 0.61 μm^{-1}, it was impeded through a longer apparent incubation period. Previous workers[165,166] on the recrystallisation of aluminium-silicon alloys observed that the early growth towards a hemisphere of the pre-existing recrystallisation interface in the SIBM mechanism, was impeded for a dispersion factor (V_v/r) > 0.2 μm^{-1}.

13.5.3 Nucleation of the recrystallised grains

In both the low and high sulphur content steels LS2-65 and HS140-104 respectively, it was observed that the nucleation of new recrystallised grains occurred on subgrain boundries and in extensively deformed areas around cementite and pearlite colonies, see figures 12.22 to 12.24. As may be seen in these figures, the new recrystallised grains continued to grow into the deformed matrix by SIBM.

The carbon content for the two steels LS2-65 and HS140-104 was 0.051 and 0.047 weight percentage respectively and, therefore, since it was not a significant variable in these steels, the cementite and pearlite colonies present in these steels and possibly acting as potential nucleation sites for recrystallisation similarly to the PSN mechanism observed in Fe-0.033%O alloy[167], may not have been different between these two steels. Hence, the availability of nucleation sites may not be one of the contributing factors to the observed difference in the recrystallisation behaviour of the steels.

As was mentioned earlier in section 6.5.2, no new recrystallisation embryos are required for the SIBM mechanism because new recrystallised grains grow from pre-existing recrystallisation interfaces and, therefore, no activation energy $\triangle G^*$ for the nucleation of thermally activated embryos and a classical incubation period τ are required. It is, therefore, the initial growth rate of these pre-existing recrystallisation interfaces to grow to a size of $L_{act} > L_{min}$ that contributes to the difference in

recrystallisation behaviour of these two groups of steels; one with high and the other with low sulphur content. It was observed that the homogeneously nucleated finer AlN particles in the low sulphur steel LS2-65 were more effective in the pinning of the dislocations, dislocation sub-boundaries and the static recrystallisation fronts, see figures 12.19 and 12.25, hence, the difference in the "apparent incubation periods" from high sulphur content steels. As may be seen in these micrographs, the AlN particles in steel LS2-65 were so small that it was only their strain fields that could be observed in the thin foils, see figure 12.25 (b).

13.6 Heterogeneous nucleation of AlN on MnS particles during hot rolling and coiling at 600 and 650 °C in low carbon Al-killed steels with various sulphur content

In this series of metallographic analysis, the steels HS140-104, LS70-38 and LS2-65 were solution treated at 1150°C for 10 minutes, hot deformed in the temperature range from 1100 to 900 °C to a total strain of 1.15, cooled at 80 °C s^{-1} to two different simulated coiling temperatures of 600 and 650 °C for 1 hour, see table 11.1 and figure 11.1. The metallographic analysis was carried out in the as-coiled condition in order to investigate the status of the AlN in all these steels prior to cold working and isothermal annealing.

13.6.1 Precipitation of AlN on MnS and its effect on static recrystallisation after cold work

In the lowest sulphur content steel LS2-65 with an absence of any MnS, the AlN nucleated homogeneously in the matrix or heterogeneously on sub- or grain boundaries during coiling, see figures 12.30 and 12.31. It was observed that these AlN particles were not only very fine (<30 nm) but sparse and infrequent and this suggested that a greater volume fraction of them were so small that they could not easily be observed in the TEM due to a lower limit of detection of about 20 nm by thin foil. The TEP results showed that after coiling for 1 hour at 600 °C, the AlN had completely precipitated as no further precipitation could be observed afterwards; see table 12.2 and figure 12.27. As opposed to the as-quenched condition, no recrystallisation arrest was observed during the isothermal annealing process in the as-coiled condition and this suggests that either partial or full precipitation of AlN had already taken place during the 1 hour coiling at 600 °C and that the particles had already grown to beyond their "full arrest size".

In the medium to high sulphur content steels HS140-104 and LS70-38, the sulphur precipitated as coarse particles of [Mn,Cu]S/MnS and [Mn,Ti,V]S/MnS respectively. Some copper sulphide particles were also observed particularly in steel HS140-104. These sulphide particles, particularly MnS, were the favoured nucleation sites for the AlN and the heterogeneous nucleation encouraged its precipitation during the coiling process after hot rolling, see figures 12.28, 12.29 and 12.33. The result was that

the AlN in medium to high sulphur content steels was generally associated with coarse sulphides and, therefore, the mean particle size of the AlN/MnS compound particles in the as-coiled steel prior to cold working and annealing, was generally much coarser, i.e. between 50 and 300 nm see figure 12.32, than in the steels with low sulphur content. Hence, no pinning of the static recrystallisation fronts was observed in these steels as may be seen from figure 12.26.

In a study[162] on the optimization of the strain aging resistance in low carbon Al-killed strip steels with 80 to 90 ppm sulphur content and which were produced by continuous annealing, it was observed that the steels with a high Mn content (0.36%Mn) were less sensitive to strain aging than those with a low Mn content (0.16%Mn) at a coiling temperature of 620 °C. This was also attributed to the heterogeneous nucleation of the AlN on MnS which promoted the precipitation of the AlN. It was concluded that the low manganese steels had provided less nucleation sites for the precipitation of the AlN hence more nitrogen was in solid solution and, therefore, caused the strain aging. These findings can be linked to the sensitivity of the low sulphur content low carbon Al-killed strip steels to the coiling temperature vis-à-vis the sluggish recrystallisation behaviour of these steels. In the absence of sulphur in the steel, there are no MnS particles which are favoured sites for the nucleation of the AlN.

Mizui et al[163] observed that there is a range of manganese content which is favourable for the optimum heterogeneous

nucleation of the AlN on these MnS particles. According to this author, an excessive increase in the manganese content of the steel can result in coarsening of the MnS particles, decreasing the density of the favoured nucleation sites for the AlN. It was also observed that the precipitation of the AlN is accelerated by an increase in the manganese level which increases the activity of the nitrogen in ferrite. Since the optimization of the manganese and the sulphur content vis-à-vis the nucleation of AlN during coiling and the recrystallisation behaviour after cold work, was not within the scope of this study, it will not be discussed further.

Although the Zener drag effect is governed by the ratio of the volume fraction of the particles V_v to the mean particle radius r (V_v/r) as stated above, in the case of the coarse MnS/AlN compound particles in the medium to high sulphur content steels it is not the V_v that matters but the particle radius r as a larger value renders the Zener drag force ineffective. Consequently, unlike in the high sulphur steels, the finer AlN particles in the low sulphur steel were more effective in retarding the recrystallisation process through the Zener pinning of the dislocation sub-boundaries and the moving static recrystallisation fronts, particularly during the early stages of the recrystallisation process before the AlN particles had coarsened and had lost their pinning effectiveness. This was summarised in figures 12.21 and 12.32 in which it is evident that the sulphur content in these steels has an indirect effect on the recrystallisation start time $t_{5\%}$ though its influence on the particle size of the AlN. The empirical equations that relate the sulphur content in ppm to the static

recrystallisation start time $t_{5\%}$ in minutes in these steels are given in table 12.2 and are as follows:

$$t_{5\%} = 33.78\exp(-0.0345S) \text{ for } 600\ ^\circ C \qquad (13.11)$$

and

$$t_{5\%} = 0.99\exp(-0.008S) \text{ for } 650\ ^\circ C. \qquad (13.12)$$

13.6.2 Modelling of the $\triangle G_v$, $\triangle G^*$ and r^* for the nucleation of AlN, Cu_2S and MnS in austenite and ferrite

In order to understand the sequence of precipitation of the MnS, AlN and Cu_2S in these steels, it is necessary to know both the thermodynamics and the kinetics of the formation of these species. The kinetics are presented in the TTT-diagrams which are in figures 4.1, 4.2 and 5.1. The parameters that have been used to model the driving force $\triangle Gv$, activation energy $\triangle G^*$ and the critical radius r^* for the homogeneous nucleation of AlN, Cu_2S and MnS in austenite and ferrite, are given in table 13.5 below. The enthalpies of formation have been derived from the equilibrium solubility equation using equation 4.3 ($\triangle H = 1.15RA$). The activation energy $\triangle G^*$, the critical radius r^* and the driving force $\triangle Gv$ have been calculated from equations 3.5, 3.6 and 3.7 respectively and these parameters have been plotted as a function of temperature in figure 13.5 below.

Table 13.5: Parameter values for the calculations of ΔGv, ΔG* and r* for the homogeneous nucleation of MnS, AlN and Cu_2S in austenite and ferrite.

Compound	Solubility model	Parameter	Value	Ref.
MnS	$Log[\%Mn][\%S]=10.6-\frac{19427}{T}$ $Log[\%Mn][\%S]=4.092-\frac{10590}{T}$	ΔH_{aust} (J mol^{-1}) ΔH_{ferr}	82500 101300	66 157
		γ_{aust} (J m^{-2}) γ_{ferr}	0.712 1.024	158
		V_m (m^3 mol^{-1})	2.164 x10^{-5}	
		a (fcc) (nm)	0.522	
AlN	$Log[\%Al][\%N]=2.44-\frac{9490}{T}$ $Log[\%Al][\%N]=6.1-\frac{14442}{T}$	ΔH_{aust} (J mol^{-1}) ΔH_{ferr}	90800 138000	Present work 49
		γ_{aust} (J m^{-2}) γ_{ferr}	0.75 0.2	151
		V_m (m^3 mol^{-1})	1.28 x10^{-5}	
		a (fcc) (nm)	0.311	36
Cu_2S	$Log[\%Cu]^2[\%S]=26.3-\frac{44971}{T}$	ΔH_{aust} (J mol^{-1}) ΔH_{ferr}	286900 286900	159
		γ_{aust} (J m^{-2}) γ_{ferr}	0.83 0.2	160
		V_m (m^3 mol^{-1})	2.751 x10^{-5}	
		a (fcc) (nm)	0.522	62

Chapter 13 Discussion

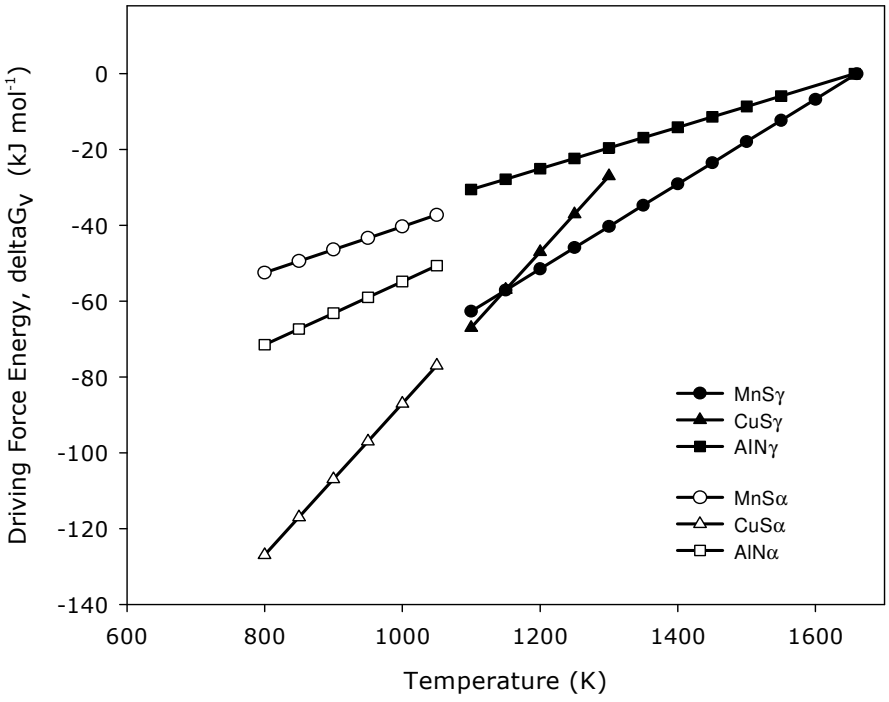

(a)

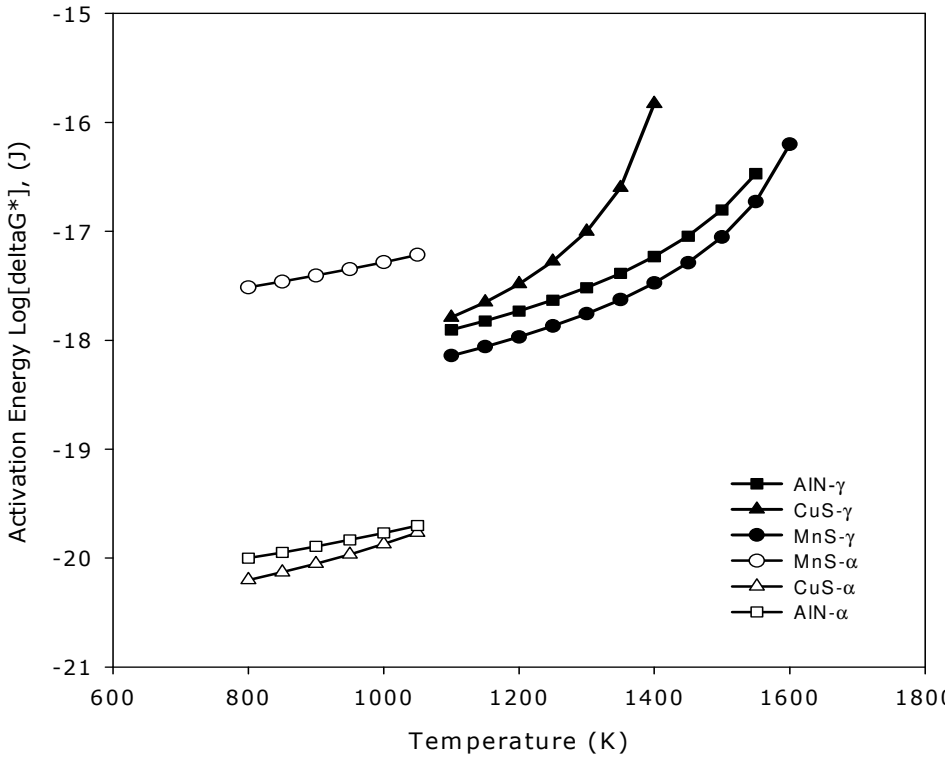

(b)

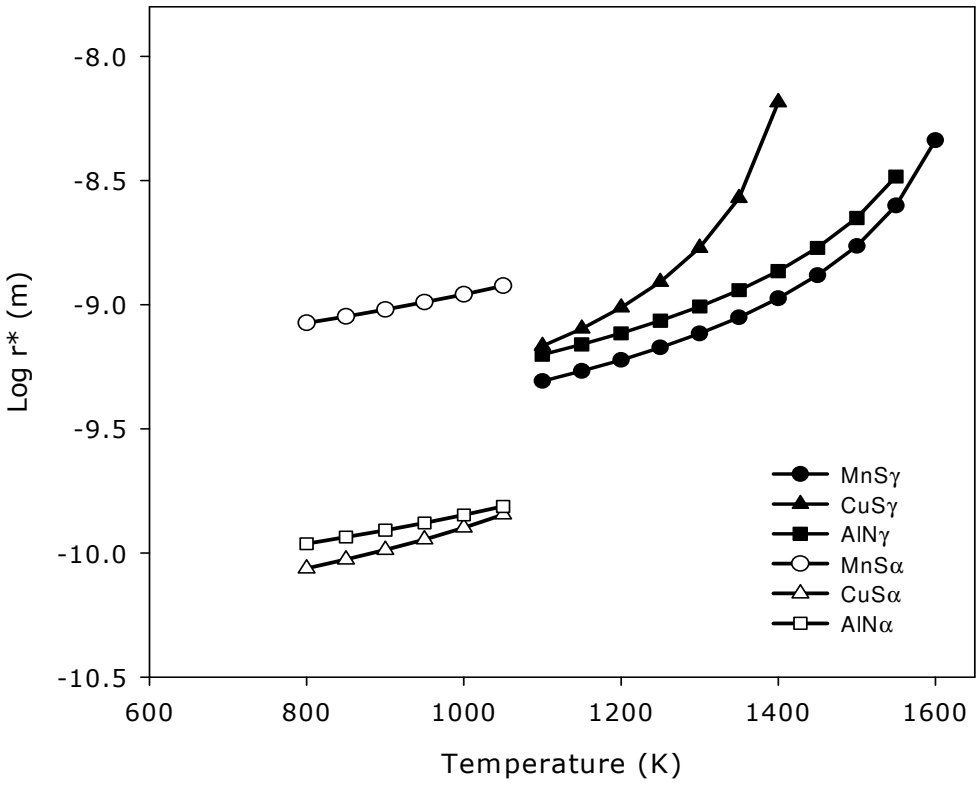

(c)

Figure 13.5: (a) Modelled driving force ΔG_v, (b) activation energy ΔG^* and (c) the critical radius r^* for the homogeneous nucleation of AlN, Cu_2S and MnS in austenite and ferrite. Solid symbols are for austenite and open ones for ferrite.

The general conclusion from figure 13.5 may be that, on the one hand, it is easier for the AlN to precipitate in α-ferrite than in austenite as both the activation energy ΔG^* and the critical radius r^* are less by two orders of magnitude while the driving force ΔG_v is higher by 20 kJ mol^{-1} compared with the values for MnS. On the other hand, it is easier for the MnS to precipitate in austenite as the activation energy ΔG^*, and the critical radius r^* are less while the driving force ΔG_v, is higher than those of the

Chapter 13 Discussion

AlN. This confirms the previous observations from other workers that AlN forms readily in ferrite without any incubation period being observed due to the higher diffusivity of aluminium and low lattice misfit δ attained through the Bain orientation between the α-ferrite matrix and the cubic (NaCl type) crystal structure AlN[11,44,66]. As others have suggested, the nucleation of AlN within austenite is limited by the nucleation barrier of hcp AlN in austenite[44].

Thermodynamically, it is known that MnS forms at higher temperatures than AlN and is normally present first upon cooling, see the ThermoCalc results in figure 12.4. As may be seen in figure 13.5 (b) and (c), AlN may precipitate easier in austenite than Cu_2S does as both ΔG^* and r^* are less for the latter. Therefore, it is logical to conclude that the AlN generally rather precipitates heterogeneously on MnS as found here and by others[52,60,162,163]. The crystallographic orientation relationship between the AlN and the MnS was found to be $(1\bar{1}1)_{MnS}//(0001)_{AlN}$ and $[110]_{MnS}//[2\bar{1}\bar{1}0]_{AlN}$ (see figure 12.33) as observed by others[52].

14. 1 Conclusions

The following conclusions were drawn from this study:

14.1.1 Low carbon Al-killed strip steels in the as-quenched condition

- The TEP technique was successfully used to study the equilibrium solubility of AlN during reheating of low carbon Al-killed strip steels ranging from low to high sulphur content and it was found that the sulphur content does not influence the equilibrium solubility of the former, thus, regardless of the association of the AlN with the MnS in the medium to high sulphur content steels. The equilibrium solubility equation thus obtained was determined as:

$$\text{Log}[\%\text{Al}][\%\text{N}] = 2.6 - \frac{9710}{\text{T}}$$

where the aluminium and the nitrogen contents are in weight percentages and T is the absolute solution temperature in Kelvin.

- During solution treatment at 1150 °C, the equilibrium dissolution of AlN in these steels was, in general, attained after soaking for 5 minutes or more. It may, therefore, be concluded that AlN dissolves relatively quickly in low carbon Al-killed strip steels during a solution or reheating treatment, regardless of the process route, i.e. whether it is the cold charge or hot charge route.

- In the as-quenched condition of both the low and high sulphur content Al-killed steels, a recrystallisation arrest was found at some isothermal annealing temperatures. The recrystallisation arrest was associated with the diffusion of aluminum atoms with an activation energy of the process that led to the arrest, being 230 kJ mol^{-1}. This is reasonably close to the published activation energy for the diffusion of aluminium in ferrite. The arrest appeared to be caused by Zener pinning by the precipitating AlN and was not affected by the sulphur content of the steel in solid solution. Recrystallisation arrest occurred in these steels with an estimated volume fraction of AlN particles of 4.6 $x10^{-4}$ or more and not in steels with a volume fraction of 2.7 $x10^{-4}$ or less.

- The total time over which arrest occurred, was a function of the annealing temperature and the termination of arrest and resumption of recrystallisation appeared to be governed by the end of precipitation of any new AlN and/or its coarsening to a point where the Zener pinning force $P_z = f(V_v/r)$ became ineffective. For steel HS140-104, in the as-quenched condition and during isothermal annealing at 610 °C, this was found to be $P_z \leq 0.53$ J mol^{-1} (41.2 kJ m^{-3}).

- The recrystallisation arrest was only observed in the medium to high nitrogen content steels with the volume

fraction $V_v \geq 4.56 \times 10^{-4}$ or a nitrogen content of about 65 ppm and higher.

- Since the start and termination of recrystallisation arrest appeared to be linked to the precipitation of the AlN, it was possible to derive an estimated TTT-diagram from the arrest data in those steels where this effect was found.

- In the as-quenched condition and through Johnson-Mehl-Avrami-Kolmogorov plots, it was established that the incubation time of the recrystallisation process increased with an increase in sulphur content in solid solution of the steels. However the kinetics of the recrystallisation process were not influenced by the sulphur content with a JMAK exponent of $n \approx 1$ for all the steels tested and neither was the sulphur content associated with the arrest phenomenon. Consequently, the recrystallisation process was shifted to longer times with an increase in sulphur content in solid solution, possibly through sulphur drag as has been suggested by others.

14.1.2 Low carbon Al-killed strip steels in the hot deformed and as-coiled condition

- In a hot deformed and as-coiled condition where the sulphur had precipitated fully as MnS before the recrystallisation started, the JMAK incubation period of the recrystallisation process decreased with an increase in the sulphur content of the steel. This was found to be due to the MnS particles that are the favoured nucleation sites for the AlN and the

heterogeneous nucleation enhanced the precipitation of the latter. The resulting compound and coarse AlN/MnS particles were generally ineffective in pinning any dislocation sub-boundaries and recrystallisation fronts and consequently had little or no effect on the recrystallisation process.

- In the very low sulphur content steels, however, the absence of any significant quantities of MnS forced the AlN to nucleate as much finer particles on dislocations and subgrain boundaries where effective Zener pinning was once again observed, leading to a much delayed start of recrystallisation but not to any actual recrystallisation arrest.

- The sensitivity of the recrystallisation start time (JMAK incubation time) to the sulphur content increased with a decrease in the coiling temperature as the finer homogeneously nucleated AlN particles remained smaller at the lower coiling temperatures (~ 600°) due to a slower coarsening rate. The sulphur (ppm) dependent empirical expressions for the recrystallisation start times $t_{5\%}$ at isothermal annealing temperature of 610 °C for steels coiled at temperatures of 600 and 650 °C were found to be:

$t_{5\%} = 33.78\exp(-0.0345S)$ for 600 °C and

$t_{5\%} = 0.99\exp(-0.008S)$ for 650 °C.

- The kinetics of the recrystallisation process were not influenced by the sulphur content with a JMAK exponent of $n \approx 2$ for all the steels tested. However, it was the JMAK constant k that differed much with the sulphur content and the coiling temperature, decreasing with the decrease in either one or both of them.

- The sulphur content in these hot worked and coiled low carbon Al-killed strip steels, therefore, plays an indirect role in the recrystallisation process after cold work by affecting the mode of nucleation of the AlN, thereby, making it either effective or ineffective in its Zener pinning force on moving recrystallisation fronts. This finding is, therefore, the main reason for the large differences found within industry in the recrystallisation behaviour of nominally equivalent steels but with varying sulphur contents, an observation that originally led to this study.

14.2 Recommendations

The following recommendations were also drawn from this study:

- Tentatively, a medium to high sulphur content of 50 to 100 ppm would be appropriate to solve the "sluggish" recrystallisation problem in these steels. However, a comprehensive study to optimize the sulphur content vis-à-vis the kinetics of the recrystallisation process and the

mechanical properties, particularly deep drawability, would be valuable.

- A higher coiling temperature (~ 650 °C) would help to alleviate the problem; however, there is a limit in taking this route because there are usually temperature gradients in the coil, with the outer wraps and the edges being cooler than the center. Higher coiling temperatures may also result in difficulties in the removal of scale from the coiled strips. Hence, increasing the sulphur content seems to be a better option.

- Since the sulphur content both directly and indirectly affects the recrystallisation behaviour of these low carbon Al-killed strip steels, there is a likelihood that the recrystallisation texture of these steels may be affected as well. Therefore, a study of the influence of the sulphur content on the development of the recrystallisation texture in these steels would be appropriate.

- In the medium to high sulphur content steels, the AlN is not only associated with MnS but with [Mn,Cu]S and [Mn,Ti,V]S complexes and it appears that there is an information gap in the literature in the understanding of the crystallographic orientation relationship of the AlN with these particles and whether their heterogeneous nucleation enhancement of the AlN may differ from that of MnS itself.

- In low sulphur content steels where the finer AlN plays a direct role in delaying the recrystallisation process, a study of the kinetics of coarsening of AlN would also be helpful as it may be used to optimise the coiling temperature vis-a-vis the subsequent cold worked recrystallisation behaviour.

References

1 BENTLEY, A. P., and von MOLTKE, T., IMMRI Report No. 25, 30th October 2001, not published.

2 STUMPF, W., "Grain size modelling of a low carbon steel during hot rolling in a Compact Strip Production (CSP) plant using the Hot Charge Route", The Journal of The South African Institute of Mining and Metallurgy, 2003, Vol. 103, pp. 617-631.

3 MUOJEKWA, C. A., JIN, D. Q., SAMARASEKERA, I. V., and BRIMCOMBE, J. K., "Thermomechanical History of Steel Strip during Hot Rolling-A Comparison of Conventional Cold Charge Rolling and Hot Charge Rolling of Thin Slabs", 37th MWSP Conference Proceedings, ISS, 1996, Vol. XXXIII, pp. 617-631.

4 STUMPF, W. E., "Hot work modelling of two equivalent low carbon strip steels produced respectively by the Cold Charge Route and by Hot Charge Route" to be published.

5 BARDES, B. P., ed. Properties and Selection: Iron and Steels, Metals Handbook Ninth Edition, Vol. 1, (1978), pp.153.

6 BLICKWEDE, D. J., Trans. A.S.M., Vol. 61, (1968), pp. 653.

7 DUCKWORTH, W. E. and BAIRD, J. D., J. Iron Steel Inst., Vol. 207, (1969), pp. 861.

8 MEYZAUD, Y. and PARNIERE, P., Mémoires Scientifiques Rev. Mét., Vol. 71, (1974), pp. 423.

9 ZOLOTEREVSKY, N. Y., PLETENEV, V.P. and TITOVETS, Y. F., "Analysis of aluminium nitride precipitation proceeding concurrently with recrystallisation in low carbon steel",

References

Modelling and Simulation Materials Science Engineering, Vol. 6, (1998), pp. 383 – 391.

10 HUTCHINSON, W. B., "Development and control of annealing texture in low carbon steels", International metals Review, Vol. 29, No. 1, (1984), pp.25 - 41.

11 WILSON, F. G. and GLADMAN, T., International Materials Review, Vol. 33, (1988) pp. 221.

12 ESHELBY, J. D., Proc. Roy. Soc., Vol. A241, (1957), pp. 376; Prog. in Solid Mechanics, Vol. 2, (1961), pp. 89.

13 RUSSELL, K. C., in "Phase Transformations", ASM, (1970), pp. 219

14 DIETER, G. E., "Mechanical Metallurgy", New York, McGraw Hill Book Co., (1976).

15 NABARRO, F. R. N., Proc. Roy. Soc., Vol. A175, (1940), pp. 519

16 LeGOUES, F. K., AARONSON, H. I. and LE, Y. W., Acta Met. Vol. 32, (1984), pp. 1854

17 LeGOUES, F. K., AARONSON, H. I. and LE, Y. W., Acta Met. Vol. 32, (1984), pp. 1857

18 LeGOUES, F. K., AARONSON, H. I. and LE, Y. W. and FIX, G. J., Proc. Inter. Conf. on "Solid-solid Phase Transformations" Ed. AARONSON et al, Met Soc. AIME, Warrendale PA, (1983), pp. 427.

19 MATTHEWS, J. W., "Dislocations in Solids", Ed. NABARRO, F. R. N., Publ. North-Holland Co., Amsterdam, (1979), pp. 463.

20 SHIFLET, G. J., materials Science and Engineering, Vol. 81, (1986), pp. 61.

References

21 LARCHÉ, F. C., "Dislocations in Solids", Ed. NABARRO, F. R. N., Publ. North-Holland Co., Amsterdam, (1978), pp. 135; and in "Solid State Phenomena", Vol. 35 – 36, (1994), pp. 173.

22 CAHN, J. W., Acta Met. Vol. 5, (1957), pp. 169.

23 LYUBOC, B. Ya and SOLV'YEV, V. A., Fizika, Metall. Vol. 19, (1965), pp. 333.

24 DOLLINS, C. C., Acta Met. Vol. 18, (1970), pp. 1209.

25 BARNETT, D. M., Scripta Met., Vol. 5, (1971), pp. 261.

26 AARONSON, H. I. and LeGOUES, F. K., Met Trans. Vol. 23A, (1992), pp. 1915.

27 TURNBULL, D., J. Chem. Vol. 20 (1952), pp. 411, ibdi, 1956, Solid State Physics, Vol. 3 (Academic Press, New York) pp. 282.

28 LOTHE, J., and POUND, G. M., J. Phys. Vol. 36, (1962) pp. 2080.

29 WERT, C. A. and ZENER, C., Journal of Applied Physics, Vol. 21, (1950) pp. 5 and Journal Phys. Chem. Solids Vol. 6, (1958), pp. 335.

30 LIFSHITZ, I, M. and SLYOSOV, V.V., Journal of Phys. Chem. Solids, Vol. 19, (1961), pp. 35.

31 WAGNER, C., Zeitschrift für Elektrochem., Vol. 65, (1961), pp. 581.

32 HILLERT, M, Jernkorntorets Ann. Vol. 141, (1957), pp. 757.

33 AARON, H. B. and KOTLER, G., "Second Phase Dissolution", Metallurgical Transactions, Vol. 2, (1971), pp. 393 – 408.

34 WHELAN, M. J., Metal Science Journal, Vol. 3, (1969), pp. 95.

References

35 JEFFREY, G. A. and WU. V. Y., Acta Crystallography, Vol. 16, (1963), pp. 559 – 566.

36 HANSEN, M. and ANDERKO, "Constitution of Binary Alloys", 2nd edition, (1958), pp. 116, New York, McGraw-Hill.

37 KANG, Y., HAO, Y., JIE, F., WANG, K. and WANG, Z., "Morphology and precipitation kinetics of AlN in hot strip low carbon steel produced by compact strip production", Materials Science and Engineering A351 (2003), pp. 265 – 271.

38 SENNOUR, M. and ESNOUF, C., "Contribution of advanced microscopy techniques to nano-precipitates characterization: case of AlN precipitation in low carbon steels", Acta Materialia, Vol. 51, No. 4, (2003), pp. 943 – 957.

39 WEVER, F., KOCH, K., ILSCHNER-GENCH, C. and ROHDE, H.: Forsch. Wirts. Nordrhein-Westfalen, Vol. 409, (1957) pp. 1 – 6.

40 NISHIZAWA, T. "Thermodynamics of microstructure control by particle dispersion" ISIJ International, Vol. 40, (2000), pp. 1269 – 1274.

41 DARKEN, L. S., SMITH, R.P., and FILER, E. W., Trans. AIME, Vol. 191, (1951) pp. 1174.

42 LESLIE, W. C., RICKETT, R. L., DOTSON, C. L., and WATSON C. S., Trans. ASM, Vol. 46, (1954) pp. 1470 – 1497.

43 SHIMOSE, T. and NARITA, K., Tetsu-to-Hagané (J. Iron Steel Institute of Japan), 1954, Vol. 40, pp. 242 – 243.

44 KONIG, P., SCHOLZ, W. and ULMER, H., Arch. Eisenhüttenwes., Vol. 32, 8, (1961), pp. 541 – 550.

References

45 ERASMUS, L. A., J. Iron Steel Inst., 202, (1964), pp. 32 – 41.

46 GALDMAN, T. and PICKERING, F. B., J. Iron Steel Inst., Vol. 205 (1967) pp. 635 – 664.

47 MARYHOFER, M., Berg. Hüttenmänn Monatsh., vol. 120 (7), (1975), pp. 312 – 321 (BISI 13768).

48 HONER, K. E. and BALIKTAY, S.: in Proc. 44th Int. Foundry Cong. Florence, (1977) Paper 11, (BISI 26033).

49 CHENG, L. M., : PhD. Thesis, University of British Columbia, Vancouver, (1999).

50 YU, H., KANG, Y. L., DONG, H. B., LIU, D. L. and FU, J., Acta Metallurgica Sinica 15, (2002) pp. 375.

51 HILLERT, M and JONSSON, S., "An assessment of the Al-Fe-N system", Metallurgical Transactions A, Vol. 23A, (1992), pp. 3141 – 3149.

52 USHIODA, H., SUZUKI, H. G., KOMATSU, H. and ESAKA, K., "Influence of sulphur on AlN precipitation during cooling after solidification and resulting hot shortness in low carbon steel", Nihon Kinzoku Gakkai shi, J. Japan Inst. Metals, Vol. 59, No. 4 (1995), pp. 373 – 380.

53 BEEGHLY, H. F., Anal. Chem., Vol. 21, No. 12, (1949) pp. 1513 – 1519.

54 VIGNES, A., PHILEBERT, J., BADIA, M. and LAVASSEUR, J., Proc. 2nd Natl. Conf. Microprobe Analysis, Boston, 1967, Paper 20.

55 FAST, J. D., Interaction of Metals and Gases, London, Publ. MacMillan New York, (1976), pp. 221.

References

56 KOZESCHNIK, E.: PhD. Thesis, Technical University Graz, Graz, (1997).

57 DUTTA, B., VALDERS, E. J. and SELLARS, C. M., Acta Metall. Mater. Vol. 40, (1992) pp. 653.

58 DUTTA, B., PALMIERE, E. J. and SELLARS, C. M., Acta Mater. Vol. 49, (2001) pp. 785.

59 TULING, A. S. and BANKS, K. M., "A TEM study of precipitation of AlN during roughing of low carbon-boron steel" IMMRI, University of Pretoria, not published.

60 ENGL, B. and DREWES, E. J., Technology of Continuously Annealed Cold Rolled Sheet Steel, PRADHAN, R., ed. "On the roll of solute nitrogen on short time annealing of sheets", Proc. Symp., The Metallurgy Society of AIME, Michigan, (1984), pp. 123 – 138.

61 KIESSLING, R. and LANGE, N., ISI Publication No. 100 (1966).

62 MEHMED, F and HARALDSEN, H, Das magnetische Verhalten der allotropen modifikationen des mangan(II)-sulfids, Z. anorg. Chem. Vol. 235, (1938), pp. 193 – 200.

63 BAKER, T. J. and CHARLES, J. A., JISI, (1972) pp. 210, 702.

64 OIKAWA, K., OHUCHI, Y. and ISHIDA, K., "Effect of Ti and Al addition on the distribution of MnS inclusion in steel during solidification" THERMEC'97, Inter. Conf. Thermomechanical Processing of Steels and Other Materials, Vol. 1, Ed. CHANDRA, T. and SAKAI, T., pp. 859.

65 TURKDOGAN, E. T., IGNOTOWICZ, S and PEARSON, J., JISI, Vol. 180, (1955), pp. 349 – 354.

References

66 LESLIE, W. C., RICKETT, R. L., DOTSON, C. L., and WATSON C. S., Trans. ASM, Vol. 46, (1954) pp. 1470 – 1497.

67 GARBARZ, B., MARCISZ, J. and WAJTAS, J., "TEM analysis of fine sulphides dissolution and precipitation in steel" Materials Chemistry and Physics, Vol. 81 (2003) pp. 486 – 489.

68 FRAWLEY, L. D., PRIESTNER, R. and HODGSON, P. D., "Effect of Sulphur in Thin Slab Direct rolled Mild Steel", THERMEC'97, Inter. Conf. Thermomechanical Processing of Steels and Other Materials, Vol. 1, Ed. CHANDRA, T. and SAKAI, T., pp. 2,169 – 2,175.

69 CHENG, W. C., JAW, J. H. and WANG, C. J., "A study of aluminium nitride in a Fe-Mn-Al-C alloy" Acta Materialia, Vol. 51, (2004), pp. 279 – 283.

70 MASSARDIER, V., VORON, L., ESNOUF, C. and MERLIN, J., "Identification of the nitrides formed during the annealing of low carbon low-aluminium steel", Journal of Material Science, Vol. 36, (2001), pp. 1363 – 1371.

71 YU, H., KANG, Y., ZHAO, Z. and SUN, H., "Morphology and precipitation kinetics of MnS in low carbon steel during thin slab continuous casting process", Journal of Iron and Steel Research International, Vol. 13 No. 5, (2006) pp. 30 – 36.

72 MADARIAGA, I. and GUTIERREZ, I., "Acicular ferrite microstructures and mechanical properties in a medium carbon forging steel", Material Science Forum, Vols. 284 – 286, (1998), pp. 419 – 426.

73 BRAMFITT, B. L., Met. Transactions, Vol. 1, (1970), pp. 1987 – 1995.

References

74 LIU, Z, KABAYASHI, Y. and NAGAI, K., "Crystallography and precipitation kinetics of copper sulphide in strip casting low carbon steel", ISIJ International, Vol. 44, (2004), pp. 1560 – 1567.

75 TITCHENER, A. L. and BEVER, M. B., Prog. Met. Phys. Vol. 7, (1958) pp. 247.

76 BEVER, M. B., HOLT, D. L. and TITCHENER, A. L., Pror. in Material Science, Vol. 17, (1973), pp. 1.

77 HAESSNER, F., Ed. Recrystallisation of Metallic Materials, 2nd edition, Publ. Reider-Verlag, Stuttgart, (1978).

78 DOHERTY, R. D., HUGHES, D. A., HUMPHREYS, F. Y., JONAS, J. J., JUNSEN, D. J., KASSNER, M. E., KING, W. E., McNELLEY, T. R., McQUEEN, H. J. and ROLLETT, A. D., "Current issues in recrystallisation: a review", Materials Science and Engineering A238, (1997), pp. 219 – 274.

79 CLAREBROUGH, L. M, HARGREAVES, M. E. and LORETTO, M. H., Proc. Roy. Soc. A232 (1955) pp. 252.

80 EGGLESTON, R. R., J. Appl. Phys. Vol. 23 (1952) pp. 1400.

81 LUTTS, A. H. and BECK, P. A., Trans. AIME, Vol. 200, (1954) pp. 257.

82 DROUARD, R., WASHBURN, J. and PARKER, E. R., Trans. AIME, Vol. 197 (1953) pp. 1226.

83 KUHLMANN, D., Z. Phys. Vol. 24, (1948) pp. 468.

84 LI, J. C. M., in Recrystallisation, Grain Growth and Textures, ed. MORGOLIN, ASM, Metals Park, Ohio, (1966) pp. 45.

85 KOLMOGOROV, A. N., Akad. Nauk. SSSR, IZV. Ser. Mat., Vol. 1, (1937), pp. 335.

References

86 JOHNSON, W. A., and MEHL, R. F., Trans., AIME, Vol. 135, (1939), pp. 416.

87 AVRAMI, M., J. Chem. Phys. Vol. 7, (1939), pp. 103; ibid, Vol. 8, (1940), pp. 212; ibid, Vol. 9, (1941), pp. 177.

88 VANDERMEER, R. A. and GORDON, P., in Recovery and Recrystallisation of Metals, ed. HIMMEL, L., Interscience, New York, (1963) pp. 211.

89 PRICE, C. W., "Use of the Kolmogorov-Johnson-Mehl-Avrami kinetics in the recrystallisation of metals and crystallisation of metallic glasses", Acta Metall. Mater. Vol. 38, No. 5, (1990) pp. 727 – 738.

90 FURU, T., MARTHINSEN, K. and NES, E., "Modelling recrystallisation," Materials Science and Technology, Vol. 6, (1990) pp. 1093 – 1102.

91 BURKE, J. E. and TURNBULL, D., Prog. Met. Phys. Vol. 3, (1952) pp. 220.

92 LESLIE, W. C., MICHALAK, J. T and AUL, F. W., "Iron and its dilute solutions," Ed Spencer et al, Publ. Interscience NY (1963) pp. 119.

93 HUMPHREYS, F. J., "Nucleation in Recrystallisation," Materials Science Forum, Vols. 467 – 470 (2004) pp. 107 – 116.

94 BAILEY, J. E., Phil. Mag. Vol. 5 (1960) pp. 833.

95 CAHN, R. W., in: Recrystallisation, Grain Growth and Textures, ed. Margolin, H. ASM, Metals Park, Ohio, (1966) pp. 99.

96 CHARMERS, B., Principles of Solidification, John Wiley and Sons, New York, (1964) pp.20.

References

97 BYRNE, J. G., "Recovery, Recrystallisation and Grain Growth", Publ. McMillan NY (1965) pp.74.

98 GOTTSTEIN, G. and SHVINDLERMAN, L. S., Scripta Metall. 27, (1992) pp. 1515.

99 BECK, P. A. and SPERRY. P. R., Journ. Appl. Physics: Vol. 21 (1950) pp. 150.

100 BAILEY, J. E. and HIRSCH, P. B., Proc. Roy. Soc. A267 (1962) pp. 11.

101 BECK, P. A., Adv Physics: Vol. 3 (1954) pp. 245.

102 LI, J. C. M., Journal of Applied Physics, Vol. 33, (1962), pp. 2968.

103 HU, H., Recovery and Recrystallisation of Metals, AIME, HIMMEL, L., ed. (1962), pp. 311.

104 WALTER, J. L. and KOCH, E. F., Acta Met. Vol. 11, (1963), pp. 923.

105 WALTER, J. L. and KOCH, E. F., Acta Met. Vol. 11, (1963), pp. 999.

106 SMITH, C. J. E. and DILLAMORE, I. L., Metal Science, Vol. 4 (1970) pp. 161.

107 ANDERSON, W. A., and MEHL, R. F., Trans. AIME, Vol. 161, (1945), pp. 140.

108 HUTCHINSON, B., JOHNSON, S. and HYDE, L., Scripta Met., Vol. 23, (1989), pp. 671.

109 KöSTER, U., "Recrystallisation involving the second phase", Metal Science, Vol. 8, (1974), pp. 151 – 160.

110 HORNBOGEN, E. and KöSTER, U., "Recrystallisation of Metallic Materials", Ed. HASSNER, F., Publ. Reider Verlag, Stuttgurt, (1978), pp. 159 (Review).

References

111 KöSTER, U. and HORNBOGEN, E., Z. f. Metallkunde, Vol. 59, (1968), pp. 792.

112 KREYE, H. and HORNBOGEN, E., Praktische Metallograpie, Vol. 9, (1970), pp. 349.

113 ZENER, C. and quoted in GLEITER, H. and CHALMERS, B., "High Angle Grain Boundaries", Publ. Pergamon Press, Oxford, (1972).

114 DIMITROV, O., FRAMAGEAU, R and DIMITROV, C, "Recrystallisation of Metallic Materials" Ed. HAESSNER, F, Publ. Riederer Verlag, Stuttgart (1971) pp. 183.

115 FROIS, C. and DIMITROV, O., Ann. Chim. Paris, Vol. 1 (1966) pp. 113.

116 LESLIE, W. C., MICHALAK, J. J. KEH, A. S. and SOBER, J., Trans ASM Vol. 58 (1965) pp. 672.

117 STüWE, H. P., PADILHA, A. F. and SILICIANO, F., Matls. Science and Eng. A333 (2002) pp. 361.

118 GOODENOW, R. H., "Recrystallisation and grain structure in rimmed and Al-killed low carbon steels" Trans. ASM, Vol. 59, (1966), pp. 804 – 823.

119 JOLLEY, W. and WITMER, D. A., in "Recovery, Recrystallisation and Grain Growth Structures in Iron and Steel" Metals Handbook, 8th Ed. Metallography, Structures and Phase Diagrams, pp. 225 – 228.

120 BAIRD, J. D. and ARROWSMITH, J. M., "Recrystallisation behaviour of some high-purity irons", J. Iron and Steel Inst., March 1966, pp. 240 -247.

121 MICHALAK, J. T. and SCHOONE, R. D., "Recrystallisation and texture development in a low carbon, Al-killed steel" Tran.

References

Metallurgy Society of AIME, Vol. 242, (1968), pp. 1149 – 1160.

122 USHIODA, K., SUZUKI, T., ASANO, H and TEZUKA, M., "Influence of Mn content and precipitates on recrystallisation texture formation in cold rolled sheet steels", 37th MWSP Conf. Proc., ISS, Vol. XXXIII, (1996) pp. 897 – 905.

123 OGAWA, R., FUKUTUSKA, T. and YAGI, Y., "Precipitation behaviour of AlN in cold worked high purity Fe-Al-N alloy", Trans. Iron and Steel Inst. Japan, Vol. 12, (1972), pp. 291 – 297.

124 KOZESCHNIK, E., PLETENEV, V., ZOLOTOREVSKY, N. and BUCHMAYR, B., "Aluminium Nitride Precipitation and Texture Development in Batch-Annealed Bake-Hardened Steel" Metallurgical and Materials Transaction A, Vol. 30A, (1999) pp. 1663 – 1673.

125 BAIRD, J. D., "Strain aging of steel – a critical review", Iron & Steel, (May, 1963) pp. 186 – 192.

126 MORRISON, W. B., "Nitrogen in the steel product", Ironmaking and Steelmaking, Vol. 16, No. 2, (1989) pp. 123 – 128.

127 MOULD, P. R.: in "Metallurgy of continuous annealed sheet steel", (ed. BRAMFITT, B. L. and MANGONON, P. L.), (1982), pp. 3 – 33, Warrendale, PA, Metallurgical Society of AIME.

128 SNOEK, J. L., Physica, s'Grav. 8 (1941) pp. 711

129 LESLIE, W. C., "The Physical Metallurgy of Steels", (1981) pp. 73.

References

130 BLATT, F. J., SHROEDER, P. A., FOILES, C. L. and GREIG, D. Thermoelectric Power of Metals, Publ. Plenum Press, New York and London.

131 BLATT, F. J., Proc. Phys. Soc., (1964), 83, pp. 1065.

132 BORRELLY, R., MERLE, P. and ADENIS, D., Light Met., (1989) pp. 703 – 712.

133 ROBERTS, R. and CRISP, R. S., Phil. Mag., (1977), Vol. 36, pp. 81- 89.

134 RAYNE, J. A. and CHANDRASEKHAR, B. S. "Elastic Constants of Iron from 4.2 to 300 K" Physical Rev. Vol. 122, No. 6 (1961), pp. 1714 – 1716.

135 NORDHEIM, L. and GORTER, C. J. (1935) Physica 2, 383.

136 BORRELLY, R. and BENKIRAT, D., Acta Metall., Vol. 33, No. 5, (1985), pp. 855 – 866.

137 BARRACLOUGH, D. R. and SELLARS, C. M., Metal Science, Vol. 13, (1979) pp. 257 – 267.

138 CLAREBROUGH, L. M., HARGREAVES, M. E. and LORETTO, M. H., Proc. Roy. Soc., A232 (1955) pp.252.

139 LUTTS, A. H. and BECK, P. A., Trans. AIME, Vol. 200, (1954), pp. 257.

140 MAGEE, K., MUKUNTHAN, K. and HAWBOLT, E. B., "The application of isothermal recrystallisation kinetics to continuous heating process", Recrystallisation '90, (ed. CHANDRA, T.), The Minerals, Metals & Materials Society, 1990.

141 HILLIARD, J. E., "Measurement of Volume in Volume", Quantitative Microscopy, DeHoff, R. T. and Rhines, F. N, eds. Publ. McGraw-Hill, (1968), pp. 45 – 76.

References

142 HAEβNER, F. and SCHöNBORN, K. H., "Untersuchung der rekristallisationskinetik in hochverformterm Kupfer und Silber mit Hilfer isothermer und an-isothermer kalorischer messungen", Z. Metallkde., Vol. 76 (1985), pp. 198 -207.

143 HAEβNER, F., "The study of recrystallisation by calorimetric methods", Recrystallisation'90, CHANDRA, T., ed. The Minerals, Metals & Materials Society, (1990), pp. 511 – 516.

144 BRAHMI, A. and BORRELLY, R., "Study of aluminium nitride precipitation in pure alloy by thermoelectric power measurements", Acta Mater. Vol. 45, No. 5, (1997), pp. 1889 - 1897.

145 FAST, J. D. and VERRIJP, M. B., J. Iron Steel Inst., 180 (1955) pp. 337

146 MERLIN, J., MERLE, P., GARNIER, S., BOUZEKRI, M. and SOLER, M., "Experimental Determination of the carbon solubility limit in ferritic steels", Metallurgical and Materials Transactions A, Vol. 33A, (2004), pp. 1655 – 1161.

147 BORRELLY, R. and BENKIRAT, D., Acta Metall. Vol. 33, (1985), pp. 855 – 866.

148 BIRON, I. BORRELLY, R., DELANUAE, P. and THOMAS, P. J., "Application of the thermoelectric power measurements to control aluminium nitride precipitation in low carbon steels", Mém. Sci. Rev. Mét., Vol. 11, (1991), pp. 725 – 733.

149 GERMAZ, M., ARYOUNI, M. and MOSSER, A., Surf. Sci. Lett., Vol. 227, No. 1-2, (1990), pp. L109 – L111.

150 OGAWA, R., FUKUTSUKA, T. and YAGI, Y., Trans. ISIJ, Vol. 12, (1972), pp. 291.

References

151 HOWE, J. M., Interfaces in Materials: atomic structure, thermodynamics and kinetics of solid-vapour, solid-liquid and solid-solid interfaces, John Wiley & Sons, Inc., New York, (1997), pp. 378.

152 WAGNER J. M. and BECHSTEDT, F., "Properties of strained GaN and AlN: *Ab initio* studies", Physical Review B 66, 115202, (2002), pp. 1 – 20.

153 WYCOFF, R. W. G., International Tables for Crystallography, Kynock Press, Birmingham, (1952-1962).

154 CHRISTIAN, J. W., in "Phase Transformation", Physical Metallurgy, CAHN, R. W., Ed. Publ. North-Holland Co., Amsterdam-London, (1970), pp. 486

155 MATHIESEN, H., in "Computer simulation of microstructural evolution", ASM Symp. Toronto, Canada, Oct. (1985), pp. 189 – 199, Warrendale, PA, Metallurgical Society of AIME.

156 MESSAGER, C and DIMITROV, O., Comptes Renus, Acad., Sc., Vol. 251, (1960), pp. 88.

157 GLADMAN, T., The Physical Metallurgy of Microalloyed Steels, Institute of Materials, London, (2002), pp. 312.

158 FURUHARA, T., YAMAGUCHI, K., SUGITA, N. MIYAMOTO, G. and MAKI, T., ISIJ Int., Vol. 43(2003) pp. 1630.

159 SHIMAZU, T., CHIKUMA, K., SAKAI, T. and TANINO, M.: Tetsu-to-Hagane, Vol. 70, (1984) S568.

160 LIU, Z., KOBAYASHI, Y. and NAGAI, K., "Crystallography and precipitation kinetics of copper sulphide in strip casting low carbon steels", ISIJ Inter., Vol. 44, (2004), pp. 1560 – 1567.

References

161 BAIRD, J. D. and ARROWSMITH, J. M., "Recrystallisation behaviour of some high-purity irons", J. Iron and Steel Inst., (1966), pp. 240 – 247.

162 DE SOUZA, T. O. and BUONO, V. T. L., "Optimization of the strain aging resistance in aluminium killed steels produced by continuous annealing", Materials Science and Engineering A354, (2003), pp. 212 – 216.

163 MIZUI, N. and OKAMOTO, A., Proc. Conf. on Development in the Annealing of Sheet Steels, Cincinnati, OH, (1992), The Minerals, Metals and Materials Society, Warrendale, PA, (199), pp. 247 – 259.

164 CORTI, C. W., COTTERILL, P. and FITZPARTICK, G., Int. Met. Rev., Vol. 19, (1974), pp. 77 – 88.

165 HUMPHREYS, F. J. and HEATHERLY, M., "Recrystallisation and related annealing phenomena", Elsevier Science, Oxford, UK, (1995).

166 CHAN, H. M. and HUMPHREYS, F. J., Acta Metall., Vol. 32, (1984), pp. 235.

167 LESLIE, W. C., MICHALAK, J. T. and AUL, F. W., "Iron and its dilute solutions", Ed. SPENCER, C. N. et al, Publ. Inetrscience NY, (1963), pp. 119.

Appendix

Item	Approximate analysis [wt%], N in ppm							Method	Temperature range [°C]	Log[Al][N]	Ref.
	C	Si	Mn	Cr	Ni	Al	N				
A	0.1	0.01	0.4			0.144		Sieverts: 5-65h	1050 - 1350	$1.95-\frac{7400}{T}$	41
B	0.05	0.008	0.35	0.02	0.03	0.02-0.08	5-88	Beeghly	810 - 1260	$1.03-\frac{6770}{T}$	42
C	Fe-Al-N							Beeghly	800 - 1300	$1.79-\frac{7184}{T}$	43
D	0.2	0.5	1.5			0.05	240	Beeghly	900 - 1350	$1.8-\frac{7750}{T}$	44
E	0.2	0.15	0.5	0.02	0.02	0-0.084	0-60	Beeghly	900 - 1200	$0.75-\frac{6180}{T}$	45
F	0.17	0.2	0.4	1	3.4	0-0.216	70	Beeghly	900 – 1200	$0.309-\frac{6015}{T}$	45
G	0.1	0.24	0.8			0.023-0.15	40-140	Beeghly	950 – 1350	$1.48-\frac{7500}{T}$	46
H	0.06		0.24			0.035-0.137	60	Beeghly	800 – 1250	$2.4(wt\%Al)+0.18-\frac{5675}{T}$	47
K	Pure Fe					0.02-0.05	50-200	Beeghly	850 - 1350	$3.577-\frac{10020}{T}$	48
L	0.4	0.45	0.8	1.3	1.5	0.03-0.04	250	Beeghly	850 – 1300	$3.079-\frac{9295}{T}$	48
M								Thermodynamic data		$4.5989-\frac{11568}{T}$	49
N								Thermodynamic data		$6.4-\frac{14356}{T}$	50
O								Thermodynamic data		$4.382-\frac{11085}{T}$	51
P	0.036-0.039		0.30			0.052-0.065	37-41	Beeghly	900 - 1350	$1.21-\frac{6690}{T}$	52